Université de Liège - Faculté des Siences Appliquées

Hasselt University - Faculty of Engineering Technology

Unreinforced clay masonry structures: Advanced characterisation of the seismic behaviour including acoustic issues

Thesis submitted in partial fulfillment of the requirements for the degree of
Doctor of Philosophy in Applied Sciences
and
Doctor in Engineering Technology
by

Christophe Mordant, Ir.

September 2016

© Copyright by Christophe G.L.M. Mordant 2016
All Rights Reserved

Author's contact details

Christophe Gaston Louis Marie MORDANT, Ir.

Structural & Stochastic Dynamics
Research Unit of the Structural Engineering Division
Dept. of Architecture, Geology, Environment and Constructions

Bât. B52/3 Analyse sous actions aléatoires en génie civil
Quartier Polytech 1
Allée de la Découverte, 9
4000 Liège, Belgium

✉ mordant.ch@gmail.com
✆ +32 4 95691594

Members of the Doctoral Jury

Prof. Luc COURARD (President)
Université de Liège, Belgium

Prof. Hervé DEGÉE (Co-Advisor)
Hasselt University, Belgium
✉ herve.degee@uhasselt.be

Prof. Vincent DENOËL (Co-Advisor)
Université de Liège, Belgium
✉ v.denoel@ulg.ac.be

Prof. Serena CATTARI
University degli Studi di Genova, Italy

Dr. Rob VAN DER PLUIJM
Wienerberger AG, Chairman EC 6, Netherlands

Prof. Bram VANDOREN
Hasselt University, Belgium

Abstract

Unreinforced masonry (URM) is traditionally used in North-Western Europe as load-bearing solution for low- to mid-rise buildings. These regions are characterised by a low-to-moderate seismicity. Hence, the earthquake action has to be considered in the structural design. An adequate consideration of the seismic action requires to properly understand how the URM structures behave under this specific dynamic action and investigations are still needed in that field. The influence of openings and walls perpendicular to the seismic action are two main issues. Moreover, the seismic response of these structures is affected by technical solutions developed to face the demand in terms of building physics performances. Even though, these solutions are not yet integrated in current standards.

This thesis aims at improving the understanding of the seismic behaviour of URM structures using a particular type of masonry bonding, for constructional efficiency purposes. Hollow clay blocks are assembled by thin-bed layered glue-mortar joints and a tongue-and-groove system for the head joints. The consequences of specific details – such as an opening, a perpendicular wall or soundproofing rubber layers – are also studied.

Four experimental campaigns are presented. Fourteen URM sub-structures including specific details are tested in static-cyclic and dynamic conditions. Details of the set-up, instrumentation layout and testing procedures are given. Processing of the data is then performed and conclusions are drawn. Regarding the shake table tests, a general rocking behaviour strongly dependent on the length of the wall and the presence of rubber, is observed. Recommendations for the consideration of soundproofing devices and for the openings are proposed. The contribution to the strength of perpendicular walls is also highlighted.

Based on the dynamic characterisation of the specimens, equivalent mechanical properties are calibrated thanks to the frequency equation, derived from the Timoshenko beam theory. Two sets of boundary conditions are defined to fit the testing configurations. The relevance of this theory is assessed and the importance of each term of the equation is discussed.

In order to extend the results to complete buildings, the tested specimens are modelled in a software implementing an equivalent frame at the macro-scale. A multi-linear material law is calibrated based on a single specimen chosen as reference, in order to reproduce the experimental force-displacement curve. This law is then used for all specimens built in the same masonry type, independently of their geometry. A good approximation is obtained, even if the consideration of perpendicular walls could be improved.

The shear capacity of non-rectangular URM walls depends on the compressive length. Its exact expression is thus developed with due consideration of the perpendicular section. Non–linearities are observed due to the presence of the perpendicular section and simplifications are made for hand calculations. Both the use of the exact and simplified expressions in the assessment of the shear resistance provide results similar to the experiments.

Finally, the modelling of the rocking motion is investigated. The walls without soundproofing devices are modelled following different existing models and their predictions are compared with experimental measurements, showing that masonry cannot be assumed as rigid. A main issue is the handling of the transition with impacts. A new model including two rigid blocks and flexible and viscous layers is developed to reproduce the rocking behaviour of walls including rubber layers. In presence of rubber, the URM wall can be considered as rigid and model predictions satisfactorily corroborate the experimental measurements.

Keywords: unreinforced masonry, seismic behaviour, soundproofing devices, static-cyclic test, shake table test.

Résumé

Le parc immobilier des pays du nord-ouest de l'Europe est, en majeure partie, constitué de bâtiments de hauteur modeste, construits en maçonnerie non armée. La conception de ces bâtiments doit être effectuée en tenant compte de l'aléa sismique car la sismicité de ces régions est qualifiée de faible à modérée. Cependant, le comportement des structures en maçonnerie non armée sous les effets d'un tremblement de terre n'est pas encore totalement appréhendé et une meilleure compréhension est nécessaire afin de garantir un niveau de sécurité suffisant. L'influence d'ouvertures et la présence de murs perpendiculaires font partie des principaux sujets à éclaircir. De plus, des solutions techniques ont été développées pour répondre aux exigences de plus en plus strictes concernant les performances énergétiques des bâtiments (PEB). Bien que ces solutions modifient le comportement des bâtiments en maçonnerie non armée, aucune disposition n'y fait mention dans les normes sismiques actuelles.

Cette thèse contribue à une meilleure compréhension du comportement sous action sismique des structures en maçonnerie non armée dont l'appareillage est réalisé avec des joints horizontaux collés et un système de tenons et mortaises. Les blocs d'argile mis en œuvre sont creux. La présence de détails particuliers – comme une ouverture, un mur perpendiculaire ou un dispositif d'insonorisation en caoutchouc – et leurs conséquences sont également étudiées.

Dans cette optique, quatre campagnes expérimentales sont présentées. Au total, quatorze structures en maçonnerie non armée ont été testées dans des conditions statiques et dynamiques. Les informations relatives aux essais (structures, instrumentation, déroulement, etc.) sont d'abord fournies. Les données sont ensuite exploitées et interprétées afin que des conclusions en soient tirées. Parmi celles-ci, des recommandations pour la prise en compte des couches de caoutchouc et la création d'ouvertures sont proposées. Un intérêt particulier est donné à la contribution des murs perpendiculaires à la résistance globale.

Afin de définir des propriétés mécaniques équivalentes pour les murs testés sur table à secousses, l'équation de fréquence est déterminée en utilisant la théorie des poutres de Timoshenko pour deux modèles adaptés aux murs considérés. L'intérêt de cette théorie est évalué et l'importance des différents termes de l'équation est étudiée.

Les structures testées sont analysées à l'aide d'un logiciel numérique dans lequel elles sont modélisées par des éléments de poutre non linéaires. La comparaison des courbes "force-déplacement" expérimentales et numériques montre une bonne correspondance, même si la prise en compte des murs perpendiculaires peut être améliorée. La loi matérielle définie pour les éléments semble être valable pour toutes structures utilisant les mêmes matériaux et appareillage, étendant de ce fait les résultats expérimentaux.

La résistance au cisaillement de murs non rectangulaires fait l'objet d'une attention spéciale. Celle-ci dépend de la longueur comprimée de la section dont l'expression exacte est développée et linéarisée. Ces deux formulations sont intégrées dans la méthode de vérification proposée par les normes et fournissent des résultats proches des valeurs expérimentales.

Finalement, le comportement en bascule est abordé. Les résultats expérimentaux des murs sans caoutchouc sont comparés aux prédictions obtenues à l'aide de modèles existants. Les principales conclusions sont que le mur en maçonnerie ne peut être considéré comme un bloc rigide et que la gestion des impacts est critique. Un nouveau modèle est développé pour les murs avec des dispositifs en caoutchouc. En présence de ceux-ci, l'utilisation d'un bloc rigide pour représenter le mur en maçonnerie est valable et le modèle reproduit de manière satisfaisante les mesures expérimentales.

Overzicht

Ongewapend metselwerk wordt traditioneel gebruikt in Noord-West Europa als dragende oplossing voor lage tot middelhoge gebouwen. Deze regio's worden gekenmerkt door een lage tot matige seismische activiteit en de seismische krachten dienen dus in het constructief ontwerp te worden beschouwd.

Dit proefschrift focust op een beter begrip van het seismische gedrag van structuren opgebouwd uit een bepaald type van ongewapend metselwerk, namelijk holle baksteen blokken gemetseld met dunne horizontale voegen van lijmmortel en een tand en groef systeem als verticale voegen. De gevolgen van specifieke details, zoals openingen in de wanden, aanwezigheid van wanden loodrecht op de richting van de aardbeving of plaatsing van geluidsisolerende rubberlagen, worden in het bijzonder onderzocht.

Vier reeksen van experimentele testen worden gepresenteerd. Veertien substructuren worden in cyclische en dynamische omstandigheden getest. Details van de proefopstelling, van de instrumentatie lay-out en van de proefprocedures worden gegeven. De resultaten worden verwerkt, gevolgd door de conclusies. Wat de dynamische proeven betreft is een algemeen “rocking” gedrag vastgesteld, sterk afhankelijk van de lengte van de wand en van de aan- of afwezigheid van een rubberlaag. Aanbevelingen voor de behandeling van elementen voor geluidsisolatie en van de openingen worden voorgesteld. De bijdrage van de loodrechte wanden aan de sterkte wordt ook benadrukt.

De Timoshenko balkentheorie wordt gebruikt om een frequentievergelijking af te leiden. De randvoorwaarden zijn gedefinieerd om met de experimentele configuraties overeen te komen. De relevantie van de gebruikte theorie en het belang van elke term van de vergelijking worden dan besproken. De frequentievergelijking wordt uiteindelijk gebruikt om equivalente mechanische eigenschappen van de proefstukken te kalibreren.

De beproefde monsters worden gemodelleerd aan de hand van equivalente raamwerkmodellen. Een multilineaire constitutieve wet wordt eerst gekalibreerd op basis van een referentie proefstuk. Deze gekalibreerde wet wordt vervolgens gebruikt voor de simulatie van alle proefstukken opgebouwd uit hetzelfde soort metselwerk, ongeacht hun geometrie en drukniveau. Een goede benadering wordt verkregen, hoewel de behandeling van loodrechte wanden zou kunnen worden verbeterd.

De afschuifsterkte van metselwerk wanden hangt van de lengte van het gedrukte deel van de wand af. Deze lengte moet in principe worden berekend rekening houdend met de haakse gedeelten van de muren. Een exacte analytische uitdrukking wordt bepaald. Niet-lineariteiten veroorzaakt door de aanwezigheid van het loodrechte gedeelte zijn vastgesteld en vereenvoudigingen zijn voorgesteld met het oog op handberekeningen. Zowel het gebruik van de exacte als van de vereenvoudigde aanpakken leveren resultaten op vergelijkbaar met de experimenten wat betreft de afschuifcapaciteit.

Tenslotte is het modelleren van de “rocking” beweging onderzocht. De muren zonder geluidsisolatielagen zijn gemodelleerd volgens verschillende bestaande modellen en de voorspellingen ervan worden vergeleken met de experimentele metingen, waaruit blijkt dat metselwerk niet kan worden beschouwd als oneindig stijf. Een belangrijk aspect van dit rocking probleem is de behandeling van de overgang bij de impact. Een nieuw model met twee stijve blokken en flexibele en viskeuze lagen is uitgewerkt om het rocking gedrag van wanden met rubberlagen te reproduceren. In aanwezigheid van rubber kan de wand wel worden beschouwd als oneindig stijf en modelvoorspellingen komen dan goed overeen met de experimentele metingen.

Acknowledgments

First and foremost, I would like to express all my gratitude to my advisors, Prof. Hervé Degée and Prof. Vincent Denoël, for their confidence and time. In spite of professional events, Prof. Degée has continued to give attention and interest in my research. Our collaboration has begun since my Master dissertation and this work was for me an unique opportunity to get interested in masonry structures. I also acknowledge Prof. Denoël for his continuous support and involvement in my work. Your suggestions and guidance enhanced the quality of this thesis.

I am also grateful to the members of the jury of my thesis for their interest and acceptance of the evaluation of my thesis.

These four years of PhD research were the occasion to meet many people. I would like to thank Hélène, Lylia and Teodora for the time spent in the same office. I also appreciated the lunch breaks and teatimes with Ana, Andrea, Timothée and my others colleagues. The various talks and laughs are a part of my best memories and I keep your gifts from abroad as a treasure.

To my beloved family, thanks a lot for your support and encouragements in all circumstances. I hope to fully enjoy future moments with you and, in particular, take care of my goddaughter Louise.

Last but not least, this thesis would not be the same without my fiancée, Caroline. I cannot thank you enough for your unconditional love, understanding and support. Definitely, the best breakfasts are made of scramble eggs, orange juice and the song “Eye of the Tiger”.

This research would not have been possible without the financial assistance of the Fund for Training and Research in Industry and Agriculture (FRIA, F.R.S. – FNRS), Brussels, Belgium. Thanks are also addressed to Wienerberger SA for the supply of the masonry blocks and, especially, to Luc Vasseur for the great enthusiasm he showed in my research.

In an earthquake, I shouldn't run out of the house - I should run into it.

Tony Danza

Contents

Abstract ix

Résumé xi

Overzicht xiii

Acknowledgement xv

I Introduction 1

- I.1 Context and motivations 2
  - I.1.1 Evolution of the wall 2
  - I.1.2 Seismic design of modern load-bearing URM walls 4
- I.2 Outline of the thesis 5
- I.3 Personal contributions 6

II Experimental campaigns on URM sub-structures including specific detailing 9

- II.1 Introduction 10
- II.2 Static-cyclic tests on simple walls including specific detailing 12
  - II.2.1 Description of the specimens 12
  - II.2.2 Testing procedure 13
  - II.2.3 Test observations and results 14
  - II.2.4 Interpretation and discussion 19
- II.3 Static-cyclic tests on T-shaped walls 24
  - II.3.1 Description of specimens 24
  - II.3.2 Testing procedure 25
  - II.3.3 Test observations and results 26
  - II.3.4 Interpretation and discussion 29
    - II.3.4.1 Push-over curves 29
    - II.3.4.2 Influence of the perpendicular wall and of the compression level 30
    - II.3.4.3 Behaviour of the wall connection 31
    - II.3.4.4 Behaviour of the flange 31
    - II.3.4.5 Equivalent mechanical properties 32
- II.4 Shake table tests on simple walls including soundproofing devices 34
  - II.4.1 Description of the specimens 34
  - II.4.2 Testing procedure 35

II.4.2.1 Instrumentation 35
II.4.2.2 Input signal and test sequences 36
II.4.3 Observations and experimental results 38
II.4.3.1 Observations 38
II.4.3.2 White noise tests 39
II.4.3.3 Shake table tests 41
II.4.4 Interpretation and discussion 46
II.4.4.1 Interaction with the steel frames 46
II.4.4.2 Rocking behaviour 46
II.4.4.3 Influence of rubber layers 47
II.4.4.4 Compressive length 48
II.4.4.5 Push-over curves 50
II.5 Shake table tests on frames with T- and L-shaped piers 52
II.5.1 Description of the specimens 52
II.5.2 Testing procedure 54
II.5.2.1 Instrumentation 54
II.5.2.2 Input signal and test sequences 54
II.5.3 Observations and experimental results 58
II.5.3.1 Observations 58
II.5.3.2 White noise tests 59
II.5.3.3 Shake table tests 66
II.5.4 Interpretation and discussion 75
II.5.4.1 Pushover curves 75
II.5.4.2 Rocking behaviour 76
II.5.4.3 Influence of the loading case 76
II.5.4.4 Torsion effects 78
II.5.4.5 Influence of the connection method 78
II.6 Conclusions 79

III Frequency equation for the identification of equivalent mechanical properties for URM walls 83
III.1 Introduction 84
III.2 Model description using Timoshenko beam theory 86
III.2.1 Equations of motion 86
III.2.2 Models and boundary conditions 88
III.3 Frequency equations 90
III.3.1 Frequency equation of the first model 90
III.3.2 Frequency equation of the second model 91
III.4 Parametric study of beam models and mode shapes 92
III.4.1 Comparison of the Euler-Bernoulli and Timoshenko beam models . . 92
III.4.2 Parameters related to the additional upper mass 93
III.4.3 Parameters related to the stiffnesses of the base and of the mass-beam connection 96
III.4.4 Mode shapes 98
III.5 Determination of equivalent mechanical properties 99
III.5.1 Fundamental frequency using standards recommendations 99
III.5.2 Characterization of the masonry mechanical properties 100

III.5.3 Characterization of the rubber mechanical properties 102
III.6 Conclusions 104

IV Numerical modelling of URM sub-structures 107
IV.1 Introduction 108
IV.2 Modelling of masonry at the macro-scale 109
IV.3 Numerical analysis of modern URM sub-structures 110
IV.3.1 Static cyclic tests on simple walls including specific details 110
IV.3.1.1 Simple wall without any specific details 110
IV.3.1.2 Walls with acoustic layers 114
IV.3.1.3 Walls with an opening 117
IV.3.2 Shake table tests on simple walls 119
IV.3.3 Static cyclic tests on T-shaped walls 121
IV.4 Conclusions 124

V Shear capacity of non-rectangular URM walls 127
V.1 Introduction 128
V.2 Compressive length for non-rectangular cross-section 129
V.2.1 Expression of the compressive length 129
V.2.2 Linearisation of the expression 132
V.2.3 Parametric study of the position and the length of the flange 133
V.3 Design procedure and comparison with experimental results 140
V.4 Conclusions 143

VI Rocking behaviour of two stacked blocks including flexible layers 145
VI.1 Introduction 146
VI.2 Rocking behaviour of specimens without rubber 147
VI.2.1 Modified Housner's theory 147
VI.2.2 Application of the modified Housner's theory 150
VI.2.3 2-stacked-block model 152
VI.3 Rocking behaviour of specimens including rubber layers 156
VI.3.1 2-stacked blocks with flexible and viscous interfaces model 156
VI.3.2 Application of the 2-stacked blocks with flexible and viscous interfaces model 160
VI.4 Conclusions 162

VII Conclusions and perspectives 165
VII.1 Conclusions 166
VII.2 Perspectives for future works 167

A Characteristics of the soundproofing rubber layer 183

B Frequency equations 187
B.1 Frequency equation - first model 189
B.2 Frequency equation - second model 189

C TREMURI - Parameters of the material law 195

D Compressive length - example of calculation **199**

Curriculum Vitae **205**

Chapter I

Introduction

I.1 Context and motivations
I.2 Outline of the thesis
I.3 Personal contributions

I.1 Context and motivations

Unreinforced masonry (URM) is a historical and widespread method of construction for a number of buildings, as for instance private dwellings, town halls, churches, aqueducts, etc. (see Figure I.1). In particular, surveys of the housing in European countries, like the United Kingdom [37] or Belgium [117], showed that the main part of the housing stock is made of masonry buildings. As stated by Hendry [42], the use of URM walls in low- to mid-rise buildings presents many advantages since a single element can fulfil different functions (load-bearing elements, fire and weather protection, thermal and acoustic insulation or division of the space) and masonry has a good durability with little maintenance if appropriately selected. The continuous use of URM structures throughout centuries is also explained by the local origin and the diversity of implemented materials (clay, concrete, calcium silicate) as well as the ease of construction.

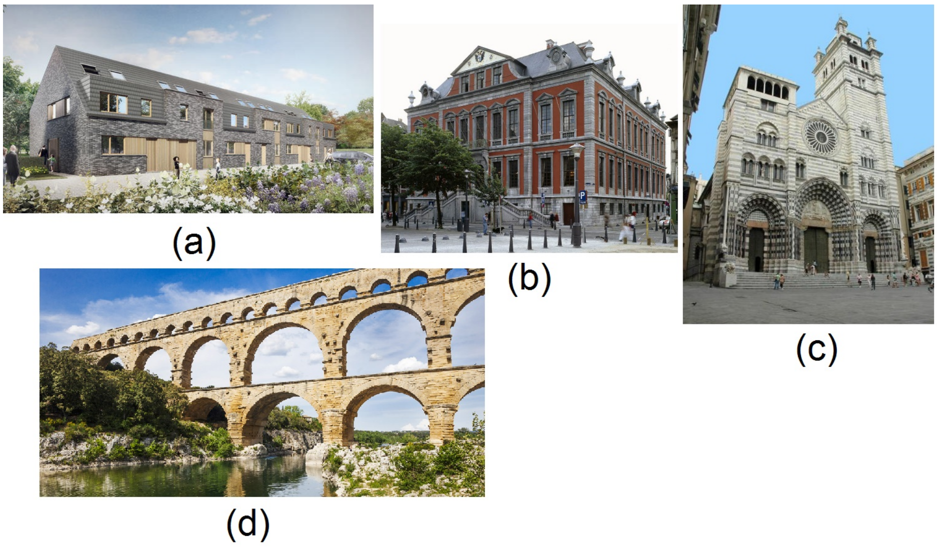

Figure I.1: Examples of masonry typologies : (a) “Le Quartier Durable” in Zulte (BE) [107], (b) “Hôtel de Ville” in Liège (BE) [36], “Catedrale di S. Lorenzo” in Genoa (IT) [30] and “Le pont du Gard” (FR) [105]

I.1.1 Evolution of the wall

Since the 1973 energy crisis, the demand in terms of building physics performances has progressively increased. A specific attention was given to the residential sector due to its weight in the total energy consumption [95]. As a consequence, URM walls have been coupled to other materials to enhance the thermal insulation. These materials can be either placed indoors, outdoors or inside the wall (hollow blocks), influencing its thermal behaviour [9, 53, 10]. In some countries like Belgium, this increasing demand has led to the transition from a monolithic masonry wall to the configuration illustrated in Figure I.2 (a). The load-bearing wall (right) has a reduced thickness, from 14 to 19 cm, and is separated from the facade (left) by a gap where thermal insulation is placed (in yellow). This solution takes advantage of the thermal inertia of the load-bearing wall and protects the insulating material against weather and external deterioration thanks to the facade. From a structural point of view, the load-bearing capacity is however reduced as the structure is thinner.

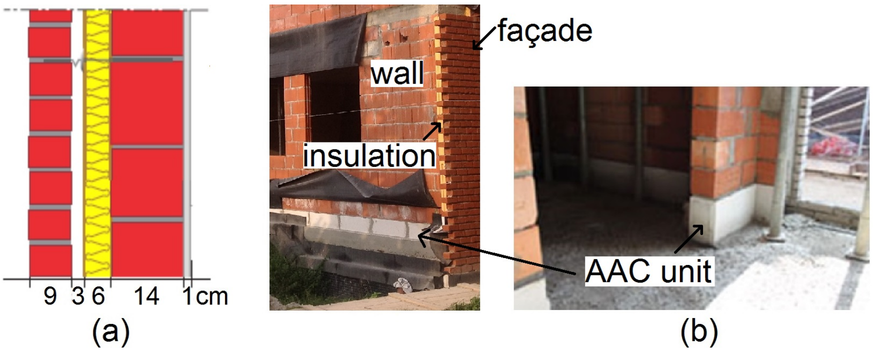

Figure I.2: Configuration of a wall in Belgium

Over the past few years, more and more demanding requirements for the thermal insulation and extensions in the range of applications of URM structures resulted in new modifications of the masonry wall, affecting its strength by reducing again its load-bearing capacity or by increasing the applied compression level. On the one hand, the insulating material becomes more and more thick and highly insulating units, e.g. autoclaved aerated concrete (AAC) blocks or foamglass (see Figure I.2 (b)), have to be implemented at the bottom of the wall to cut thermal bridges. These units are used at the first course of the walls of ground floor to create a thermal break and avoid condensation and mould growth [75]. Their compressive strength is usually lower than the strength of traditional units in clay or concrete. On the other hand, multi-storey apartment buildings, up to 5-6 levels, are now built in pure URM and AAC ("Ytong") units are used as load-bearing solution, as illustrated in Figure I.3 (a) and (b) respectively. These new applications have arisen from the interest of engineers in the load-bearing masonry structures during the past decades, leading to the progressive and continuous switch from good-practice habits to an engineering way of designing these structures. A new generation of structural design codes, for instance the Eurocode 6 [26], translates the improvements in the technical knowledge of masonry structures. It allows the use of the material at a performance level closer to its real ultimate limit state than even in the past, with a sufficient reliability. In addition to the thermal aspects, standards have been developed to guarantee the individual comfort in general. For apartment buildings in particular, it is necessary to provide a sufficient acoustic insulation between adjacent flats. Such a requirement can only be met by the implementation of specific detailing, as for example the use of rubber elements at the bottom and top of the walls to cut the propagation of acoustic vibrations (see Figure I.4).

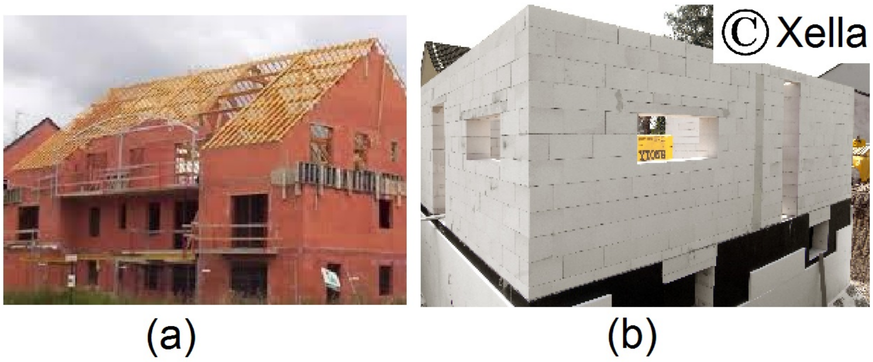

Figure I.3: New applications of URM structures

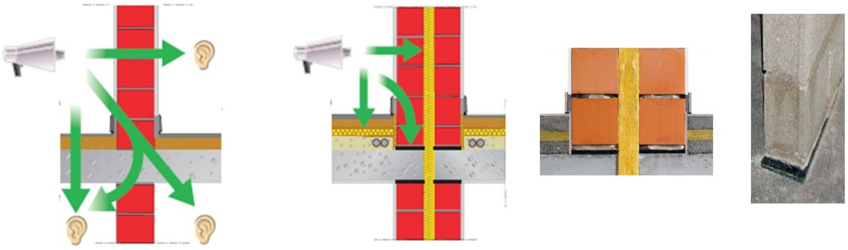

Figure I.4: Acoustic insulation of apartment buildings in load-bearing masonry

This thesis focuses on URM sub-structures made of hollow clay blocks and glue-mortar. The blocks are relatively thin (from 10 to 20 cm) and have a high compressive strength, up to 15 MPa or even more. Thin-bed layered glued joints are implemented with open "tongue-and-groove" head joints for constructional efficiency purposes. The walls include soundproofing rubber layers at their bottom and top.

I.1.2 Seismic design of modern load-bearing URM walls

Besides the gravity loads, URM structures in general have to withstand the seismic loading. Past earthquakes have revealed the poor performances of this type of structures under the seismic action. This is particularly the case for regions with a high seismicity (see the 2009 L'Aquila earthquake [20] or 2016 Amatrice earthquake in Italy), but also for low-to-moderate seismic areas like North-Western European countries, among which Belgium. As an example, the 1983 Liège earthquake caused large damages to private dwellings in the city centre in spite of its moderate magnitude ($M_L = 5.0$ [17]), as shown in Figure I.5. The quality of materials and construction technologies as well as the lack of connection (wall-to-wall or wall-to-floor/ceiling) are the main reasons of the damages [17, 63]. In general, two modes of damage are observed in URM buildings because of earthquakes: the "first damage mode", involving out-of-plane damage and collapse mechanisms (local failure), and the "second damage mode" associated to in-plane response of the walls (global failure) [70].

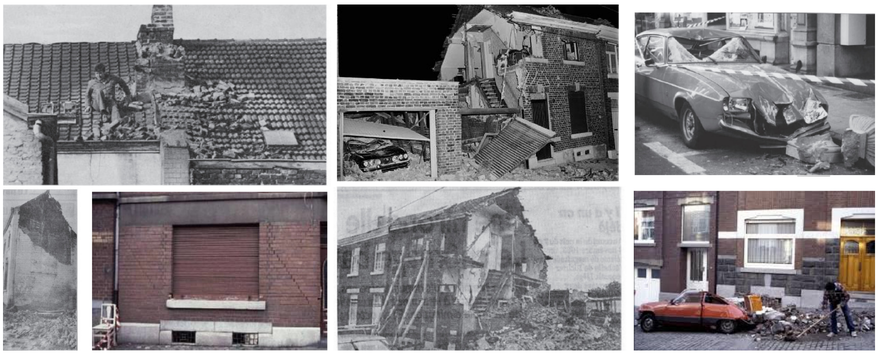

Figure I.5: 1983 Liège earthquake ([17, 58, 86])

The vulnerability of URM buildings partly originates from the non-engineered character of these buildings. Therefore, the adequate consideration of the earthquake impact requires a proper understanding of the structural behaviour under these horizontal dynamic actions. The basic principles of this characterisation and the consequent analysis and design methodologies were proposed by M. Tomaževič [123] and are at the basis of a specific chapter on masonry structures in the Eurocode 8 [116] whose application has become mandatory since 2011 in the European Union. These general considerations need however to be specifically transposed to each particular type of masonry. As recommended by G. Magenes [70], “the use of new materials and constructions systems should be always thoroughly validated with specific reference to seismic response, not only to vertical load bearing strength”. Researchers have also pointed out the over-conservatism and the mismatch with common construction habits of the current standards design rules when comparing the resistance predicted based on code rules with experimental results on full-scale houses [27, 47]. Available methods for the consideration of the coupling of walls by spandrels and the contribution of walls perpendicular to the seismic action are questionable. Moreover, the presence of specific details at the bottom and top of the walls for thermal and acoustic reasons influences the structural stability as it creates a discontinuity between walls and floors. This goes in a way opposite to the basic principle of the seismic resistance (“box-type” behaviour), yet these devices are not currently considered in the seismic codes. Another issue concerns the seismic risk which has become significantly higher because of the decreased thickness of the wall and the increasing height and inherent mass of the buildings, reducing the resistance margin to cope with unexpected seismic action.

This thesis aims at better understanding the seismic in-plane behaviour of the studied URM sub-structures and at investigating the consequences of the presence of soundproofing rubber devices on this behaviour. Particular attention is also given to the contribution of walls perpendicular to the seismic action, as well as the influence of the coupling between walls by spandrels on the seismic response.

I.2 Outline of the thesis

The present thesis includes five main chapters:

- Chapter II - Experimental campaigns on URM sub-structures including specific detailing;
- Chapter III - Frequency equation for the identification of equivalent mechanical properties for URM walls;
- Chapter IV - Numerical modelling of URM sub-structures;
- Chapter V - Shear capacity of non-rectangular URM walls;
- Chapter VI - Rocking behaviour of two-stacked blocks including flexible layers.

All chapters deal with a specific topic related to the study of URM structures and begin with a literature review of this topic.

The experimental campaigns which initiated this work are described in Chapter II. A total of eight full-scale URM walls are tested in static-cyclic conditions in the first two campaigns. The walls present different particularities, like rubber layers at their bottom and top, an opening or a T-shaped cross-section. Last two campaigns consist in shake table tests on URM sub-structures. Test sequences with increasing acceleration levels are performed on four simple walls including soundproofing rubber devices and on two frames with URM piers which have a non-rectangular cross-section. Two different types of masonry units are used and the specimens are built in clay URM with thin-bed layered glued joints and a tongue-and-groove system for the head joints. These campaigns are parts of the Convention First 6231 and the SERIES project from the European Union Seventh Framework Program (FP7/2007-2013) under grant agreement n°227887. In Chapter II , the experimental set-up and the instrumentation layout are summarized and the post-processing of the test measurements is given.

Based on the characterisation of the dynamic properties (natural frequencies, damping ratio and mode shapes) of simple walls, Chapter III derives the expression of the so-called frequency equation from the Timoshenko beam theory, assuming relevant boundary conditions corresponding to the experimental reality. A parametric study is then carried out to study the influence of the different parameters and the importance of the consideration of the shear deformability. The frequency equation is finally used to identify couples of equivalent elastic and shear moduli leading to the same frequency as the fundamental frequency assessed experimentally.

Chapter IV discusses the different modelling strategies existing for URM structures. For computational reasons, the macro-scale approach is chosen and the tested specimens are modelled with equivalent frames in TREMURI. A material law is defined for the beam elements and the values of its parameters are specific to the studied type of masonry, using the equivalent mechanical properties obtained in Chapters II and III, for instance. The numerical predictions are compared to the experimental measurements by means of the global force-displacement curves.

The shear capacity of non-rectangular URM walls is examined in Chapter V. The expression of the compressive length for this type of cross-section is determined. The main parameters are highlighted and simplifications are proposed for current practice. The design procedure given in the Eurocode 6 [26] is then applied to assess the shear resistance of the tested specimens with T- or L-shaped cross-section. In this procedure, the calculation of the compressive length is performed according to the developed exact and simplified expressions. Comparisons with experimental measurements and numerical simulations are finally carried out.

In Chapter VI, the rocking behaviour of rigid blocks is investigated. Existing models are implemented with an event-driven strategy, assuming one or two blocks resting on a rigid support. Numerical simulations resorting to these models attempt at reproducing the experimental observations made during the shake table tests on simple walls. A new rocking model with 2-stacked blocks including flexible and viscous interfaces is developed and is used for walls with rubber devices.

The conclusions summarize the main contributions of this thesis and perspectives for future works are given.

I.3 Personal contributions

The experimental campaigns summarized in this thesis focus on clay URM sub-structures built in thin-bed layered glue-mortar joints and using a tongue-and-groove system for the head joints, for constructional efficiency purposes. These campaigns distinguish themselves from previous experimental programs in three different aspects:

- the in-plane behaviour of URM walls coupled with rubber material used for acoustic reasons is characterised both in static and dynamic conditions. The different test series allow the direct comparison between an URM wall including or not soundproofing devices and the consequences of their presence are highlighted.

- the in-plane seismic response of an URM wall is affected by different factors, among which the compression level, the presence of an opening or the connection to a wall perpendicular to the seismic action. Their influence and contribution are investigated in the four presented campaigns.
- the effects of a global torsion and of two different connection methods between perpendicular sections of a wall are examined in shake table tests.

Based on the outcomes of these experimental research, the following original and personal works are produced:

- regarding the identification of equivalent mechanical properties for URM structural elements, a solution using the natural frequencies of the element is proposed. The expression of the so-called frequency equation is developed assuming a cantilever beam with an additional mass connected at its free end. The connection can be flexible or rigid. This expression differs from previous works by a new formulation of the boundary conditions at the free end and by the consideration of a flexible connection between the free end of the beam and the additional mass. It is believed that the proposed model shall be a reference for future work which would also need to include thin flexible layers.
- the modelling of URM sub-structures with an equivalent frame model uses an existing program (TREMURI). The parameters of the implemented multi-linear material law are however calibrated for a new type of masonry and a sensitivity analysis of the model response to these parameters is performed.
- the design of URM walls subjected to a shear loading is performed according to recommendations of the Eurocode 6. In the given methodology, the calculation of the compressive length is of prime importance. A clear and explicit expression of the compressive length is proposed with due consideration of any perpendicular walls, provided their connection to the shear wall is effective. This expression is linearised for practical use by hand calculations.
- in order to reproduce the rocking behaviour observed during shake table tests, a particular attention is given to the modelling of simple walls including soundproofing devices. A new rocking model with two-stacked rigid blocks is developed and sets itself apart from existing models with regard to the presence of flexible and viscous layers between the lower block and the support and between the lower and upper blocks, in particular.

Chapter II

Experimental campaigns on URM sub-structures including specific detailing

---

II.1 Introduction
II.2 Static-cyclic tests on simple walls including specific detailing
II.3 Static-cyclic tests on T-shaped walls
II.4 Shake table tests on simple walls including soundproofing devices
II.5 Shake table tests on frames with T- and L-shaped piers
II.6 Conclusions

II.1 Introduction

The interest in the behaviour of load-bearing masonry subjected to lateral loads and, in particular, in its seismic response have arisen since the early 70s. The experimental investigations first focused on reinforced masonry [78, 127, 98, 77, 44]. URM structures were disregarded because of a number of failures observed in past earthquakes and their non-engineered character, leading to a lack of confidence in the material properties. Two of the first experimental campaigns on URM walls were carried out by Kwok et al. in 1987 [56] and Mengi and McNiven in 1989 [79] in the perspective of developing a mathematical model for their in-plane behaviour. The former submitted walls to cyclic loads, while these structural elements were tested on a shake table by the latter.

For twenty-five years, several experiments on load-bearing URM have been performed with different ways to represent the seismic action. First, Anthoine et al. [5] and Griffith et al. [39] carried out static-cyclic tests on simple masonry walls built in a traditional bonding, i.e. 1-cm thick mortar bed joints and head joints filled with mortar. Magenes et al. [71] extended these tests to a two-storey building. More recently, masonry typologies widely used in European historical or old buildings were investigated [69, 18, 82]. The behaviour of walls implementing a masonry bonding consisting in thin-bed layered glued joints with a tongue-and-groove system for the head joints, received attention from da Porto et al. [25]. They compared the in-plane behaviour of clay masonry assembled with various types of head and bed joints. This behaviour for AAC masonry walls was also the purpose of cyclic tests performed by Costa et al. [23]. Second, Schermer [111, 112] and Zilch and Schermer [132] operated pseudo-dynamic tests on simple classical and AAC masonry walls. Such tests on full-scale single-storey building were also reported by Paquette et Bruneau [93]. Finally, a number of shake table tests were performed in the last ten years. This type of test provides a better representation of the seismic action. For instance, it allows to catch dynamic phenomena actually observed during real earthquakes. Bergamo et al. [7] conducted some tests on an 1:2 scale tuff URM. After some repairs, the specimen was tested again in order to compare both responses. Bothara et al. [12], Tomazevic and Weiss [124] and Nakagawa et al. [85] investigated the response of a 1:2 scale building with a timber floor, assessed the values of the behaviour factor q thanks to 1:5 scale buildings and developed a new numerical method validated by shake table tests on a full-scale brick masonry house respectively. Interest in the out-of-plane behaviour arose at the same time, leading to some experimental tests [1, 48, 22]. In addition to all these separated tests, the "ESECMaSE" project [108] combined static-cyclic, pseudo-dynamic and shake table tests on different masonry types, constituting the main and most complete experimental campaign to date. Nevertheless, most research projects mainly focused on historical and traditional masonry. There is still a need to better understand masonry types implementing thin-bed layered joints and a tongue-and-groove system for thermal and efficiency purposes.

Besides the experimental testing on classical masonry sub-structures, the influence of rubber soundproofing devices on the behaviour of the classical walls has been studied under gravity loads, but it remains unassessed under shear loading or in dynamic conditions. Although its primary use is different, such a solution can be compared to other specific detailing used to avoid moisture, e.g. damp proof courses and soft layer wall bearings [126], or to base isolation system [51]. Other authors have performed monotonic, static-cyclic and dynamic shear tests on masonry triplets including insulation layers with different materials [40, 131, 83].

As a contribution to the issues discussed in Chapter I, four experimental campaigns are presented in this chapter. The tested specimens are load-bearing clay URM sub-structures built in a particular masonry bonding. The first two campaigns consist in static-cyclic tests carried out at the University of Liège. The last two are performed on the shake table at the EQUALS laboratory of the University of Bristol in the framework of the European FP7 project SERIES. For each campaign, the specimens are first described with their instrumentation and testing procedure. The experimental observations and rough results are then provided. Finally, the results are interpreted and discussed in details.

The different experimental sets aim at :

- improving the comprehension of the studied type of masonry under horizontal shear (campaigns 1 & 2);
- improving the understanding of its dynamic behaviour (campaigns 3 & 4);
- investigating the influence of soundproofing devices on the general behaviour, both in static-cyclic and dynamic conditions (campaigns 1 & 3);
- investigating the efficiency of a new connection type between perpendicular walls and comparing this solution to the classical masonry interlocking (alternated masonwork), both in static-cyclic and dynamic conditions (campaigns 2 & 4);
- assessing the contribution of a perpendicular wall to the in-plane stiffness and strength (2 & 4);
- studying the frame behaviour involved by the presence of an opening in the wall, both in static-cyclic and dynamic conditions (campaigns 1 & 4);
- studying the consequences of a global torsion (campaign 4);
- examining the effects of various load cases (campaign 4).

II.2 Static-cyclic tests on simple walls including specific detailing

II.2.1 Description of the specimens

The first campaign comprises five specimens with the same overall dimensions ($h = 2.800$ m $\times$ $L = 3.000$ m $\times$ $t = 0.138$ m). A first wall without any specific detail is chosen as reference (specimen A1). Two walls include 1-cm thick soundproofing rubber layers at their bottom and top. These layers are continuous (specimen A2) or cut in half (specimen B2). A door opening is created with a reinforced concrete (RC) lintel in the last two walls. The opening is 0.9-m long (L_{ope}) and 2.0-m high (h_{ope}). The support length of the RC lintel is increased from one wall (specimen A3, length of 0.150 m) to the other (specimen B3, length of 0.450 m). The piers have different lengths, namely $L_{long} = 1.200$ m and $L_{short} = 0.900$ m, leading to asymmetric configurations. A sketch of the specimens is given in Figure II.1.

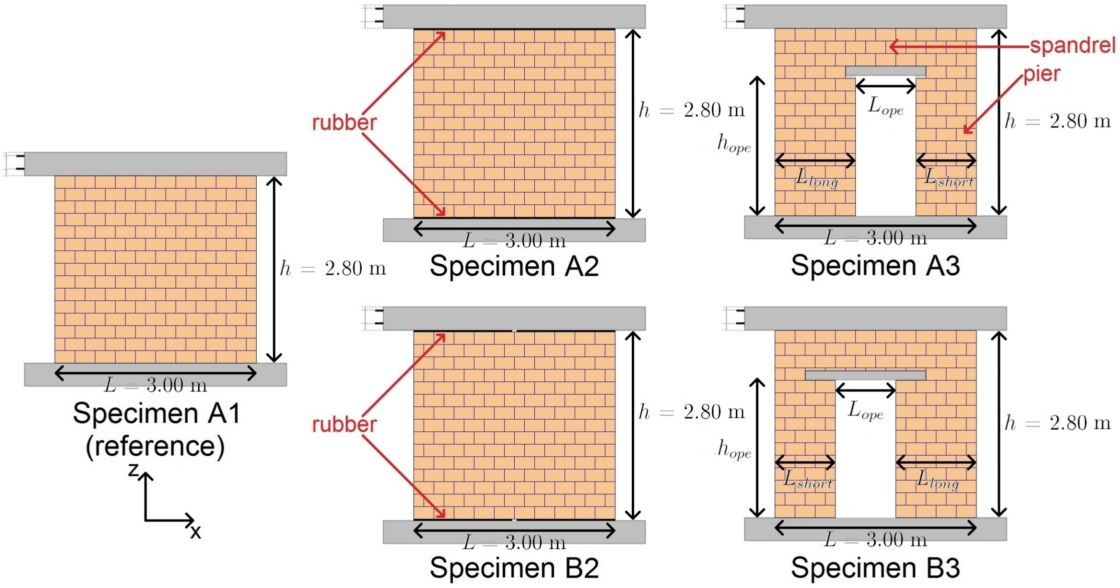

Figure II.1: Static-cyclic tests on simple walls - Sketches of the specimens A1 to B3

All walls are built in thin bed-layered masonry with a tongue-and-groove system for the head joints. They are constructed by professional masons between two RC beams representative of the floors. The units constituting the walls are clay blocks with nominal dimensions (h×l×t) of 0.188 m × 0.300 m × 0.138 m. The material and mechanical properties are given in Table II.1. The tests according to EN 1052-1 do not include the evaluation of the elastic modulus. No specific characterisation has been carried out for the shear behaviour. Usual standard values are therefore considered.

The characteristic shear strength is

$$f_{vk} = 0.5\, f_{vk0} + 0.4\, \sigma_d \tag{II.1}$$

where f_{vk0} [MPa] is given in Table II.1, σ_d [MPa] is the design compressive stress. This strength is limited to $0.045\, f_b$ ($= 0.585$ MPa) as the vertical joints are empty.

The characteristics of the soundproofing layers can be found in Annex A where the elastic modulus of the rubber is given, ranging from 3.0 to 12.0 MPa.

Table II.1: Static-cyclic tests on simple walls - Material and mechanical properties of the masonry units

Properties	Symbol	Value	Units
Density	ρ	850	kg/m^3
Normalised compressive strength of units (En 772-1 Annex A)	f_b	13	MPa
Measured charact. masonry compressive strength (EN 1052-1)	f_k	5.6	MPa
Characteristic compressive strength (EN 1996-1-1)	f_k	4.2	MPa
Characteristic compressive strength (NBN EN 1996-1-1)	f_k	3.9	MPa
Initial shear strength (NBN EN 1996-1-1)	$f_{vk,0}$	0.3	MPa

The preliminary assessment design in accordance with the Eurocodes 6 and 8 predicts the maximum sustainable horizontal shear. The value obtained is 137.7 kN for the specimen A1. The verification of walls with rubber is not covered in the current standards. Furthermore, there is no differentiation with regard to the support length of the RC lintel. The assessment of specimens A3 and B3 leads therefore to the same result, namely 45.4 kN which corresponds to the sum of the capacities of each pier, neglecting their coupling thanks to the spandrel.

II.2.2 Testing procedure

The experimental set-up is illustrated in Figure II.2. The test sequence first consists in the vertical compression of the walls up to 1 MPa. Two hydraulic jacks are used to compress the walls. They are located under the testing slab and the vertical load is transferred to the top of the wall through 2 pairs of Dywidag bars. The load is distributed along the length of the wall thanks to a steel beam placed on the upper RC beam. There is no constraint on the wall since the bars are free to move horizontally. Then, a horizontal displacement is imposed cyclically to the upper RC beam. The imposed displacement is increased every 3 cycles with an increment depending on the wall response. To this purpose, another hydraulic jack is used and its reaction is equilibrated by a truss system connected to the testing slab. There is no particular measure implemented to avoid play in connections when the horizontal load changes direction.

The tests are first performed on specimens A. The experimental outcomes of these tests are used to design the specimens B and lead to differences in terms of instrumentation layout. This latter includes 5 LVDT devices measuring the global displacements of the RC beams (see Figure II.3 left). The distance between sensors V_1 and V_2 is 2.100 m. The global horizontal displacement at the level of the lintel H_{Int} is also recorded whenever relevant (specimens A3 and B3). Two load cells measure the vertical load acting on the wall and the horizontal force applied to the upper RC beam. For the specimens B only (Figure II.3 right), additional LVDTs are placed to measure the horizontal displacement of the corners of the wall and, when there are rubber layers, to study the relative horizontal and vertical displacements between the masonry wall and the RC beams.

An important remark about the test configuration concerns the walls with an opening because of their asymmetry. The horizontal load is applied to the specimen A3 such that the shorter pier is over-compressed when the sign of the load is positive. The opposite is observed in the case of the specimen B3.

The experimental data will be available in the institutional Open Repository and Bibliography of the University of Liège (ORBi [87]).

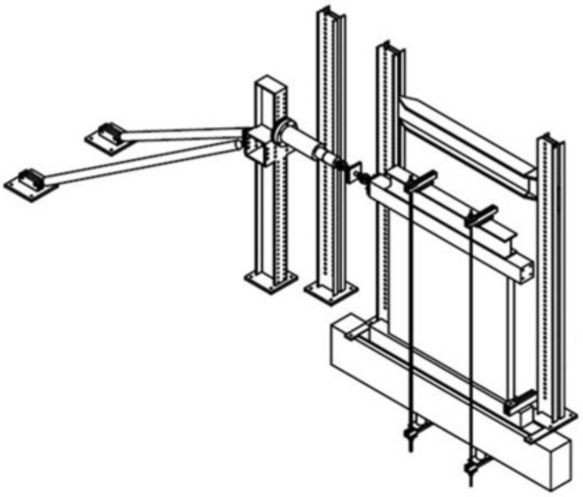

Figure II.2: Static-cyclic tests on simple walls - Experimental set-up

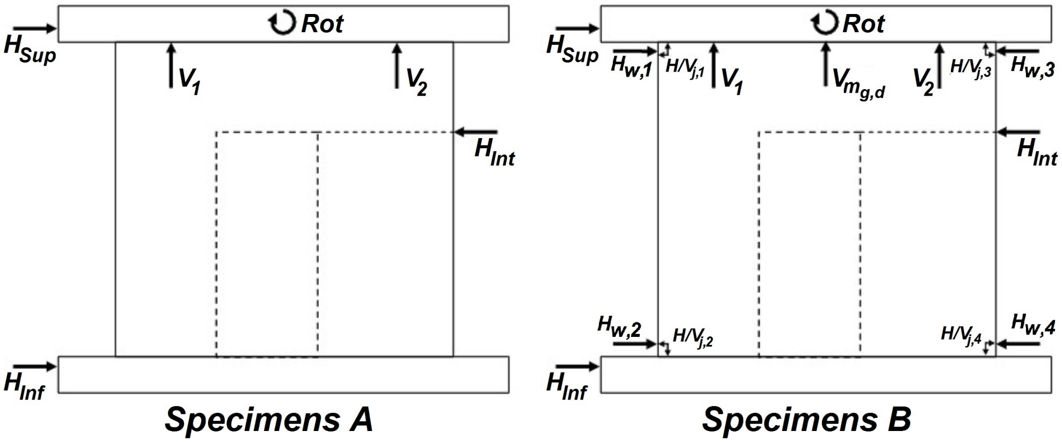

Figure II.3: Static-cyclic tests on simple walls - Instrumentation layouts

II.2.3 Test observations and results

This section presents the rough experimental observations and results. These latter and the conclusions stemming from will be interpreted and discussed in details in the next section.

Observation of the crack pattern provides clues for the determination of the failure mode. The specimen A1 exhibits a diagonal cracking, translating a shear failure (see II.2.4). Crushing of the toe is however observed under the maximum displacement. The collapse mechanism is therefore an interaction between shear and bending failures (see Figure II.4 (a) and (b)). Regarding the specimens including rubber layers, the specimen A2 displays a vertical cracking in the upper two layers of blocks. This one has been initiated during the compression phase. The cyclic test spreads the vertical crack on the superior two-thirds of the wall and causes the diagonal extension of this latter down to the corners of the wall (Figure II.5 (a)). Toe crushing is also observed after the final cycle (Figure II.5 (b)). The failure pattern of the specimen B2 shows sub-vertical cracking starting from the top of the wall and progressively reaching its bottom (Figure II.5 (c)). These observations lead to the conclusion that the failure mode of walls with soundproofing devices is a shear-bending one. Concerning the walls with an opening, a premature collapse of the wall A3 happens. It is due to the crushing of the block directly supporting the lintel in the shorter pier, as shown in Figure II.6 (a). This unexpected failure is avoided for the wall B3 by increasing the support length of the lintel. This last specimen has a shear failure mode since a diagonal cracking of the piers, starting from the blocks located under the lintel, is observed (Figure II.6 (b)). No significant damages are spotted in the spandrel.

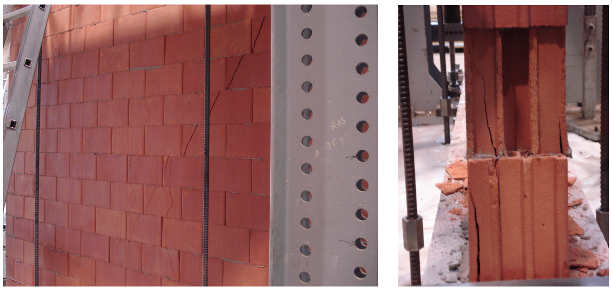
(a) (b)

Figure II.4: Static-cyclic tests on simple walls - Crack pattern of specimen A1

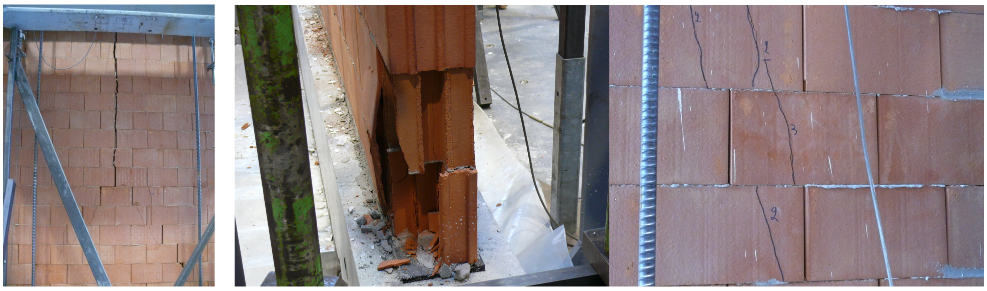
(a) (b) (c)

Figure II.5: Static-cyclic tests on simple walls - Crack pattern of specimens A2 and B2

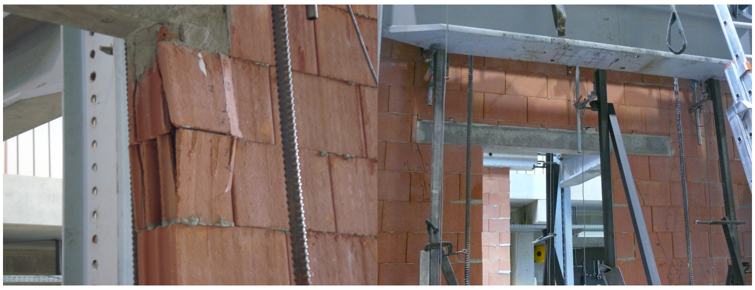
(a) (b)

Figure II.6: Static-cyclic tests on simple walls - Crack pattern of specimens A3 and B3

The response of the specimens is characterised by the force-displacement curve. For the compression phase, this curve is defined by introducing

$$P_{comp} \qquad \text{and} \qquad d = 0.5\,(V_1 + V_2) \tag{II.2}$$

as the vertical compression obtained by the direct measurement of the vertical load and the average value of the recorded vertical displacements of the upper RC beam, respectively. The curve related to static-cyclic phase requires the introduction of

$$P_{shear} \qquad \text{and} \qquad \delta = \frac{H_{sup} - H_{Inf}}{h} \tag{II.3}$$

as the horizontal shear given by the direct measurement of the horizontal load and the drift of the specimen derived from the horizontal displacements of the upper and lower RC beams, respectively. The vertical displacementsV_1 and V_2 are slightly different at the end of the compression phase, inducing a rotation of the upper RC beam and a horizontal displacement. As a consequence, the $P_{shear} - \delta$ curve does not start at the origin of the axes. The curves are plotted in Figure II.7 for the compression and in Figure II.8 for the static-cyclic phase.

In Figure II.7, the force P_{comp} is equal to 417.8 kN and the displacement d is about 1.1 mm for the reference wall (black). P_{comp} is halved for the specimens A2 (cyan) and B2 (blue), whereas d is three to four times larger. Regarding the walls with an opening, P_{comp} is about 300 kN for both walls. The displacement d however differs from A3 (magenta) to B3 (red), with a magnitude of 1.1 mm and 0.7 mm respectively. Information given by Figure II.8 is tabulated in Table II.2. The results are presented in terms of maximum force $P_{shear,max}$ and drift δ_{max} measured in the positive and negative directions. The positive (negative) direction refers to a positive (negative) drift. A last result is the dissipated energy, calculated by the integral of the $P_{shear} - \delta$ curve.

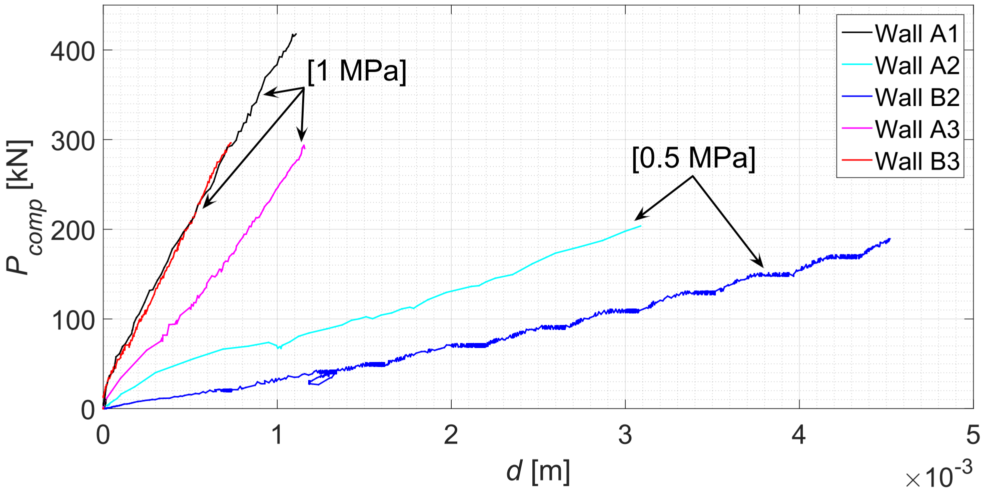

Figure II.7: Static-cyclic tests on simple walls - Force-displacement curves (vertical compression)

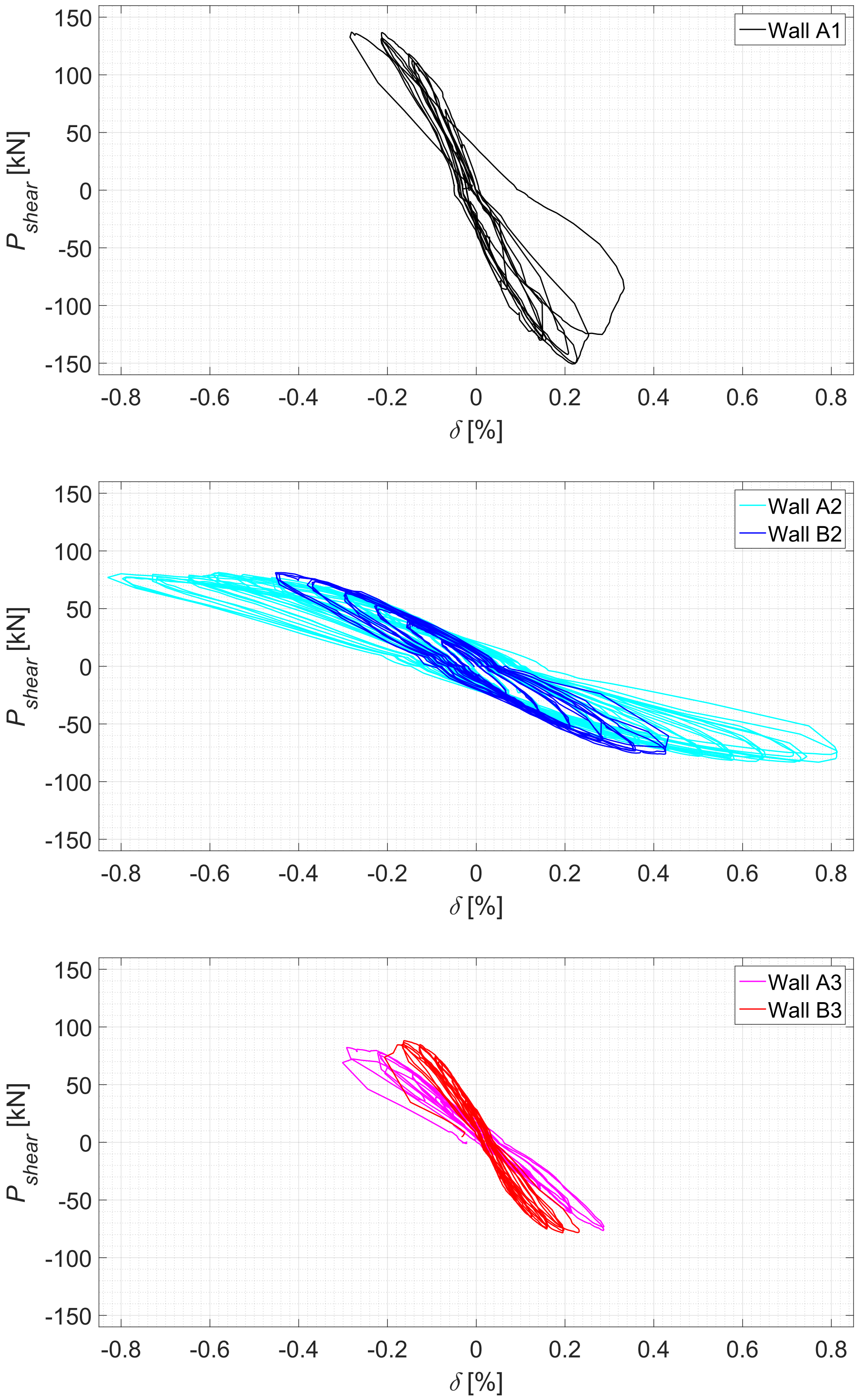

Figure II.8: Static-cyclic tests on simple walls - Force-displacement curves (static-cyclic)

Table II.2: Static-cyclic tests on simple walls - Information from the force-displacement curves (static-cyclic)

Specimen		A1	A2	B2	A3	B3
$P_{shear,max}$ [10^3 N]	Neg.	137.1	81.28	81.12	82.20	88.14
	Pos.	150.7	83.18	76.21	76.50	78.42
δ_{max} [%]	Neg.	0.29	0.83	0.45	0.30	0.21
	Pos.	0.33	0.81	0.43	0.29	0.23
Dissipated energy [10^3 Nm]	/	2.79	17.80	5.31	1.24	1.41

The behaviour of the different components of the specimens B2, A3 and B3 can be studied separately. For the specimen B2, the masonry wall and the rubber layers both contribute to the global behaviour. The time evolution of the vertical and horizontal displacements are drawn in Figure II.9, during the compression phase and static-cyclic test respectively. In Figure II.9 (left), the dashed-dotted curve gives the total shrink attributable to the presence of rubber devices. In the case of walls with an opening (A3 and B3), there are two contributions, i.e. the piers and the spandrel. The first considers the relative displacement of the top of the piers (2.0-m high) with respect to their base. The second is the difference of horizontal displacements between the RC lintel and the upper RC beam.

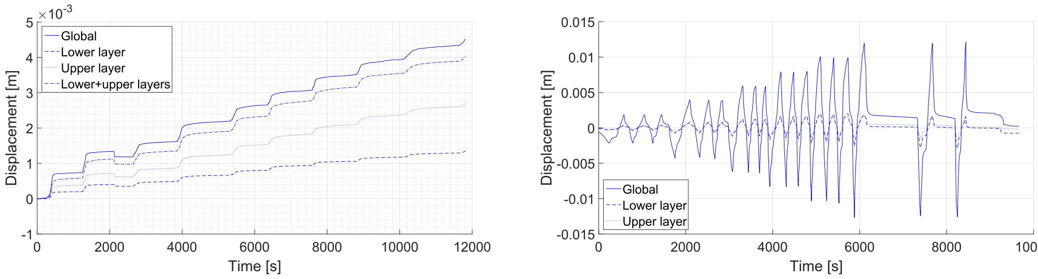

Figure II.9: Static cyclic tests on simple walls - Time-evolution of the vertical (left) and horizontal (right) displacements

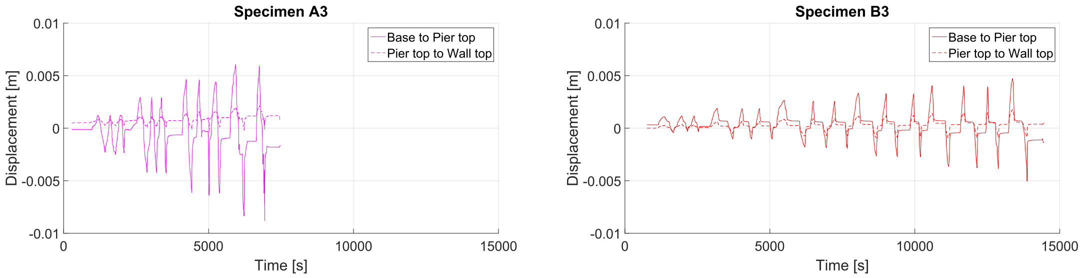

Figure II.10: Static cyclic tests on simple walls - Time-evolution of the horizontal displacement of specimens A3 (left) and B3 (right)

II.2.4 Interpretation and discussion

Force-displacement and push-over curves

Despite the symmetry of the reference wall, the corresponding $P_{shear} - \delta$ curve depends on the loading direction. In terms of maximum shear, the magnitude is about 10 % higher in the positive direction. In comparison to the standards predictions, the experimental result is slightly lower in the negative direction (-0.4 %), but the difference becomes significant in the other direction (+ 9.5 %). This dependence is likely due to a non-uniform distribution of the vertical compression, as highlighted by the vertical displacements V_1 and V_2 at the end of the compression phase. As a consequence, the resultant of the vertical compression is not applied at the neutral axis of the wall and the shear capacity differs from one direction to the other. The presence of the rubber seems to make more uniform the vertical load distribution, reducing the dependence on the load direction (2 to 6 %). On the contrary, this latter is expected for the walls with an opening and the difference is equal to 6.9 % for the specimen A3 and to 11.0 % for B3. The result for A3 could be larger whether there has been no local failure. In presence of an opening, the preliminary assessment clearly underestimates the ultimate shear (relative difference of 68 % at least), certainly due to the neglection of the frame effect.

Starting from their envelope, the $P_{shear} - \delta$ curves can be converted into equivalent elastic-perfectly-plastic bilinear push-over curves (Figures II.11 to II.13 , in grey). These latter are characterised by three parameters, namely the initial stiffness k_{ini} [N/m], the yield drift d_y [-] and the ductility μ [-] which are tabulated in Table II.3. A procedure according to Tondelli [125] is followed to build these curves and consists in: (i) defining the initial stiffness as the secant stiffness at 50 % of the maximum measured force, (ii) defining the ultimate drift as the maximum drift of the envelope and (iii) determining the yield force such that the area under the bilinear curve is equal to the area under the envelope.

In Figure II.13, the push-over curve is not determined in one direction for the wall A3 because of the early collapse of this specimen. It is worth noticing that the vertical load distribution also influences the initial stiffness: the more compressed the wall, the stiffer. Table II.3 effectively shows a relative difference of 22.1 % for the specimen A1. The information provided by the push-over curves is further commented here after.

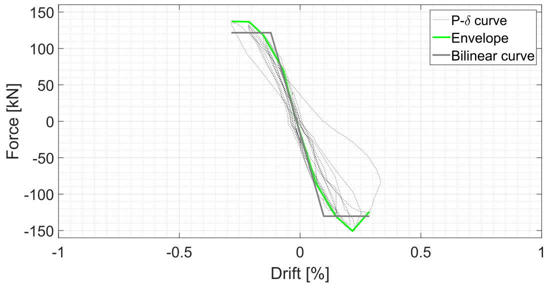

Figure II.11: Static-cyclic tests on simple walls - Envelope and equivalent elastic-perfectly plastic push-over curve (reference)

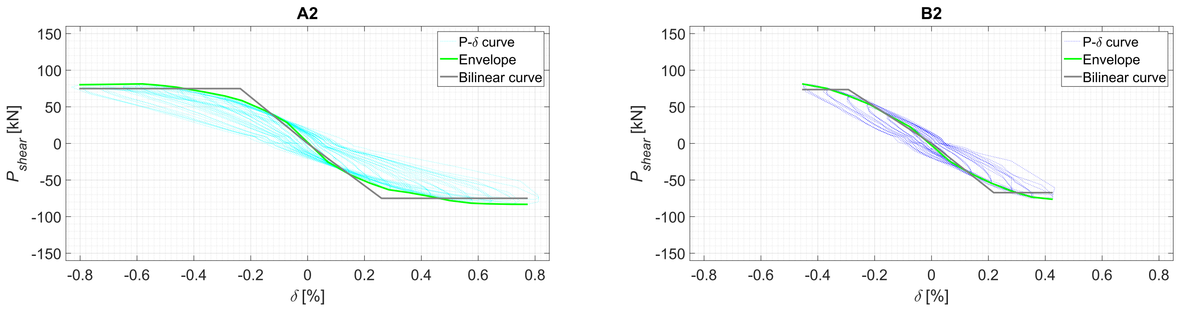

Figure II.12: Static-cyclic tests on simple walls - Envelope and equivalent elastic-perfectly plastic push-over curve (specimens with rubber)

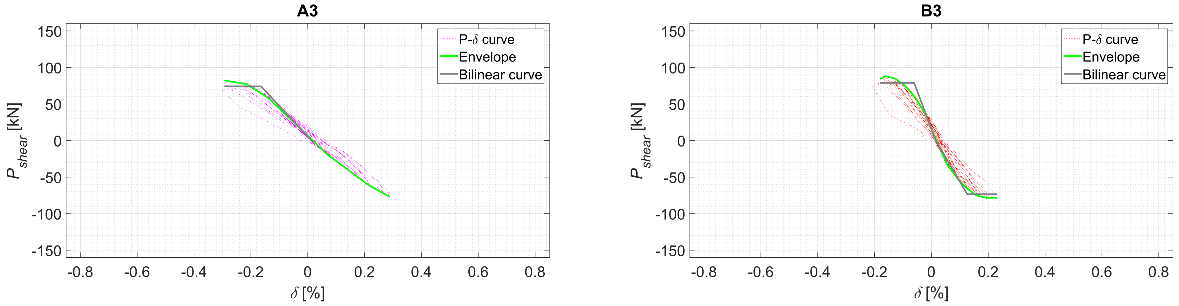

Figure II.13: Static-cyclic tests on simple walls - Envelope and equivalent elastic-perfectly plastic push-over curve (specimens with rubber)

Table II.3: Static-cyclic tests on simple walls - Parameters of the bilinear curves

Specimen		A1	A2	B2	A3	B3
Initial stiffness k_{ini} [10^7 N/m]	Neg.	3.20	1.08	0.91	1.49	3.71
	Pos.	4.11	1.08	1.07	/	2.37
Yield drift δ_y [%]	Neg.	0.12	0.24	0.29	0.16	0.06
	Pos.	0.10	0.26	0.22	/	0.13
Ductility μ [-]	Neg.	2.32	3.38	1.55	1.78	2.94
	Pos.	2.90	2.97	1.94	/	1.82

Influence of rubber layers

Soundproofing layers modify the behaviour of the masonry wall, both in compression and static-cyclic phases.

Two main consequences of their presence are pointed out during the first phase of the test sequence. First, the compression level is halved in comparison to the reference configuration because of the development of a vertical crack in the case of the wall with continuous layers. The appearance of such a crack at the top of the wall is explained by the Poisson's effect and the interaction between masonry and rubber. Under an axial load, the transverse deformation is more important for the rubber than for the masonry, involving tensile stresses in this latter. Masonry being a low-tensile strength material and the head joints being empty, vertical cracks can rapidly appear. The use of discontinuous layers (wall B2) should aim at dividing the main crack into smaller ones with reduced opening, but no appreciable improvements are obtained. Observations indeed reveal that the rubber is pushed inside the alveoles of the masonry units, leading to their deterioration. The second consequence is the larger vertical displacement. According to Figure II.7, a 0.5 MPa compression load induces a vertical displacement of about 0.5 mm in the case of the wall A1. This displacement is multiplied by 6.7 (10.4) when considering the wall A2 (B2). The main contribution to the vertical displacement comes from the rubber, as illustrated in Figure II.9 (left) by the dashed-dotted curve. For the wall B2, the total deflection is around 4.5 mm with 4.0 mm resulting from the rubber. The normal stiffness of the overall specimens with rubber layers is therefore reduced, as shown in Figure II.7 where the slope of the curves in blue and cyan is smaller than the one of the black curve.

Regarding the behaviour under a horizontal shear, specimens with rubber show a lower strength capacity and larger drifts. Table II.2 gives a reduction of about 45 % in terms of maximum load when rubber is added. The increase of maximum drift varies from 50 to 185 % approximately. A significant part (up to 50%) of the horizontal displacement is concentrated in the flexible layers, as illustrated in Figure II.9 (right). This affects the lateral stiffness of wall with a decrease of 72 % on average in comparison to the configuration A1 (see Table II.3). The influence of the soundproofing devices on the ductility is mitigated. It is improved in the case of the continuous layers (+2.4 % up to +45.7 %), but lowered when the rubber is cut in half (-33 %). In terms of energy dissipation, the presence of rubber is favourable. The amount is doubled in the case of the wall B2 and multiplied by 6 when the wall A2 is considered. It is also worth noticing that the hysteretic behaviour of the wall A2 damages more rapidly than the one of the wall B2 (Figure II.8 (middle)). The propagation of the vertical cracks initiated during the compression phase could explain why the slope of the $P_{shear} - \delta$ curve is smaller even for the first cycle and why it degrades faster.

Practically, the designer has to limit the compression level acting on the walls to avoid early cracking and, thus, ensure a better cyclic behaviour. A proper assessment of the stiffness of the walls including rubber layers is also required to consider the right fundamental period since the seismic design is usually based on the elastic response spectrum. A particular attention should also be given to long term effects related to the deformation of the rubber, to avoid problems of differential settling at the level of a whole building.

Influence of an opening

The presence of an opening in the wall should have an effect on its axial and lateral stiffness. This former is reduced in the case of the specimen A3, but not for B3 which behaves similarly to A1 under compression (Figure II.7). The masonwork and the scattering of the mechanical properties of the materials are two possible reasons. The reduction of the latter is clear for both specimen, except for B3 in the negative direction (Table II.3). The reason is the same as the one alluded to the axial stiffness.

The comparison with the reference wall outlines a decrease of the strength capacity around 40 %. Contrary to the specimen B3 which is stiffer, the maximum drift of wall A3 is similar to the wall A1. The presence of an opening reduces the ductility of the specimen (-20 % in average) as well as the energy dissipation (about -50 %).

An important requirement to ensure a good seismic behaviour and avoid premature collapse is to lengthen the support of the lintel. This length has however to be limited, otherwise cracking can be observed in static conditions. The determination of the optimum support length is out of the scope of this thesis. The support length of the lintel is also of prime importance in the perspective of considering a coupling between the piers thanks to the spandrel and, thereby, improving the shear capacity.

Equivalent mechanical properties

A current practice for the analysis of a masonry buildings consists in the modelling of the heterogeneous components (units + mortar) of the wall with an equivalent element. From a numerical point of view, the wall can be modelled at the macro-scale for computational reasons, using an equivalent beam element (see Chapter IV). This element is assumed to be homogeneous and isotropic. Its mechanical properties are usually calculated with empirical formulae combining the properties of the units and mortar. The Eurocodes (EN - 1052) also proposes testing procedure to assess the elastic modulus for instance. Another possibility for the determination of equivalent elastic and shear moduli is based on the exploitation of the force-displacement (Figure II.7) and push-over (Figure II.11) curves.

On the one hand, the slope of the curves in Figure II.7 corresponds to the axial stiffness k [N/m] of the specimen, given by Eq. II.4:

$$k = \frac{P_{comp}}{d} = \frac{E\,A}{h} \tag{II.4}$$

where E [N/m²] is an equivalent Young modulus and A [m²] is the cross-section area of the specimen. Eq. II.4 allows the determination of E. The results are tabulated in Table II.4, with a magnitude of 2466 MPa for the simple URM wall (A1) for instance. The values related to the specimens A2 and B2 depend on the deformability of both the masonry wall and the rubber layers. Eq. II.5 translates this dependence:

$$E_{specimen,A2/B2} = \frac{h\,E_m\,E_r}{h_m\,E_r + 2h_r\,E_m} \tag{II.5}$$

where h [m] is the height of the specimen, equal to the sum of h_m [m], the height of the masonry panel, and two times h_r [m], the height of a rubber layer. E_m and E_r [N/m²] are equivalent elastic modulus for masonry and rubber respectively. Eq. II.5 is derived from Eq. II.4 considering that the specimen is composed of masonry and rubber elements connected in series. The modulus E_m can be assumed as equal to 2466 MPa for three reasons. First, the specimen A1 and the masonry panel of A2 and B2 are identical. Second, the behaviour of the masonry alone can be supposed linear under compression, as shown by the black curve in Figure II.7. Third, Figure II.9 (left) shows that the vertical displacement of the specimen B2 is around 4.5 mm (solid line) under a compression level of 0.5 MPa (P_{comp} = 210 000 N). The contribution of the rubber devices to this displacement is about 4.0 mm (dashed-dotted line). The contribution of the masonry is therefore of 0.5 mm. The point (0.5 mm, 210 000 N) being located on the black curve in Figure II.7, the assumed value for E_m is relevant. It follows $E_r = 3.682 \cdot 10^6$ N/m² (A2) or $E_r = 2.479 \cdot 10^6$ N/m² (B2). The equivalent elastic modulus for the specimens A1 and A3 are close to each other. This latter is much higher for the specimen B3, as concluded previously.

Table II.4: Static cyclic tests on simple walls - Elastic modulus

Specimen	A1	A2	B2	A3	B3
Elastic modulus [MPa]	$2.466 \cdot 10^3$	$4.294 \cdot 10^2$	$3.064 \cdot 10^2$	$2.295 \cdot 10^3$	$3.668 \cdot 10^3$

On the other hand, the lateral stiffness of the walls has been assessed by the push-over curves and its value is given in Table II.3. The reference wall can be considered as a cantilever beam since it is clamped at the base and free to rotate at the top. Its stiffness under a horizontal load applied to its top is therefore given by

$$k_{ini} = \left(\frac{H^3}{\alpha EI} + \frac{H}{k'GA} \right)^{-1} \tag{II.6}$$

where I [m^4] is the inertia, k [-] is a shape factor, equal to 5/6 for rectangular cross-section and $\alpha = 3$ because the top is free. The parameter G [N/m^2] is an equivalent shear modulus, defined as a percentage of the equivalent elastic modulus E found here above. This definition is the same as the one expressed in the Eurocode 6 [34]. The results are given in Table II.5. They are the average between the positive and the negative directions. Regarding the specimens with rubber, the lateral stiffness is the sum of the contribution of the masonry panel and the rubber layers. The ratio G/E for the rubber is taken as 1/3 given that the corresponding Poisson's coefficient is 0.5. Concerning the specimens A3 and B3, the parameters A and I take into account the area and inertia of the two piers. The coefficient α is equal to 6 at least because the piers can be considered as simply supported at the top. This coefficient is taken as 12 in the case of the wall which has the lintel supported on 0.45 m because the lintel and the RC beam create a kind of clamping.

Table II.5 shows differences between the walls A1, A2 and B2, even though the masonry panels has the same geometry and constituents. Differences are also observed between specimens A1 and A3/B3 which have different geometries. Two main sources seem to influence the ratio G/E: the compression level and the length of the wall. The ratio increases when the compression level is increased, while the opposite is observed when the wall is longer. Additional investigations are necessary to confirm these conclusions.

The equivalent mechanical properties determined in this section will be used as an input for the modelling of the experimental specimens in Chapter IV.

Table II.5: Static cyclic tests on simple walls - ratio G/E for masonry

Specimen	A1	A2	B2	A3	B3
G/E [%]	22.723	8.920	13.059	36.603	27.675

II.3 Static-cyclic tests on T-shaped walls

II.3.1 Description of specimens

A set of three specimens (C1-3) is considered in the second campaign. They are all identical and composed of two precast masonry walls connected together with a continuous mortar joint over the entire height. The first masonry panel is called *shear wall* in the following. It has global dimensions of $h = 2.800$ m × $L_{shW} = 2.500$ m × $t_{shW} = 0.150$ m. The second one, with global dimensions of $h = 2.800$ m × $L_{fl} = 1.500$ m × $t_{fl} = 0.150$ m, is perpendicular to the shear wall and is named *flange* (Figure II.14). The specimens have thus a T-shaped cross-section. Different compression levels are applied to the specimens C1-3.

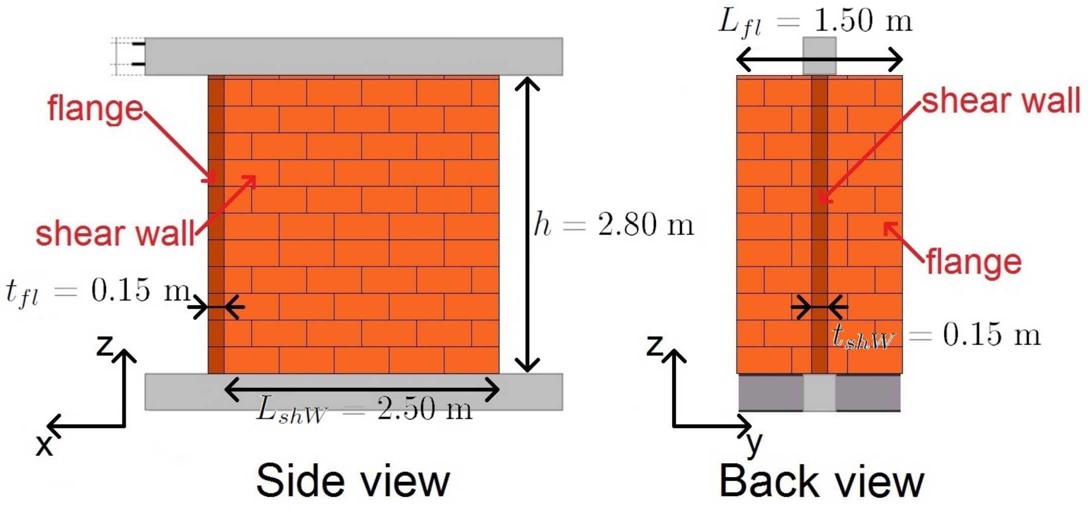

Figure II.14: Static-cyclic tests on T-shaped walls - Sketch of the specimens

The precast walls are built in thin bed-layered masonry with a tongue-and-groove system for the head joints. They are placed between two RC beams representative of the floors. The units constituting the walls are clay blocks with nominal dimensions (height×length×thickness) of 0.249 m × 0.500 m × 0.150 m. The material and mechanical properties are given in Table II.6. The tests according to EN 1052-1 do not include the evaluation of the elastic modulus. No specific characterisation has been carried out for the shear behaviour. Usual standard values are therefore considered. The characteristic shear strength is

$$f_{vk} = 0.5\, f_{vk0} + 0.4\, \sigma_d \qquad \text{(II.7)}$$

where f_{vk0} is given in Table II.6 and σ_d is the design compressive stress. This strength is limited to $0.045\, f_b (= 0.675$ MPa) as the vertical joints are empty.

The preliminary assessment design according to the Eurocode 6 for the verification rules predicts the shear resistance. The obtained values are 104.5 kN, 128.2 kN and 148.4 kN, for the walls C1, C2 and C3 respectively. The presence of the flange is neglected and the considered length for the shear wall is 2.650 m (see Chapter V).

Table II.6: Static-cyclic tests on T-shaped walls - Material and mechanical properties of the masonry units

Properties	Symbol	Value	Units
Density	ρ	850	kg/m^3
Normalised compressive strength of units (En 772-1 Annex A)	f_b	15	MPa
Measured characteristic masonry compressive strength (EN 1052-1)	f_k	6.5	MPa
Characteristic compressive strength (EN 1996-1-1)	f_k	4.7	MPa
Characteristic compressive strength (NBN EN 1996-1-1)	f_k	4.4	MPa
Initial shear strength (NBN EN 1996-1-1)	$f_{vk,0}$	0.3	MPa

II.3.2 Testing procedure

The test sequence is divided in two phases. The first one is the vertical compression of the shear wall only (see position of the steel and RC beams in Figure II.15). The compression level is different for each wall, varying from 0.75 MPa to 1.25 MPa. The walls are then subjected to a static-cyclic test with an imposed horizontal displacement of the upper RC beam. This latter is increased every 3 cycles. The introduction of the compression and the carrying out of the static-cyclic test are performed in accordance with the procedure followed in the previous section (see Section II.2). The flange is decompressed when the horizontal shear is positive. The experimental data will be available in ORBi [87].

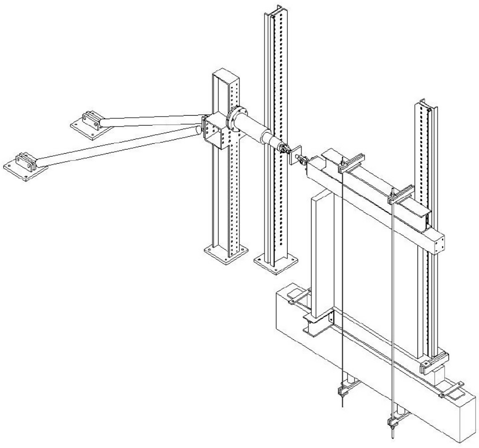

Figure II.15: Static-cyclic tests on T-shaped walls - Experimental set-up

The instrumentation layout includes 16 sensors, as illustrated in Figure II.16. Two LVDT devices measure the horizontal displacement of the upper and lower RC beams, namely H_{Sup} and H_{Inf}. Four are dedicated to the measurement of the vertical displacement of the upper RC beam. The distance between V_1 and V_2 is 2.100 m. The rotation of this latter is also taken. The horizontal displacement of the top corners of the shear wall is recorded (sensors $H_{w,1-2}$), as well as the one of the flange just above mid-height (sensors $H_{g,m,d}$). The four last devices are used to study the behaviour of the vertical joint connection, at four different points, through either the vertical or the horizontal relative displacement between the shear wall and the flange ($H_{j,1-2}/V_{j,1-2}$). Two additional load cells measure the vertical load acting on the wall and the horizontal force applied to the upper RC beam.

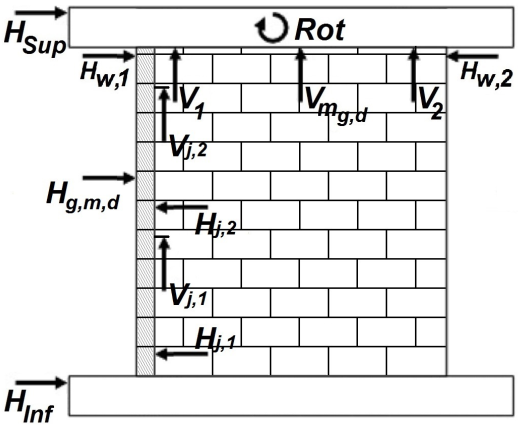

Figure II.16: Static-cyclic tests on T-shaped walls - Instrumentation layouts

II.3.3 Test observations and results

This section presents the rough experimental observations and results. These latter and the conclusions stemming from will be interpreted and discussed in details in the next section.

The crack pattern observed for the three specimens is similar, with diagonal cracks (see Figure II.17). Such a configuration translates a shear failure. No damage is observed at the connection between perpendicular walls, leading to the conclusion that the continuous vertical mortar joint is fully efficient in this test configuration.

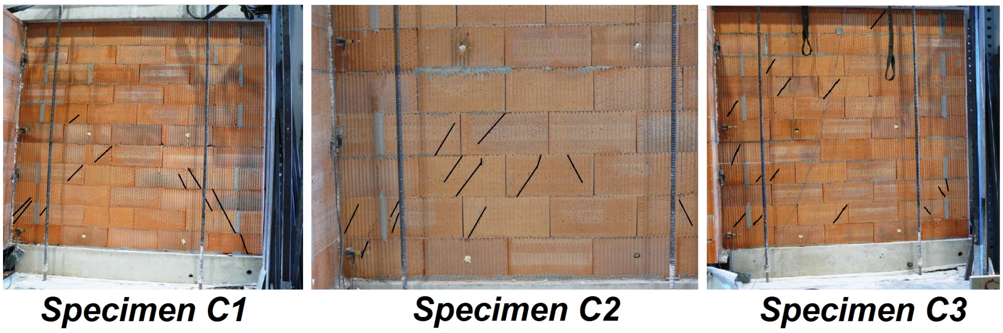

Figure II.17: Static-cyclic tests on T-shaped walls - Crack patterns

The force-displacement curves characterising the response of the specimens are shown in Figure II.18 and Figure II.19 for the compression and static-cyclic phases respectively. The forces P_{comp} and P_{shear} have been defined in the previous section, as well as the vertical displacement d and the drift δ (see Section II.2.3 with Eqs II.2 and II.3). The different compression levels are visible in Figure II.18, where the wall C1 reaches a maximum vertical force around 280 kN, while this compression force is about 375 kN for wall C2 and 470 kN for wall C3. The behaviour of the three specimens under compression is approximately the same, as it can be expected given that the same units and mortar are used in any case. Table II.7 summarizes the main results of the static-cyclic test in terms of maximum forces and drifts. The dissipated energy is also given. The positive direction refers to a positive drift δ (flange over-compressed).

The study of the connection of the flange to the shear wall being a main objective of this experimental campaign, the vertical/horizontal force versus the vertical/horizontal relative displacement between these sections is plotted in Figure II.20. The same interest is given to the behaviour of the flange during the static-cyclic test. This latter is perpendicular to the direction of the imposed displacement. Hence, its out-of-plane behaviour is represented. The time evolution of the horizontal drifts δ_k just above the mid-height of the flange is drawn for the wall C1 in Figure II.21. The drifts δ_k are calculated as follows:

$$\delta_k = \frac{H_k - H_{Inf}}{h_s} \tag{II.8}$$

with $h_s = 1.680$ m, the vertical distance between the sensors measuring the out-of-plane displacement of the flange H_k and the lower RC beam and $k = g$, m or d.

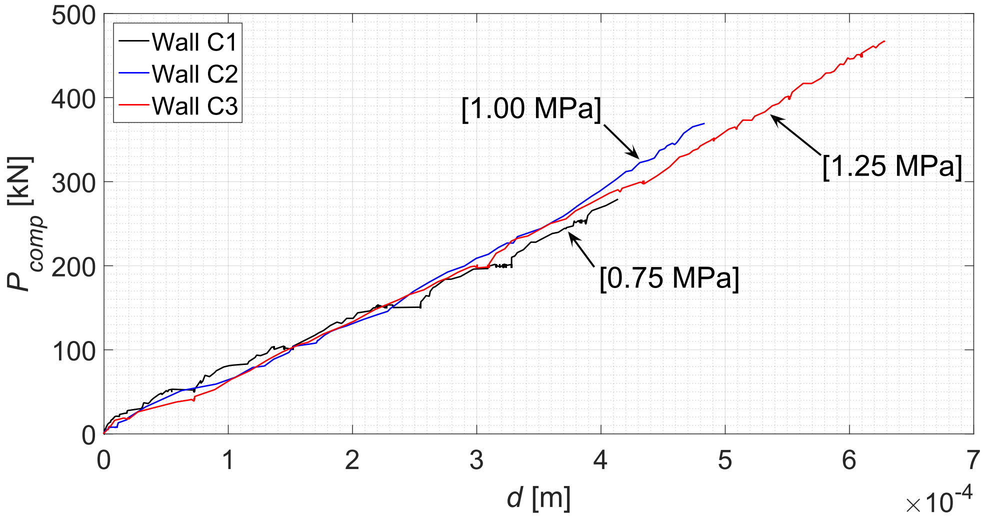

Figure II.18: Static-cyclic tests on T-shaped walls - Force-displacements curves (compression)

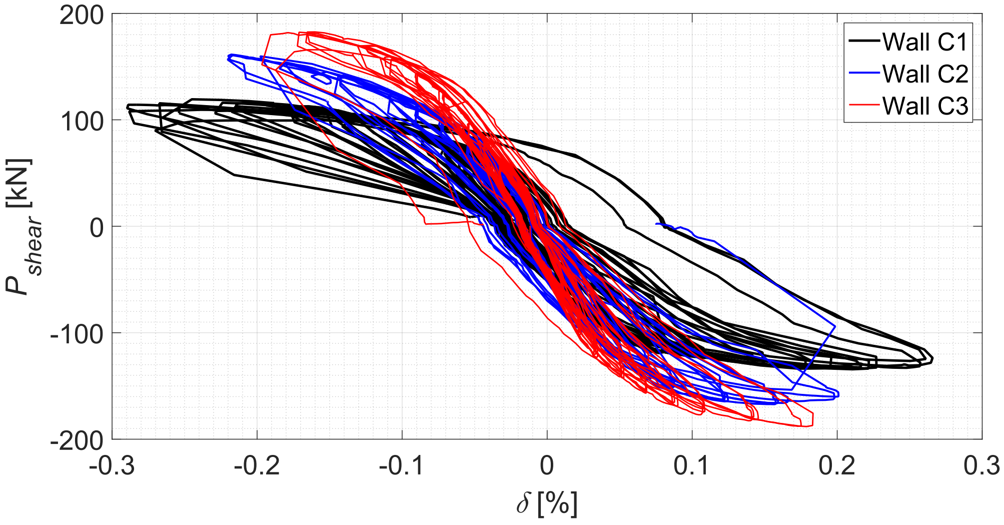

Figure II.19: Static-cyclic tests on T-shaped walls - Force-displacements curves (static cyclic)

Table II.7: Static-cyclic tests on T-shaped walls - Information from the force-displacement curves (static cyclic)

Specimen		C1	C2	C3
Max. load [10^3 N]	Neg.	119.4	161.4	182.6
	Pos.	134.2	167.2	188.1
Max. drift [%]	Neg.	0.29	0.22	0.18
	Pos.	0.25	0.20	0.18
Dissipated energy [10^3 Nm]	/	9.17	5.17	4.39

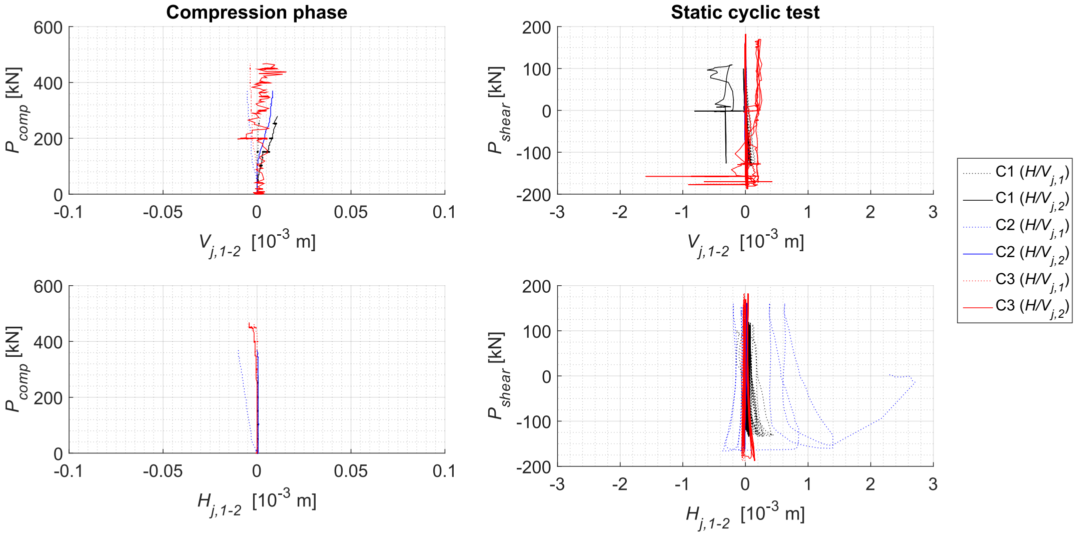

Figure II.20: Static-cyclic tests on T-shaped walls - Joint behaviour

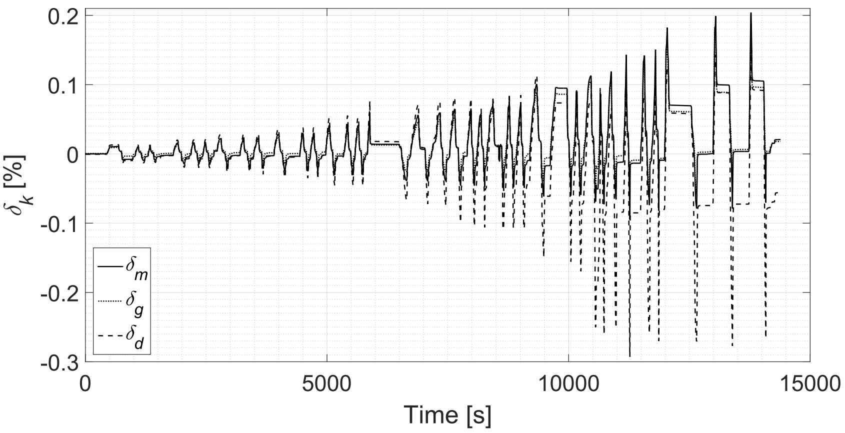

Figure II.21: Static-cyclic tests on T-shaped walls - Out-of-plane behaviour of the flange (wall C1)

II.3.4 Interpretation and discussion

II.3.4.1 Push-over curves

Derived from the envelope of the force-displacement curves, the push-over curves are obtained following the procedure used in Section II.2. The results are illustrated in Figures II.22 to II.24 and the main parameters of the bilinear curves are tabulated in Table II.8. A clear difference is observed according to the load direction. The compression level influences also the wall response. Details on these differences are given in the next section.

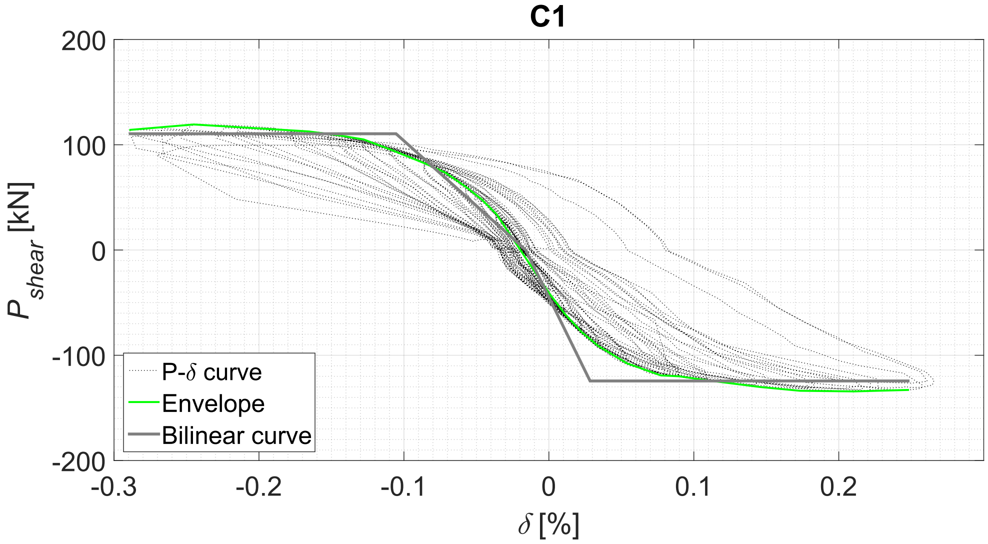

Figure II.22: Static-cyclic tests on T-shaped walls - Envelope and equivalent elastic-perfectly plastic push-over curve

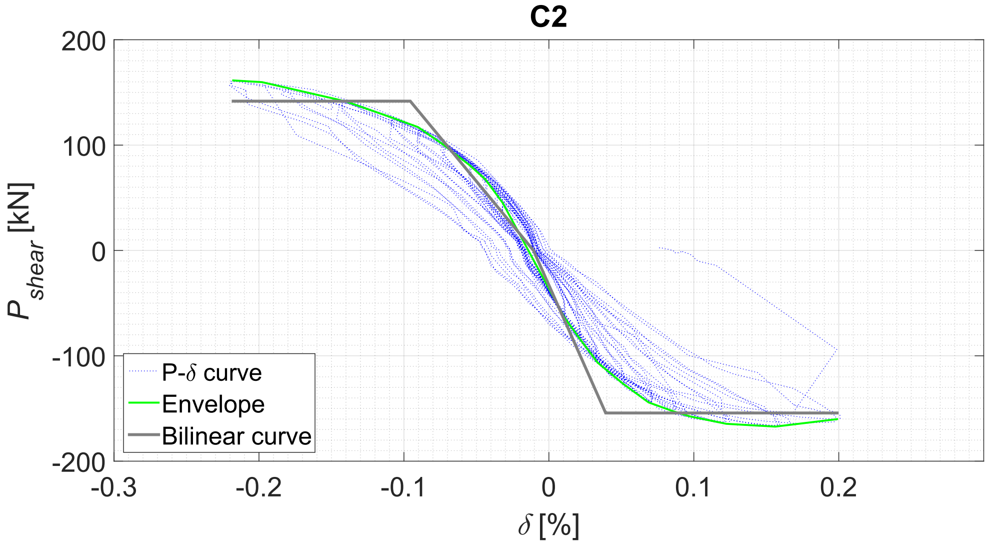

Figure II.23: Static-cyclic tests on T-shaped walls - Envelope and equivalent elastic-perfectly plastic push-over curve

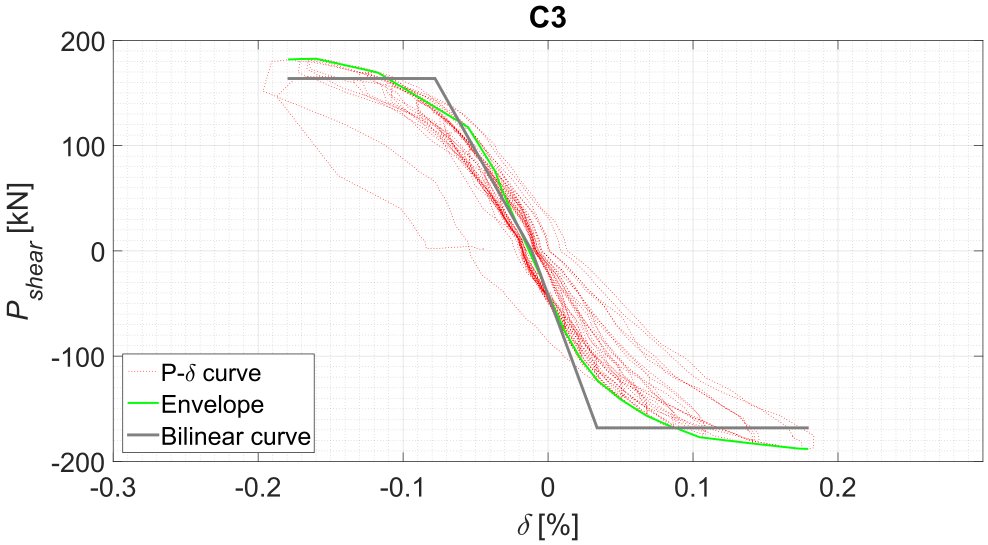

Figure II.24: Static-cyclic tests on T-shaped walls - Envelope and equivalent elastic-perfectly plastic push-over curve

Table II.8: Static-cyclic tests on T-shaped walls - Parameters of the bilinear curves

Specimen		C1	C2	C3
Initial stiffness k_{ini} [10^6 N/m]	Neg.	44.10	59.54	87.58
	Pos.	100.03	110.68	133.25
Yield drift δ_y [%]	Neg.	0.11	0.10	0.08
	Pos.	0.03	0.04	0.03
Ductility μ [-]	Neg.	2.74	2.28	2.29
	Pos.	8.72	5.08	5.29

II.3.4.2 Influence of the perpendicular wall and of the compression level

Contrasting the predictions of the preliminary assessment with the experimental results underlines the influence of a perpendicular wall in the cyclic behaviour of masonry. In current standards, the contribution to the strength of walls perpendicular to the seismic action is not explicitly defined. Therefore, it is usually disregarded. In terms of maximum load, the application of design rules results in an underestimation of the actual resistance. Based on the results given in Table II.7, the relative difference between the theoretical and actual values ranges from 12.5 % to 23.3 %.

Deeper investigations evidence larger discrepancies with the assessed values when the specimen is pulled so that the flange is over-compressed (positive direction). Thus, the influence of the perpendicular wall differs according to the testing direction. Data in Table II.7 effectively show clear differences between the two directions of test. Regarding the specimen subjected to compression stresses of 0.75 MPa, the maximum load is 11.0 % larger when considering the positive direction. The relative difference decreases to 3.5 % and 2.9 % gradually with the increase of vertical compression stresses to 1.00 MPa and 1.25 MPa. On the contrary, the maximum drift measured during the tests is lower in the positive direction in comparison to the negative one, but the disparity further reduces with the increase of compression. This physical quantity varies from 14.2 % to 0.1 % for the lowest and highest compression levels respectively. Regarding the bilinearised push-over curves in Figure II.22 and the numerical values in Table II.8, the conclusions on the initial stiffness (the ductility) are similar to those on the maximum load. This parameter is 55.9 % (68.6 %) higher in the positive direction in the case of the specimen C1. For the specimens C2 and C3, the difference is 46.2 % (55.1 %) and 34.3 % (56.7 %) respectively. In terms of yield drift, the opposite is observed with larger values in the negative direction. This last parameter is multiplied by 3.7 times from the positive to the negative direction for test on C1. The multiplication factor is 2.4 for C2 and 2.3 for C3.

The influence of a perpendicular wall on the behaviour of the specimens is clearly identified thanks to the experimental outcomes. It however affects the results in a different way according to the test direction and the compression level applied to the section of the specimen oriented along the testing direction. Masonry being assumed as a no-tensile strength material, the first effect can be explained as follows. When pushing in the negative direction, the flange tends to uplift and it contribution to the shear strength rapidly vanishes. The sustainable horizontal shear is however increased in comparison to the configuration without any flanges because the gravity centre of the cross-section is shifted such as the compressive length is longer under the same shear (see Chapter V). In the positive direction, the flange is over-compressed and contributes to the shear strength by increasing the cross-section area in contact with the support. An important point is to ensure the transmission of the internal forces between the shear wall and the flange by ensuring an effective connection, otherwise the contribution of the flange will be limited. The second effect is a possible consequence of the better participation of the flange to the global behaviour. Indeed, a higher compression level could mobilise a larger part of the flange and could homogenise the behaviour of the sections of the piers, involving a higher strength. Differences between the positive and negative directions are also reduced because the specimen remains longer in contact with its basement, independently of the load direction. Nevertheless, increasing the compression level also involves the reduction of the drift capacity since, for instance, the failure of the specimen C1 occurs for larger drift than for the specimen C3.

II.3.4.3 Behaviour of the wall connection

Figure II.20 allows the study of the behaviour of the connection between perpendicular sections of the walls. The measurements show that the vertical as well as the horizontal displacements are lower than 0.05 mm during the compression phase (graphs on the left). The magnitudes remain insignificant during the static-cyclic test. Indeed, the relative displacements are very low (under 0.1 mm). Some curves however show displacements higher than 0.1 mm. These values correspond to the post-collapse behaviour.

The wall connection can therefore be assumed as perfectly rigid and fully efficient in this test configuration and the contribution of the flange to the shear strength is complete.

II.3.4.4 Behaviour of the flange

The time evolution of the horizontal drift measured at three points of the flange (δ_g, δ_m and δ_d) in Figure II.21 displays a larger drift at the right side of the flange than at the intersection with the shear wall. The drift at the left side is also lower than the one at the intersection. Theses differences are unexpected, theoretically, given the symmetry of the specimen. Nonetheless, this can be explained by the presence of an asymmetry: either the lengths of the flange on the left/right of the shear wall are not exactly the same, or the imposed horizontal displacement of the upper RC beam is not perfectly centered.

The flange is therefore subjected to torsion. This internal force would be observable in the shear wall, but this is not captured by the instrumentation layout.

II.3.4.5 Equivalent mechanical properties

Equivalent mechanical properties are assessed with the same procedure as in Section II.2. The results are given in Table II.9 and will be using later for the macro-scale modelling of the walls with isotropic non linear beam elements. To this purpose, equations II.4 and II.6 are used. The definition of the different parameters can be questionable, especially for the area to consider. Indeed, the compression load is introduced by a steel beam placed on the shear wall only. The intersection between this latter and the flange is also loaded. A possible area is therefore given by:

$$A = L_{shW}\, t_{shW} + t_{shW}\, t_{fl} \tag{II.9}$$

One can however suppose that a longer part of the flange contributes to the stiffness. From the point of view of the flange, the compression load can be assumed as a punctual load. The load is therefore transferred to the base with a downward diffusion at an angle of 30° on both sides. Thus, the length of the flange on both side of the intersection involved in the stiffness varies linearly with the height of the specimen H [m]. The defined triangle is then converted into a rectangle with an equivalent length $L_{fl,effective}$ [m] such as their vertical areas are the same (see Figure II.25). This length is constant over the height and is used to assess the cross-section area of the flange taking part to the stiffness. The area to consider then becomes:

$$\begin{aligned} A &= L_{sh}\, t_{sh} + t_{shW}\, t_{fl} + 2\, L_{fl,eff}\, t_{fl} \\ &= L_{sh}\, t_{sh} + t_{shW}\, t_{fl} + 2\left[\left(h + \left(h - \frac{L_{fl,eff}}{\tan 30°}\right)\right)\frac{L_{fl,eff}}{2}\,\frac{1}{h}\right] t_{fl} \end{aligned} \tag{II.10}$$

where $L_{fl,eff}$ [m] is the length of the flange on both sides of the intersection. The area is limited to $L_{sh} \cdot t_{sh} + L_{fl} \cdot t_{fl}$ which is the cross-section area of the specimen.

The equivalent elastic modulus presents a variation of maximum 12.1 %. The scattering can be a consequence of the variability in the material properties or in the masonwork. The cross-section area of the flange participating to the stiffness can also influence the result (see above). This one is the same for all specimens, but one could assume that a higher compression affects a longer part of the flange, leading to a longer equivalent length with the compression level. The difference in terms of G/E ratio comes from the elastic modulus E itself on the one hand. On the other hand, this equivalent mechanical properties depends on the compression level. As already observed, the higher the compression level, the higher the lateral stiffness.

Table II.9: Static-cyclic tests on T-shaped walls - Equivalent mechanical properties

Specimen	C1	C2	C3
E [MPa]	$3.311 \cdot 10^3$	$3.765 \cdot 10^3$	$3.655 \cdot 10^3$
G/E [%]	23.33	23.68	39.60

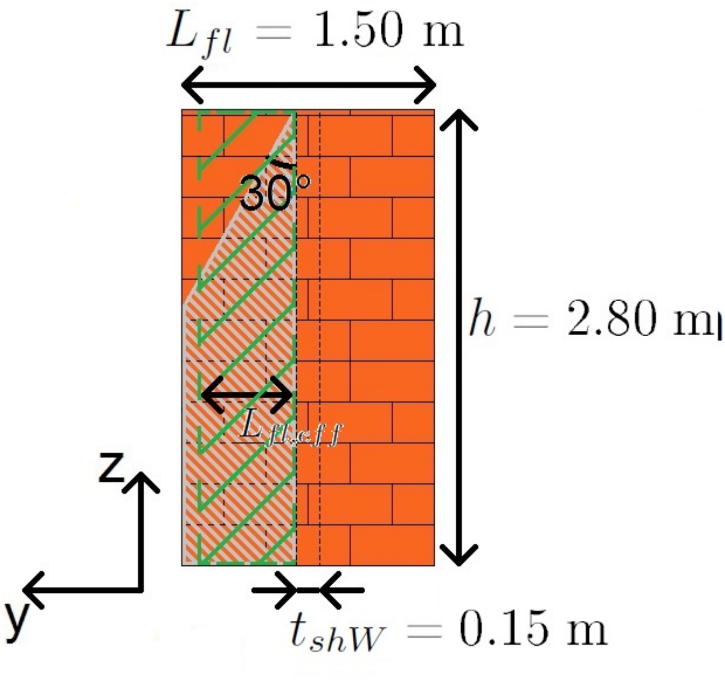
$L_{fl} = 1.50$ m
30°
$h = 2.80$ m
$L_{fl,eff}$
z
y
$t_{shW} = 0.15$ m

Figure II.25: Static-cyclic tests on T-shaped walls - Calculation of the effective length of the flange

II.4 Shake table tests on simple walls including sound-proofing devices

II.4.1 Description of the specimens

The third campaign studies the in-plane dynamic behaviour of four simple walls of 1.880-m high and 0.138-m thick. The walls are constructed by professional masons. Two *long walls* (2.100-m long) and two *short walls* (0.720-m long) are designed to fail in shear and bending respectively. Figure II.26 illustrates the different lengths by showing the first course of blocks.

All specimens are built in thin-bed layered masonry with glued joints and empty head joints (tongue-and-groove system). The units constituting the walls are clay masonry blocks with nominal dimensions (h x l x t) of 0.188 m × 0.300 m × 0.138 m. These units are the same as those used in the first campaign described in Section II.2. The mechanical and material properties are therefore given in Table II.1. One wall of each length includes 1-cm thick soft layers at its bottom and top, used for acoustic reasons and made of recycled rubber (Figure II.27).

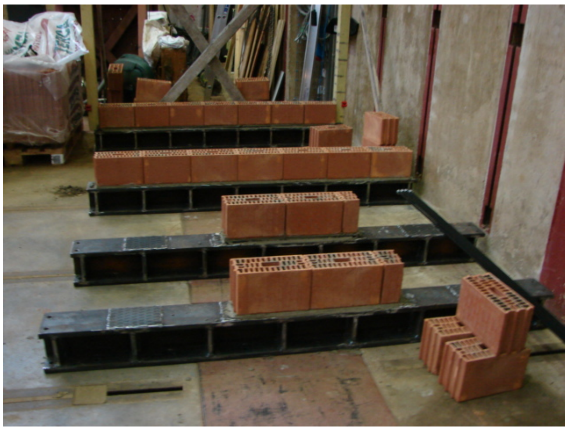

Figure II.26: Shake table test on simple walls - First course of the long (back) and short (front) walls

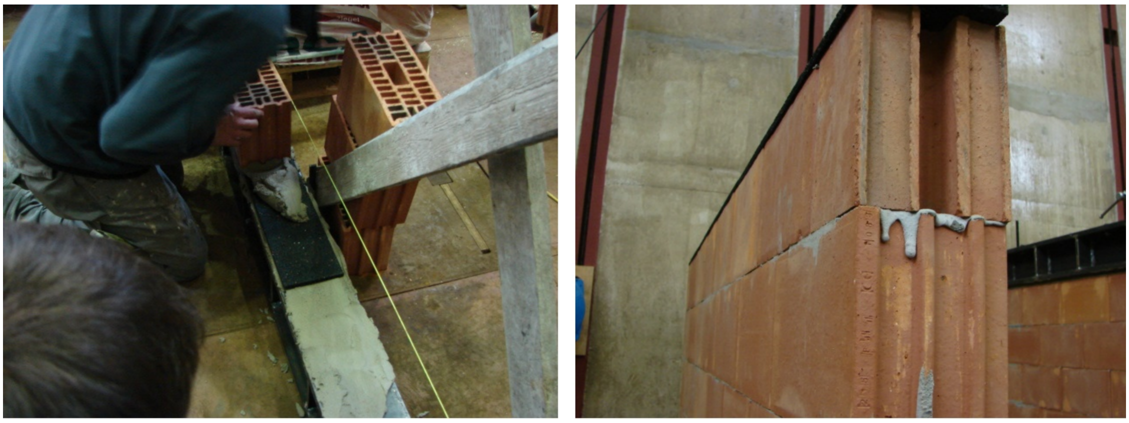

Figure II.27: Shake table test on simple walls - Rubber layers at the bottom (left) and the top (right) of walls

The walls are loaded by an additional 5-ton steel mass placed at their top to simulate the structural load (Figure II.28), leading to a compression stress of 0.169 MPa and 0.494 MPa for the long and short walls respectively. Each wall is built between two HEM 160 beams to allow its transport onto the shaking table. Interfaces between the masonry wall (the rubber layers) and the steel beams are made of a classical mortar joint. On both sides of the walls, steel frames are fixed on the table to prevent damages to the equipment of the laboratory coming from the falling down of the additional mass. This latter has steel guides fixed at its extremities, preventing excessive uplift and out-of-plane displacement.

A preliminary assessment design is performed according to the rules of the EN-1996-1-1 [34] and EN-1998-1 [116], resulting in the assessment of the maximum acceleration sustainable by the walls, namely 0.20 g and 0.07 g for the long and short walls respectively.

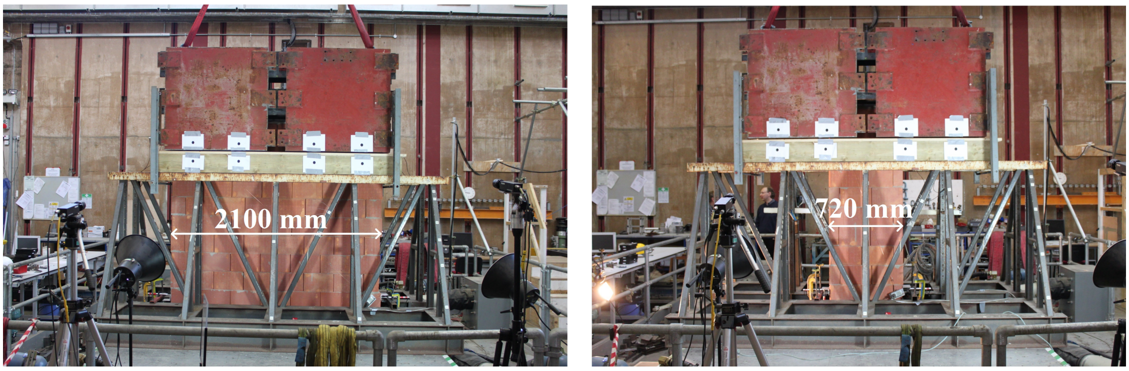

Figure II.28: Shake table test on simple walls - Long (left) and short (right) walls

II.4.2 Testing procedure

II.4.2.1 Instrumentation

All specimens are instrumented according to the same layout. The instrumentation comprises 7 accelerometers, 14 potentiometers and an Imetrum Video-Gauge vision system with 8 markers. The displacements and accelerations of the shake table are also recorded in the three space directions, whereas its rotations and angular accelerations are measured in two directions. The instrumentation setup is described in Figure II.29 for the long wall without (w/o) rubber. Table II.10 gives the position of the markers with four located on the additional mass and four on the steel frame (see Figure II.28).

The accelerometers are distributed along the wall height, especially for in-plane modal identification. The position of LVDT sensors is defined to study the behaviour of interfaces between the wall and its basement as well as the additional mass, in particular when there are rubber layers. This particular attention for the bottom and to of the wall is due to the interest in the consequences of the use of soundproofing devices on the dynamics of the masonry wall. Another reason is the low-tensile strength of masonry, allowing the uplift of the base of the wall. Two Celesco devices measure the diagonal displacements of the wall. The behaviour of the additional mass is characterized by the optical measurement system. Details on the exact position and the type of devices will be available in ORBi [87].

Regarding the instrumentation of short walls, the position of the instrumentation devices only differs from the long wall for the x-coordinate. The position of markers is the same.

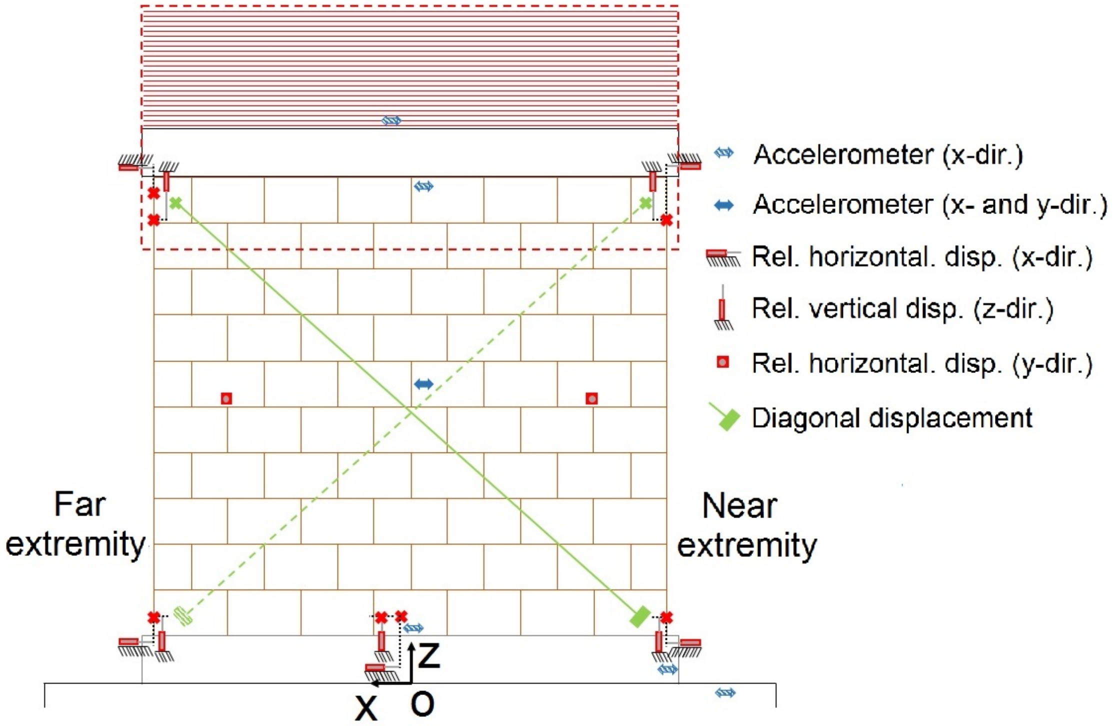
Accelerometer (x-dir.)
Accelerometer (x- and y-dir.)
Rel. horizontal. disp. (x-dir.)
Rel. vertical disp. (z-dir.)
Rel. horizontal. disp. (y-dir.)
Diagonal displacement
Far extremity
Near extremity
Z
X
O

Figure II.29: Shake table test on simple walls - Instrumentation setup (long wall w/o rubber)

Table II.10: Shake table test on simple walls - Position of the markers for optical measurement system

Name	Position [x ; y ; z]	Measurement	Direction	Note
tnnh (tnnv)	[-0.85 ;-0.29 ; 1.80]	x(z)-displacement	+	Marker on the mass
tnh (tnv)	[-0.36 ;-0.29 ; 1.80]	x(z)-displacement	+	Marker on the mass
tph (tph)	[0.36 ;-0.29 ; 1.80]	x(z)-displacement	+	Marker on the mass
tpph (tppv)	[0.85 ;-0.29 ; 1.80]	x(z)-displacement	+	Marker on the mass
bnnh (bnnv)	[-0.85 ;-0.29 ; 1.65]	x(z)-displacement	+	Marker on the steel frame
bnh (bnv)	[-0.36 ;-0.29 ; 1.65]	x(z)-displacement	+	Marker on the steel frame
bph (bpv)	[0.36 ;-0.29 ; 1.65]	x(z)-displacement	+	Marker on the steel frame
bpph (bppv)	[0.85 ;-0.29 ; 1.65]	x(z)-displacement	+	Marker on the steel frame

II.4.2.2 Input signal and test sequences

The input acceleration is applied in the x-direction, along the wall. It consists in a waveform derived from a random motion using the Required Response Spectra (see ET372 Seismic Qualification Test Procedures, Schedule No. 2) with 5 % damping.

The test sequence is composed of shake table tests at different intensity levels increased step by step, with some repeated levels. Table II.11 summarizes the number of runs and the different target peak ground accelerations (PGA). Before each shake and after the last one, a *white noise test* is performed to characterise the in-plane dynamic properties of the walls. The input for the white noise test is a random excitation with uniform frequency content between 1 Hz and 100 Hz and at a level of about 0.1 g RMS generated using an Advantest

R9211C Spectrum Analyzer. Several attempts are performed before the first seismic test to ensure a proper assessment of the dynamic properties. The first shake is carried out after the third identification, except for the short wall without rubber (second one).

Table II.11: Shake table test on simple walls - Target PGA [g] (x-direction)

Test	S01	S02	S03	S04	S05	S06	S07	S08	S09
Long wall w/o rubber	0.049	0.097	0.097	0.194	0.291	0.388	0.4850	0.582	0.679
Long wall with rubber	0.049	0.097	0.097	0.194	0.291	0.388	0.485	0.582	0.6790
Short wall w/o rubber	0.049	0.073	0.073	0.097	0.146	0.146	0.1940	0.1940	0.243
Short wall with rubber	0.049	0.073	0.073	0.0970	0.146	0.146	0.194	/	/

Due to the control system of the shake table, differences between the measurements (actual PGA) and the target PGA are evidenced, see Table II.12. These differences are highlighted in Figure II.30 thanks to the comparison between the input and actual accelerations in terms of acceleration and displacement spectra. These latter are normalized with respect to the target PGA. The measurements recorded during the first shake are considered as an example. The differences are maximized in the neighbourhood of the fundamental period (see Section II.4.3.2) of the walls. An acceleration is also measured in the out-of-plane direction (y-direction) (Table II.13). This parasitic acceleration can reach 11.74 % of the in-plane one.

The experimental data will be available in ORBi [87].

Table II.12: Shake table test on simple walls - PGA [g] (x-direction)

Test	S01	S02	S03	S04	S05	S06	S07	S08	S09
Long wall w/o rubber	0.039	0.078	0.078	0.158	0.239	0.323	0.450	0.572	0.688
Long wall with rubber	0.043	0.090	0.088	0.187	0.278	0.356	0.457	0.569	0.639
Short wall w/o rubber	0.041	0.065	0.063	0.087	0.136	0.133	0.178	0.187	0.234
Short wall with rubber	0.042	0.060	0.061	0.080	0.124	0.128	0.171	/	/

Table II.13: Shake table test on simple walls - PGA [g] (y-direction)

Test	S01	S02	S03	S04	S05	S06	S07	S08	S09
Long wall w/o rubber	0.005	0.009	0.007	0.012	0.017	0.021	0.024	0.032	0.053
Long wall with rubber	0.004	0.004	0.004	0.008	0.001	0.016	0.019	0.048	0.045
Short wall w/o rubber	0.004	0.004	0.005	0.004	0.006	0.008	0.014	0.021	0.022
Short wall with rubber	0.003	0.003	0.004	0.004	0.013	0.007	0.015	/	/

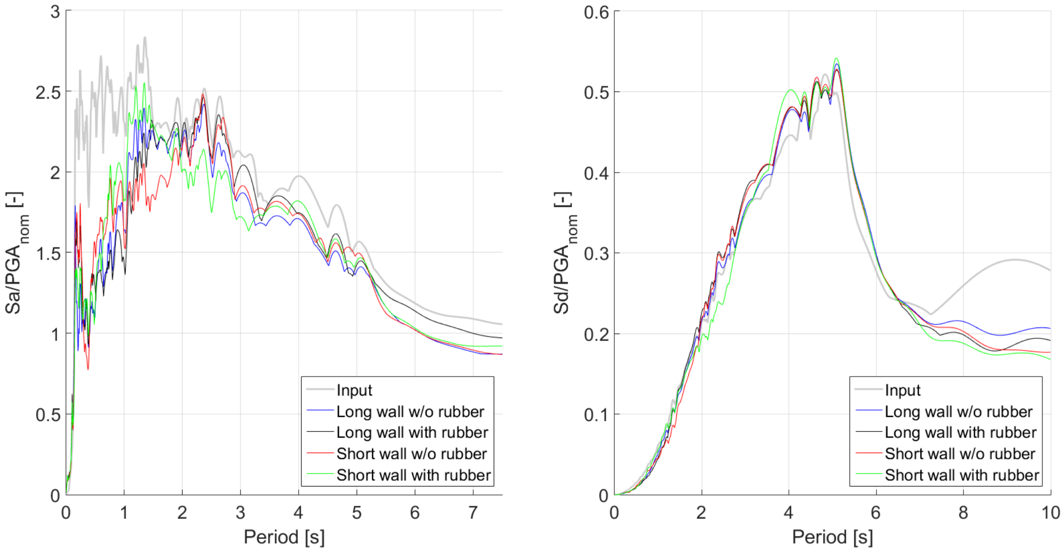

Figure II.30: Shake table test on simple walls - Comparison of acceleration and displacement spectra (1st shake)

II.4.3 Observations and experimental results

This section is first dedicated to the proceedings of the tests, with conclusions based on naked-eye observations. Results of the white noise tests then provide information about the dynamic properties of the walls in terms of transfer functions, natural frequencies and related mode shapes. Finally, measurements recorded during the shake table tests are used to describe the seismic response of the walls. This latter is characterised by several parameters with respect to the actual PGA, namely the maximum acceleration and displacement of the top of the wall and mass, together with the maximum rotation of the additional mass. The force-displacement curves are also drawn and a particular attention is given to the behaviour of the wall base.

All the results and the conclusions stemming from will be interpreted and discussed in details in the next section.

II.4.3.1 Observations

The test sequence and the increment of the target PGA depend on the length of the wall considering that the design acceleration leading to the collapse is different. Moreover, the short walls are subjected twice to a repeated acceleration level (S02/03 and S05/06) because of interactions between the additional mass and the steel frames in presence of rubber layers (S05). Shocks are also observed during the test at the highest acceleration level for both short walls. In terms of PGA, the walls are subjected to a magnitude about three times higher than the PGA obtained by the preliminary assessment design (see Table II.12).

A general rocking behaviour occurs during the last three or four tests on each wall. As to the long wall without rubber, it consists in several uplifts corresponding to strong shakes of the table. The short wall without soundproofing layers shows a continuous alternation of rotations around the bottom corners of the wall. The walls with rubber reveal smooth oscillations, even for lowest acceleration levels, without any clear uplift of any corner. The damages are mainly concentrated in the mortar joint, located at the base of the walls. This is illustrated in Figures II.31 with (a) and (b) corresponding to the long walls without and with rubber and (c) and (d) to the short walls without and with rubber. Cracks are also scattered on the wall, but are rather limited (Figure II.32). A last phenomenon is observed in the case of the long wall without acoustic devices. The additional mass rocks on the masonry wall and induces out-of-plane displacements when it goes back to the vertical position. No instability however happens.

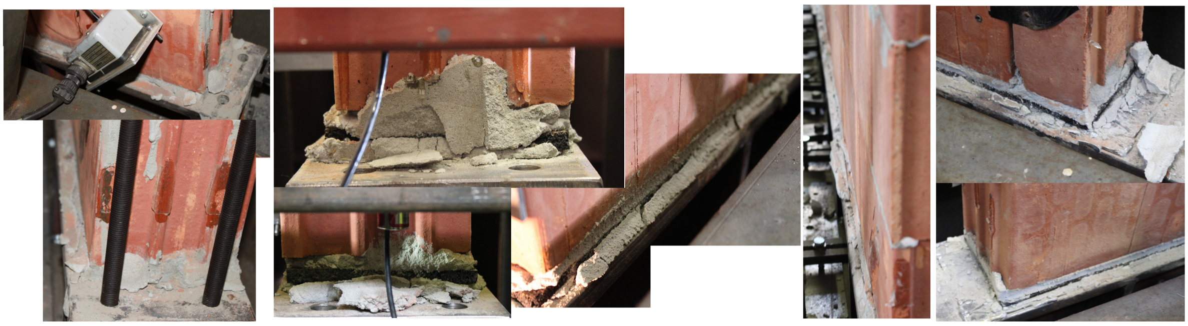
(a) (b) (c) (d)

Figure II.31: Shake table test on simple walls - Damages at the base of the walls without (a-c) and with (b-d) rubber

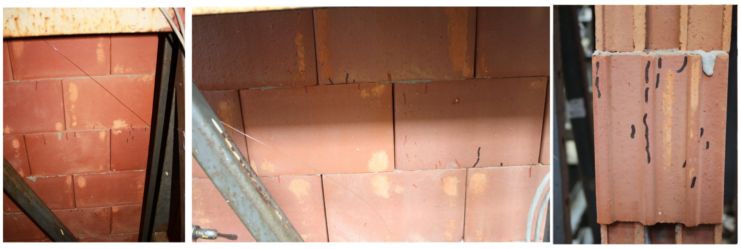
(a) (b) (c)

Figure II.32: Shake table test on simple walls - Cracks in the short wall without rubber

II.4.3.2 White noise tests

Transfer functions are derived from the Power Spectral Density (PSD) estimated with Welch's periodogram method and using the accelerations recorded during the white noise tests. The transfer functions corresponding to the long walls are plotted in Figure II.33, in blue in absence of rubber and in black when present. Figure II.34 illustrates the same results for the short wall, in red and green respectively. The dynamic identification at four stages is given, namely before (solid curve) and after the first shake (dashed curve), in the middle of the test sequence (dot-dashed curve) and after the last shake (dotted curve). The two main identified peaks are sharper and higher in the case of the test performed after the first shake in comparison to the one carried out before, except for the short wall including rubber (green curve). A leftward shift is then observed for all walls as the seismic tests go along, together with an increasing damping.

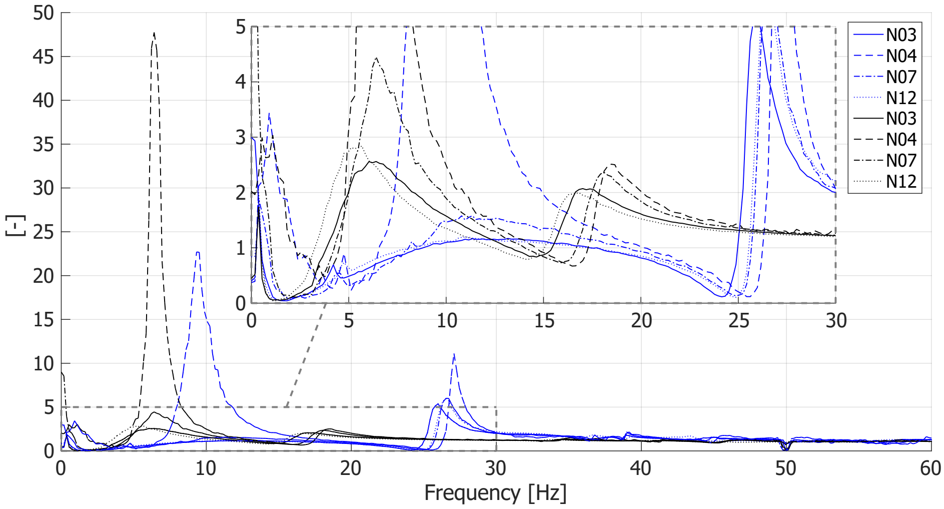

Figure II.33: Shake table test on simple walls - Transfer functions of the long walls without (blue) and with (black) rubber

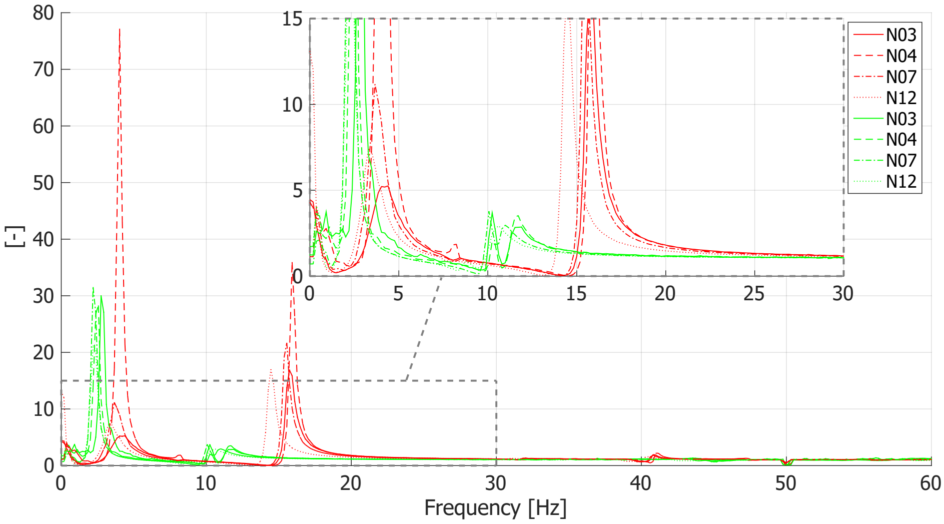

Figure II.34: Shake table test on simple walls - Transfer functions of the short walls without (red) and with (green) rubber

The natural frequencies of the walls are the abscissa of the peaks identified here above. They are given in Figure II.35 for every white noise tests preceding a shake and after the last shake. Only one point is given for the first peak related to the long wall without rubber because of its flatness. For the other walls, a general tendency is visible and shows a progressive decrease seismic test after seismic test. The mode shapes corresponding to the first two natural frequencies are given in Figure II.36. Assuming that the specimen behaves as a two-degree-of-freedom system (wall + mass), the two modes are the classical ones with a phase coincidence and opposition respectively.

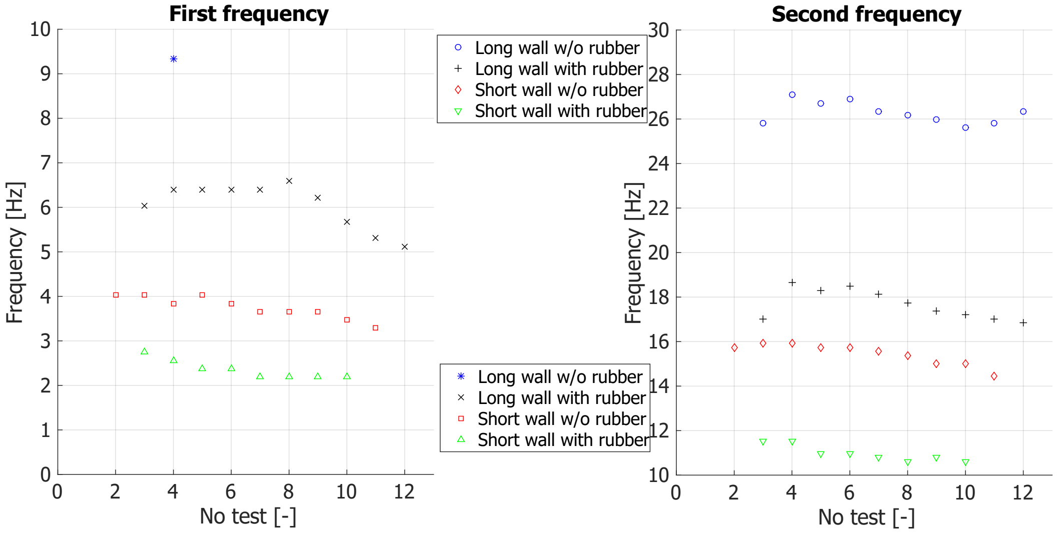

Figure II.35: Shake table test on simple walls - Identified natural frequencies of the walls

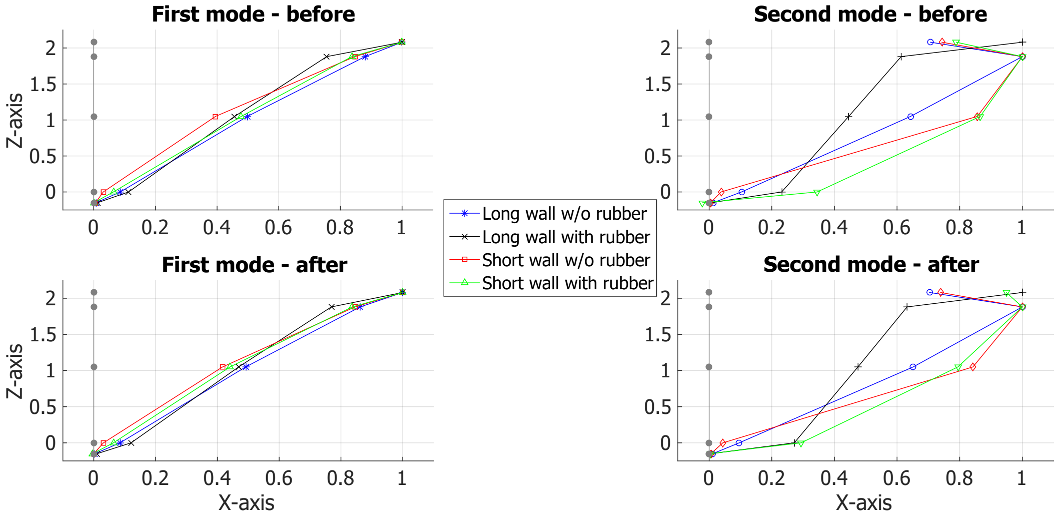

Figure II.36: Shake table test on simple walls - Mode shapes of the long walls

II.4.3.3 Shake table tests

Three physical quantities are described with respect to the actual PGA and characterise the seismic response of the walls. The first two quantities are measured at the top of the wall and the centroid of the additional mass. The first one is the maximum acceleration and is shown in Figure II.37. Graphs (a) and (b) give the results for the long wall without and with rubber respectively. Graph (c) provides those for the short wall without any devices, while graph (d) is focused on the short wall including soundproofing layers. The second quantity is the maximum horizontal drift, represented in Figure II.38 according to the layout used in Figure II.37. All graphs also include a grey straight line representing the perfectly elastic behaviour. The response of the walls is finally described by the rotations of the base of the wall and of the additional mass, which are plotted in Figure II.39.

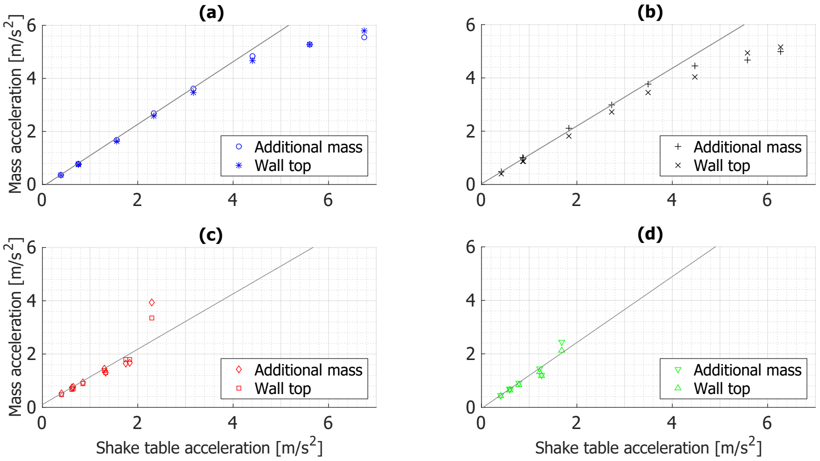

Figure II.37: Shake table test on simple walls - Maximum acceleration at the top

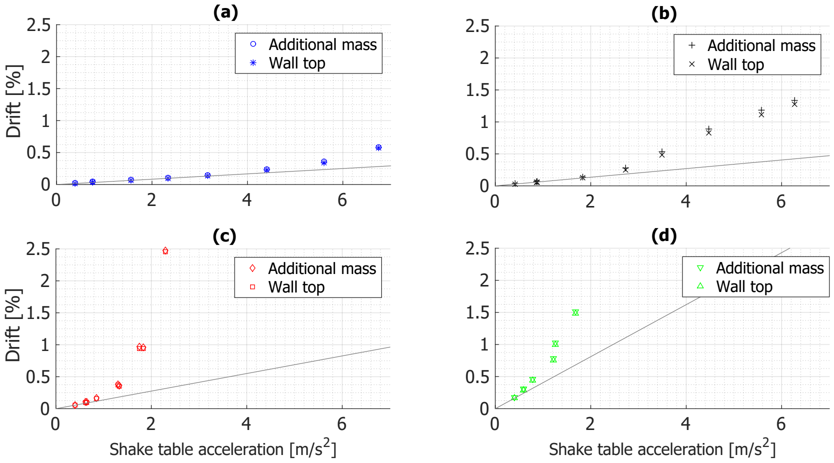

Figure II.38: Shake table test on simple walls - Maximum relative horizontal displacement at the top of the wall

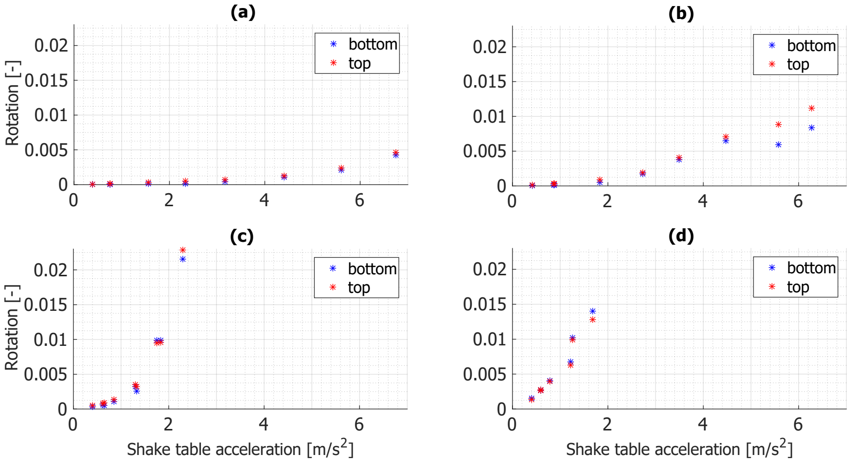

Figure II.39: Shake table test on simple walls - Maximum rotation of the bottom and top of the wall

Another result representative of the seismic response is the force displacement curve. The horizontal force at the top of the wall is not directly measured during the tests, but can be estimated by the acceleration at this level. This force P_{top} and the drift δ_{top} of the centroid of the additional mass are given by

$$P_{top}\left(t\right) = m\ddot{x}\left(t\right) \tag{II.11}$$

$$\delta_{top}\left(t\right) = \frac{\left(x\left(t\right) - x_g\left(t\right)\right)}{h_{top}} \tag{II.12}$$

where m [kg] is the magnitude of the additional mass and $\ddot{x}\left(t\right)$ [m/s^2] is the acceleration measured at its centroid. The horizontal displacement of the additional mass $x\left(t\right)$ [m] and of the shake table $x_g\left(t\right)$ [m] are obtained by integration of the corresponding acceleration. The height h_{top} [m] is the distance between the base of the wall and the gravity centre of the additional mass, equals to 2.08 m. Figure II.40 plots the $P_{top} - \delta_{top}$ curves for the shakes after the first repeated acceleration level. Figure II.40 follows the same layout described here above.

The $P_{top} - \delta_{top}$ curves exhibit a plateau around 20 kN for the long walls and around 8 kN for the short walls. Regarding these latter, the plateau is over-passed during the last shake. The test S05 also shows a slightly higher maximum force in the case of the short wall including rubber (see Figure II.40 (d)).

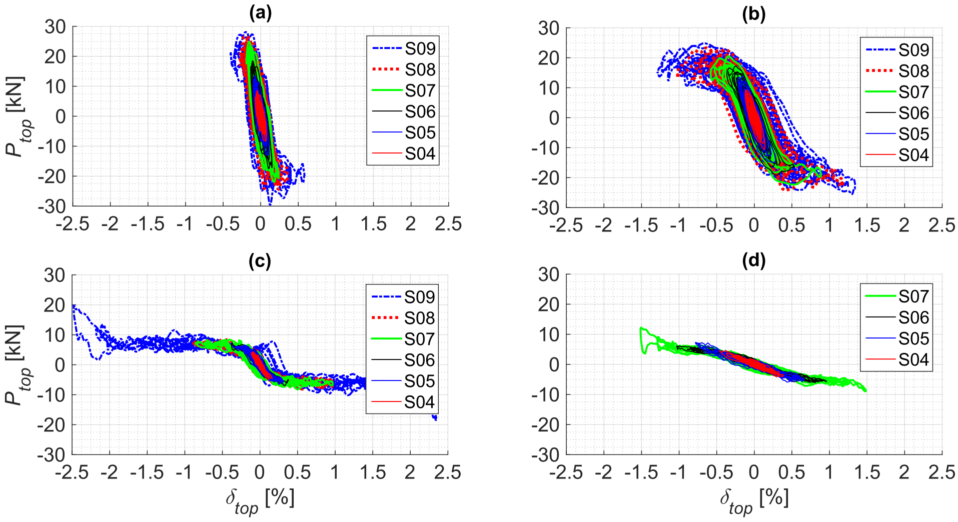

Figure II.40: Shake table test on simple walls - Force-displacement curves

Last results are focused on the behaviour of the base of the walls. The time evolution of the vertical and horizontal relative displacements is measured at three points of the base (see Section II.4.2). The results illustrated in Figures II.41 to II.44 correspond to the test S09 for the long walls and S06 for the short walls.

A positive vertical displacement translates an uplift of the base of the wall. The maximum is larger than the minimum, a negative magnitude being governed by the stiffness of the base layer (mortar or rubber). The signals corresponding to the relative vertical displacement at mid-length and at the far extremity are similar because the sensor at mid-length is slightly closer to the far side. In Figure II.42, the far extremity signal seems to be bounded. This observation is only a consequence of an inappropriate sensor which runs its course. Regarding the horizontal displacement, the three signals evolve similarly, but the signal corresponding the to near extremity has a reduced magnitude, especially for the short wall without rubber.

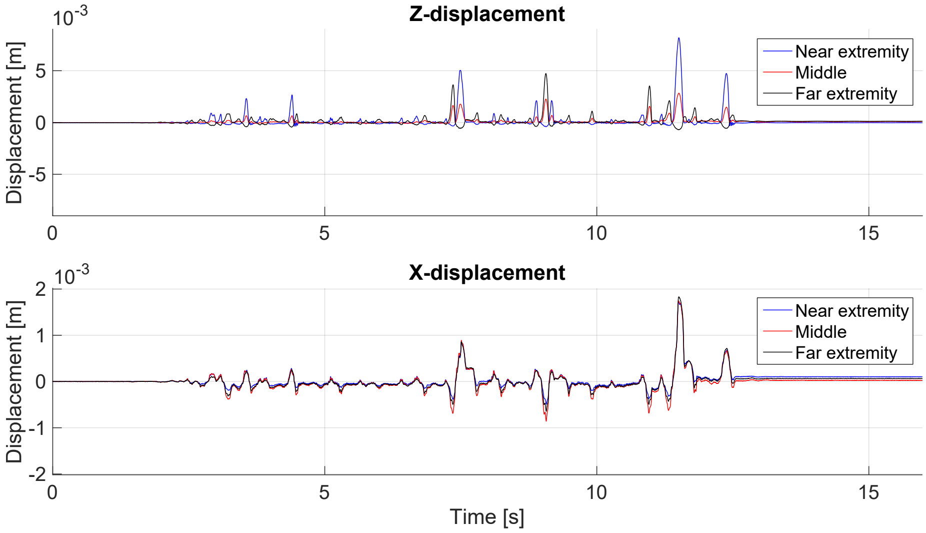

Figure II.41: Shake table test on simple walls - Time evolution of the z- and x-displacements of the wall base (long wall without rubber)

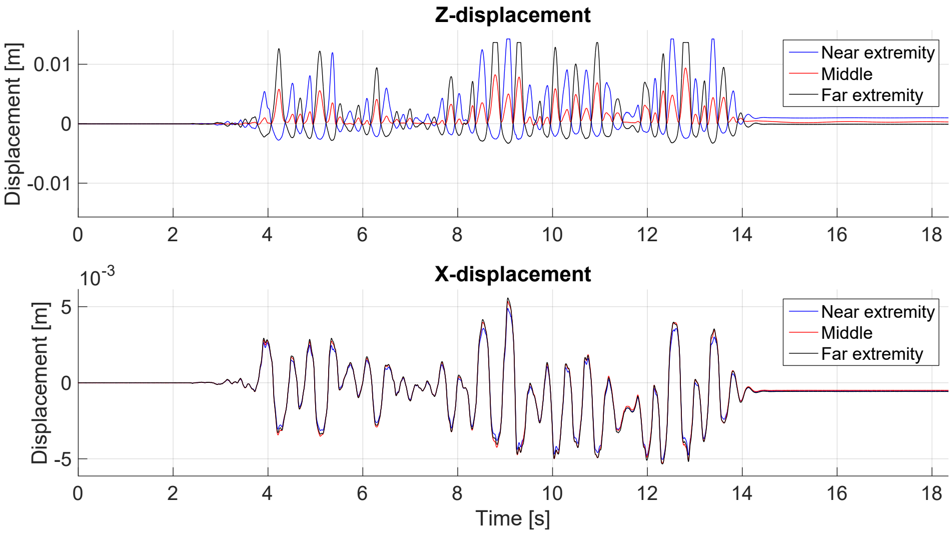

Figure II.42: Shake table test on simple walls - Time evolution of the z- and x-displacements of the wall base (long wall with rubber)

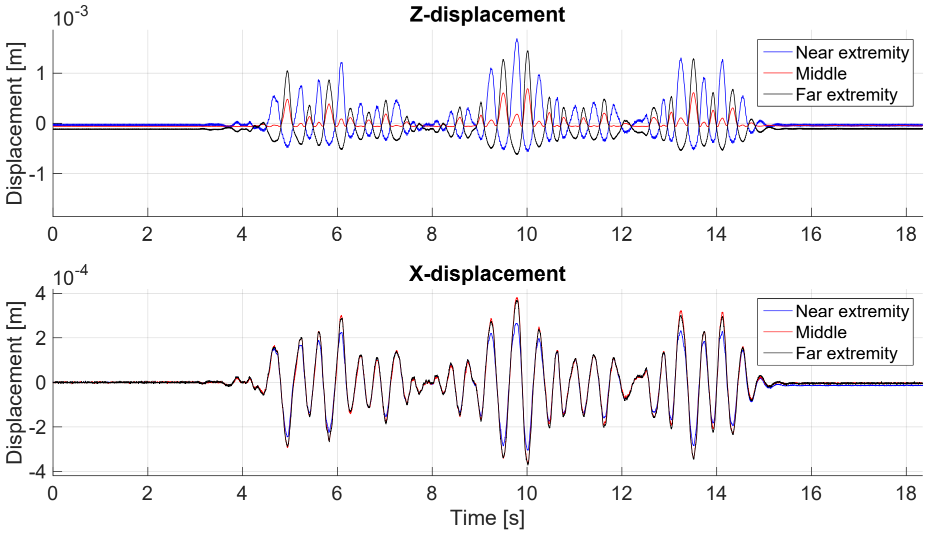

Figure II.43: Shake table test on simple walls - Time evolution of the z- and x-displacements of the wall base (short wall without rubber)

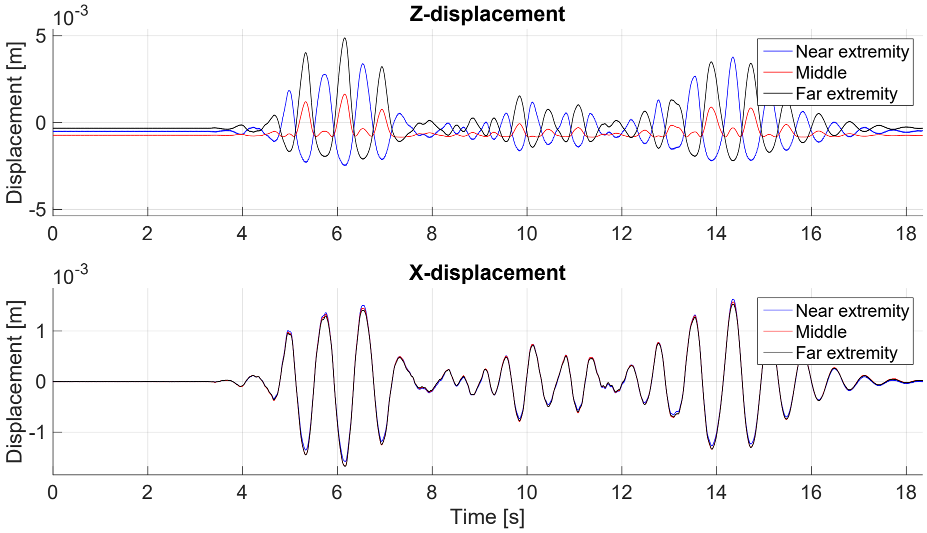

Figure II.44: Shake table test on simple walls - Time-evolution of the z- and x-displacements of the wall base (short wall with rubber)

II.4.4 Interpretation and discussion

II.4.4.1 Interaction with the steel frames

A total of three runs on the short walls have to be disregarded because of interactions with the steel frames. It concerns the shakes S05 and S07 for the wall including rubber and the S09 for the other wall. More precisely, contacts occur between the frames and the guides of the additional mass, disturbing the behaviour of the wall. These impacts explain the presence of accelerations at the top of the specimen above the straight line representing the elastic behaviour (see Figure II.37 (c) and (d)) and, therefore, the exceedance of the plateau in the $P_{top} - \delta_{top}$ curves (Figure II.40 (c) and (d)). The others consequences are the limitation of the horizontal displacement of the top of the wall and of the rotation of the additional mass (see graphs (c) and (d) in Figures II.38 and II.39).

II.4.4.2 Rocking behaviour

A general rocking behaviour is observed during seismic tests at the highest acceleration levels and influences the seismic response of the walls. The main consequence is the capacity of walls to sustain a PGA three times higher than predicted by the current standards for the seismic design of URM which only consider the classical collapse mechanisms in bending, in shear or by overturning. Rocking is a well known and efficient process for the dissipation of energy induced by earthquakes for RC structures [116] and could be therefore consider for URM structures.

Different observations made in the previous sections bear witness to this behaviour. First, the concentration of the damages in the bottom mortar joint is a characteristic damage pattern of the rocking. Then, the comparison of the rotations measured at the bottom and at the top of the walls shows the transition from a cantilever-beam like behaviour to rocking (see Figure II.39). The former involves zero-rotation (or insignificant) at the clamped base and free rotation at the top, while the latter requires similar rotations at the bottom and top. This transition is demonstrated in Figure II.45 for the short wall without rubber. The measurement of rather important horizontal relative displacements at the wall base is also explained by the rocking of the wall (Figure II.43). Finally, rocking causes a more than proportional increase of the maximum horizontal drift and rotation (Figures II.38 and II.39) at the top of the specimen with respect to the PGA. The tremors of the table activate inertial forces at the level of the additional mass, which create a destabilizing overturning moment. Due to the lack of tensile strength, this moment implies the uplift of the wall when the restoring moment coming from the gravity is exceeded, leading to the rotation of the wall with respect to its support and to an induced horizontal drift of the additional mass. An increase of PGA has a double effect. On the one hand, a higher PGA means a larger destabilizing overturning moment since the inertial force increases. On the other hand, the restoring moment decreases given that the induced horizontal drift of the mass reduces the distance between the centroid of this latter and the rotating point of the wall (i.e. the bottom corner if the wall is considered as a rigid body). The combination of these two effects explains why the maxima of the rotation and drift at the top of the walls increase more than proportionally with respect to the PGA. In terms of accelerations, the points in Figure II.37 deviate increasingly under the straight line because the motion generated by rocking goes in the opposite direction of the table motion. Contrary to the maximum horizontal drift, the maximum top accelerations augment therefore less than proportionally with respect to the

PGA.

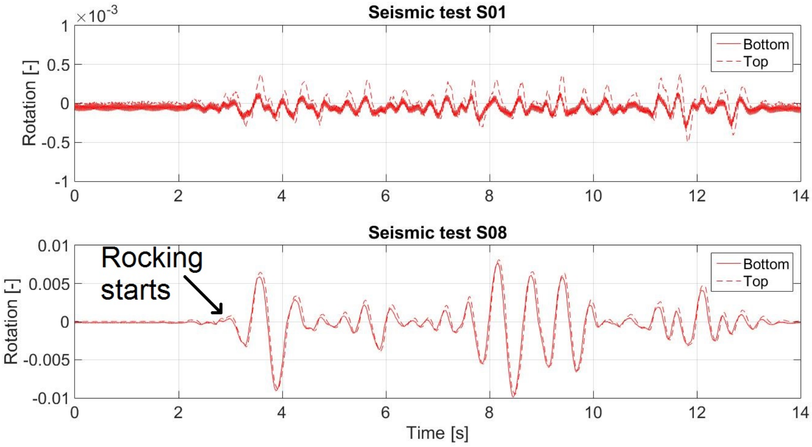

Figure II.45: Shake table test on simple walls - Time evolution of the rotations of the wall base and top (S01 and S08) - short wall without rubber

Rocking is strongly dependent on the wall length (aspect ratio) and on the presence of the rubber. The aspect ratio is a well known parameter of the rocking motion (see Chapter VI). A longer wall requires a higher acceleration to observe an uplift since the restoring moment is larger. This is illustrated in Figures II.37, II.38 and II.39 given that the markers corresponding to the long walls remain closer to the straight line for higher PGA than those related to the short walls. Moreover, the comparison of Figures II.41 and II.43 highlights the effects of the wall length: the corners of the long wall are only lifted from time to time, while the short wall shows a clear alternating uplift of its corners. Regarding the rubber, the presence of soundproofing layers completely modifies the behaviour. There is a transition from a classical rocking behaviour on a rigid support to a wall moving on a flexible layer, leading to larger drift and rotation at the same PGA. The walls also exhibit significant rotation a longer time after the end of the shake when there are acoustic devices. It translates a lower damping of the structure, as shown in Figures II.43 and II.44 for instance.

Finally, rocking provides an interesting ductility to the walls. Indeed, the plateau in the $P_{top} - \delta_{top}$ curves appears once the inertial force is large enough to overturn the wall. It do not correspond to the ultimate limit state as supposed by equivalent static design procedure. The consequence of an increase of PGA is a larger horizontal drift. This can be translated by a behaviour factor q which allow the wall to sustain larger seismic acceleration. The assessment of the q-factor is based on equivalent push-over curves (see below).

II.4.4.3 Influence of rubber layers

Rubber layers have consequences on the dynamic properties of the walls and, thus, on the seismic response.

First, the natural frequencies of the studied walls are reduced when they include soundproofing devices. This can be seen in the transfer functions, with a leftward shift of the peaks (see Figures II.33 and II.34). Table II.14 summarizes the frequencies obtained by peak picking. The presence of acoustic layers decreases of 1/3 the fundamental frequency of the undamaged walls. The frequency drop observed in Figure II.35 can be assessed thanks to Table II.14. Such phenomenon has been already discussed by Michel [81]. The identification performed after S06 on short walls gives a relative difference with the undamaged configuration of 9.1 % and 20.0 % for situations without and with rubber respectively. The deterioration is therefore more important for the soundproofed specimen. As concluded in Section II.2, interaction between the masonry and the rubber can be detrimental for the overall behaviour.

Table II.14: Shake table test on simple walls - Natural frequencies of the walls

Test		N02	N03	N04	N05	N06	N07	N08	N09	N10	N11	N12
Long wall w/o rubber	1st	/	/	9.33	/	/	/	/	/	/	/	/
	2nd	/	25.80	27.08	26.71	26.90	26.35	26.16	25.98	25.62	25.80	26.35
Long wall with rubber	1st	/	6.04	6.40	6.40	6.40	6.40	6.59	6.22	5.67	5.31	5.12
	2nd	/	17.02	18.66	18.30	18.48	18.11	17.75	17.38	17.20	17.02	16.83
Short wall w/o rubber	1st	4.02	4.02	3.84	4.02	3.84	3.66	3.66	3.66	3.48	3.29	/
	2nd	15.74	15.92	15.92	15.74	15.734	15.55	15.37	15.00	15.00	14.45	/
Short wall with rubber	1st	/	2.74	2.56	2.38	2.38	2.20	2.20	2.20	2.20	/	/
	2nd	/	11.53	11.53	10.98	10.98	10.80	10.61	10.80	10.61	/	/

Then, the mode shapes present transverse deformation concentrated at the bottom and top of the masonry walls when there are rubber layers (Figure II.36). One third of the deformation is located in the two 1-cm thick layers approximately. The presence of rubber also reduces the influence of the wall length as the mode shapes related to walls of different lengths seem to be more similar (closer to a straight line).

Finally, the seismic response is influenced as the rocking behaviour is modified in presence of rubber (see previous section).

II.4.4.4 Compressive length

A main characteristic of masonry wall subjected to a horizontal shear is the compressive length. In the present campaign, this length is calculated by a linear interpolation of the vertical relative displacement at the three points of the base of the wall. This procedure is based on the assumption that the wall cross-section remains plane. The comparison between real measurements, depicted by markers, and the linear interpolation at a given time however contradicts this assumption, as illustrated in Figure II.46. The difference probably comes from the opening of the vertical joints of the masonry. This also explains why the horizontal displacements of the wall base are not perfectly the same along the time (see Figure II.43).

Figure II.47 plots the minimum compressive length of each shake with respect to the actual PGA. As expected, the compressive length decreases faster for the short wall than for the long one. However, the main learning of Figure II.47 is that the compressive length under a same acceleration level is higher when there are rubber layers. This positive effect has to be balanced with the higher horizontal drift observed previously.

Regarding the long walls, the last runs (from S07 for the long wall without rubber and from S06 for the one with rubber) give a zero compressive length. These values have to be disregarded as the measurements are irrelevant. Indeed, the progressive deterioration of the joint at the base of the wall seems to produce pieces of mortar (see Figure II.31) which remain under the wall and prevent this latter to come back to its initial position, as shown in

Figure II.48 for S06 with the long wall with rubber. Meaningless results are then obtained, as a transition from rocking around one side to another without a return to the vertical position for instance.

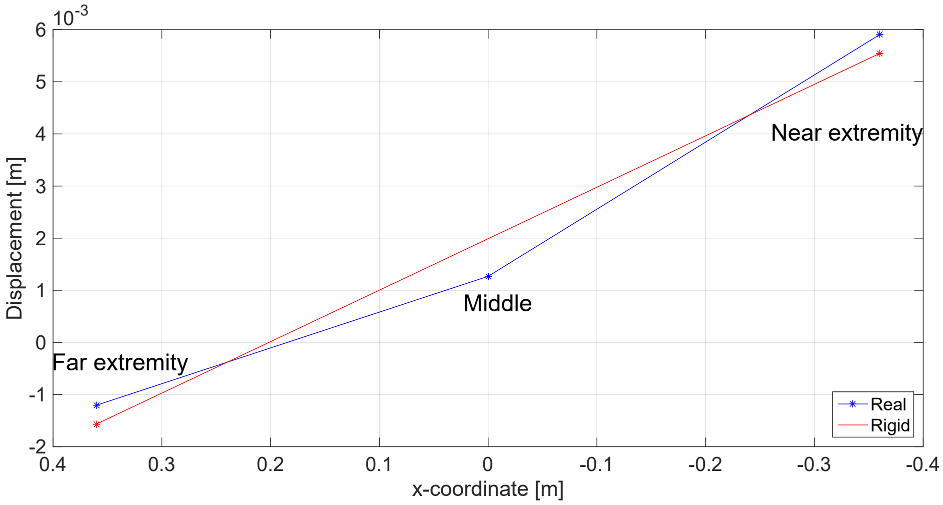

Figure II.46: Shake table test on simple walls - Difference of horizontal relative displacement at different points of the base

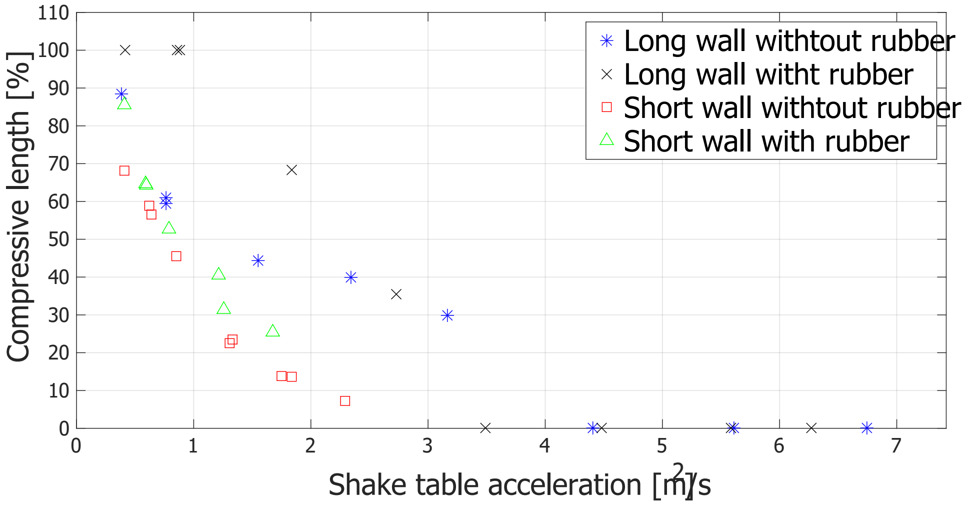

Figure II.47: Shake table test on simple walls - Minimum compressive length with respect to the actual PGA

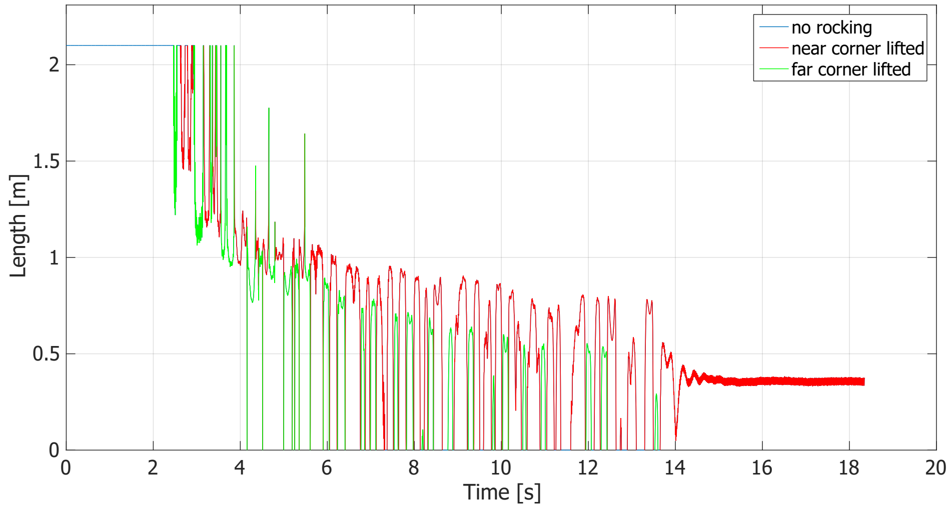

Figure II.48: Shake table test on simple walls - Time evolution of the compressive length (S06 - long wall with rubber)

II.4.4.5 Push-over curves

Starting from the force-displacement curves, equivalent push-over curves can be derived by plotting the minimum (maximum) force with respect to the maximum (minimum) relative displacement for each relevant shake (see Figure II.49). The positive direction refers to the part of the force-displacement curves with a positive drift.

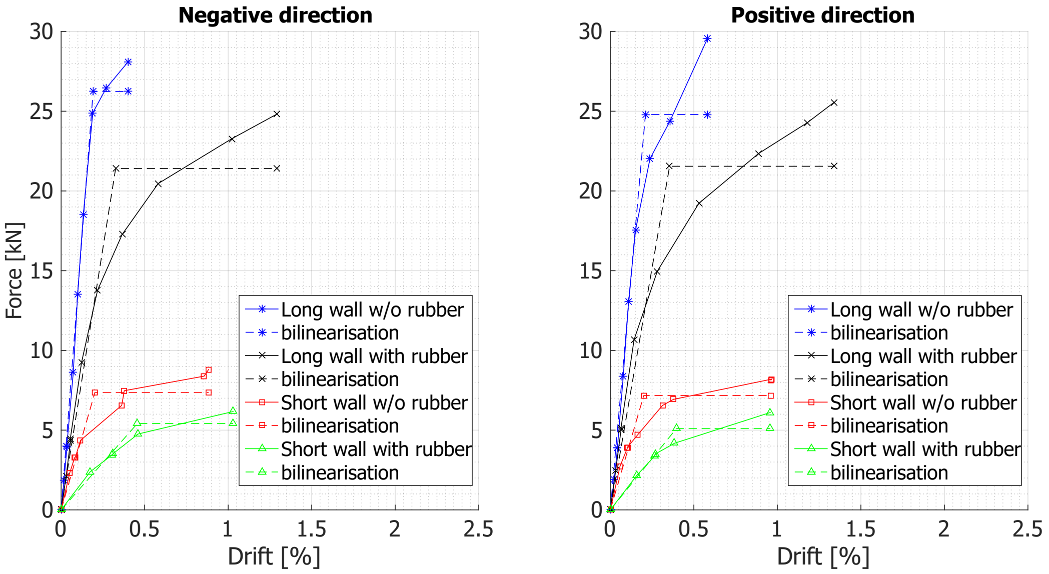

Figure II.49: Shake table test on simple walls - Push-over curves in the negative (left) and positive (right) directions

Comparison between the blue and black curves related to the long walls (red and green for the short walls) shows a clear decrease of stiffness in presence of rubber. When comparing push-over curves in negative and positive directions, it appears that the walls seem to be slightly stiffer in the negative direction, except for the short wall with rubber. There is no geometrical nor mechanical reason to explain this difference, apart from the distribution of the mass along the wall.

Figure II.49 also includes bilinear curves for each wall in negative and positive direction. They are derived according to the procedure used in Section II.2.4 and characterised by the same parameters (Table II.15). No wall completely failed during the tests; the curves in Figure II.49 are therefore incomplete. The curves are however sufficiently developed to estimate the main parameters, except for the ductility which could be larger.

Table II.15: Shake table test on simple walls - Parameters of the bilinear curves

	Initial stiffness k_{ini}[N/m]		Yield drift d_y[%]		ductility μ[-]	
	Negative	Positive	Negative	Positive	Negative	Positive
Long wall w/o rubber	$6.586 \cdot 10^6$	$5.669 \cdot 10^6$	0.192	0.210	2.089	2.768
Long wall with rubber	$3.154 \cdot 10^6$	$2.920 \cdot 10^6$	0.326	0.355	3.955	3.776
Short wall w/o rubber	$1.751 \cdot 10^6$	$1.723 \cdot 10^6$	0.202	0.200	4.374	4.801
Short wall with rubber	$5.705 \cdot 10^5$	$6.199 \cdot 10^5$	0.456	0.395	2.257	2.424

Table II.15 shows variations from -8.7 % to +13.9 % for the initial stiffness in both directions. The highest difference is observed for the long wall without rubber. The initial stiffness is reduced by 58 % on average when rubber layers are placed at the extremities of the walls, while the yield drift is doubled. An interesting observation is that the yield drift is approximately the same for both walls without rubber, regardless of their length. This leads to the conclusion that these walls have the same behaviour. The ductility can be translated into a q-factor provided by the rocking behaviour.

II.5 Shake table tests on frames with T- and L-shaped piers

II.5.1 Description of the specimens

The fourth and last campaign includes two specimens. They relate to frame-like structures due to the presence of an opening. Their geometry differs with regard to the cross-section of the piers, as illustrated in Figure II.50. The *shear walls* refer to the sections of the piers oriented in the plane of the frame. The *flanges* correspond to the perpendicular sections. The masonry units are clay blocks of the same type as those used in the first and third campaigns (see Sections II.2 and II.4). The mechanical and material properties are thus given in Table II.1. The horizontal elements, namely a RC lintel and a RC slab, are similar for both frames. Additional steel parallelepipeds are fixed on the slab to simulate the structural load. The total weight of these prisms is equal to 5 tons.

Other differences are defined in the design of the specimens. On the one hand, the T-shaped piers are oriented such as this frame has no axis of symmetry. The specimen with L-shaped piers shows a single axis of symmetry, perpendicular to the plane of the frame. The main consequence is an expected global torsion when testing the T-shaped frame. The orientation of the piers indeed influences the stiffness along both directions. Concerning the L-shaped frame, a torsion can be observed when shaking along the frame direction due to the distance between the gravity centre of the slab and the rotation centre of the specimen. On the other hand, the L-shaped frame presents different connection methods for the perpendicular sections of masonry piers. A classical masonwork is performed for the left one (y-positive) and the sections of the right one (y-negative) are glued to each other with a continuous vertical joint along the height. The difference is visible in Figure II.50. The latter method is similar to the one used in the second campaign described in this thesis (see Section II.3). This difference aims at studying the influence of the connection type on the global behaviour. The classical masonwork is enforced for the specimen with T-shaped piers.

The specimens are built by professional masons on HEM 160 steel beams for transportation reasons. Steel connectors are placed between the masonry frame/RC lintel and the RC slab. Their use is required to simulate different loading cases on the specimens. Thereby, the L-shaped frame is subjected to a compression uniformly distributed on its piers (full loaded) and another acting on the flanges only (flanges loaded). Figure II.51 gives the positions of the connectors in the case of the L-shaped frame with the slab resting on the whole piers. The second loading configuration is obtained by removing the two connectors located on the shear walls. Regarding the T-shaped frames, the connectors are juxtaposed at the intersection of the sections of the piers.

A preliminary assessment design is performed according to the rules of the EN-1996-1-1 [34] and EN-1998-1 [116]. The different loading cases are considered and the assessment is performed for an earthquake acting along the frame (y-acceleration) and perpendicular to it (x-acceleration). The results are given in Table II.16. In Table II.16, the y-acceleration is obtained under the assumption of a redistribution of the seismic action between piers when one of them fails in shear, but is still able to sustain gravity loads.

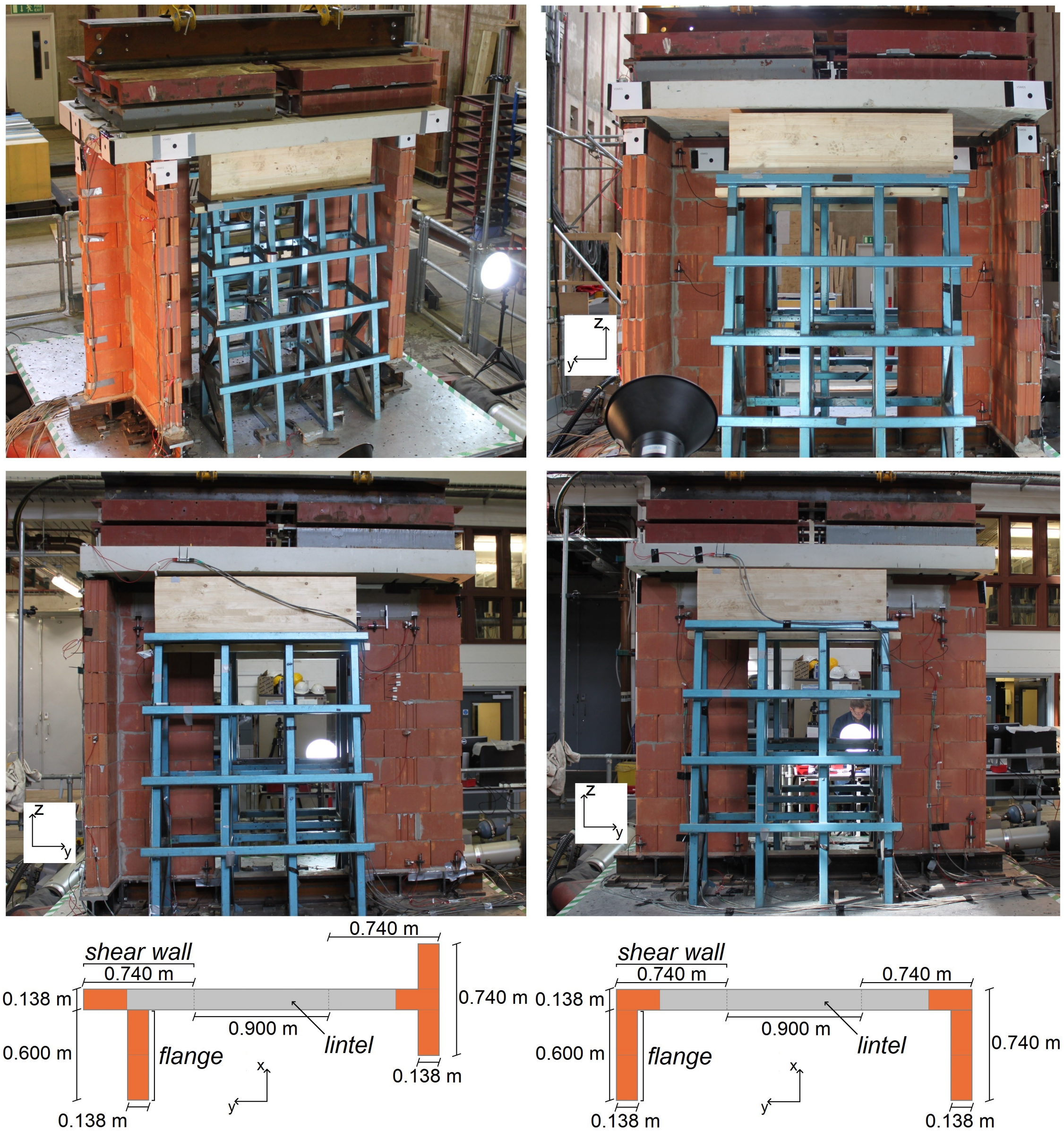
z
y
z
y
z
y
shear wall
0.740 m
0.740 m
0.138 m
0.600 m
0.900 m
lintel
flange
x
y
0.138 m
0.740 m
0.138 m
shear wall
0.740 m
0.740 m
0.138 m
0.600 m
0.900 m
lintel
flange
x
y
0.740 m
0.138 m
0.138 m

Figure II.50: Shake table tests on T- or L-shaped frames - Pictures of the specimens (left: T-shaped ; right: L-shaped)

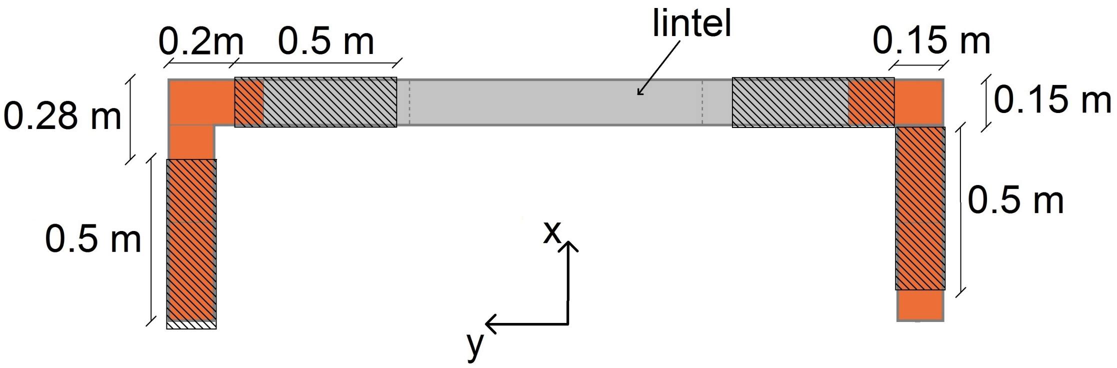
0.2m
0.5 m
lintel
0.15 m
0.28 m
0.15 m
0.5 m
0.5 m
x
y

Figure II.51: Shake table tests on T- or L-shaped frames - Position of steel connectors

Table II.16: Shake table tests on T- or L-shaped frames - Results of the preliminary assessment design

Specimen	X-acceleration [g]	Y-acceleration [g]
T-shaped frame	0.046	0.763
L-shaped frame (full loaded)	0.0633	0.829
L-shaped frame (flanges loaded)	0.0814	0.654

II.5.2 Testing procedure

II.5.2.1 Instrumentation

The instrumentation of the frames comprises accelerometers, potentiometers and an Imetrum Video-Gauge vision system. A total of 26 accelerometers are distributed on the table, the specimen and the slab. Four are dedicated to the in-plane behaviour of this latter (x- and y-directions) and 2 measure the x- and y-accelerations at the level of the table. The last 20 devices are placed on the masonry piers, recording the acceleration in both horizontal directions at the bottom and the top of the shear walls and flanges, as well as the mid-height in-plane acceleration of the sections of piers. Two of these devices are missing for the T-shaped frame (top of the flange on the right pier). Regarding the potentiometers, they mainly focus on the behaviour of the base of the piers. The relative displacement of the RC lintel with respect to the piers is also measured by 6 LVDTs. Additional sensors (6) are located at the intersection of the shear walls and flanges to capture the behaviour of the connection, in the case of the L-shaped frame only.

The instrumentation layout is illustrated in Figures II.52 and II.53 for the T- and L-shaped frames respectively. In these Figures, the vision system includes 14 markers spotted by black dots. These target the horizontal (x or y) and vertical (z) displacements of the top of the piers and of the slab. Due to optical effects, their measurements are only relevant when the table shakes in the direction of the recorded horizontal displacement. For example, VS targets on the back side (forward view) cannot be used for shake in the x-direction because these targets measure the y- and z-displacements.

Details on the exact position and type of devices will be available in ORBi [87].

II.5.2.2 Input signal and test sequences

The experimental data will be available in ORBi [87]. The specimens are subjected to a horizontal acceleration in both directions separately. The input acceleration signal is the same as the one used for tests on simple masonry walls including soundproofing devices (see Section II.4). Its PGA is scaled to reach different intensity levels, as shown in Table II.17. These levels are increased step by step without any repetition. Before each run, white noise tests are performed to characterise the dynamic properties of the specimen in the two horizontal directions.

The test sequences are therefore an alternation between the dynamic characterisation of the specimens in both horizontal directions and a shake carried out in one direction and with a PGA given in Table II.17. Regarding the frame with L-shaped piers, the direction of the input acceleration is alternated.

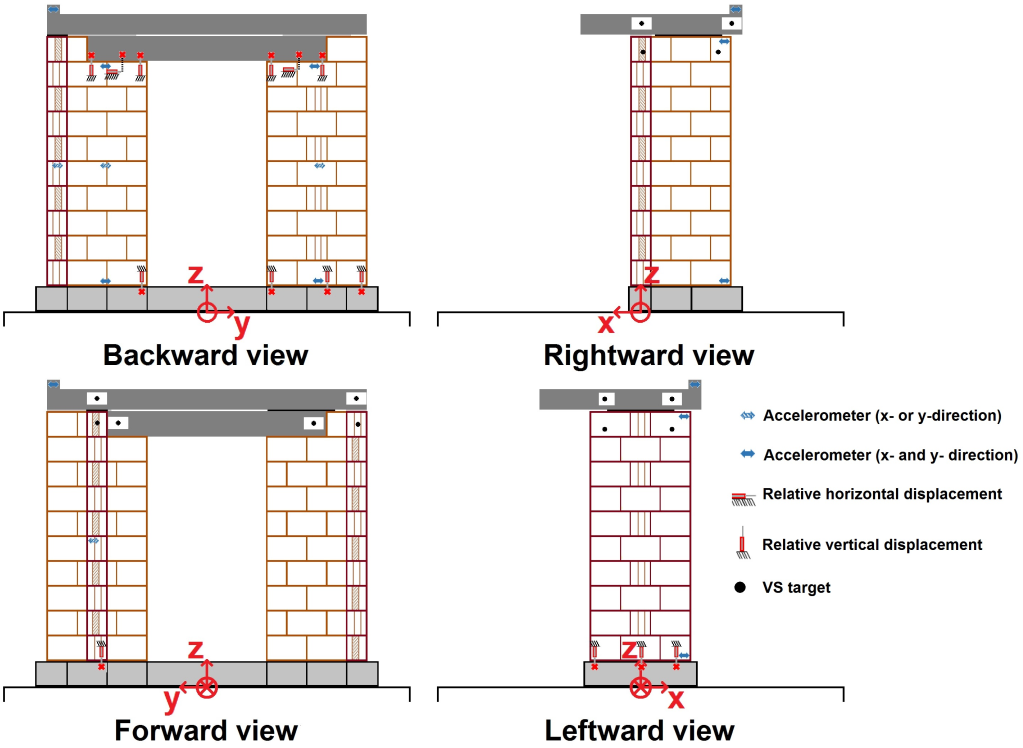
z
y
x
Backward view
Rightward view
Forward view
Leftward view
Accelerometer (x- or y-direction)
Accelerometer (x- and y- direction)
Relative horizontal displacement
Relative vertical displacement
VS target

Figure II.52: Shake table tests on T- or L-shaped frames - Instrumentation layout (T-shaped)

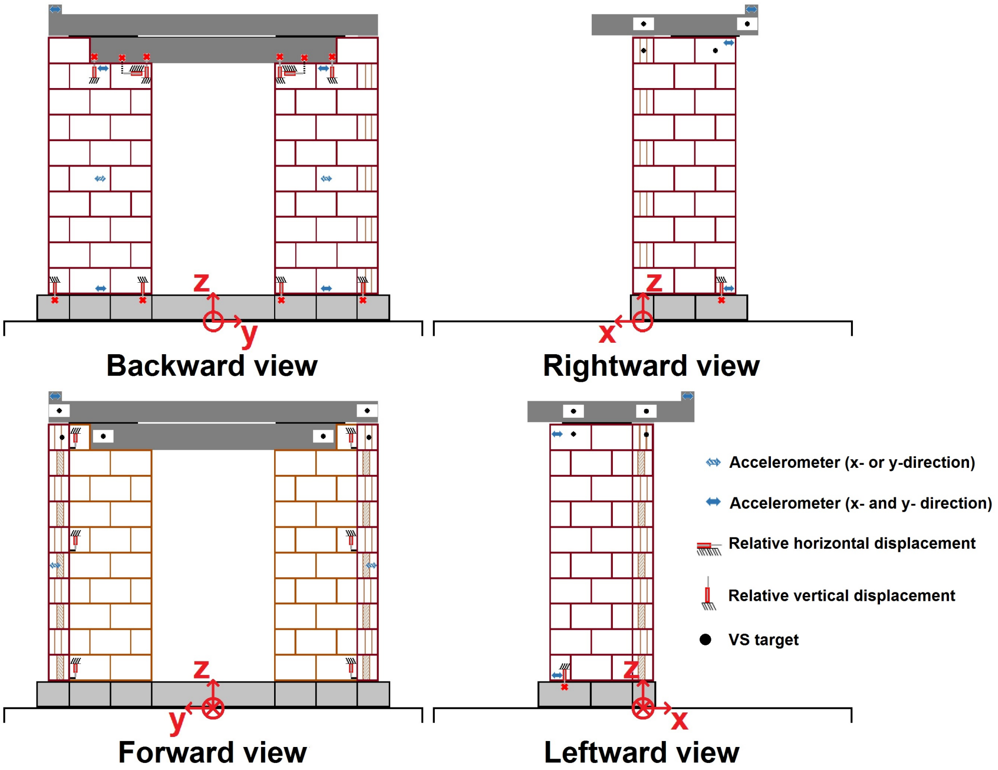
z
y
x
Backward view
Rightward view
Forward view
Leftward view
Accelerometer (x- or y-direction)
Accelerometer (x- and y- direction)
Relative horizontal displacement
Relative vertical displacement
VS target

Figure II.53: Shake table tests on T- or L-shaped frames - Instrumentation layout (L-shaped)

The actual PGA differ from and are mostly lower than the target values. This difference can be quite important, with a relative difference up to 22.7 %. The highest disparity is observed for the last shake on the L-shaped walls when the slab is supported by the flanges only (53.7%). The reason is the activation of the emergency stop during the test to avoid damages to the table because of the specimen. This test is therefore rejected. The seismic runs are supposed to be unidirectional, but an acceleration is measured in the perpendicular direction. This parasitic acceleration at the table is significant as it is up to 28.7 % of the main one.

Figure II.54 to II.56 plot the acceleration and displacement spectra of the table. These latter are normalised with respect to the target PGA in the main direction of test. The runs performed along the frame (y-direction) are drawn in solid line. Those perpendicular to the frame (x-direction) are in dotted-dashed line. The acceleration spectra derived from the measurements differ from the input one (in grey). The main difference is around 0.15-0.20 s. This location corresponds approximately to the first natural frequency of the specimens (see Section II.5.3.2).

The differences in terms of target/actual PGA and spectra can be explained by the limitation of the control system of the table, as it was for the campaign on simple walls.

Table II.17: Shake table tests on T- or L-shaped frames - Target PGA [g]

Test	Dir.	S01	S02	S03	S04	S05	S06	S07	S08	S09
T-shaped full loaded	x	0.000	0.000	0.000	0.049	0.097	0.194	0.291	0.000	/
	y	0.078	0.155	0.310	0.000	0.000	0.000	0.000	0.466	/
L-shaped full loaded	x	0.000	0.049	0.000	0.097	0.000	0.146	0.000	0.194	/
	y	0.078	0.000	0.155	0.000	0.233	0.000	0.310	0.000	/
L-shaped flanges loaded	x	0.000	0.049	0.000	0.097	0.000	0.146	0.000	0.194	0.000
	y	0.078	0.000	0.097	0.000	0.146	0.000	0.194	0.000	0.243

Table II.18: Shake table tests on T- or L-shaped frames - Actual PGA [g]

Test	Dir.	S01	S02	S03	S04	S05	S06	S07	S08	S09
T-shaped full loaded	x	0.007	0.018	0.001	0.038	0.083	0.176	0.276	0.107	/
	y	0.073	0.147	0.285	0.004	0.006	0.017	0.041	0.477	/
L-shaped full loaded	x	0.006	0.038	0.015	0.087	0.036	0.135	0.077	0.180	/
	y	0.065	0.004	0.144	0.013	0.221	0.023	0.269	0.042	/
L-shaped flanges loaded	x	0.011	0.040	0.014	0.080	0.0260	0.125	0.039	0.110	0.058
	y	0.063	0.006	0.083	0.016	0.133	0.029	0.192	0.030	0.197

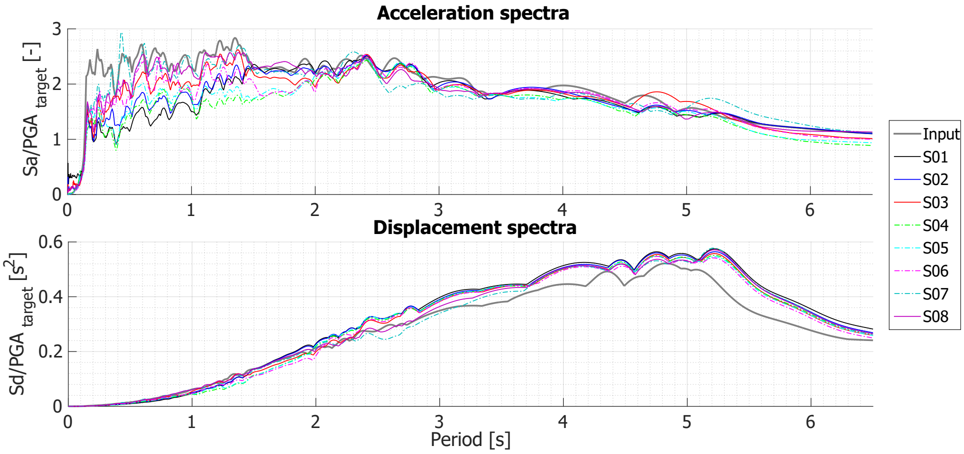

Figure II.54: Shake table tests on T- or L-shaped frames - Acceleration and displacement spectra (T-shaped)

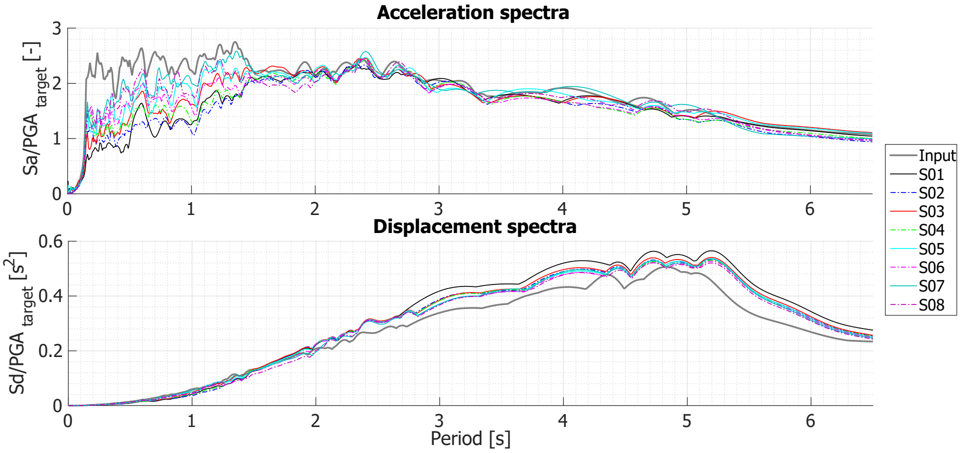

Figure II.55: Shake table tests on T- or L-shaped frames - Acceleration and displacement spectra (L-shaped, full loaded)

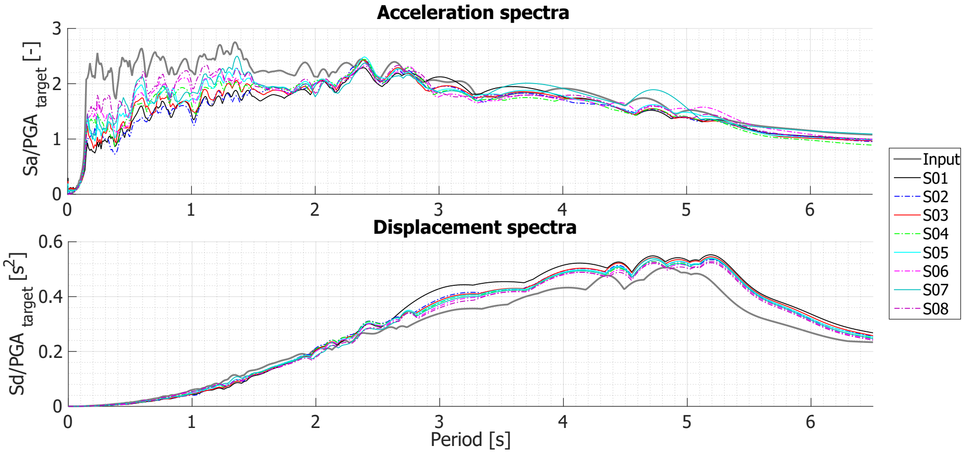

Figure II.56: Shake table tests on T- or L-shaped frames - Acceleration and displacement spectra (L-shaped, flanges only)

II.5.3 Observations and experimental results

II.5.3.1 Observations

Rocking of the piers only occurs for the highest acceleration levels. Dependence on the shake direction and on the position of the flanges is visible. Considering runs at similar intensity, the rocking amplitude seems to be indeed larger when the table shakes perpendicularly to the frame (x-direction) and when the test is performed on the T-shaped frame.

Observations of the specimen damaging first highlight a lack of strength in the connection between the lintel and the piers. Early cracks are observed in the mortar joint, as shown in Figure II.57. The lintel slides on its supports and the coupling of masonry piers is therefore ensured by the RC slab alone. The limited contribution of the lintel to the global strength is certainly a consequence of the poor restraint brought by the steel connectors. It can be observed in Figure II.57 that the contact area between the slab and the frame corresponds to the area of the steel connectors, with a rather limited part on the lintel.

Then, Figures II.58 and II.59 depict the collapse mechanisms. The left pier of the T-shaped frame presents joint openings and sliding of blocks translating a failure in torsion. Some blocks effectively seem to suffer of a counterclockwise shift (Figure II.58 (a-c)). The first courses of right pier suffer vertical cracks, joint openings and damaging of the mortar bed joint (Figure II.58 (d)). Horizontal cracks are observed all over this joint, translating the uplift of the base of the specimen (Figure II.58 (e)). The tests on L-shaped frame also end due to the deterioration of its left pier when the slab is supported by the flanges only. In this case, the failure is located at the intersection of the shear wall and the flange (Figure II.59). The method used for this connection is an alternated masonwork. In comparison to the connection with a continuous vertical glued joint, the likely weakness is the reduced shear area whereby the horizontal load induced by the slab and the additional mass is transferred between the flange and the shear wall. This reduction is a consequence of the empty vertical joints.

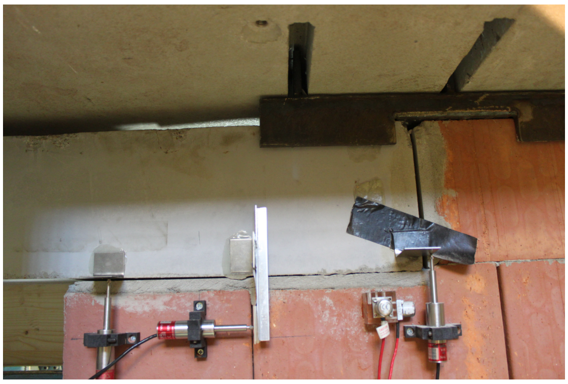

Figure II.57: Shake table tests on T- or L-shaped frames - cracks of the mortar joint between masonry piers and RC lintel

Finally, the frames are subjected to lower PGA than expected by the preliminary assessment design. The relative differences are 37.6 % and 69.4 %, for the T- and L-shaped specimens respectively. The repeated runs, the uncertainties on the slab position and the influence of the steel connectors are main reasons for these differences. Moreover, the values given in Table II.16 consider a redistribution of strength between the piers. During the experimental campaign, shakes are however stopped when the first pier is heavily damaged. The over-strength coming from the redistribution is 15.7 % in the case of fully loaded T-shaped frame. It is about 70 % for the other specimen with load distributed on the flanges, leading to an expected maximum acceleration close to the measured one. In conclusion, the collapse of T-shaped frame happens earlier than predicted due to torsion effects, while the L-shaped frame is able to sustain a slightly higher PGA.

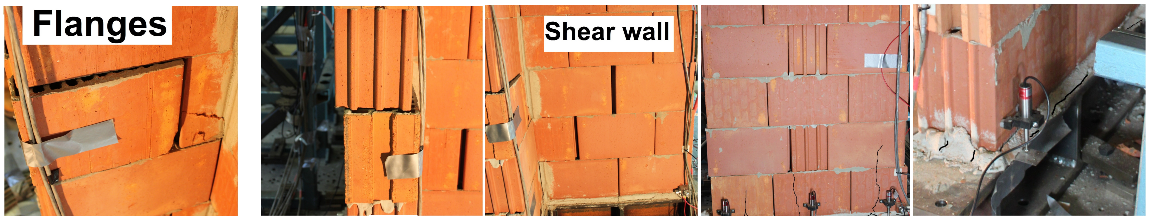

(a) (b) (c) (d) (e)

Figure II.58: Shake table tests on T- or L-shaped frames - collapse of the T-shaped frame

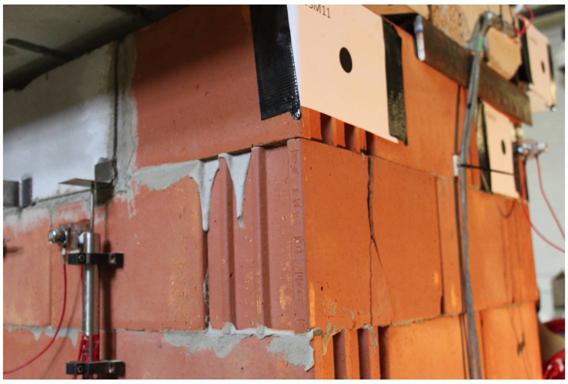

Figure II.59: Shake table tests on T- or L-shaped frames - collapse of the T-shaped frame

II.5.3.2 White noise tests

Information provided by the white noise tests is expressed in terms of transfer functions, natural frequencies and corresponding mode shapes.

The transfer functions are determined following the procedure described in II.4.3.2. Even white noise tests characterise these dynamic properties related to the x-direction, while the odd ones correspond to those in the y-direction. The results are plotted in Figures II.60 to II.63 for both specimens. Each graph uses the records of one of the four accelerometers located on the slab, above the left or the right pier. They show the effects of the first and last shakes, as well as these of the change of load case by plotting the identification performed before and after them. No identification is carried out after the last run on the L-shaped frame partially loaded. As already observed in II.4.3.2, the peak seems to shift leftwards as the test sequence proceeds.

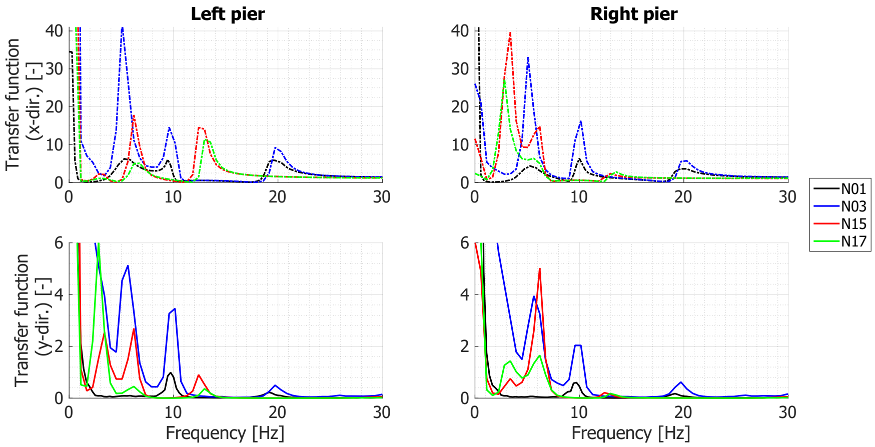

Figure II.60: Shake table tests on T- or L-shaped frames - Transfer functions of the T-shaped (x-direction)

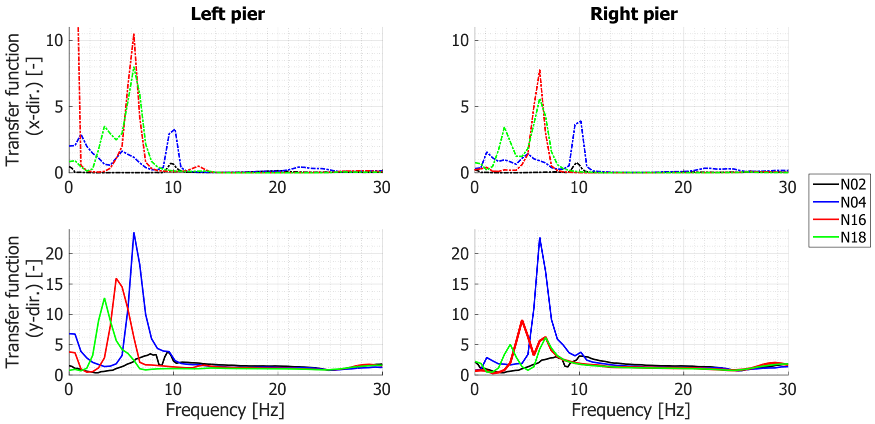

Figure II.61: Shake table tests on T- or L-shaped frames - Transfer functions of the T-shaped (y-direction)

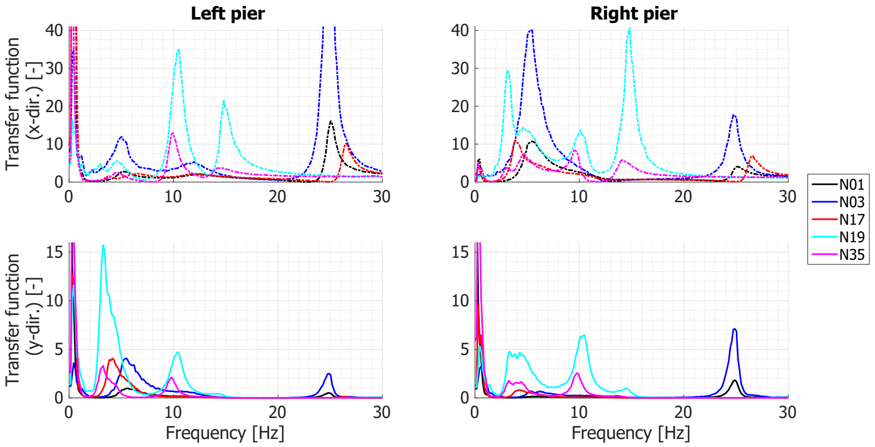

Figure II.62: Shake table tests on T- or L-shaped frames - Transfer functions of the L-shaped (x-direction)

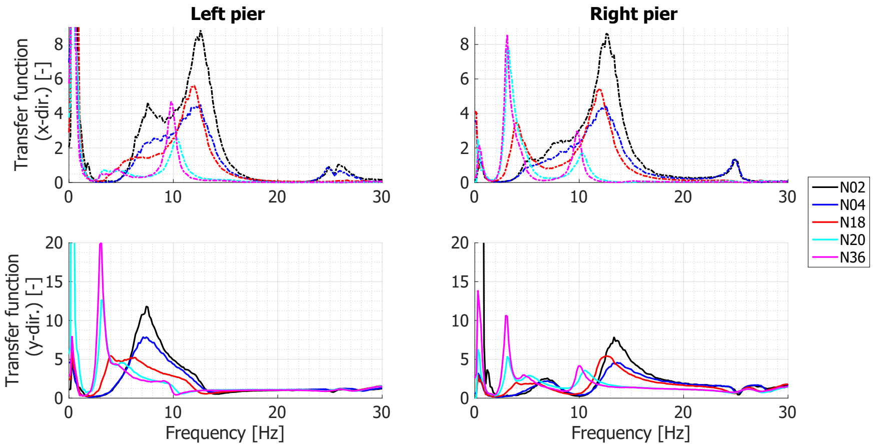

Figure II.63: Shake table tests on T- or L-shaped frames - Transfer functions of the L-shaped (y-direction)

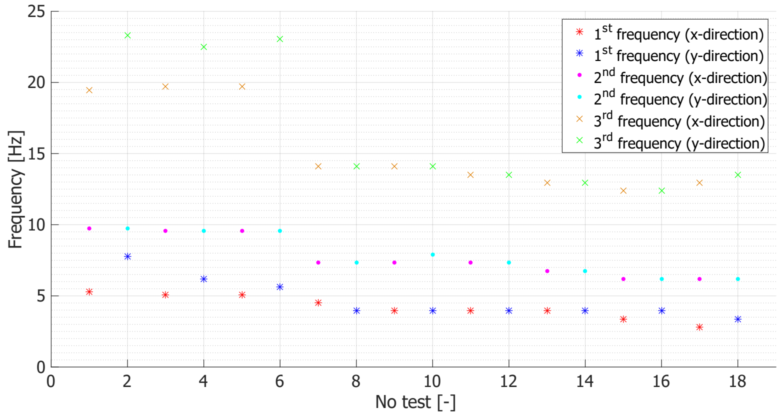

Figure II.64: Shake table tests on T- or L-shaped frames - Natural frequencies of the T-shaped frame

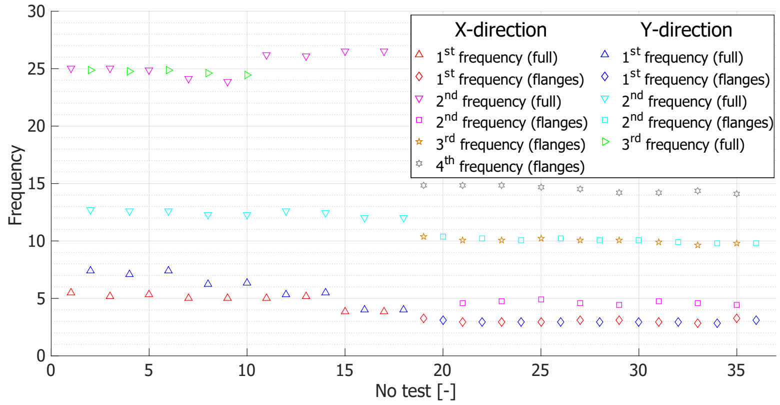

Figure II.65: Shake table tests on T- or L-shaped frames - Natural frequencies of the L-shaped frame

The determination of the natural frequencies (Figures II.64 and II.65) is not directly carried out by a peak picking based on the transfer functions. They are calculated as the eigen values of the cross-PSD matrix. Three peaks are identified for each specimen in the two horizontal directions, except for the L-shaped frame in the x-direction for which there are two or four peaks depending on the loading case. A frequency drop is globally observed.

The corresponding mode shapes are plotted in Figure II.66 for the T-shaped frame, in Figure II.67 for the L-shaped frame fully loaded and Figure II.68 for the L-shaped frame loaded on its flanges only. The mode shapes in the x- and y-directions are given in the left and the right of the figures respectively.

The first and third modes related to the T-shaped specimen are mainly translational mode in the direction of excitation. A rotation however exists given the asymmetry of the specimen. The difference between these modes lies in the mass behaviour: in the first mode, the mass is in phase with the masonry frame, while it is in φ-opposition in the case of the third mode. The second mode is a torsional one with a small translation. The different distances between the centroid of the RC slab and the rotation centres of the piers explains the translational component. Same conclusions are obtained from the study of the mode shapes corresponding to the L-shaped frame loaded on all sections of piers, with two differences for the x-direction. First, there is no torsional mode. Second, the torsional component in translational modes is larger due to the position of the steel connectors. These latter are indeed located differently on the left and right piers, as illustrated in Figure II.51. The transition to a frame where the load only acts on the flanges involves the emergence of two additional modes in the x-direction. In the y-direction, the third mode is not given because the peak identification is not possible.

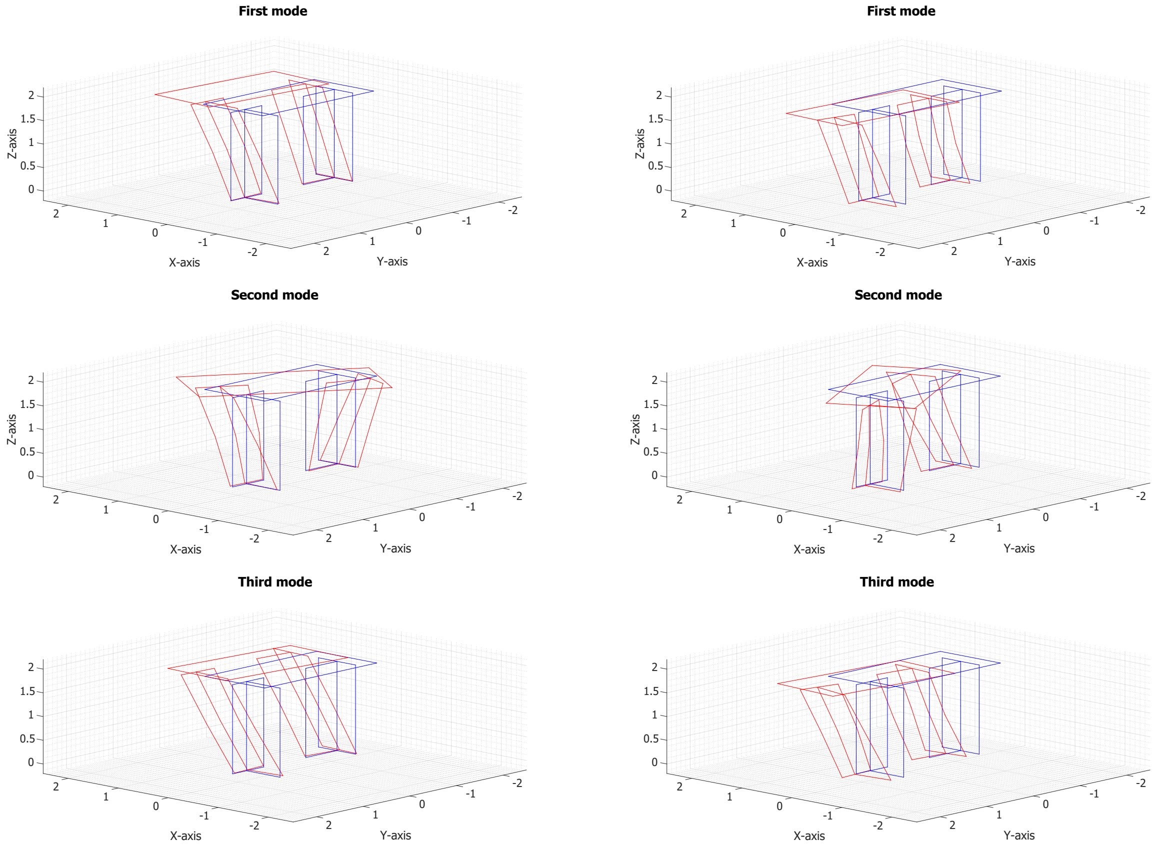

First mode

First mode

Second mode

Second mode

Third mode

Third mode

Figure II.66: Shake table tests on T- or L-shaped frames - Mode shapes of the T-shaped (left: x-direction ; right: y-direction)

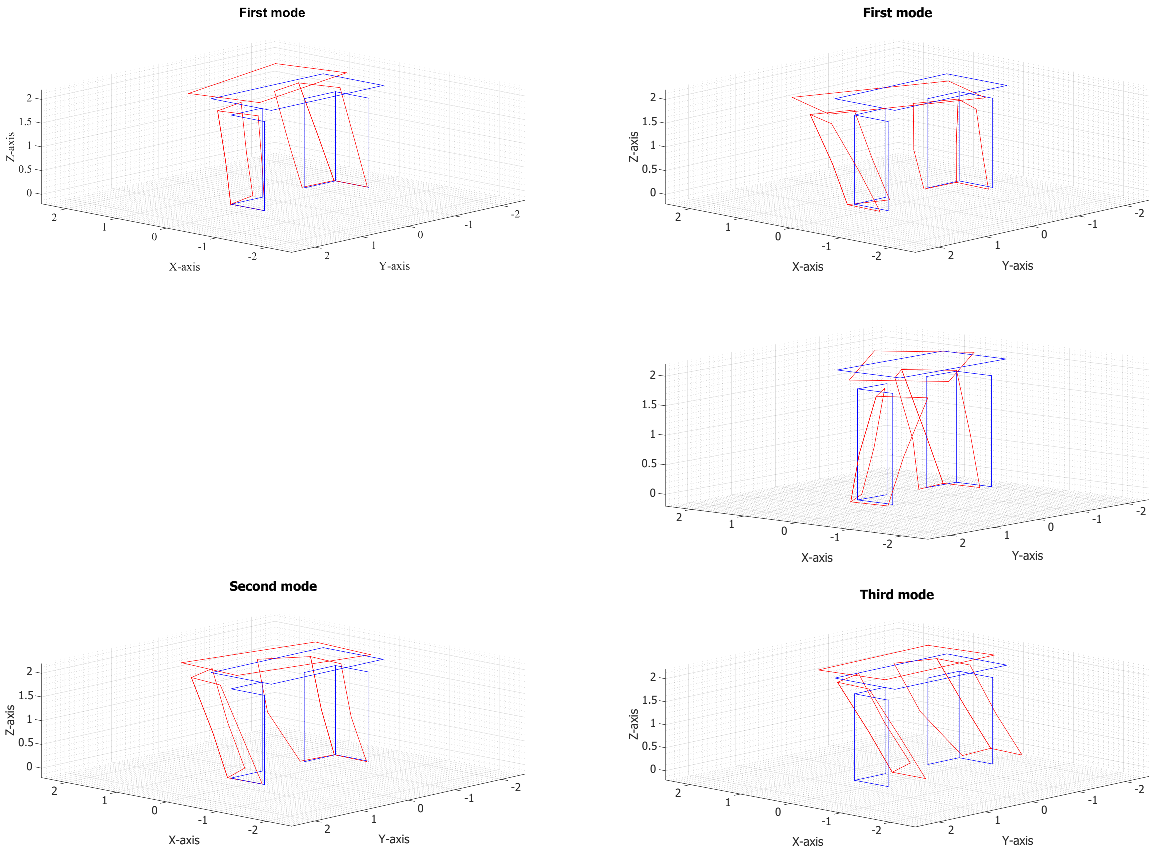

Figure II.67: Shake table tests on T- or L-shaped frames - Mode shapes of the L-shaped (full loaded - left: x-direction ; right: y-direction)

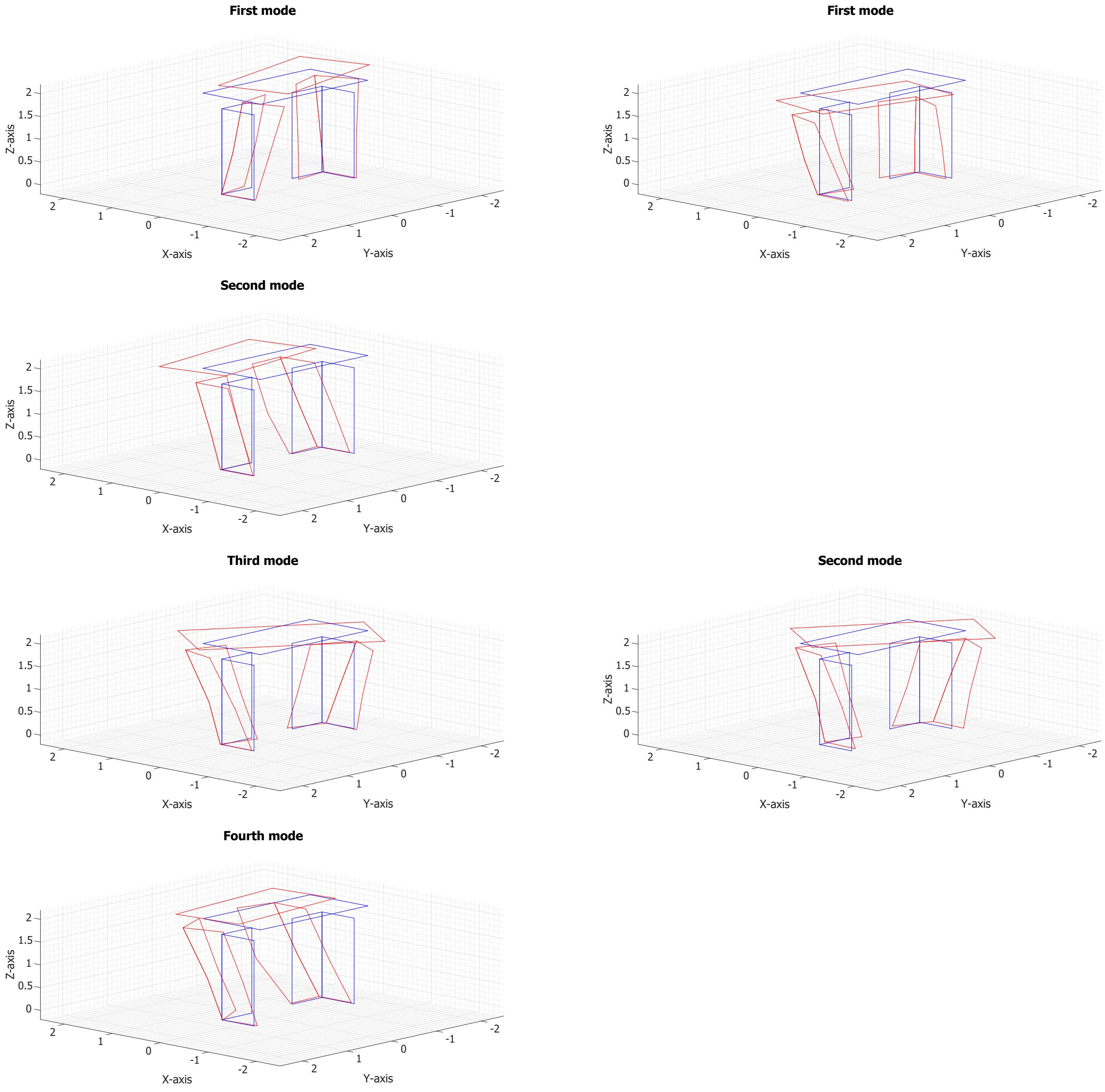

Figure II.68: Shake table tests on T- or L-shaped frames - Mode shapes of the L-shaped (flanges loaded - left: x-direction ; right: y-direction)

II.5.3.3 Shake table tests

The seismic response of the specimens can be characterised by the study of different physical quantities with respect to the actual PGA. The considered quantities are (i) the in-plane accelerations of the RC slab, (ii) the horizontal drifts of the RC slab and its rotations around the three axes, (iii) the rotations of the base of the piers around the x- and y-axes and (iv) the rotations of the piers around z-axis. Another characteristic representative of the seismic response is the force-displacement curve. Finally, attention is given to the behaviour of the RC lintel and, in the case of the specimen with L-shaped piers, to the behaviour of the connection of the sections of the piers.

Physical quantities with respect to the actual PGA

(i) Figure II.69 plots the maximum accelerations in both horizontal directions. Each graph corresponds to a specific specimen and loading case: results for the T-shaped frame are plotted at the top and those for the L-shaped frame at the bottom, with the slab resting on the whole piers (left) and on the flanges only (right). The acceleration is measured at two different locations in each direction. Considering both devices recording the acceleration in a same direction, the measured maxima differ from one point to the other when the PGA increases.

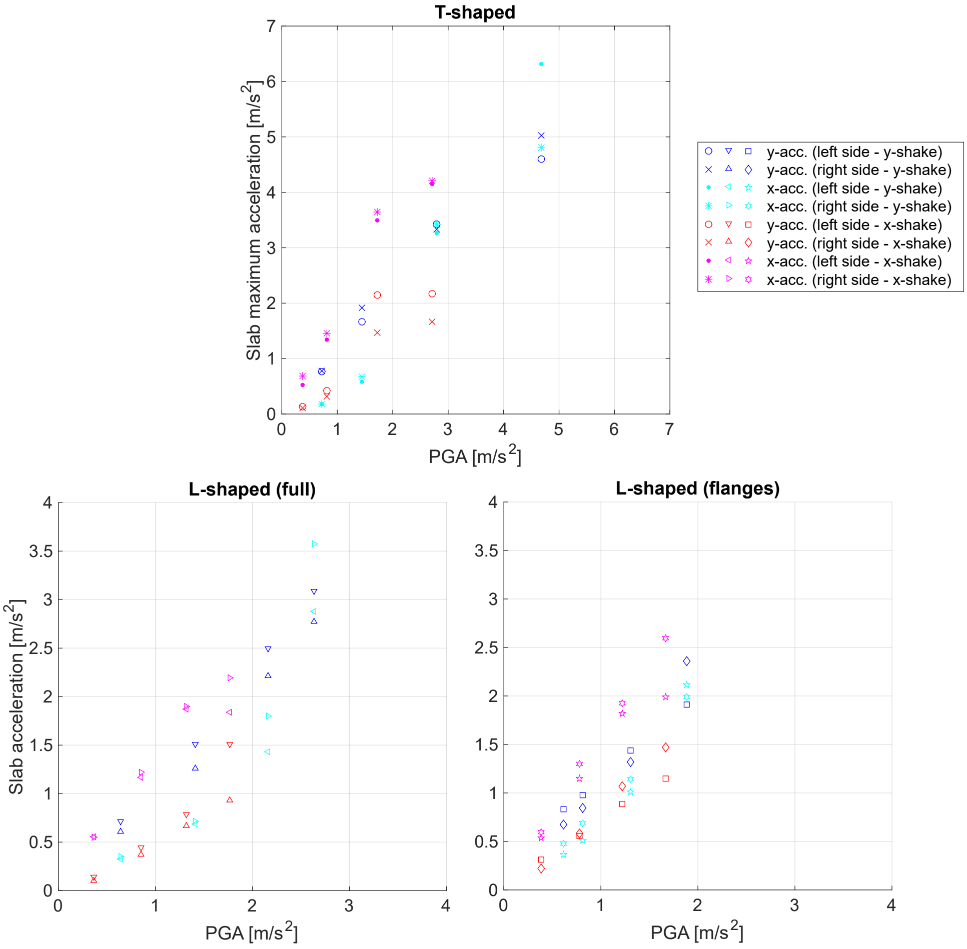

Figure II.69: Shake table tests on T- or L-shaped frames - Maximum slab accelerations with respect to the actual PGA

Moreover, a less than proportional increase is outlined in the case of the T-shaped specimen. Such a tendency is not observed for the frame with L-shaped piers. A possible reason is that this specimen is subjected to lower PGA than the T-shaped frame. The acceleration measured in the direction perpendicular to the shake is significant. This latter is even larger than the acceleration in the shake direction for the tests along the frame, at the highest levels .

(ii) Regarding the horizontal drifts of the slab and its rotations, they are given in Figure II.70. They increase more than proportional with the PGA, regardless of the tested specimen, load configuration or test direction. It is worth noticing that the study of the y-rotation is not available for shakes in the y-direction because of the instrumentation layout. Considering shakes with a same acceleration level on the T-shaped specimen, it is observed that a shake in the x-direction involves a drift in this direction which is larger than the drift measured in the y-direction under an y-shake. This observation is also valid for the frame with L-shaped piers fully loaded, but not when the slab rests on the flanges only.

(iii) Figure II.71 shows the x- and y-rotations of the base of the piers and compares them to the x- and y-rotations of the slab. In general, the rotation around the axis perpendicular to the shake direction increases more than proportionally with respect to the PGA and differences are observed between the sections of the same pier. One of these sections is subjected to in-plane loading, while the out-of-plane behaviour of the perpendicular section is activated, explaining the differences. The shake direction influences the ratio between the maximum rotations at the base of the piers and at the slab. When the specimens are tested along the y-direction (frame plane), the rotation at the base is larger than the rotation at the level of the slab. The opposite is observed when the shake is performed in the x-direction.

(iv) Figure II.72 plots the z-rotation of the slab as well as of the base and top of the piers. This quantity gives information on the torsional behaviour. It is derived from the accelerations measured at the different considered levels. There are two values for z-rotation at the base of the right pier, using either the accelerometers in the x-direction or in the y-direction. Regarding the T-shaped frame, a shake in the x-direction involves larger rotations than a shake at the same acceleration level in the y-direction. This difference in terms of load direction is not observed for the frame with L-shaped piers. The loading case however affects the magnitude of the z-rotation. Indeed, larger values are observed when the slab is only supported by the flanges, under the similar acceleration levels.

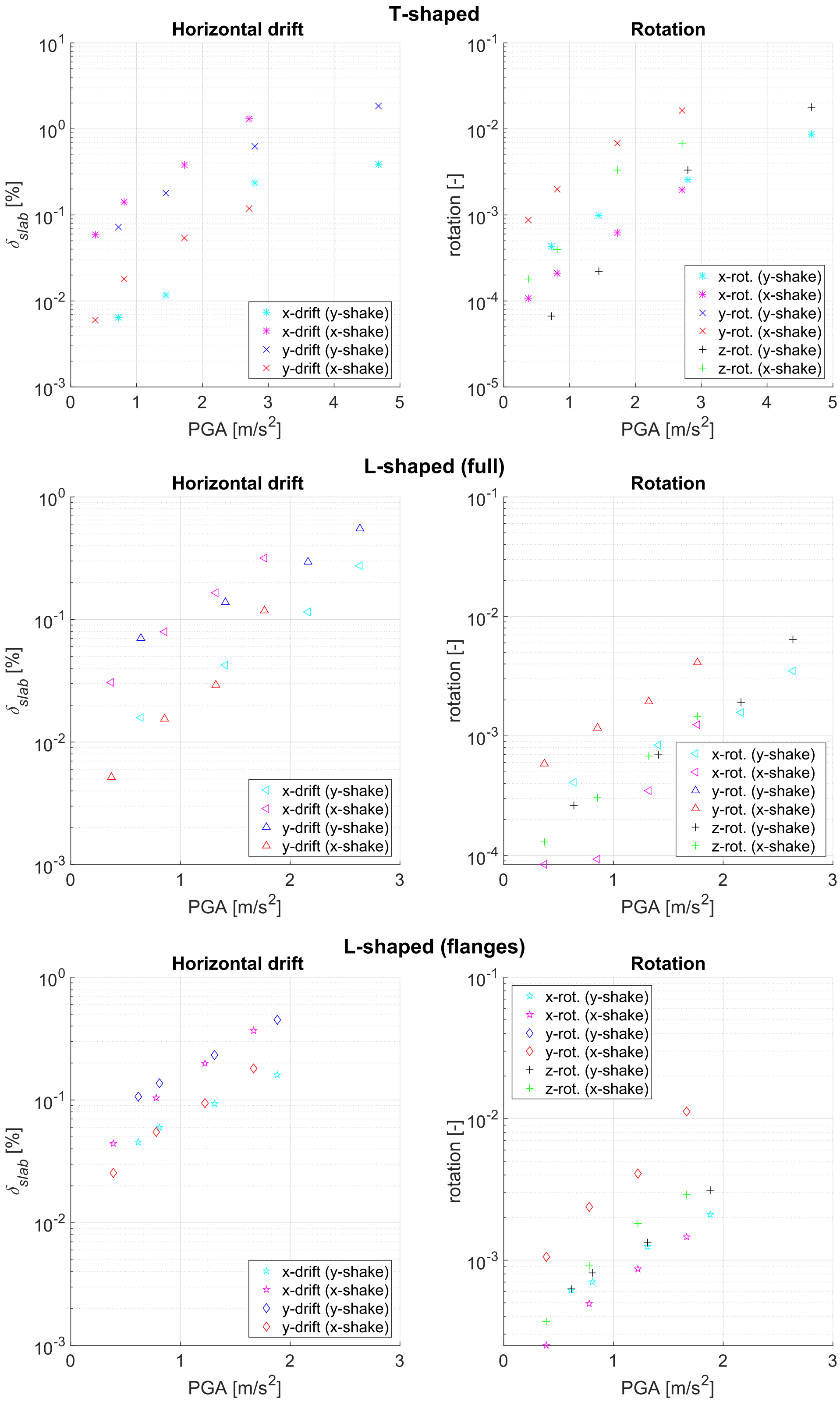

Figure II.70: Shake table tests on T- or L-shaped frames - Maximum slab displacements and rotations with respect to the actual PGA

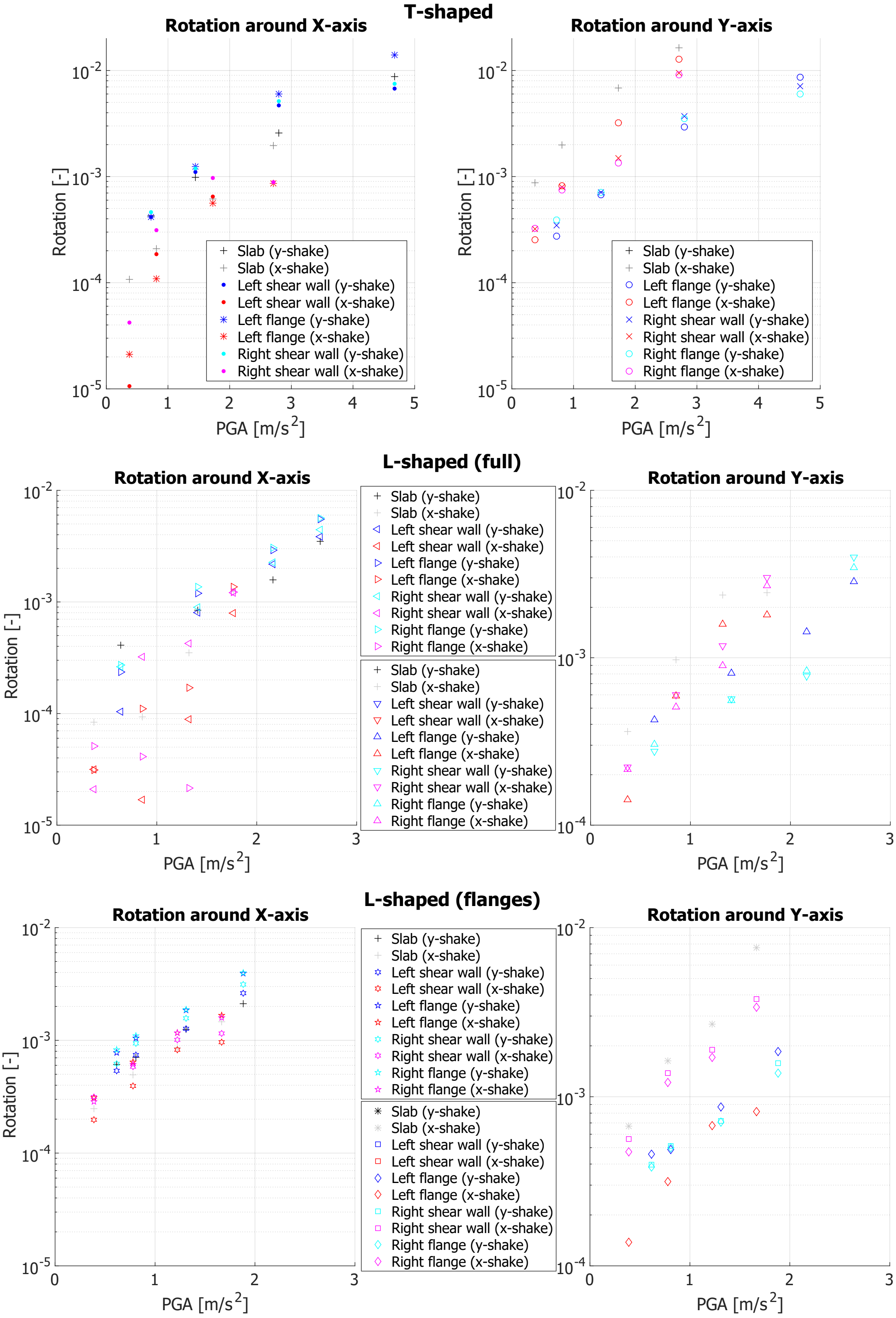

Figure II.71: Shake table tests on T- or L-shaped frames - Maximum rotations at the slab and at the base of the piers with respect to the actual PGA

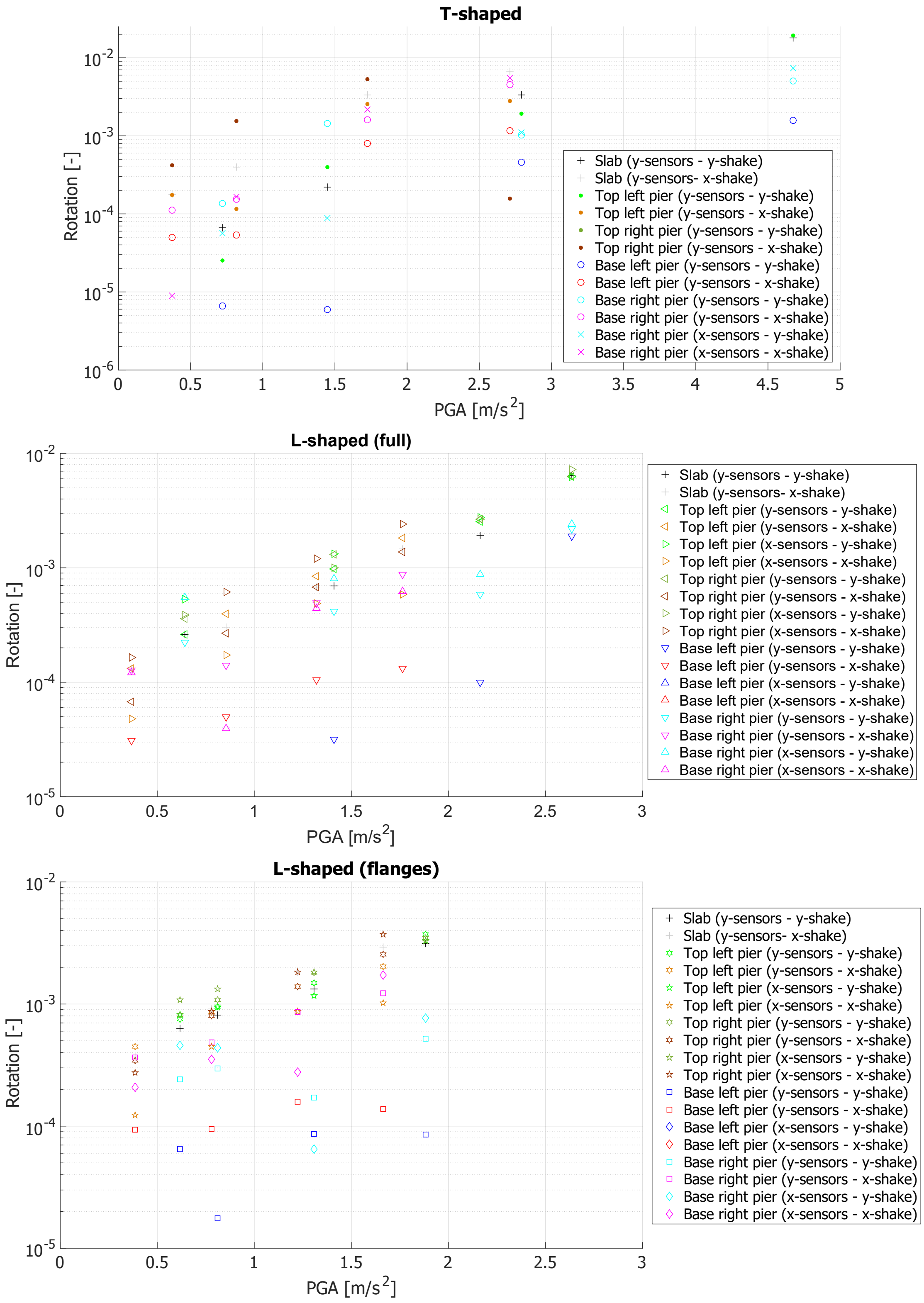

Figure II.72: Shake table tests on T- or L-shaped frames - Maximum z-rotation with respect to the actual PGA (T-shaped)

Force-displacement curves

The force-displacement curves are plotted in Figure II.73. The horizontal force and the drift being not directly measured, we define

$$P_{slab} = m\,a \tag{II.13}$$

$$\delta_{slab} = \frac{d_{slab} - d_{table}}{h_{slab}} \tag{II.14}$$

where m [kg] is sum of the mass coming from the additional mass and the RC slab and a [m/s^2] is the average acceleration measured at level of the slab. The horizontal displacements d_{slab} [m] and d_{table} [m] are obtained by integration of the acceleration measured on the slab and the shake table respectively. Only the measurements in the direction of the shake are considered. The height h_{slab} [m] is the distance between the base of the specimen and the slab. Figure II.73 includes the curves corresponding to the last three shakes for the three specimens (left, middle and right) and for both directions of test (top and bottom). For each direction of shake, the same type of line is used when the acceleration level is similar, i.e. when the target PGA is the same. As already observed in Section II.4, the $P_{slab} - \delta_{slab}$ curve exhibits a plateau in some cases. It is clearly located around 11 kN and 15 kN for the T-shaped frame, for a x- and y-shake respectively. Regarding the L-shaped frame, a plateau is initiated under the first loading configuration subjected to x-shake at about -10 kN and under the second load case between ±7.5-10 kN for y-shake.

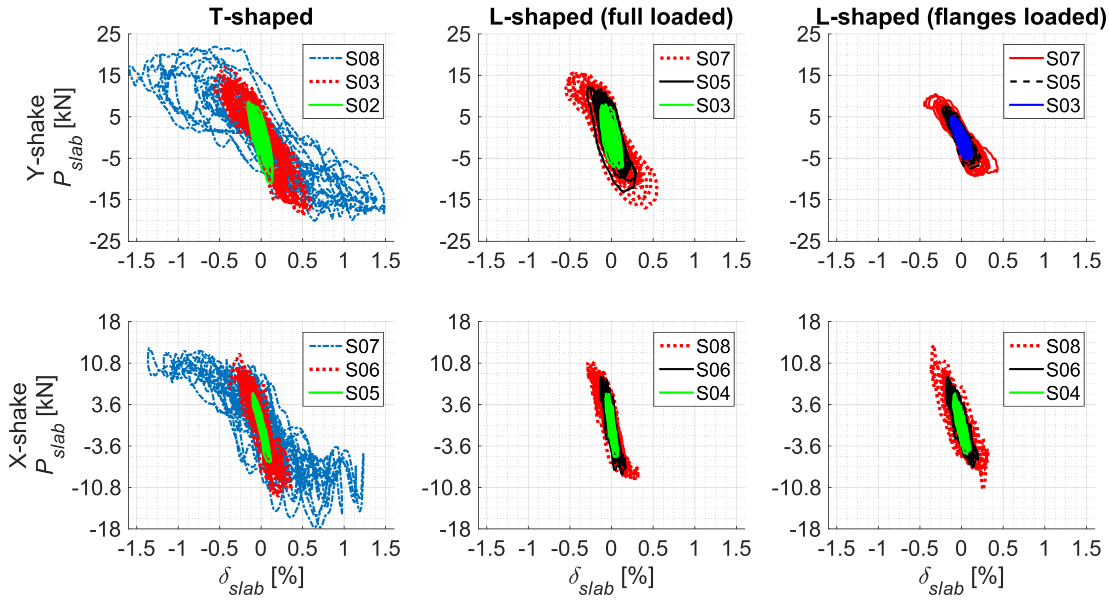

Figure II.73: Shake table tests on T- or L-shaped frames - $P - \delta$ curves

Behaviour of the lintel

The behaviour of the lintel is studied by its vertical and horizontal displacements with respect to both piers.

Figure II.74 shows the relative horizontal displacements as a function of the drift of the slab in the shake direction, for the T-shaped specimen shaken in the y-direction (S03). An opening between the lintel and the piers can be observed, ranging from 1 to 2 mm. The relative displacement related to one pier shows an asymmetry between the positive and negative drift of the slab. A possible explanation is that the lintel goes against the right pier when the drift is negative, limiting the sliding. This latter is not zero because previous runs have certainly created a gap. This restraint is not activated for the right side when the slab drift is positive, leading to larger slides.

Figures II.75 to II.77 give the maximum relative displacement with respect to the PGA. The sliding can reach 10 mm in the case of the T-shaped frame (Figure II.75). It is also more important when the specimens are tested in the y-direction, expect for the configuration of L-shaped frame loaded on its flanges only (Figure II.77). In this case, there is no steel connectors on the RC lintel and this latter behaves almost independently of the masonry frame. These results lead to the conclusion that the coupling of the piers is only effective thanks to the slab.

Connection of the sections of the URM piers

The vertical relative displacement between the sections of piers is plotted in Figures II.78 and II.79. It is only studied for the L-shaped specimen. The results in these figures show rather limited displacement with a maximum around 0.2 mm. This value corresponds to micro-cracks, leading to the conclusion of an efficient connection method for both piers.

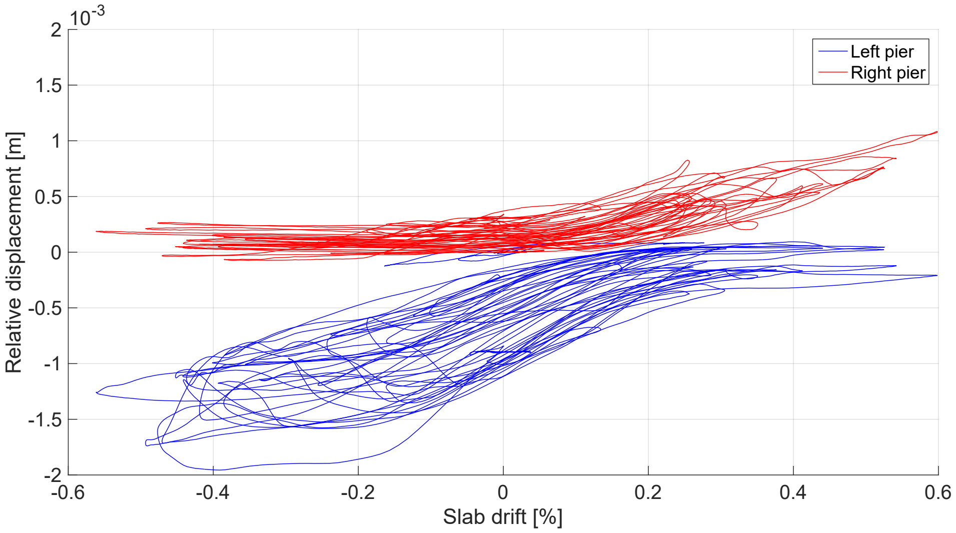

Figure II.74: Shake table tests on T- or L-shaped frames - Slab horizontal displacement with respect to the relative displacement of the lintel to the piers (S03 - T-shaped)

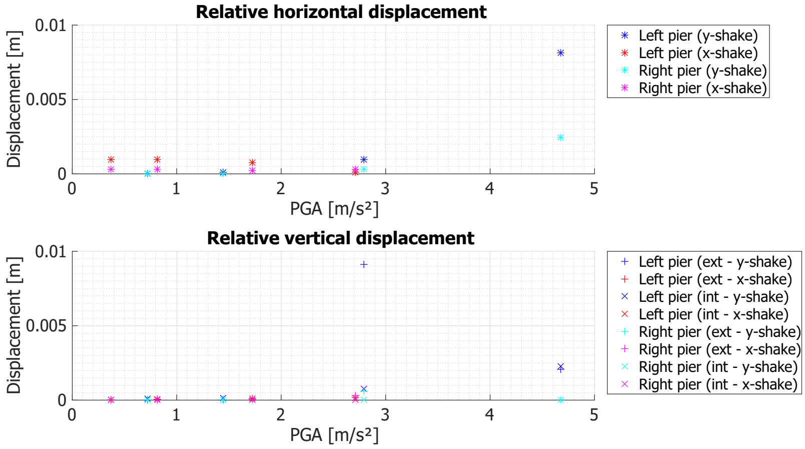

Figure II.75: Shake table tests on T- or L-shaped frames - Maximum relative displacements of the lintel with respect to the actual PGA (T-shaped)

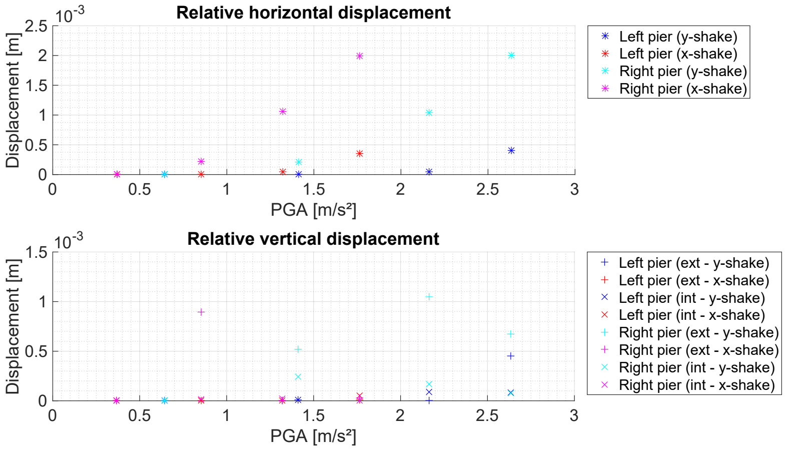

Figure II.76: Shake table tests on T- or L-shaped frames - Maximum relative displacements of the lintel with respect to the actual PGA (L-shaped - full loaded)

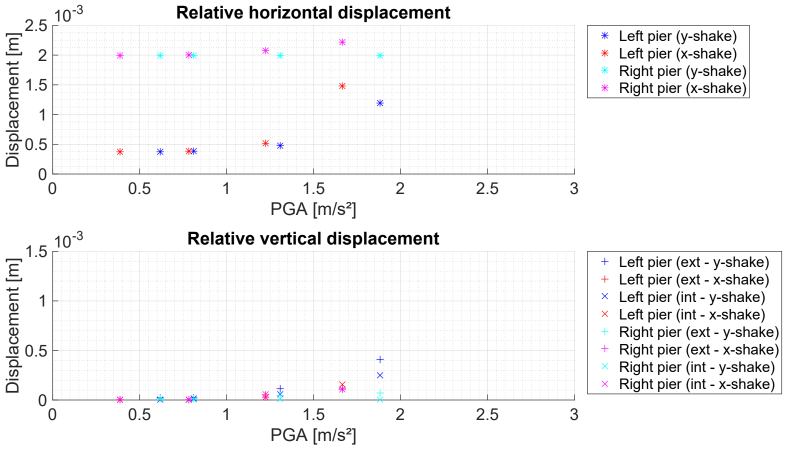

Figure II.77: Shake table tests on T- or L-shaped frames - Maximum relative displacements of the lintel with respect to the actual PGA (L-shaped - flanges loaded)

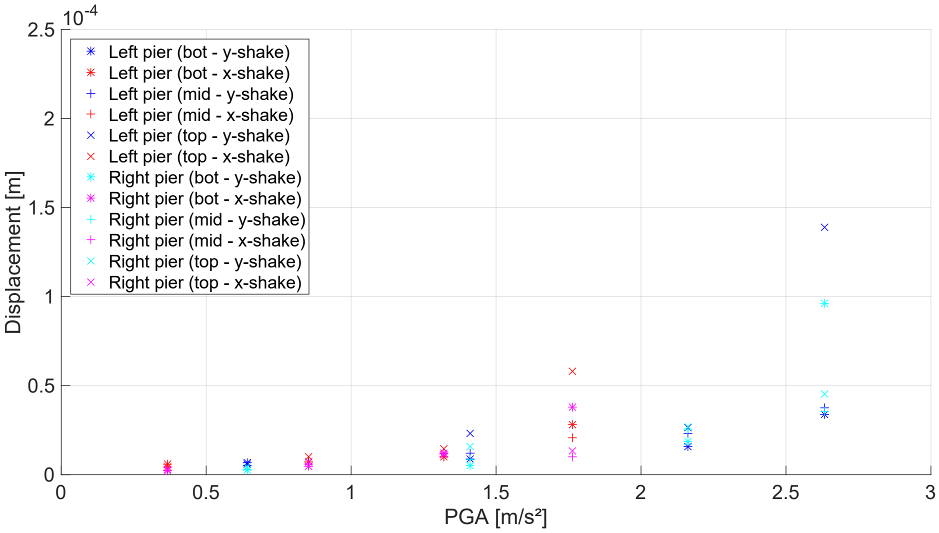

Figure II.78: Shake table tests on T- or L-shaped frames - Maximum relative z-displacement at the intersection with respect to the actual PGA (L-shaped - full loaded)

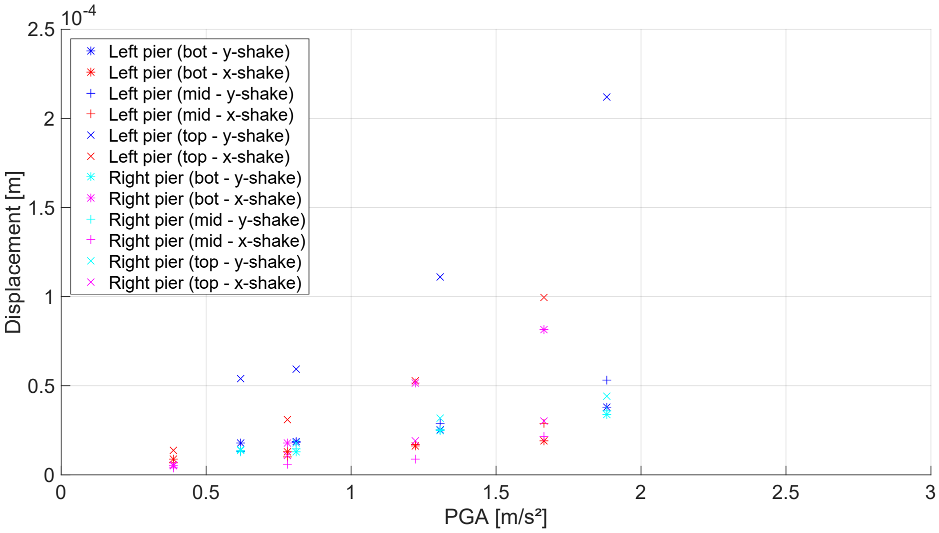

Figure II.79: Shake table tests on T- or L-shaped frames - Maximum relative z-displacement at the intersection with respect to the actual PGA (L-shaped - flanges loaded)

II.5.4 Interpretation and discussion

II.5.4.1 Pushover curves

Based on the force-displacement curves (Figure II.73), the methodology described in II.4.4.5 is followed to obtain equivalent push-over curves. These latter are plotted in Figure II.80. The negative (positive) direction corresponds to combinations of the minimum (maximum) drift and maximum (minimum) force measured during shakes with an increasing acceleration level in one direction on the same specimen. The push-over curves are only complete for configurations for which collapse happens, the behaviour of the others being not fully developed. Differences exist between the positive and negative directions and can be explained by the geometry of the specimens.

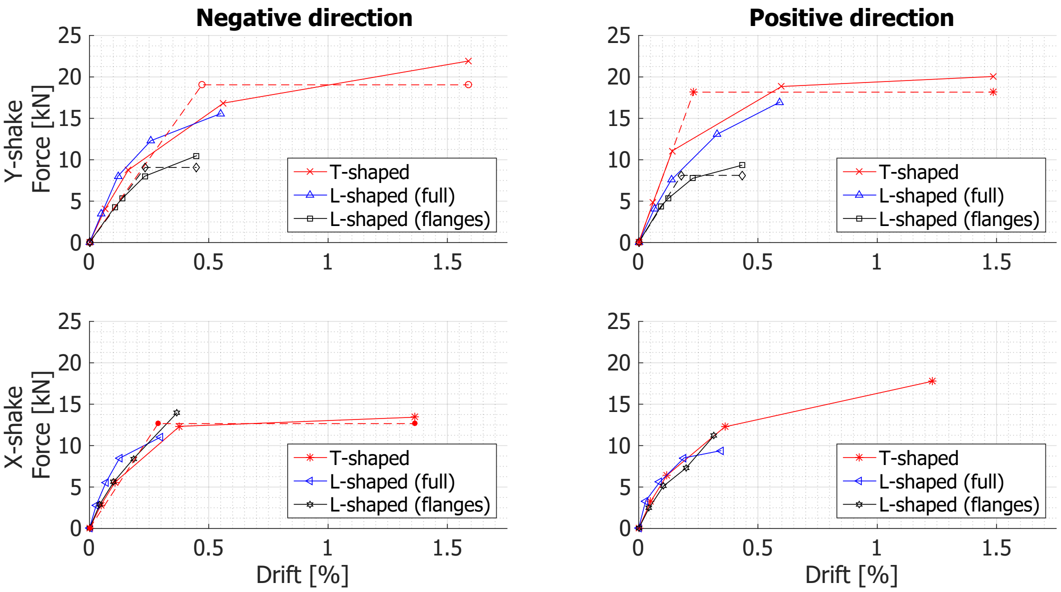

Figure II.80: Push-over curves in the negative (left) and positive (right) directions

Figure II.80 also includes bilinear curves. They are calculated for complete push-over curves in order to have relevant conclusions given the applied procedure. It is also done for the x-shakes on T-shaped frame in the negative direction because the plateau is well defined. The parameters of the bilinear curves are given in Table II.19.

Table II.19: Parameters of the bilinear curves

Specimen	Dir.	Initial stiffness k_{ini}[N/m]		Yield drift d_y[%]		ductility μ[-]	
		Negative	Positive	Negative	Positive	Negative	Positive
T-shaped	y	$4.036 \cdot 10^4$	$7.877 \cdot 10^6$	0.472	0.231	3.367	6.443
	x	$4.001 \cdot 10^4$	/	0.288	/	4.744	/
L-shaped (flanges)	y	$3.890 \cdot 10^4$	$4.539 \cdot 10^4$	0.449	0.433	1.925	2.420
	x	/	/	/	/	/	/

A relative difference of 48.8 % in terms of stiffness is observed between the negative and positive directions for y-shakes on the T-shaped frame. This quantity is higher in the positive direction due to the position of the flange of the right pier. This latter is effectively over-compressed when the drift is positive. Regarding the L-shaped with the flanges loaded, the stiffness in higher (+14.3 %) in the positive direction. The specimen being symmetric, this difference either comes from the position of the steel connectors or from the connection method. In terms of yield drifts, the influence of the position of the flange is of first order. A significant difference between both directions exists for the T-shaped frame (51.1 %), while the drift is rather similar for the L-shaped frame (3.6 %).

II.5.4.2 Rocking behaviour

Tests at the highest acceleration levels highlight a general rocking behaviour. The observations and experimental results given in the previous section bring elements that confirm this behaviour.

First, the presence of horizontal cracks and their concentration at the base of the piers reveal the uplift of these latter.

Then, the more than proportional increase of the horizontal drift/rotation of the slab with respect to the actual PGA translates a nonlinear behaviour (Figure II.70). This is confirmed by the less than proportional increase of the slab accelerations (Figure II.69). These nonlinearities are supposed to be involved by a rocking behaviour because the rotations at the base of the piers become rapidly significant (Figure II.71). This is demonstrated by the comparison between the bottom and slab rotations. On the one hand, the rotations of the base of the piers are larger than the rotation of the slab when comparing the x-rotations under y-shakes. In this case, the specimen can be represented as 3 blocks where two are vertically oriented, i.e. the piers, and the third one is horizontal and supported by the first two, i.e. the slab. In a first approximation, they are assumed as rigid. Due to the presence of steel connectors, the specimen is not symmetric. When the piers rock, their rotations differ from each other and create a rotation of the slab. This latter is zero if the uplifts of the contact points between the piers and the slab are the same. Otherwise, the slab rotates and the magnitude increases with the difference of uplifts. This explains why the rotation of the slab is lower than one or both rotations of the piers. On the other hand, the study of the y-rotation when x-shakes are performed shows that the rotation of the slab is larger, except for the test S08 on the L-shaped frame with the whole piers loaded. In this case, the left and right piers are considered separately and the specimen can be modelled as two rocking stacked blocks.

Finally, the development of plateaus with a bounded force in the $P_{slab} - \delta_{slab}$ curves support the conclusion of a general rocking behaviour. As explained in Section II.4, the plateau corresponds to the force required to overturn the specimen. Once it is reached, the specimen can rock and a higher acceleration level only leads to larger horizontal displacements.

It is also worth noticing that the rotations of the flanges are generally larger than those of the shear wall. The restraint brought by the steel connectors is less important for these sections of the piers.

II.5.4.3 Influence of the loading case

The frame with L-shaped piers is subjected to shake table tests with two different loading configurations. In the first one, the slab with the additional distributed 5-ton steel mass is placed on the whole section of the piers. The second one partially loads the L-shaped piers and there are steel connectors between the slab and the flanges only. An important point is that the seismic tests are carried out on the same specimen, the second configuration being thenceforth predamaged. The transition between loading configurations is characterised by white noise tests in both horizontal directions before (WN 17/18) and after (WN 19/20) the change.

In terms of natural frequencies, the influence of the loading case is obvious in Figure II.65. In the frame plane (y-direction), the magnitude of the natural frequencies is reduced. In the perpendicular direction (x-direction), two additional natural frequencies appear. The fundamental frequency located around 4 Hz seems to be split in two, a first one lower in magnitude and a second one higher. The second natural frequency is reduced by 44.1 %. A last frequency is present and is slightly higher than 10 Hz.

This analysis of the mode shapes in Figures II.67 and II.68 shows that the shapes are the same in the y-direction. In the perpendicular direction, the first mode (translational mode) of the full loaded configuration is divided in two modes with clear differences. The first mode corresponding to the lower frequency exhibits transverse deformation (y-direction), while the second mode related to the higher frequency is similar to the first mode of the full loaded configuration. Due to the shakes on the previous loading case, the specimen is possibly no more aligned with the axes of the shake table. The deformation in the y-direction is more visible after the change of loading case because the section of the piers oriented in the y-direction is not compressed anymore and, hence, its contribution to the transverse stability is heavily decreased. This explains why there is one peak in the first loading case and two in the second one. Regarding the frequency around 10 Hz, the mode shape clearly identifies a torsional mode with a translational contribution. This mode is not observed in the case of the slab resting on the whole piers because of the position of steel connectors apparently. There are 4 connectors which give an important restraint and avoid this deformation mode. After the change, it remains 2 connectors only and torsion can occur. Torsion is even more important due to differences between the right and left piers. The connector is indeed placed closer to the intersection in the case of the right pier. For both loading configurations, the peak with the highest frequency corresponds to a translational deformation with some torsion and the RC slab in phase opposition.

Another influence of the loading case concerns the maximum measured drift and rotation of the slab in the shake direction. For both directions, they are larger when the slab is supported by the flanges only. Such an observation is expected when testing the specimen in y-direction given that the loaded walls are subjected to an out-of-plane acceleration. In the x-direction, there are two possible reasons. First, the absence of connectors on the shear walls reduces the restraint because the support length is shorter. Second, the shear walls being uncompressed, their contribution to the stiffness is insignificant and this loss is not balanced by the increase of the stiffness of the flanges coming from the over-compression. In order to assess the gain/loss of each contribution, additional investigations on the effects of the compression level on the stiffness of masonry walls under horizontal shear is required.

A last consequence of the change of load distribution is the modification of seismic behaviour. When subjected to different loading cases, the L-shaped frame displays a plateau at different levels of shear (Figure II.73). This level is higher in the x-direction for the second load configuration. The opposite is observed in the y-direction. It is well known that masonry can sustain higher horizontal shear when the compression level is increased. The observations of this campaign lead to the same conclusion.

II.5.4.4 Torsion effects

Figure II.72 provides information about the rotation around the vertical axis. This rotation is due to the torsion of the specimen. Regarding the T-shaped frame, torsion is more important when the seismic action is perpendicular to the frame plane. Indeed, the torsion centre of the specimen differs from the gravity centre of the slab. The difference comes from the asymmetry of the specimen because of the orientation of the piers. The bending inertia of the left pier is larger along the x-direction and its gravity centre is closer to the one of the slab. Moreover, the torsion centre and the centroid of the right pier are different in this direction. Shake table tests in the frame plane also develop torsion because of the distance between the centroid of the slab and the torsion centre of the piers, which is approximately 15 cm. Concerning the L-shaped frame, torsion is only expected in y-direction for the same reasons than the other specimen. In the perpendicular direction, the specimen is supposed to be symmetric, but the position of the steel connectors involve torsional effects.

These considerations explain the results plotted in Figure II.72. For instance, the z-rotation of the right pier is larger than the one of the left pier when considering the T-shaped frame subjected to a x-shake. On the contrary, the torsion is more important for the left pier under y-shakes. The rotation is lower at the base of the pier because of the friction between the pier and its basement. In terms of magnitude, the results related to the different specimens and loading cases can be compared by considering similar PGA. For x-shake, maximum z-rotations are similar for the T-shaped frame (S06) and the L-shaped frame with the slab supported by the flanges only (S08). The rotation is divided by two when the slab rests on the whole piers of the L-shaped frame (S08). Under y-shakes, the rotation is larger for L-shaped frame in general and the highest magnitude is observed when the piers are partially loaded.

The rotation around the vertical axis can be either calculated with the devices measuring the displacement/acceleration in the x- or y-direction. Differences are however observed between the values obtained. Investigations on these differences show that the distance between sensors oriented in the same direction is not the same from one direction to an other. This influences the results because the out-of-plane deformability of walls is included in the measurements. The longer the distance, the more important the effects of the out-of plane deformability.

II.5.4.5 Influence of the connection method

Figures II.78 and II.79 summarize the maximum vertical relative displacement between the sections of both piers in the case of the L-shaped frame. The maximum observed being around 0.2 mm, both methods involve a rigid connection of perpendicular walls. An important difference is however observed in the view of the collapse mechanism. Indeed, the pier with an alternated masonwork fails at its intersection. It seems that the shear wall stabs the flange. The other pier with the flange glued to the shear wall does not present any damages at the connection. A possible explanation is that the contact length between the sections of the two piers is shorter in the case of the alternated masonwork. Due to the type of head joints, this latter is effectively divided by two in comparison to the continuous vertical glued joint. This reduced length leads to a lower capacity to transfer the shear from one section to another. The continuous vertical glued joint is therefore a better connection method. This conclusion is only valid for the considered testing configuration.

II.6 Conclusions

This chapter is focused on a set of experimental campaigns aiming at improving the understanding of the seismic behaviour of a particular type of load-bearing URM structures including soundproofing rubbers layers. The studied masonry consists in clay blocks bonded with thin bed-layered glued joints and empty head joints, using a tongue-and-groove system for thermal and efficiency purposes. The specific detailing has been developed by masonry producers to face the increasing demand in terms of building physics performances. Such an innovative solution adds complexity to the seismic behaviour of masonry structures. A total of 14 specimens have been tested. The campaigns implement static-cyclic tests with controlled horizontal displacement or shake table tests at increasing acceleration levels. In both cases, simple walls are first tested as reference. They cover three different lengths and two different heights. Their response are then compared to specimens of the same global dimensions, but with specific details. These latter are either the presence of acoustic devices at the bottom and top of the walls, the existence of a door opening created by a reinforced concrete lintel or the connection to a perpendicular wall.

First, static-cyclic and dynamic tests on simple walls including rubber layers highlight significant differences in the behaviour when the soundproofing devices are present. In static conditions, the compression level applied to the walls has to be reduced due to the interaction between rubber and masonry. The lateral stiffness of the specimens is also influenced negatively by the acoustic devices. These two consequences induce larger horizontal displacements and a lower strength capacity. The energy dissipation is however improved in presence of these devices. Similar conclusions arise from the shake table tests. The fundamental frequency is reduced by one third and white noise tests performed between each seismic shake show a higher frequency drop when there is rubber. The progressive damaging of walls observed during the test sequence is therefore hastened.

Second, a door opening requires the design of a lintel with a sufficient support length to avoid a premature and local failure. A 0.45 m long support was enough for the tested configuration. An opening leads to a reduction of the strength capacity, but experimental results outline the importance of the contribution of the spandrel to the global strength. This horizontal element allows the consideration of a frame effect, enhancing the behaviour of separate piers.

Third, the compression level affects not only the strength capacity, but also the stiffness of masonry walls. Static-cyclic tests on identical T-shaped walls subjected to different compression levels lead to the conclusion that the more compressed the wall, the stiffer and stronger. White noise tests on the L-shaped frame carried out before and after the change of loading configuration gives similar conclusions.

Fourth, the contribution of a wall perpendicular to the seismic action can be significant. The only condition is the necessity to ensure a proper connection between the different sections. The benefits are larger when the additional wall is over-compressed, but positive effects are observed in both situations.

Regarding the shake table tests, a general rocking behaviour is observed for the highest acceleration levels. In the case of simple walls, this allows the specimens to withstand ground motion up to three times the amplitude forecast by an equivalent static design method. This opens clear perspectives for accounting for the favourable dynamic effects in the design procedure. Soundproofing devices even enhance this efficiency thanks to a better dissipation of the seismic energy. This conclusion should however be mitigated in the context of the design of entire buildings because of larger associated displacements. Moreover, it is necessary to cope with perpendicular elements for which torsional effects and improper connection can be detrimental.

In the perspective of modelling the masonry structural elements with equivalent non-linear isotropic beam elements, the sequence for static-cyclic tests gives the possibility to determine equivalent mechanical properties. Indeed, the equivalent elastic modulus is assessed thanks the compression phase of the specimens and the static-cyclic phase provides the magnitude of the equivalent shear modulus. Such a methodology is not applicable to the shake table tests because the identification of the dynamic properties of walls does not allow to distinguish between the shear and bending contributions to the stiffness.

Chapter III

Frequency equation for the identification of equivalent mechanical properties for URM walls

---

III.1 Introduction
III.2 Model description using Timoshenko beam theory
III.3 Frequency equations
III.4 Parametric study of beam models and mode shapes
III.5 Determination of equivalent mechanical properties
III.6 Conclusions

III.1 Introduction

The determination of the mechanical properties of masonry elements is an intricate topic since these structures combine different materials which are bonded together in many different ways. The current standards propose procedures to calculate, for instance, the elastic modulus (EN 1052-1). When there is no relevant data, they also recommend values depending on the compressive strength.

In the previous chapter, the seismic behaviour of load-bearing clay URM sub-structures has been investigated in static-cyclic and dynamic conditions. The preliminary assessment design included the characterisation of the masonry according to the rules of EN 1052-1, but only for the compressive strength. Nevertheless, the testing procedure and the instrumentation allowed the calculation of equivalent mechanical properties in the case of static-cyclic tests. Indeed, the compression phase provided information about the equivalent elastic modulus. The bilinearisation of the push-over curves deduced from the force-displacements curves was then used to calibrate the equivalent shear modulus, assuming the same Young's modulus in the normal and lateral directions. The elastic and shear moduli are called equivalent because the masonry walls were modelled as a beam made of a homogeneous and isotropic material. Regarding the shake table tests, records of the loading of the specimens with the additional mass gave noisy signals. The compression phase is therefore unusable to estimate the masonry equivalent elastic modulus and the procedure followed for static-cyclic tests cannot be applied.

This chapter focuses on the determination of equivalent mechanical properties for the masonry simple walls subjected to shake table tests. It is the first necessary step in the perspective of modelling masonry structures at the macro-scale with equivalent beam elements or equivalent frames (see Chapter IV). The proposed methodology is based on the results of the dynamic characterisation of the specimens between each shake. White noise tests effectively led to the estimation of the natural frequencies of the walls. The mass distribution being known, these latter allow the assessment of the stiffness of the walls and, hence, of their equivalent mechanical properties since these physical quantities are connected. This connection is achieved thanks to the study of transverse vibrations of beams.

Transverse vibrations of beams have been extensively studied for a few centuries. This interest has led to a huge number of research works. The problem is still investigated today given its large range of applications and for two other reasons. On the one hand, several assumptions may be formulated to project the most general equations of the Theory of Elasticity [120] onto beam, rod or elastica models. Among available beam theories, the well-known model proposed by Bernoulli and Euler relies on the importance of the bending effect and results in acceptable approximations for a number of engineering problems. Nevertheless, the model is inaccurate for the higher modes and non-slender beams. Improvements were then introduced by Lord Rayleigh (1877) [118] and the shear model, thanks to the integration of the rotary inertia and the shear distortion effects of the cross-section respectively. Finally, Timoshenko proposed a beam theory combining all these effects and giving a more adequate solution to the problems of higher modes and non-slender beams [119, 121]. On the other hand, the solution of these equations depends on the boundary conditions. The most classical ones are the “free-free”, “clamped-clamped”, “hinged-hinged” or “clamped-free” ends, but other possibilities exist, as for instance a partially clamped end. There are therefore as many solutions as combinations of theories and boundary conditions.

Solving the differential equations of motion analytically requires the development of the so-called frequency equation. Han et al. detailed these developments [41] for the four abovementioned models and for the classical boundary conditions. Other authors studied this problem with some specific details and with the view of practical applications. Low [65, 64] focused on the frequency analysis of an Euler-Bernoulli beam bearing a concentrated mass at an arbitrary location and developed a modified Dunkerley formula to approximate the exact solution with less computational time. Because of its increasing use as robot arms, machines or structures, Bruch & Mitchell [14], Oguamanam [88], Salarieh & Gorashi [109] and Ansari et al. [4] investigated the free vibrations of an Euler-Bernoulli or Timoshenko cantilever beam with a rigid tip in the perspective of studying the behaviour of a flexible member. More recent contributions dealt with non-homogeneous or cracked beams [60, 50]. The influence of the support conditions was also considered, as for example Timoshenko beams on Pasternak foundations [15] and beams on elastic end supports [61]. A particular attention to forced vibrations of Timoshenko beams was given by Majkut [72].

Beside the study of transversally vibrating beams, a similar theoretical approach has been used to examine the stability of beams. Several research programs have been carried out over the past twenty years [35, 33], with some focused on shear beams [129], investigating the consequences of variable sections [84] or of an elastically restrained base [43].

In this chapter, the Timoshenko beam theory is used and the boundary conditions are adapted to reproduce the experimental configurations described in Section II.4. The choice of the Timoshenko beam theory is involved by the geometry of the tested masonry walls given their significant shear deformability. A comparison with the Euler-Bernoulli beam theory is however performed. Regarding the boundary conditions, two different models are required to catch the specificities of the specimens. The first model is a classical cantilever beam with an additional mass located at the free end (Figure III.1 (b)), corresponding to walls without soundproofing layers. The second model has two particularities due to the rubber devices: (i) the base end is elastically restrained and (ii) the additional mass is not rigidly connected at the free end (see Figure III.1 (c)). The identification of equivalent mechanical properties for the masonry structural element and rubber is carried out thanks to the establishment of the dimensionless frequency equation of these two models. In addition to this, the influence of the additional mass is investigated through different parameters (mass, rotary inertia, etc.) and the importance of the different terms of the frequency equations is studied.

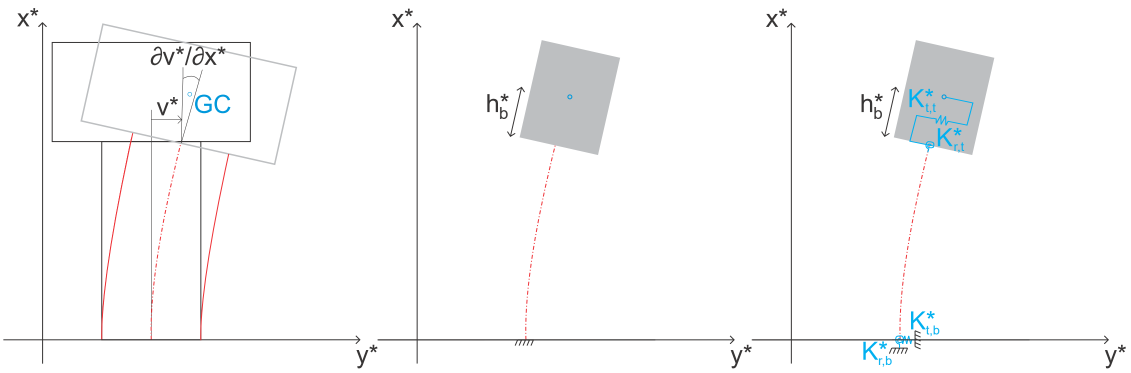

(a) (b) (c)

Figure III.1: General sketch of a specimen (a) and model for beam with clamped base and rigidly connected mass or (b) with partially clamped base and elastically connected mass (c).

III.2 Model description using Timoshenko beam theory

III.2.1 Equations of motion

The Timoshenko beam theory includes bending, shear distortion and rotary inertia effects. Two space- and time-dependent fields describe the behaviour of the beam, namely the transverse displacement $v\,(x,t)$ and the angle of rotation due to bending $\alpha\,(x,t)$. Two governing differential equations are derived from Hamilton's variational principle

$$\rho\, A\frac{\partial^2 v}{\partial t^2} - k' G\, A\left(\frac{\partial^2 v}{\partial x^2} - \frac{\partial \alpha}{\partial x}\right) = f\,(x,t) \tag{III.1}$$

$$\rho\, I\frac{\partial^2 \alpha}{\partial t^2} - E\, I\frac{\partial^2 \alpha}{\partial x^2} - k' G\, A\left(\frac{\partial v}{\partial x} - \alpha\right) = 0 \tag{III.2}$$

where ρ is the density of the beam, A and I are its cross-section area and bending inertia, k' is a shape factor, E and G represent the elastic and shear moduli of the beam respectively and $f\,(x,t)$ is the transverse applied force per unit length. This set of equations can be nondimensionalized by introducing

$$x^\star = h_w \qquad \text{and} \qquad t^\star = \frac{1}{\omega_1} = h_w^2\sqrt{\frac{\rho\, A}{E\, I}} \tag{III.3}$$

as a reference length (the length of the beam, i.e. the height of the wall in the following application) and time (the traveling time of a wave in bending along the beam), respectively. The space and time parameters are therefore normalized as

$$x^* = \frac{x}{x^\star} \quad ; \quad t^* = \frac{t}{t^\star} \tag{III.4}$$

while the transverse displacement of the beam is scaled as $v^* = \frac{v}{x^\star}$. Assuming no transverse force per unit length and a linear elastic, isotropic and homogeneous beam with a constant cross-section, the equations of motion III.1 and III.2 can be decoupled. With the dimensionless coordinates, they read

$$\frac{\partial^4 v^*}{\partial x^{*^4}} - \Omega_a^* \frac{\partial^4 v^*}{\partial x^{*^2} t^{*^2}} + \frac{\partial^2 v^*}{\partial t^{*^2}} + \Omega_b^{*^2}\frac{\partial^4 v^*}{\partial t^{*^4}} = 0, \tag{III.5}$$

$$\frac{\partial^4 \alpha}{\partial x^{*^4}} - \Omega_a^* \frac{\partial^4 \alpha}{\partial x^{*^2} t^{*^2}} + \frac{\partial^2 \alpha}{\partial t^{*^2}} + \Omega_b^{*^2}\frac{\partial^4 \alpha}{\partial t^{*^4}} = 0 \tag{III.6}$$

with the dimensionless groups

$$\Omega_a^* = \frac{I}{A\, h_w^2}\left(1 + \frac{E}{k'G}\right) \quad ; \quad \Omega_b^{*^2} = \left(\frac{I}{A\, h_w^2}\right)^2 \frac{E}{k'G}. \tag{III.7}$$

As the forms of both differential equations III.5 and III.6 are the same, the topology of the unknown fields themselves are the same. These latter can be expressed in the frequency domain by setting $v^*(x^*,t^*) = \phi(x^*)e^{j\omega^* t^*}$ and $\alpha(x^*,t^*) = \psi(x^*)e^{j\omega^* t^*}$, with $\omega^* = \frac{\omega}{\omega_1}$ the dimensionless circular frequency and j the unit complex number. This translates the time synchronization of the transverse displacement and of the angle of rotation due to bending [41, 72]. Plugging this ansatz into eqs. III.5 and III.6 yields

$$\left[\phi'''' + \Omega_a^* \omega^{*^2} \phi'' - \omega^{*^2} \phi + \Omega_b^{*^2} \omega^{*^4} \phi\right] e^{j\omega^* t^*} = 0 \tag{III.8}$$

$$\left[\psi'''' + \Omega_a^* \omega^{*^2} \psi'' - \omega^{*^2} \psi + \Omega_b^{*^2} \omega^{*^4} \psi\right] e^{j\omega^* t^*} = 0 \tag{III.9}$$

where the prime symbol indicates derivatives with respect to x^*. These 4th order homogeneous ODEs result in the general solution for the mode shapes $\phi(x^*)$ and $\psi(x^*)$

$$\phi = K_1 e^{z_1^* x^*} + K_2 e^{z_2^* x^*} + K_3 e^{z_3^* x^*} + K_4 e^{z_4^* x^*} \tag{III.10}$$

$$\psi = Q_1 e^{z_1^* x^*} + Q_2 e^{z_2^* x^*} + Q_3 e^{z_3^* x^*} + Q_4 e^{z_4^* x^*} \tag{III.11}$$

where

$$z_{1,2}^* = \pm\sqrt{-\frac{\Omega_a^*}{2}\omega^{*^2} - \sqrt{\left(\frac{\Omega_a^{*^2}}{4} - \Omega_b^{*^2}\right)\omega^{*^4} + \omega^{*^2}}} = \mp a^* \tag{III.12}$$

$$z_{3,4}^* = \sqrt{\pm\left[\frac{\Omega_a^*}{2}\omega^{*^2} - \sqrt{\left(\frac{\Omega_a^{*^2}}{4} - \Omega_b^{*^2}\right)\omega^{*^4} + \omega^{*^2}}\right]} = \left\{\begin{array}{l} b^* \\ \tilde{b}^* \end{array}\right. \tag{III.13}$$

are the roots of the characteristic polynomial. The variables a^*, b^* and $\tilde{b}^*$ are the dimensionless wave numbers.

Finally, Eqs. III.10 and III.11 can be turned into trigonometric or hyperbolic expressions. Two pairs of solutions are derived from Eqs. III.10 and III.11 since z_3^* and z_4^* are either real or imaginary, depending on the circular frequency ω^* with respect to the critical frequency $\omega_c^* = \Omega_b^{*^{-1}}$. When the circular frequency is smaller than the critical frequency ($\omega^* \Omega_b^* \leq 1$), the spatial (wave) solutions are expressed by

$$\phi = C_1 \sin a^* x^* + C_2 \cos a^* x^* + C_3 \sinh b^* x^* + C_4 \cosh b^* x^*, \tag{III.14}$$

$$\psi = D_1 \sin a^* x^* + D_2 \cos a^* x^* + D_3 \sinh b^* x^* + D_4 \cosh b^* x^*. \tag{III.15}$$

On the contrary, when the circular frequency is larger than the critical frequency ($\omega \Omega_b \geq 1$), the solutions read

$$\phi = \tilde{C}_1 \sin a^* x^* + \tilde{C}_2 \cos a^* x^* + \tilde{C}_3 \sin \tilde{b}^* x^* + \tilde{C}_4 \cos \tilde{b}^* x^*, \tag{III.16}$$

$$\psi = \tilde{D}_1 \sin a^* x^* + \tilde{D}_2 \cos a x^{**} + \tilde{D}_3 \sin \tilde{b}^* x^* + \tilde{D}_4 \cos \tilde{b}^* x^*. \tag{III.17}$$

The parameters C_1, C_2, C_3, C_4 and D_1, D_2, D_3, D_4 (resp. $\tilde{C}_1, \cdots, \tilde{C}_4$ and $\tilde{D}_1, \cdots, \tilde{D}_4$) in Eqs. III.14 and III.15 (resp. Eqs. III.16 and III.17) are eight coefficients to be determined to satisfy the boundary conditions. These coefficients can however be reduced to four as explained in [41], observing that they are related by

$$\begin{array}{ll} D_1 = -\varphi_a^* C_2 & D_2 = \varphi_a^* C_1 \\ D_3 = \varphi_b^* C_4 & D_4 = \varphi_b^* C_3 \end{array} \tag{III.18}$$

and

$$\begin{array}{ll} \tilde{D}_1 = -\tilde{\varphi}_a^* \tilde{C}_2 & \tilde{D}_2 = \tilde{\varphi}_a^* \tilde{C}_1 \\ \tilde{D}_3 = -\tilde{\varphi}_b^* \tilde{C}_4 & \tilde{D}_4 = \tilde{\varphi}_b^* \tilde{C}_3 \end{array} \tag{III.19}$$

with $\varphi_a^* = \frac{{a^*}^2+\lambda^2 {b^*}^2}{(1+\lambda^2)a^*}$, $\varphi_b^* = \frac{{b^*}^2+\lambda^2 {a^*}^2}{(1+\lambda^2)b^*}$, $\tilde{\varphi}_a^* = \frac{{a^*}^2-\lambda^2 {b^*}^2}{(1+\lambda^2)a^*}$, $\tilde{\varphi}_b^* = \frac{{b^*}^2-\lambda^2 {a^*}^2}{(1+\lambda^2)b^*}$ and $\lambda = \frac{E}{k'G} = \frac{2(1+\nu)}{k'}$.

Once the boundary conditions are specified, there are four relations between the four unknown coefficients $C_1,\cdots,\ C_4$ ($\tilde{C}_1,\cdots,\ \tilde{C}_4$ respectively, if $\omega^*\Omega_b^* \geq 1$) which can be written as a matrix. The frequency equation is then obtained by setting the determinant of this matrix to zero, avoiding the trivial solution corresponding to zero coefficients, and revealing therefore the natural frequencies of the considered problem.

III.2.2 Models and boundary conditions

Two models of a cantilever beam are considered and include specific details. The first model has an additional mass rigidly connected at the free end of the beam, as shown in Figure III.1 (b). The second model is sketched in Figure III.1 (c) and differs from the first one due to a partially clamped bottom end and to an elastic connection of the additional mass at the free end. In the applications considered below, these differences are the consequences of flexible elements located at the beam ends and they are modelled by rotational and translational springs. In both models, the additional mass weighs m [kg] and possesses a rotary inertia I_{cin} [kg.m^2]. Moreover, the centroid of the mass is at a distance h_b [m] from the tip end of the beam. The springs defining the partially clamped end are characterised by stiffnesses in rotation $K_{r,b}$ and in translation $K_{t,b}$, while $K_{r,t}$ and $K_{t,t}$ are the stiffnesses in rotation and in translation of the springs representing the flexible connection of the additional mass at the free end. These parameters are scaled in the same manner as above, leading to the following dimensionless quantities $m^* = \frac{m\omega_1^2 h_w^3}{EI}$, $I_{cin}^* = \frac{I_{cin}\omega_1^2 h_w}{EI}$, $h_b^* = \frac{h_b}{h_w}$, $K_{r,b}^* = K_{r,b}\frac{h_m^3}{EI}$, $K_{t,b}^* = K_{t,b}\frac{h_m}{EI}$, $K_{r,t}^* = K_{r,t}\frac{h_m^3}{EI}$ and $K_{t,t}^* = K_{t,t}\frac{h_m}{EI}$.

Details of the beam top with the additional mass are depicted in Figure III.2, showing the contributions of the bending (blue) and shear (red) effects in terms of angle of rotations. The usual simplification for the shear deformation is given in Figure III.2 (b). Under bending and shear effects, the centroid of the additional mass is subjected to a rotation α with respect to the x-axis. The angle γ, representing the shear effects, only increases the variation of the transverse displacement along the height. This observation will be useful for the formulations of the bending moment and shear force.

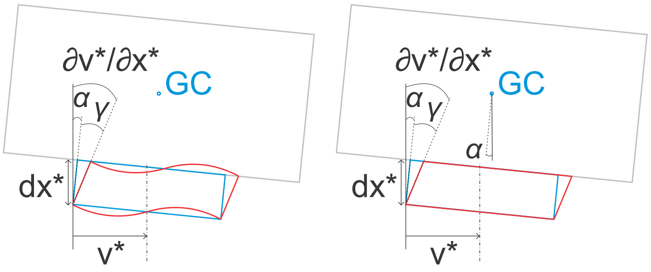

(a) (b)

Figure III.2: Details of the model free end.

To be consistent with the Timoshenko beam theory described above, a homogeneous beam with linear and indefinitely elastic material is assumed and the cross-section of the beam is doubly symmetric. The consequences of the specific details are practically translated by modifying the boundary conditions of the classical cantilever beam. These latter are here expressed in a dimensionless form for the clamped ($x^* = 0$) and free ($x^* = 1$) ends respectively,

$$v^* = 0 \quad ; \quad \alpha = 0 \qquad \text{at } x^* = 0 \tag{III.20}$$

$$M^* = -\alpha' = 0 \quad ; \quad V^* = k'G^*A^*\left(v^{*'} - \alpha\right) = 0 \qquad \text{at } x^* = 1 \tag{III.21}$$

with $G^* = Gh_w^4/EI$, $A^* = A/h_w^2$ and $M^*(x^*, t^*)$ and $V^*(x^*, t^*)$ representing the dimensionless bending moment and the shear force, defined as

$$M^* = \frac{M}{M^\star} \qquad \text{and} \qquad V^* = \frac{V}{V^\star} \tag{III.22}$$

where $M(x,t)$ and $V(x,t)$ are the bending moment and the shear force and

$$M^\star = \frac{EI}{h_w} \qquad \text{and} \qquad V^\star = \frac{EI}{h_w^2} \tag{III.23}$$

First model

In the first model, the additional mass only influences the conditions at the free end ($x^* = 1$), involving non-zero bending moment and shear force

$$M^* \quad = -\alpha' \quad = m^* h_b^* \left(\ddot{v}^* + h_b^* \ddot{\alpha}\right) + I_{cin}^* \ddot{\alpha}$$

$$V^* \quad = k'G^*A^*\left(v^{*'} - \alpha\right) \quad = -m^*\left[\ddot{v}^* + h_b^*\ddot{\alpha} - h_b^*\ddot{v}^{*'} - h_b^{*^2}\ddot{\alpha}'\right] + I_{cin}^*\ddot{\alpha}' \tag{III.24}$$

The magnitude m^* and inertia I_{cin}^* of the mass as well as the distance h_b^* are identified as the three main parameters characterising the influence of the additional mass. The prime and dot symbol indicate derivatives with respect to x^* and t^* respectively.

Second model

In addition to the mass, the presence of flexible devices in the second model affects the boundary conditions at both ends. On the one hand, the beam base ($x^* = 0$) cannot be considered as clamped anymore. A rotation and a transverse displacement are allowed and their magnitude depends on the stiffness of the springs

$$v^* = \frac{V^*}{K_{t,b}^*} = \frac{k'G^*A^*}{K_{t,b}^*}\left(v^{*'} - \alpha\right) \quad ; \quad \alpha = -\frac{M^*}{K_{r,b}^*} = \frac{\alpha'}{K_{r,b}^*}. \tag{III.25}$$

On the other hand, a relative rotation $\triangle\alpha$ and a relative displacement $\triangle v^*$ are possible between the top of the beam and the base of the additional mass due to the elastic connection. These contributions have to be taken into account and lead to the boundary conditions at the free end ($x^* = 1$)

$$\begin{aligned}
M^* &= -\alpha' \\
&= m^* h_b^* \left[\ddot{v}^* + \triangle\ddot{v}^* + h_b^* \left(\ddot{\alpha} + \triangle\ddot{\alpha}\right)\right] + I_{cin}^* \left(\ddot{\alpha} + \triangle\ddot{\alpha}\right) \\
&= m^* h_b^* \left(\ddot{v}^* + h_b^* \ddot{\alpha}\right) + m^* h_b^* \left[\frac{k' G^* A^*}{K_{t,t}^*}\left(\ddot{v}^{*'} - \ddot{\alpha}\right) + \frac{h_b^* \ddot{\alpha}'}{K_{r,t}^*}\right] + I_{cin}^* \left(\ddot{\alpha} + \frac{\ddot{\alpha}'}{K_{r,t}^*}\right)
\end{aligned}$$

$$\begin{aligned}
V \quad ^* = {}& k' G^* A^* \left(v^{*'} - \alpha\right) \\
= {}& -m^* \left[\ddot{v}^* + \triangle\ddot{v}^* + h_b^* \left(\ddot{\alpha} + \triangle\ddot{\alpha}\right)\right] + m^* h_b^* \left(\ddot{v}^{*'} + \triangle\ddot{v}^{*'} + h_b^* \ddot{\alpha}' + h_b^* \triangle\ddot{\alpha}'\right) + I_{cin}^* \left(\ddot{\alpha}' + \triangle\ddot{\alpha}'\right) \\
= {}& -m^* \left(\ddot{v}^* + h_b^* \ddot{\alpha}\right) - m^* \left[\frac{k' G^* A^*}{K_{t,t}^*}\left(\ddot{v}^{*'} - \ddot{\alpha}\right) + \frac{h_b^* \ddot{\alpha}'}{K_{r,t}^*}\right] + m^* h_b^* \left(\ddot{v}^{*'} + h_b^* \ddot{\alpha}'\right) \qquad \text{(III.26)} \\
& + m^* h_b^* \left[\frac{k' G^* A^*}{K_{t,t}^*}\left(\ddot{v}^{*''} - \ddot{\alpha}'\right) + \frac{h_b^* \ddot{\alpha}''}{K_{r,t}^*}\right] + I_{cin}^* \left(\ddot{\alpha}' + \frac{\ddot{\alpha}''}{K_{r,t}^*}\right)
\end{aligned}$$

Equations III.24 to III.26 neglect the second order effects and, therefore, the influence of the gravity is not considered.

III.3 Frequency equations

The frequency equation is established for the case of a circular frequency smaller than the critical frequency ($\omega^* \Omega_b^* \leq 1$). The equation for a circular frequency greater than the critical one can be obtained by replacing b^* with $j\tilde{b}^*$.

III.3.1 Frequency equation of the first model

Equations III.20 and III.24 provide some relations between the four unknown coefficients, see Eq. III.14. These relations are written in the matrix form

$$\mathbf{Ac} := \begin{bmatrix} 0 & 1 & 0 & 1 \\ \varphi_a^* & 0 & \varphi_b^* & 0 \\ A_{31} & A_{32} & A_{33} & A_{34} \\ A_{41} & A_{42} & A_{43} & A_{44} \end{bmatrix} \begin{Bmatrix} C_1 \\ C_2 \\ C_3 \\ C_4 \end{Bmatrix} = \mathbf{0} \qquad \text{(III.27)}$$

where $\mathbf{c}$ is the vector gathering the integration constants of the mode shapes $\phi(x)$ and $\psi(x)$. In matrix $\mathbf{A}$, we have introduced

$$\begin{aligned}
A_{31} &= \left(a^* \varphi_a^* + \bar{P}\right) \sin a^* + \varphi_a^* \bar{Q} \cos a^* \\
A_{32} &= \left(a^* \varphi_a^* + \bar{P}\right) \cos a^* - \varphi_a^* \bar{Q} \sin a^* \\
A_{33} &= -\left(b^* \varphi_b^* - \bar{P}\right) \sinh b^* + \varphi_b^* \bar{Q} \cosh b^* \qquad \text{(III.28)} \\
A_{34} &= -\left(b^* \varphi_b^* - \bar{P}\right) \cosh b^* + \varphi_b^* \bar{Q} \sinh b^*
\end{aligned}$$

and

$$
\begin{aligned}
A_{41} &= (a^* - \varphi_a^*)\left(1 + \frac{\bar{P}}{k'G^*A^*}\right)\cos a^* - \left(\frac{\omega^{*^2} m^*}{k'G^*A^*} + \frac{a^*\varphi_a^*}{k'G^*A^*}\bar{Q}\right)\sin a^* \\
A_{42} &= -(a^* - \varphi_a^*)\left(1 + \frac{\bar{P}}{k'G^*A^*}\right)\sin a^* - \left(\frac{\omega^{*^2} m^*}{k'G^*A^*} + \frac{a^*\varphi_a^*}{k'G^*A^*}\bar{Q}\right)\cos a^* \\
A_{43} &= (b^* - \varphi_b^*)\left(1 + \frac{\bar{P}}{k'G^*A^*}\right)\cosh b^* - \left(\frac{\omega^{*^2} m^*}{k'G^*A^*} - \frac{b^*\varphi_b^*}{k'G^*A^*}\bar{Q}\right)\sinh b^* \\
A_{44} &= (b^* - \varphi_b^*)\left(1 + \frac{\bar{P}}{k'G^*A^*}\right)\sinh b^* - \left(\frac{\omega^{*^2} m^*}{k'G^*A^*} - \frac{b^*\varphi_b^*}{k'G^*A^*}\bar{Q}\right)\cosh b^*
\end{aligned}
\qquad \text{(III.29)}
$$

where

$$
\bar{Q} = \omega^{*^2}\left(m^* h_b^{*^2} + I_{cin}^*\right); \quad \bar{P} = \omega^{*^2} m^* h_b^*. \qquad \text{(III.30)}
$$

Setting the determinant of the matrix **A** to zero leads to the frequency equation. This equation needs to be solved for ω^* which lies in a^*, b^*, $\bar{Q}$ and $\bar{P}$. The complete expression is given in Appendix B in the case $\omega^*\Omega_b^* \leq 1$

III.3.2 Frequency equation of the second model

In the second model, based on Eqs. III.25 and III.26, the frequency equation reads

$$
\mathbf{Ac} := \begin{bmatrix} \hat{A}_{11} & 1 & \hat{A}_{13} & 1 \\ \varphi_a^* & \hat{A}_{22} & \varphi_b^* & \hat{A}_{24} \\ \hat{A}_{31} & \hat{A}_{32} & \hat{A}_{33} & \hat{A}_{34} \\ \hat{A}_{41} & \hat{A}_{42} & \hat{A}_{43} & \hat{A}_{44} \end{bmatrix} \begin{Bmatrix} C_1 \\ C_2 \\ C_3 \\ C_4 \end{Bmatrix} = \mathbf{0} \qquad \text{(III.31)}
$$

where

$$
\begin{aligned}
\hat{A}_{11} &= -\frac{k'G^*A^*}{K_{t,b}^*}(a^* - \varphi_a^*) \\
\hat{A}_{13} &= -\frac{k'G^*A^*}{K_{t,b}^*}(b^* - \varphi_b^*) \\
\hat{A}_{22} &= \frac{a^*\varphi_a^*}{K_{r,b}^*} \\
\hat{A}_{24} &= -\frac{b^*\varphi_b^*}{K_{r,b}^*}
\end{aligned}
\qquad \text{(III.32)}
$$

and

$$\begin{aligned}
\hat{A}_{31} &= A_{31} - \frac{a^*\varphi_a^*}{K_{r,t}^*}\bar{Q}\sin a^* + \frac{k'G^*A^*}{K_{t,t}^*}\left(a^* - \varphi_a^*\right)\bar{P}\cos a^* \\
\hat{A}_{32} &= A_{32} - \frac{a^*\varphi_a^*}{K_{r,t}^*}\bar{Q}\cos a^* - \frac{k'G^*A^*}{K_{t,t}^*}\left(a^* - \varphi_a^*\right)\bar{P}\sin a^* \\
\hat{A}_{33} &= A_{33} + \frac{b^*\varphi_b^*}{K_{r,t}^*}\bar{Q}\sinh b^* + \frac{k'G^*A^*}{K_{t,t}^*}\left(b^* - \varphi_b^*\right)\bar{P}\cosh b^* \\
\hat{A}_{34} &= A_{34} + \frac{b^*\varphi_b^*}{K_{r,t}^*}\bar{Q}\cosh b^* + \frac{k'G^*A^*}{K_{t,t}^*}\left(b^* - \varphi_b^*\right)\bar{P}\sinh b^* \qquad \text{(III.33)} \\
\hat{A}_{41} &= A_{41} - \frac{a^*\varphi_a^*}{k'G^*A^*K_{r,t}^*}\left[a^*\bar{Q}\cos a^* - \bar{P}\sin a^*\right] - \frac{\left(a^* - \varphi_a^*\right)}{K_{t,t}^*}\left[\omega^{*^2}m^*\cos a^* + a^*\bar{P}\sin a^*\right] \\
\hat{A}_{42} &= A_{42} + \frac{a^*\varphi_a^*}{k'G^*A^*K_{r,t}^*}\left[a^*\bar{Q}\sin a^* + \bar{P}\cos a^*\right] + \frac{\left(a^* - \varphi_a^*\right)}{K_{t,t}^*}\left[\omega^{*^2}m^*\sin a^* - a^*\bar{P}\cos a^*\right] \\
\hat{A}_{43} &= A_{43} + \frac{b^*\varphi_b^*}{k'G^*A^*K_{r,t}^*}\left[b^*\bar{Q}\cosh b^* - \bar{P}\sinh b^*\right] + \frac{\left(b^* - \varphi_b^*\right)}{K_{t,t}^*}\left[\omega^{*^2}m^*\cosh b^* + b^*\bar{P}\sinh b^*\right] \\
\hat{A}_{44} &= A_{44} + \frac{b^*\varphi_b^*}{k'G^*A^*K_{r,t}^*}\left[b^*\bar{Q}\sinh b^* - \bar{P}\cosh b^*\right] + \frac{\left(b^* - \varphi_b^*\right)}{K_{t,t}^*}\left[\omega^{*^2}m^*\sinh b^* + b^*\bar{P}\cosh b^*\right]
\end{aligned}$$

The frequency equation is expressed in Appendix B in the case $\omega^*\Omega_b^* \leq 1$. Notice this second case degenerates into the first model as the stiffnesses $K_{t,t}^*$, $K_{r,t}^*$, $K_{t,b}^*$, $K_{r,b}^*$ tend to infinity.

III.4 Parametric study of beam models and mode shapes

The coefficients of the matrix **A**, leading to the expression of the frequency equation, highlight the importance of the geometrical and mechanical properties of the beam through the dimensionless groups Ω_a^* and Ω_b^*. Additional parameters also influence this equation due to the presence of an additional mass at the top, such as the mass m^* and its rotary inertia I_{cin}^*, as well as the distance h_b^* from the beam free end to the centroid of the mass. The second model has four extra parameters. These are the stiffnesses in rotation and in translation of the material placed at the beam ends, namely ($K_{r,b}^*$, $K_{t,b}^*$) and ($K_{r,t}^*$, $K_{t,t}^*$) for the base and top ends respectively. In comparison to the classical cantilever beam, those parameters obviously add complexity in the frequency equation.

III.4.1 Comparison of the Euler-Bernoulli and Timoshenko beam models

Equations III.5 and III.6 express the decoupled equations of motion according to the Timoshenko beam theory. When $\Omega_a^* \ll 1$ and $\Omega_b^* \ll 1$, these equations regularly degenerate into the equation of motion given by the Euler-Bernoulli (E-B) theory. This section aims at studying the evolution of the wave numbers a^* and b^* (or $\tilde{b}^*$) as a function of the dimensionless groups Ω_a^* and Ω_b^*. The variations of these latter are correlated in the light of the expressions of the wave numbers given in Eqs. III.12 and III.13. Indeed, the radicand of these equations has to be positive, leading to the condition

$$\Omega_b^{*^2} - \frac{\Omega_a^{*^2}}{4} \leq \frac{1}{\omega^{*2}}. \tag{III.34}$$

Figure III.3 gives a mapping of the wave numbers a^* and b^* (or $\tilde{b}^*$) respectively, for a dimensionless circular frequency ω^* equal to unity. It shows white areas which correspond to couples $\left[\Omega_a^*; \Omega_b^{*^2}\right]$ not complying with the condition given by Eq. III.34. Setting the dimensionless groups Ω_a^* and Ω_b^* to zero provides identical and unit wave numbers ($a^* = b^* = 1$). It corresponds to the E-B beam theory. In the Timoshenko beam theory, these groups are however non-zero. Considering the geometry of the specimens without rubber described in Section II.4 and the mechanical properties as recommended in the Eurocodes, namely $E = 1000\, f_k$ and $G = 0.4\, E$, we obtain

$$\Omega_a^* = 0.0489 \quad ; \quad \Omega_b^{*^2} = 4.4819 \times 10^{-4} \tag{III.35}$$

for the short wall and

$$\Omega_a^* = 0.4159 \quad ; \quad \Omega_b^{*^2} = 0.0324 \tag{III.36}$$

for the long wall. These couples of values are represented in Figure III.3 with red and green points respectively. The wave numbers are $a^* = 0.9888$ and $b^* = 0.9885$ for the short wall, while the wave numbers for the long wall are $a^* = 0.8901$ and $b^* = 0.8708$. Consequently, an E-B model is sufficient to model the short wall, whereas a Timoshenko beam is required for the long wall.

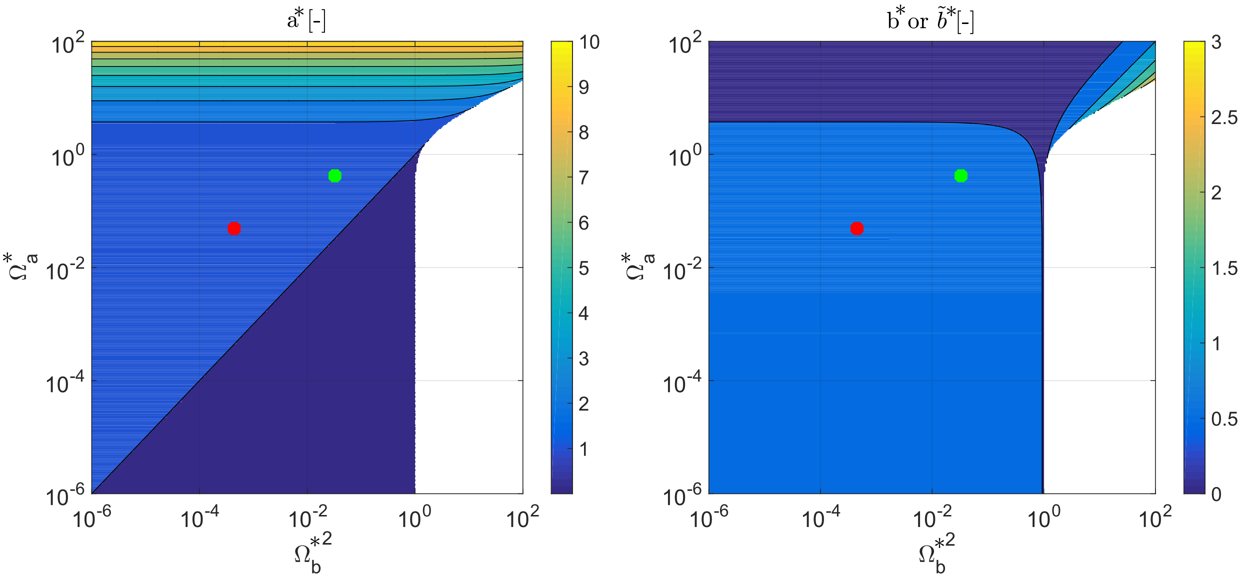

Figure III.3: Influence of Ω_a^* and $\Omega_b^{*^2}$ on wave numbers a^* and b^* (or $\tilde{b}^*$).

III.4.2 Parameters related to the additional upper mass

Figure III.4 plots the dimensionless frequency equation of the first model considering the material and geometrical properties of the short wall given in Section II.4. The values of the parameters related to the mass are also derived from the quantities given this section. The mechanical properties of the masonry are also chosen according to the Eurocodes recommendations. These choices result in $\Omega_a^* = 0.0489$ and $\Omega_b^{*^2} = 4.4819 \times 10^{-4}$. Variations around this nominal configuration are also represented: (i) no additional mass (yellow), (ii) an upper mass without gap h_b^* between the beam end and the centroid of the mass (green), (iii) an additional mass without rotary inertia I_{cin}^* (red) and (iv) a combination of (ii) and (iii) (black). Figure III.5 gives the same results in the case of the long wall, whose nominal configuration is characterized by $\Omega_a^* = 0.4159$ and $\Omega_b^{*^2} = 0.0324$. Beside the solid curves representing the Timoshenko model, dashed lines with similar colours represent the frequency equations obtained by the E-B beam theory (i.e. enforcing $\Omega_a^* = \Omega_b^{*^2} = 0$) under the same assumptions.

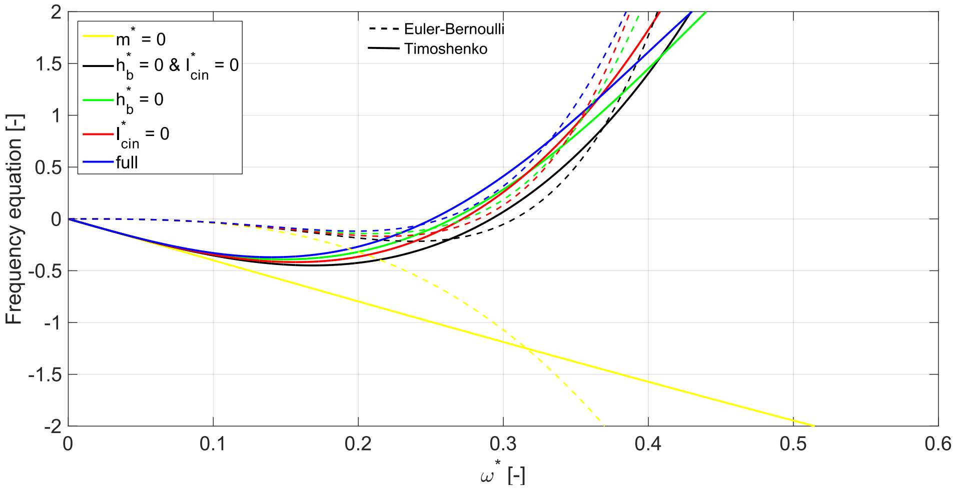

Figure III.4: Frequency equations with different assumptions (1st model) - short wall.

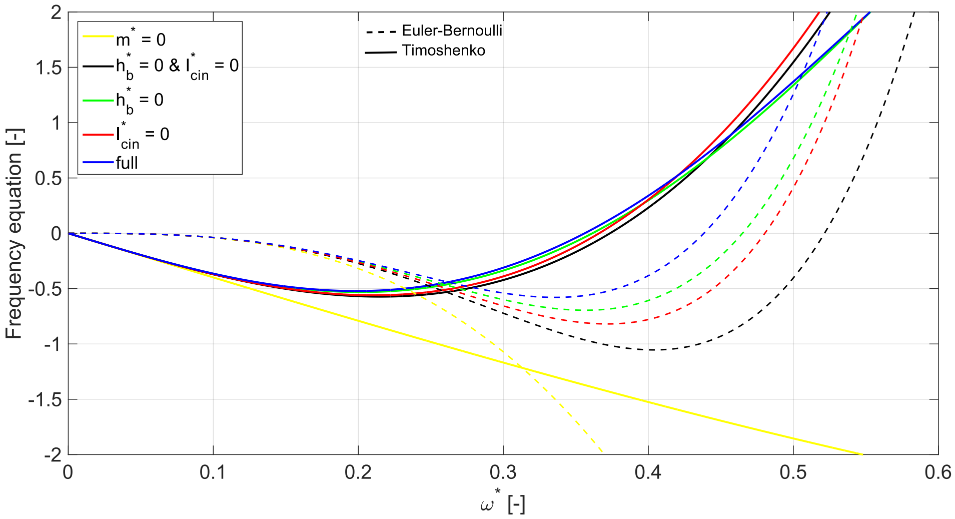

Figure III.5: Frequency equations with different assumptions (1st model) - long wall.

Comparison of the different curves in Figures III.4 and III.5 shows the importance of the additional mass. This latter indeed provides more than 90 % of the total mass and involves a large decrease of the first circular frequency of the beam. The influence of the gap h_b^* and the rotary inertia I_{cin}^* is more important for the short wall than for the long wall. Numerical values are given in Table III.1. The variation is effectively higher for the short wall (from 5.3 % to 16.2 %), whereas it is less significant for the long wall (less than 4.9 %). Therefore, the contribution of the rotary inertia and the distance between the top of the wall and the centroid of the mass have to be considered, especially for the short wall.

Figures III.4 and III.5 also compare the frequency equations developed when considering E-B (dashed lines) and Timoshenko (solid lines) beam theories. The fundamental circular frequencies for both theories are also tabulated in Table III.1. Under the assumptions (ii) to (iv), the relative difference between theories is lower than 5 % regarding the short wall. This difference ranges between 19 % and 30 % in the case of the long wall. These numbers show that the E-B model can be sufficient for the short wall, but the Timoshenko model is necessary for the long wall, as already observed from the graphical representations. The E-B theory with assumption (i) leads to the same result for both walls. This comes from the nondimensionalization defined in Section III.2.

Table III.1: Fundamental circular frequency with different assumptions (1$^{\text{st}}$ model) - numerical values.

Wall	Full	$m^* = 0$	$h_b^* = 0$	$I_{cin}^* = 0$	$h_b^* = I_{cin}^* = 0$
		(i)	(ii)	(iii)	(iv)
Long (Timoshenko)	0.3560	2.1254	0.3614	0.3660	0.3735
Long (Euler-Bernoulli)	0.4383	3.5160	0.4649	0.4803	0.5215
Short (Timoshenko)	0.2513	3.1820	0.2648	0.2718	0.2918
Short (Euler-Bernoulli)	0.2579	3.5160	0.2737	0.2829	0.3075

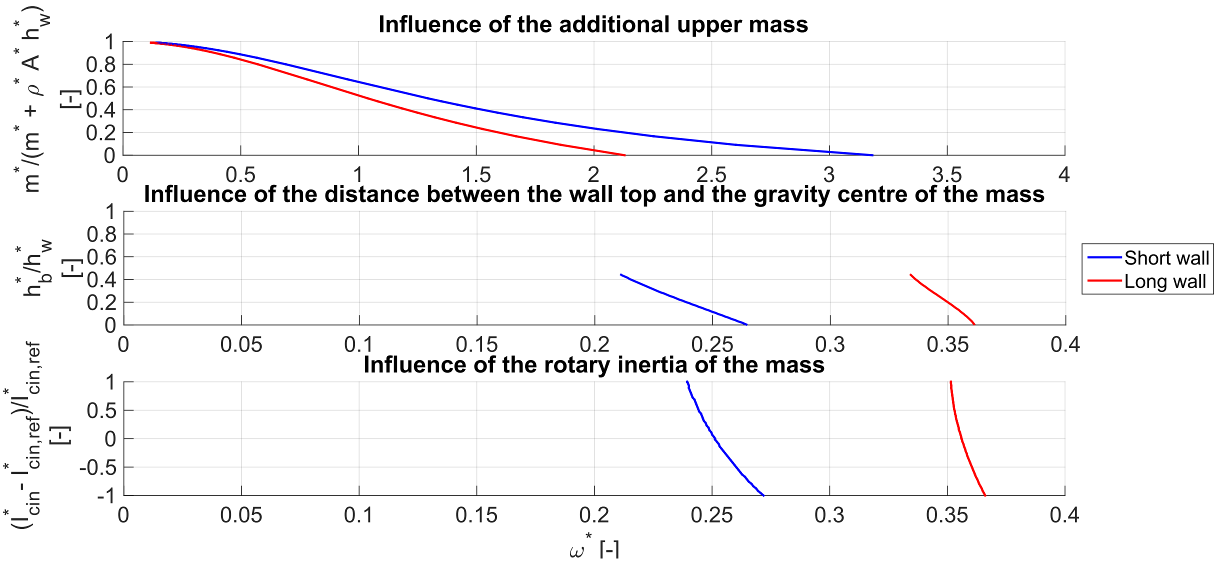

Figure III.6: Influence of the parameters related to the mass. (a) Influence of the additional mass at the top, (b) Influence of the distance between the top of the wall and the centroid of the mass, (c) Influence of the rotary inertia of the mass.

Regarding the frequency equation obtained with the Timoshenko beam theory, further studies on the influence of the different parameters related to the mass have been performed. The results are given in Figure III.6. The influence of the magnitude of the additional mass m^* (top), of the gap h_b^* (middle) and of the rotary inertia I_{cin}^* (bottom) are given for the short (in blue) and long (in red) walls. The results are in accordance with the values tabulated in Table III.1. For example, values obtained under the assumption of no additional mass (i) or $h_b^* = 0$ (ii) correspond to the intersection of the curves in Figure III.6 (top and middle) with the x-axis. Figure III.6 (bottom) provides the tabulated values with $I_{cin}^* = 0$ (assumption (iii)) when the ordinate is equal to -1. Again, Figure III.6 highlights the higher importance of the parameters in the case of the short wall and other observations can be made. First, the first circular frequency is very sensitive to variations of the additional mass. The interpretation of this results has to be carefully taken because the total mass of the specimen varies and any increment of mass has also consequences on the rotary inertia. Second, the rotary inertia I_{cin}^* seems to have the lowest influence on the frequency equation, especially for the long wall.

III.4.3 Parameters related to the stiffnesses of the base and of the mass-beam connection

The influence and the importance of the presence of rubber layers leading to a beam with an elastically restrained bottom end and an elastically connected additional mass at the top, is studied by comparing the frequency equation obtained with the assumption of (i) a cantilever beam with an additional mass rigidly connected at its free end (first model case), (ii) the same beam with an elastically restrained base, (iii) the same beam with an elastically connected mass at the top and (iv) the beam combining the effects of (ii) and (iii). The material and geometrical properties are those of the short and long walls given in Section II.4. The parameters related to the additional mass are based on the quantities given in the same section. The couple of mechanical characteristics of the rubber (E_{rubber}, G_{rubber}) are chosen in the range of usual values, but are the same for the bottom and top ends. The frequency equations are re-normalized with the same circular frequency than the first model since the beam is the same.

The results are given in Figure III.7 (short wall) and Figure III.8 (long wall) and the comparison is summarized in Table III.2 with several observations.

Table III.2: Fundamental circular frequency with different assumptions (2^{nd} model) - numerical value.

Wall	Without rubber	With rubber	$1/K_{r,b}^* = 1/K_{t,b}^* = 0$	$1/K_{r,t}^* = 1/K_{t,t}^* = 0$
Long	0.3561	0.0761	0.1311	0.0906
Short	0.2513	0.0600	0.1336	0.0652

The effect of the rubber layers on the natural frequency is more or less the same for both walls, as the decrease of the fundamental circular frequency is around 75%. This conclusion is mitigated when there is only the elastically connected mass (column 3) given that the decrease is about 45 % for the short wall and 63% for the long wall. Both rubber layers influence the results, even if placing a rubber layer at the bottom end only (column 4) leads to a larger decrease. Indeed, Table III.2 highlights that adding the soundproofing layer between the top of the wall and the additional mass in the presence of a layer located at the base of the wall does not involve a significant drop. The decreases produced by the two rubber layers are not additive, certainly due to interaction between the effects of both layers.

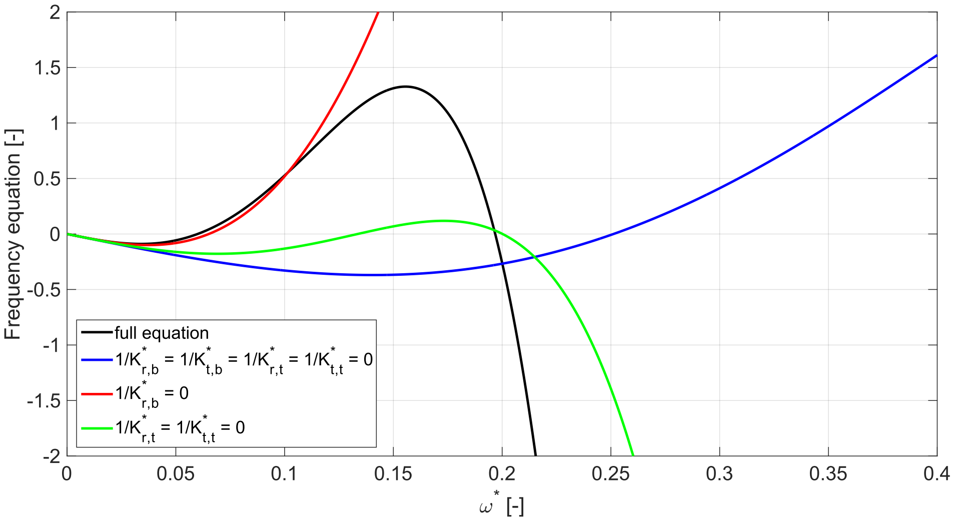

Figure III.7: Influence of the base stiffness and the mass-to-wall connection stiffness (short wall with rubber).

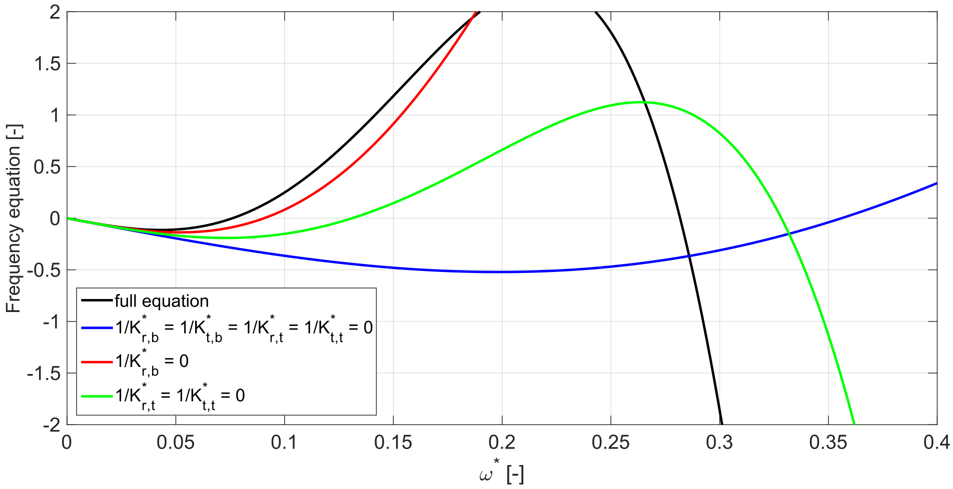

Figure III.8: Influence of the base stiffness and the mass-to-wall connection stiffness (long wall with rubber).

III.4.4 Mode shapes

The roots of the frequency equation provide the natural frequencies of the model. They are associated with coefficients C_1, C_2, C_3 and C_4 (respectively $\tilde{C}_1, \cdots, \tilde{C}_4$, if $\omega^*\Omega_b^* \geq 1$) and, thereby, the mode shapes $\phi(x^*)$ and $\psi(x^*)$.

The mode shapes related to the first circular frequency for each of the four tested specimens are represented in terms of displacements $\phi(x^*)$ (Figure III.9 left) and rotations $\psi(x^*)$ (Figure III.9 right). These are normalized such that the maximum displacement (rotation) is unity. Differences in terms of displacements between the walls without rubber devices are first observed. The mode shape of the long wall can be well approximated by a straight line, while the mode shape for the short wall presents a vertical tangent at the base. The shapes in terms of rotations are similar in each case. Such results are in accordance with previous conclusions, where the short wall could be considered as an Euler-Bernoulli beam and the shear effects are more significant for the long wall, requiring therefore a Timoshenko model. A comparison is then made between walls with the same geometry, but including or not soundproofing elements. The presence of these latter involves non-zero displacement and rotation at the bottom of the wall. In particular, the rotation is mainly concentrated at the bottom of the beam, and more or less constant along the wall. The displacement mode shapes for the long and short walls are close to a straight line when there are rubber devices. It is therefore important not to conclude to the need of a Timoshenko beam model when a straight displacement mode shape is observed (e.g. short wall), as it may simply result from the compliance of the end connections.

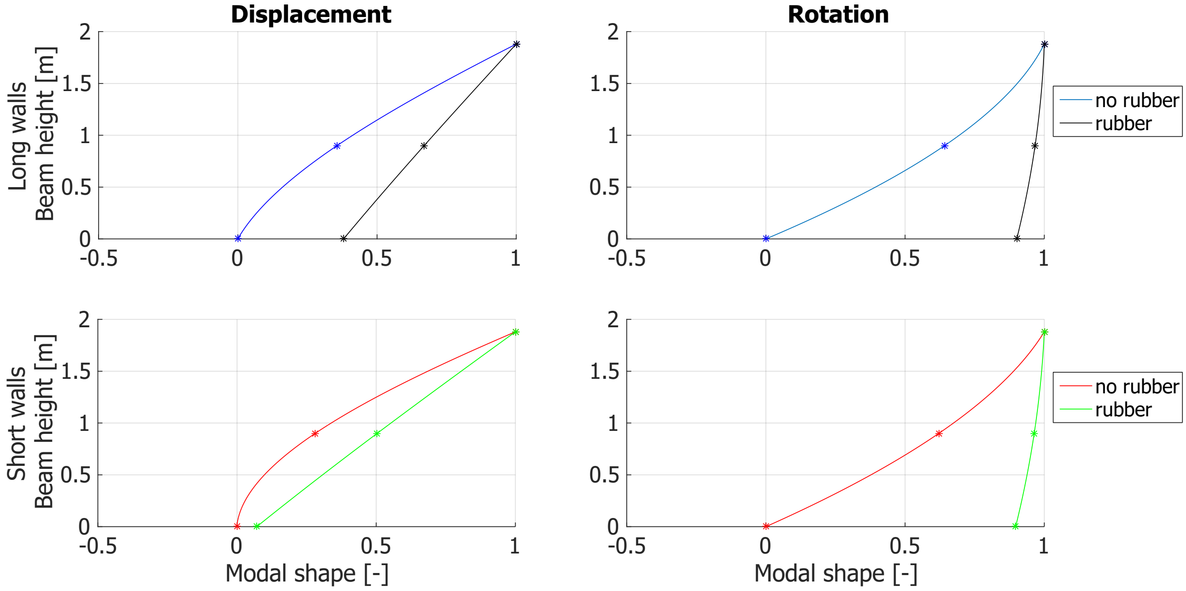

Figure III.9: Modal shapes (left : displacement - right : rotation).

III.5 Determination of equivalent mechanical properties

The expression of the frequency equation of the Timoshenko beam model depends on the two dimensionless groups Ω_a^* and ${\Omega_b^*}^2$, i.e. the ratio of the gyradius of the cross-section, the beam length and the elastic-to-shear moduli ratio. These groups are explicit in the governing equations and implicit in the waves numbers a^*,b^* and $\tilde{b}^*$. In the present chapter, other parameters also play an important role in the model, like the mass and the geometry of the additional mass (m^*, h_b^* and I_{cin}^*) or stiffnesses involved in the boundary conditions $K_{r,b}^*$, $K_{t,b}^*$, $K_{r,t}^*$ and $K_{t,t}^*$. The determination of some of these parameters is straightforward, especially for the geometrical ones. Regarding URM structures, others are more difficult to assess because of the heterogeneity of the material (units + mortar) and the large range of masonry types (clay or concrete units with mortar, glued or empty joints, etc.).

In the perspective of modelling the URM structural elements with equivalent homogeneous and isotropic beam elements at the macro-scale, the use of the frequency equation to determine equivalent mechanical properties is relevant. Indeed, the establishment of this equation considers a beam model and is based on similar assumptions for the material. Another possibility to estimate the properties is the use of empirical formulae. These latter are however developed from experimental tests and do not fit the specificities of every type of masonry.

In the following, the frequency equation is first used to determine the fundamental frequency of URM walls without soundproofing devices. Due to the lack of characterisation of the elastic and shear moduli of the masonry, recommendations of the Eurocodes are first considered. Then, a parametric study is carried out in order to define the couples of equivalent mechanical properties leading to the frequency obtained by the experiments. Finally, the more relevant couple (E, G) is used as an input for the frequency equation related to walls including rubber and a parametric study is developed to identify equivalent mechanical properties for the rubber.

III.5.1 Fundamental frequency using standards recommendations

The Eurocode 6 advises that (§3.7.2.(2)) “In absence of a value determined by tests in accordance with EN 1052-1, the short term secant modulus of elasticity of masonry, E, for the use in structural analysis, may be taken to be $K_E f_k$” and recommends the value of 1000 for K_E. Notice that the value of K_E is not divided by two to take into account cracking because the used experimental results correspond to the undamaged configuration. It also defines the shear modulus G as 40 % of the elastic modulus E (§3.7.3.(1)). It follows,

$$E = 3900\text{MPa} \quad ; \quad G = 1560\text{MPa}. \tag{III.37}$$

Substituting these values in the frequency equation corresponding to the simple URM walls provides the fundamental frequencies tabulated in Table III.3. Comparing these results with the values obtained from the experiments (Table II.14) shows relative difference of 54.71 % and 20.24 % for the long and short walls respectively. The recommendations of the Eurocodes lead therefore to an overestimation of the mechanical properties in the case of URM walls with thin bed-layered joints and using a tongue-and-groove system for the head joints. The discrepancy can either come from the assessment of the elastic modulus or from the ratio between the shear and elastic moduli G/E. In the case of masonry with empty vertical joints, the definition of a unique ratio for the estimation of the shear modulus independently from the length of the wall is quite surprising. Indeed, the number of joints increases with the length of the wall and a higher deformability in shear could be expected.

Table III.3: Fundamental frequency of walls without rubber using the standards recommendations

	Long wall	Short wall
Frequency [Hz]	20.82	5.04
Dimensionless frequency [-]	0.057	0.040

III.5.2 Characterization of the masonry mechanical properties

Based on the observations in the previous section, a parametric study is performed with the aim of identifying the couples (E, G) that should be used in the frequency equation in order to recover the eigen frequencies measured experimentally. Instead of adjusting E and G separately, we take advantage of the fact that the ratio G/E usually lies in a specific range. We will therefore identify two parameters, namely the elastic modulus E and the ratio G/E. Figure III.10 plots the results of the study for the long and short walls without rubber. The blue and red lines are the lieu of the pairs $(E, G/E)$ providing, with the Timoshenko beam model, the same fundamental frequency as that identified from the experiments for the long and short walls respectively.

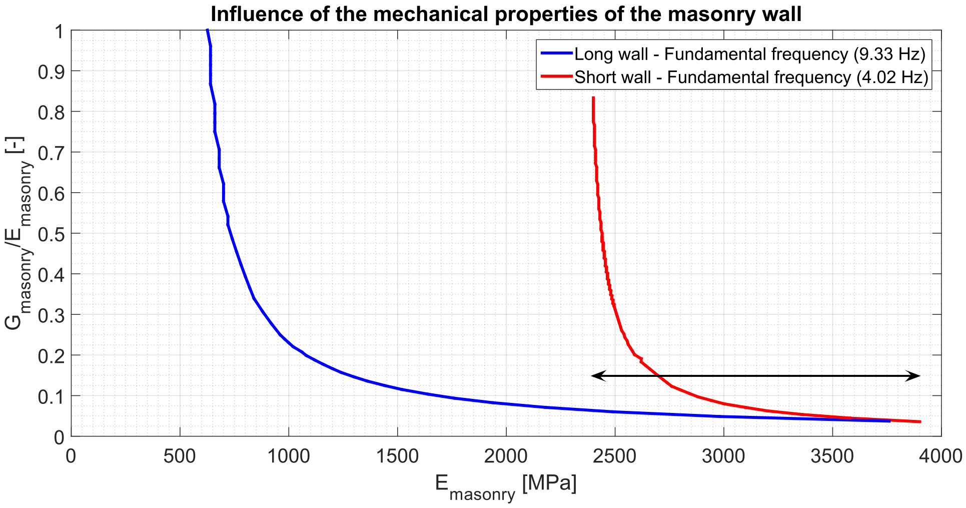

Figure III.10: Characterization of the masonry mechanical properties.

Comparison of curves in Figure III.10 highlights a higher dependency on the G/E ratio of the long wall because the curve related to this latter shows a more important increase of the elastic modulus when the G/E ratio decreases, at least when $G/E \lesssim 0.4$, which is expected anyway. For instance, a variation from 0.4 to 0.2 of the G/E ratio involves an increase of 5 % of the elastic modulus in the case of the short wall, while this increase is about 35 % in the case of the long wall. Such a sensitivity is intuitively expected, when considering the ratio between the bending and shear deformabilities of the walls. The shear deformability of the short wall is about ten times lower than the bending one, while the orders of magnitude are the same for the long wall (Table III.4). This statement is further emphasized in Figures

III.11 and III.12. Indeed Figure III.11 illustrates the high dependence to the G/E ratio of the results for the long wall because the curves differ, while they are clearly similar for the short wall (Figure III.12).

Table III.4: Bending and shear deformabilities of masonry walls.

	Bending deformability [m/N]	Shear deformability [m/N]
Long wall	$9.3607\ 10^{-9}$	$9.5557\ 10^{-9}$
Short wall	$2.3226\ 10^{-7}$	$2.7871\ 10^{-8}$

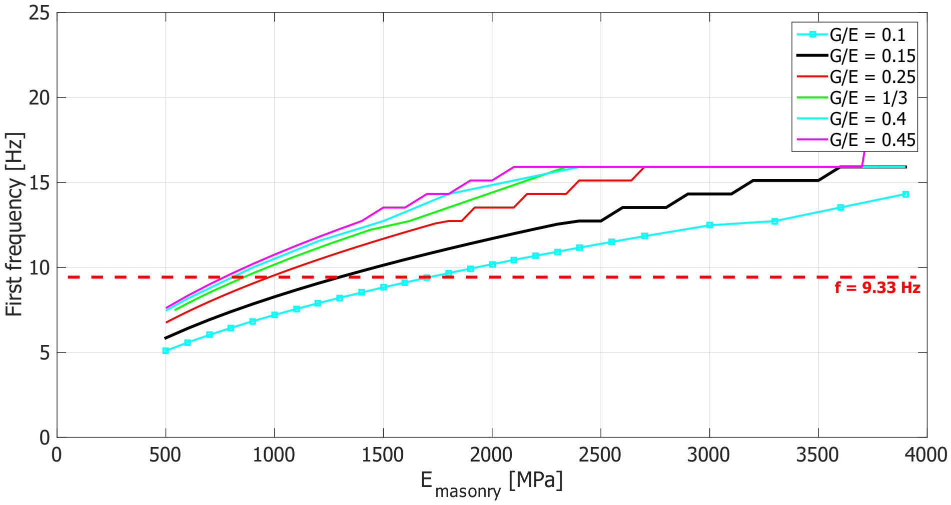

Figure III.11: Dependence to the shear deformability (long wall).

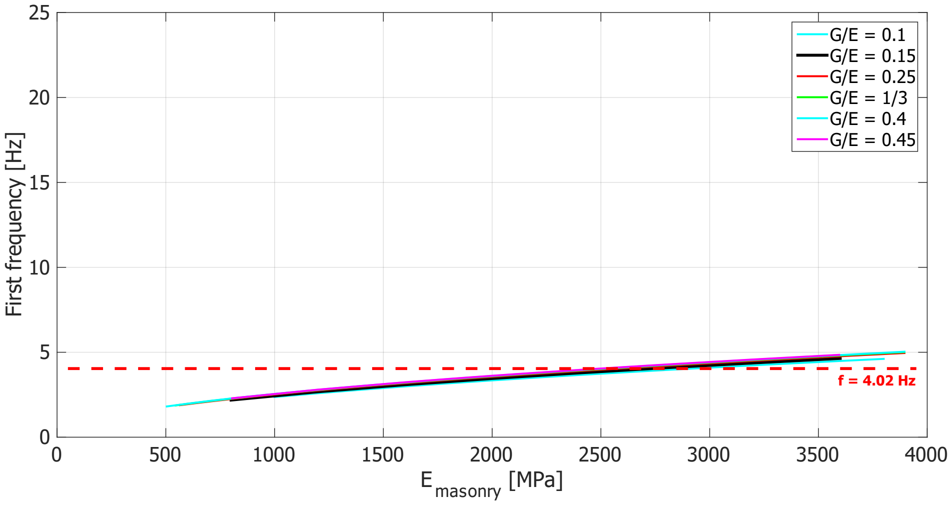

Figure III.12: Dependence to the shear deformability (short wall).

In terms of numerical values, Figure III.10 shows that the (identified) equivalent elastic modulus of the short wall is most likely around 2500 MPa which agrees with a ratio G/E ratio between 1 and 1/3. For the long wall, the identified equivalent elastic modulus seems to be in the range [650 MPa; 900 MPa] for the same G/E range.

The considered limits on the interval $[1/3; 1]$ for the G/E ratio come from the classical limitation of the Poisson's ratio. This ratio connects the elastic and shear moduli together and can vary from -1 to 0.5 for a continuous material. However, such an assumption is questionable in the case of masonry with empty vertical joints and the G/E ratio may be smaller than 1/3 (Poisson's ratio virtually larger than 0.5). Assuming $\nu \in [-1; 9]$, we notice $G/E \in [0.05; +\infty]$ which is relevant to the analysis of URM structures modelled by equivalent frames. The use of such a model is widespread and provides relevant results with a good computational time [57]. This type of value is also observable for other materials [59]. Furthermore, one could expect to find the same equivalent elastic modulus for both walls, regardless of its length. Indeed, the presence of vertical empty joints should not influence the bending behaviour and, consequently, the value of the elastic modulus. On the contrary, the shear deformability might suffer from size effects, which are not accounted for in our homogenized Timoshenko beam model, resulting therefore in an equivalent shear modulus smaller for the long wall. According to these considerations, the relevant value of the elastic modulus ranges from around 2400 MPa to 3900 MPa (see black arrow in Figure III.10) and the corresponding G/E ratio is about 3.85 % to 100 % for the short wall and about 3.7 % to 6.9 % for the long wall.

The recommended ratio of 40 % given by EC 6 [34] seems to be relevant for walls with a few vertical joints, as for example the short wall. The corresponding equivalent elastic modulus is about 2465 MPa, which is $K_E = 632\ f_k$. For longer walls, the ratio G/E has to be reduced (6.25 %) to take into account the extra vertical gaps between the units. A lower limit should exist, but its determination requires more experimental investigations. These conclusions are supported by results found in [38] or [24]. In the latter, uniaxial and diagonal compression tests were carried out on specimens with average dimensions of 1000 mm × 1000 mm × 300 mm. The masonry bonding was similar to the one considered here. Indeed, the characteristic compressive strength (NBN-EN 1996-1-1) f_k is 5.493 MPa for units of group 2. The authors give an elastic modulus of 4424 MPa, namely 805 f_k, and the ratio G/E is equal to 17.02 %. The experimental campaign detailed in Section II.2 led to the same conclusions. In particular, the equivalent elastic modulus found in this campaign is similar to the values considered here.

III.5.3 Characterization of the rubber mechanical properties

The previous section deals with the characterisation of masonry equivalent mechanical properties and the comparison with current standards recommendations. It results in the determination of acceptable couples of equivalent elastic and shear moduli for the first model, leading to the natural frequency measured experimentally. Among the possible combinations, two will be chosen as references for the short and long walls respectively

$$E = 2465 MPa \quad ; \quad G/E = 0.4 \qquad \text{(short wall)} \tag{III.38}$$

$$E = 2465 MPa \quad ; \quad G/E = 0.0625 \qquad \text{(long wall).} \tag{III.39}$$

As equivalent mechanical properties for the masonry are determined and the geometry is clearly defined, the expression of the frequency equation of the second model has only two unknowns left, namely the mechanical properties of the rubber layers, placed at the base of the wall and between the wall top and the additional mass at the top. These properties are translated via the values of the stiffnesses $K^*_{r,b}$, $K^*_{t,b}$, $K^*_{r,t}$ and $K^*_{t,t}$ present in the frequency equation.

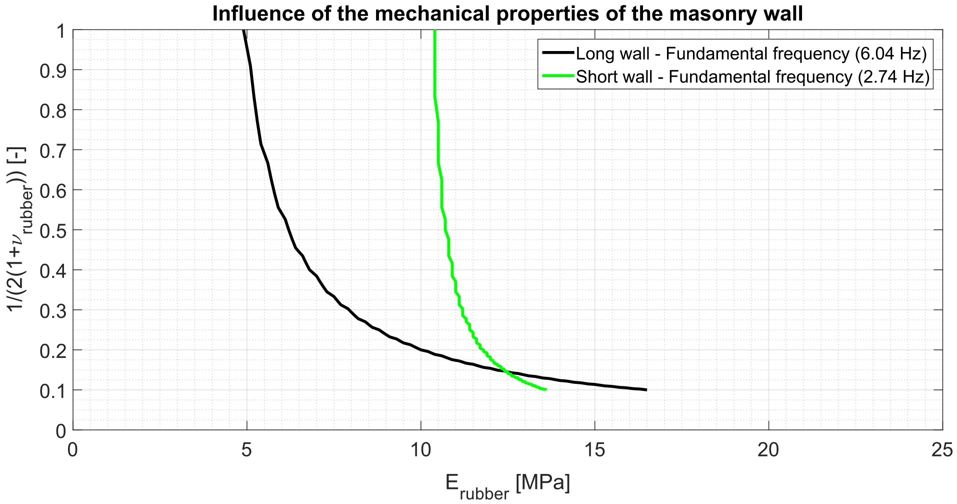

Figure III.13: Characterization of the mechanical properties of the rubber layers.

The results presented in Figure III.13 provide the coupled values (E_{rubber}, ν_{rubber}) giving the first natural frequency experimentally measured. The mechanical properties of the rubber layer are the same for the top and bottom as the same material is used. Contrary to the masonry wall, the rubber layers can be considered as a homogeneous and continuous body. There is therefore a relation between the elastic and shear moduli thanks to the Poisson ratio

$$G_{rubber} = \frac{E_{rubber}}{2(1+\nu_{rubber})}. \tag{III.40}$$

For rubber elements, the Poisson ratio is close to the incompressibility limit $\nu = 0.5$ and leads to a G_{rubber}/E_{rubber} ratio of 1/3. The corresponding elastic modulus is 11.1 MPa for the short wall and 7.5 MPa for the long one. Figure III.13 also exhibits a greater dependence to the Poisson ratio for the long wall in comparison to the short wall.

These results are in accordance with the experimental measurements and the producer's prescriptions (see Annex A). The difference between the identified values, 11.1 MPa and 7.5 MPa, has several origins. On the one hand, the rubber layer works under different compression stresses for the short and long walls. It is well known that the rubber exhibits a lower deformability under a larger stress, hence the rubber placed at the extremities of the short wall has a larger elastic modulus. On the other hand, the mechanical properties of the rubber devices show some significant variability due to their manufacturing process, i.e. they are made of recycled rubber, involving a possible scatter in the properties.

III.6 Conclusions

This chapter is dedicated to the development of the frequency equation of a modified cantilever beam, using the Timoshenko beam theory. Two models are studied to consider the modifications of the classic cantilever beam. The first model consists in a classical cantilever beam with an additional mass rigidly connected at the free end. The second one includes an elastically restrained base and a flexible connection between the free end and the additional mass. These modifications are taken into account through a proper modification of the boundary conditions. First, the deduced frequency equations highlight the importance of the dimensionless groups Ω_a^* and ${\Omega_b^*}^2$ which include the geometrical and mechanical parameters of the beam, as well as the stiffnesses of the base and mass-to-beam connection. Then, the frequency equations are used to characterise equivalent mechanical properties of load-bearing clay URM walls including soundproofing devices. For the first model, the characterisation leads to the definition of combined values for equivalent elastic and shear moduli of the masonry walls, E and G, expressed by the combination of an equivalent elastic modulus E and the G/E ratio. The second model is focused on the mechanical properties of the soundproofing devices. Finally, a comparison of the results in terms of mechanical properties with current standards recommendations for masonry structures shows an overestimation of the recommended values for the considered type of masonry. This chapter however proves that the modelling of masonry walls thanks to equivalent beams using the Timoshenko beam theory is possible.

Chapter IV

Numerical modelling of URM sub-structures

IV.1 Introduction
IV.2 Modelling of masonry at the macro-scale
IV.3 Numerical analysis of modern URM sub-structures
IV.4 Conclusions

IV.1 Introduction

Masonry is a heterogeneous material composed of units and mortar. The numerical analysis of URM structures can be performed following three modelling strategies with different levels of detail. These are discussed by P. Roca et al. [106] for historical constructions. In general, the micro-modelling offers the highest level of accuracy. It consists in the detailed representation of masonry components, i.e. the units, the mortar and unit-mortar interface, using the finite element method. It is however time-consuming which makes difficult the study of complete or large URM structures.

Just the opposite, the macro-scale approach considers the masonry as a homogeneous material with equivalent properties combining those of the mortar and the units. The determination of these equivalent properties based on experimental data is the topic of the Chapter III. The structure is divided into piers and spandrels modelled by single elements, which are vertically and horizontally oriented respectively. A review of the different types of macro-elements has been carried out in [74, 110, 92]. These can be sorted into one-dimensional and two-dimensional elements. Shear springs are the simplest example of the first group, but the most widespread for the analysis of URM structures is the equivalent frame model [13, 68, 46, 57] where the piers and spandrels are represented by beams connected together with rigid nodes. The interest in this approach is due to the similarities with steel and RC structures and the possibility to apply conventional methods of structural mechanics. It also provides results for entire buildings with a good accuracy and a computational effort suitable for current engineering practice. Besides, this method is specifically recommended in national and international codes. Referring to the Eurocode [116], the design of 3D buildings characterised by a regularity in plan and in elevation can be performed by the separate analysis of 2D structures oriented in the two main directions of the buildings. The elements of the second group have been introduced to improve the modelling of buildings with an irregular arrangement of openings for which the use of one-dimensional macro-elements can lead to geometrical inconsistencies. For instance, Caliò et al. [16] developed an articulated quadrilateral with rigid edges in which two diagonal springs govern the shear behaviour. Springs are also distributed in the sides for the flexural and sliding shear behaviour as well as the interaction with adjacent elements.

The third strategy is the meso-scale model which is located between the approaches at the micro- and macro-scales. The meso-scale description was initially proposed by Page [90] and modified Lourenço [62]. In this latter, the units are considered as elastic elements, while the mortar and the unit-mortar interface are modelled by interface elements with non-linear behaviour, including shear, tensile and compression failures. The meso-scale was used by several authors [96, 31, 6], assuming rigid elements for the units or implementing a 3D cyclic finite element able to model the in-plane and out-of-plane behaviour of masonry under monotonic and cyclic loadings for instance. Nevertheless, the computation demand for large structures remains a main drawback and other authors suggested a multi-scale approach [76, 80] or coupled a 3D meso-scale model with a domain partitioning [67].

In the perspective of extending the outcomes of Chapter II to complete buildings, this chapter aims at reproducing numerically the experimental results using macro-elements. Other strategies are disregarded because they are time-consuming. In the following, the TREMURI program [57] is used. An overview of the program is first described. Then, the parameters required for the analysis are given. The model and its results are commented for the specimens tested in static-cyclic and dynamic conditions. Conclusions are finally drawn.

IV.2 Modelling of masonry at the macro-scale

The TREMURI program is specifically oriented to the seismic analysis of masonry structures and simulates the non-linear behaviour of complete 3D buildings in static and dynamic conditions. To this purpose, it implements an equivalent frame model using non-linear beams for the piers and the spandrels which are connected together by rigid nodes, as explained in [57]. This procedure requires a limited computational effort. Under the assumption of a proper connection between the elements, local failures are prevented and the overall response of buildings is governed by the in-plane behaviour of the structural elements. The contribution to the strength of walls perpendicular to the seismic action is therefore neglected, but their presence influences the strength capacity through the distribution of the compression force between the elements. The first step of the analysis is the identification of the main structural components (piers and spandrels) which can be challenging in presence of openings, regarding the determination of the height of the piers especially. An example is given in Figure IV.1 with the height of the piers limited to the height of the opening. Different criteria are also available for the verification of the shear strength and the choice is based on the comparison of the different criteria limiting the strength domain.

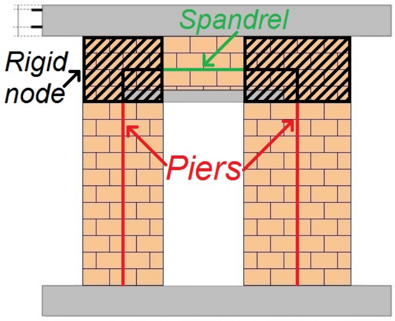

Figure IV.1: TREMURI program - definition of the piers, spandrels and rigid nodes

In comparison to the content of the reference paper [57], the version of the program used in the following has been improved. In particular, the behaviour of masonry panels is assumed multi-linear, instead of bilinear elastic perfectly plastic, as depicted in Figure IV.2. The new material law includes an elasto-plastic phase and different levels of damage (DL0 to DL5). Its parameters are given in Annex C. The units are those of the International System. Another improvement is the possibility to run cyclic analysis with displacement/force controlled or dynamic analysis in addition to the classical pushover.

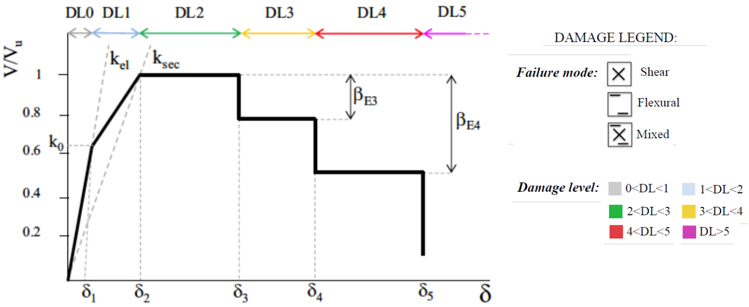

Figure IV.2: TREMURI program - material law of the used version

IV.3 Numerical analysis of modern URM sub-structures

The URM sub-structures to be analysed in this section are those tested in the experimental campaigns described in Chapter II. The adopted methodology is the following. First, the geometry of the models representing the specimens is defined. Most of these specimens are simple walls including specific details and are studied by means of vertical beams. Others have to be modelled as frames due to the presence of an opening. The definition of the piers and spandrels is not unique and different possibilities are compared (see IV.3.1.3). Then, the material law to be affected to the beam elements is determined. Two types of masonry units have been used in the experimental campaigns, thus requiring two sets of parameters for the material law. These latter are calibrated with the walls A1 and C1 respectively, chosen as references. These laws are assumed to be valid for all specimens implementing the same type of units. As the spandrels behave differently to the piers [8], a particular material law is used for the corresponding elements. Finally, a static or dynamic analysis is performed and the experimental response is compared to the numerical predictions through the force-displacement curve.

The determination of the parameters of the material law is crucial. Some of them (E, G, ρ, f_m, f_{v0}, f_{vm} and μ) can be assessed based on the data and outcomes of Chapters II and III. A first guess is made for some others (k_{sec}/k_{el}, k_0, α_T, β_T, γ_T, α_{PF}, β_{PF}, γ_{PF}, δ_{PF}, $\beta_{E,T3}$, $\beta_{E,T4}$, $\beta_{E,PF}$, $Mix\,SN$ and $Mix\,DX$), using an example (see Annex C). These values have to be validated for the current masonry by a sensitivity study. The drift capacities ($\delta_{3,T}$, $\delta_{3,PF}$, $\delta_{4,T}$ and $\delta_{4,PF}$) depend on the studied masonry and are calibrated thanks to the measurements related to wall A1 or wall C1, except for the ultimate drift ($\delta_{5,T}$ and $\delta_{5,PF}$) which values are recommended in the Eurocodes [116]. A last parameter governs the choice of the criterion for the verification of the shear resistance. Different criteria are available and define a strength domain (see [19]) which depends on the geometry, the compression level and the properties of the masonry. The criterion producing the minimum strength has to be chosen.

IV.3.1 Static cyclic tests on simple walls including specific details

IV.3.1.1 Simple wall without any specific details

The geometry of specimen A1 is illustrated in Figure II.1 and is chosen as the first reference specimen. The numerical model is a simple beam of 2.800 m high defined by two 2D-nodes. The cross-section of the beam is 3.000 m × 0.138 m. A cyclic analysis with displacement controlled is performed. The values of the displacement are obtained by peak picking on the experimental signal corresponding to the time-history of the horizontal displacement measured at the top of the wall with respect to its base. The results of the numerical simulations are compared to the experimental force-displacement curve in Figure IV.3, after the calibration of the material law (see below).

These curves are in good agreement, showing a relevant reproduction of the overall response of the wall by TREMURI. The graph showing the initial response in Figure IV.3 highlights that the used parameters lead to a correct estimation of the initial stiffness of the wall. In particular, the increase of damage level is well caught, as identified by the circles in Figure IV.3 (full response). The failure mode is also in accordance with the experimental observations, namely a mix between shear and bending failures. The maximum shear capacity is however slightly underestimated. The relative difference is about $+1.2$ % and -7.5 % for negative and positive drifts respectively. This difference is certainly a consequence of the distribution of the vertical compression. The compression is introduced in the model thanks to a concentrated load applied to the node located at the top of the beam, assuming therefore an uniform distribution. On the contrary, the compression was distributed along the length of the wall during the experimental tests and the measurements show a non-uniform distribution.

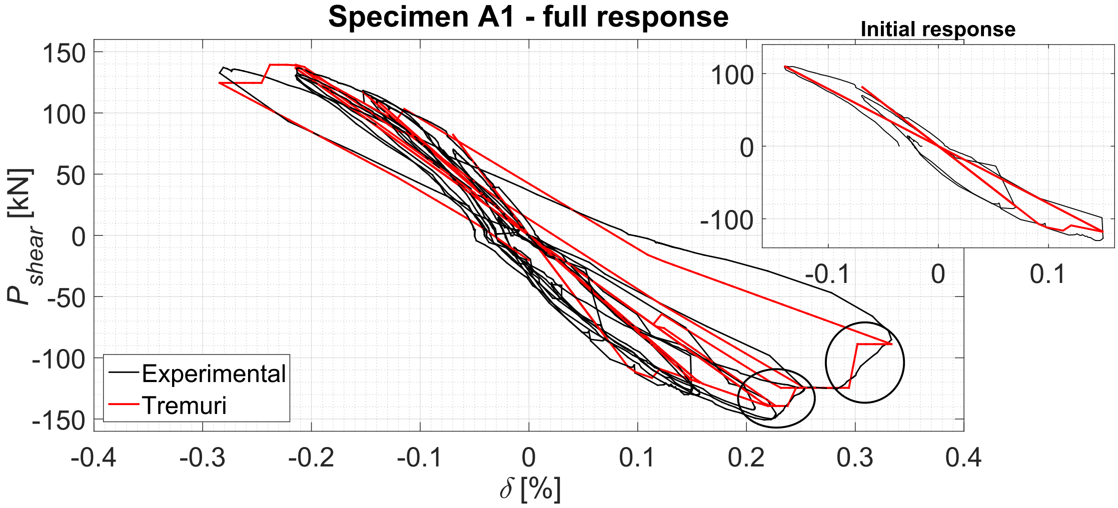

Figure IV.3: TREMURI - Comparison of numerical predictions and experimental measurement (Wall A1)

Table IV.1: TREMURI - Parameters of the material law related to specimen A1

Param.	Value	Param.	Value	Param.	Value	Param.	Value
E	$1.33 \cdot 10^9$	$\delta_{3,PF}$	0.00260	α_{PF}	0.8	$\beta_{E,3}$	0.825
G	$3.03 \cdot 10^8$	μ	0.4	β_{PF}	0.8	$\beta_{E,4}$	0.500
ρ	850	k_{sec}/k_{el}	1.850	γ_{PF}	0.5	$\beta_{E,PF}$	0.850
f_m	$3.90 \cdot 10^6$	k_0	0.700	δ_{PF}	0.6	$Mix\,SN$	0.950
f_{v0}	$3.00 \cdot 10^5$	elem. type	0	$\delta_{4,T}$	0.00135	$Mix\,DX$	1.250
f_{vm}	$5.85 \cdot 10^5$	α_T	0.8	$\delta_{4,PF}$	0.00320		
verif. crit.	2	β_T	0.8	$\delta_{5,T}$	0.00400		
$\delta_{3,T}$	0.00110	γ_T	0.0	$\delta_{5,PF}$	0.00800		

Concerning the material law, the calibrated parameters are tabulated in Table IV.1. The parameters E et G correspond to the elastic and shear moduli derived from the experimental tests and divided by the ratio k_{sec}/k_{el}. The first guess of this latter is 2, but it is set to 1.85 for the studied type of masonry. The influence of this ratio is shown in Figure IV.4. The main difference is in terms of drifts and slope of the curve when the displacement increases. The parameters governing the residual resistances have also to be changed. The first guess values indeed underestimate them, as illustrated in Figure IV.5. The parameter γ_{PF} related to the hysteric response in bending is modified to improve the numerical predictions with respect to the unloading phase (see Figure IV.6). The other parameters influencing the elasto-plastic phase, the hysteric response and the interaction zone (k_0, α_T, β_T, γ_T, α_{PF}, β_{PF}, $Mix\,SN$ and $Mix\,DX$) follow the values given in the example. The density of the masonry ρ and the compressive and shear strengths (f_m, f_{v0}, f_{vm} and μ) are taken from the experimental campaign (see Table II.1). The values for the drift capacities ($\delta_{3,T}$, $\delta_{3,PF}$, $\delta_{4,T}$ and $\delta_{4,PF}$) and the modified parameters described here above result from a calibration by trial and error.

In terms of drift capacity and residual resistance, the comparison of the considered type of masonry with the traditional type studied in [19] leads to the conclusions that the studied masonry exhibits a higher stiffness and strength, but has a more brittle behaviour.

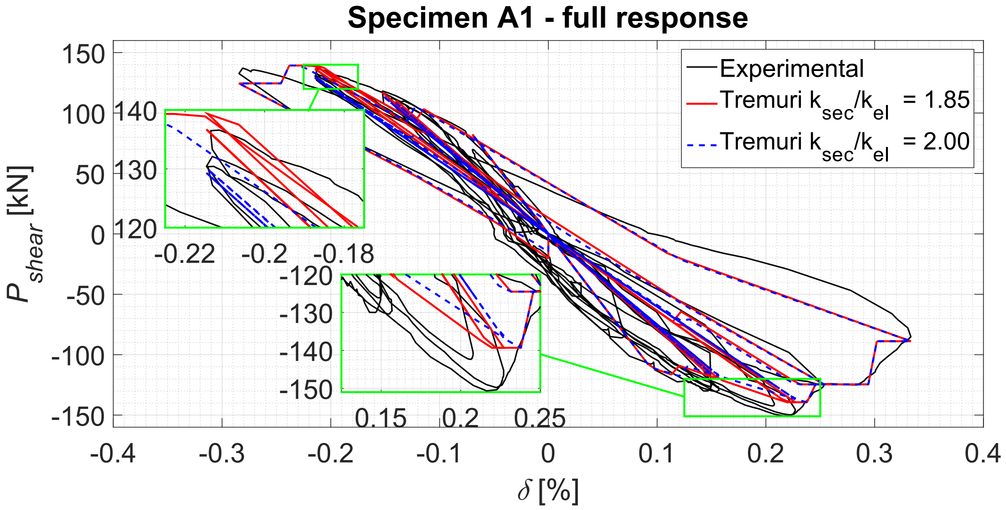

Figure IV.4: TREMURI - Influence on the numerical response of the k_{sec}/k_{el} ratio

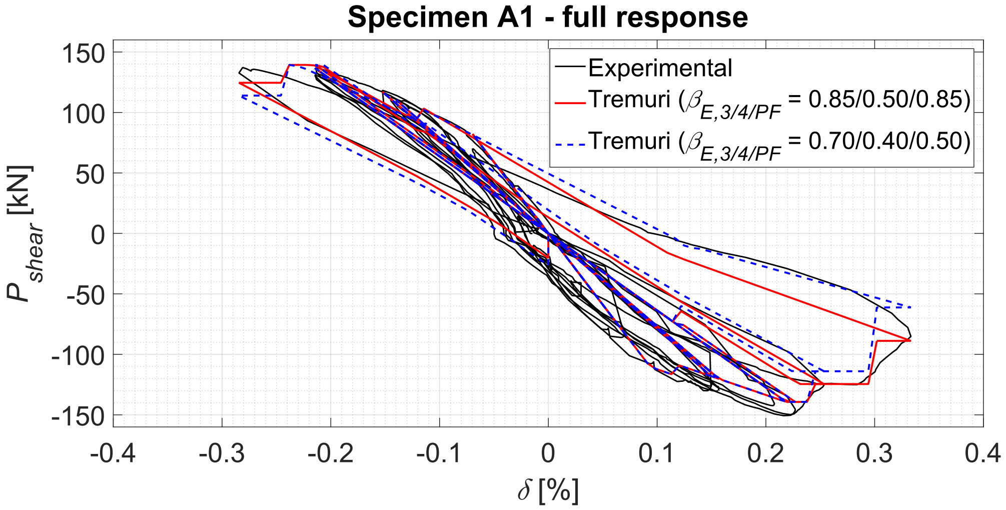

Figure IV.5: TREMURI - Influence on the numerical response of the parameters $\beta_{E,T3}$, $\beta_{E,T4}$ and $\beta_{E,PF}$

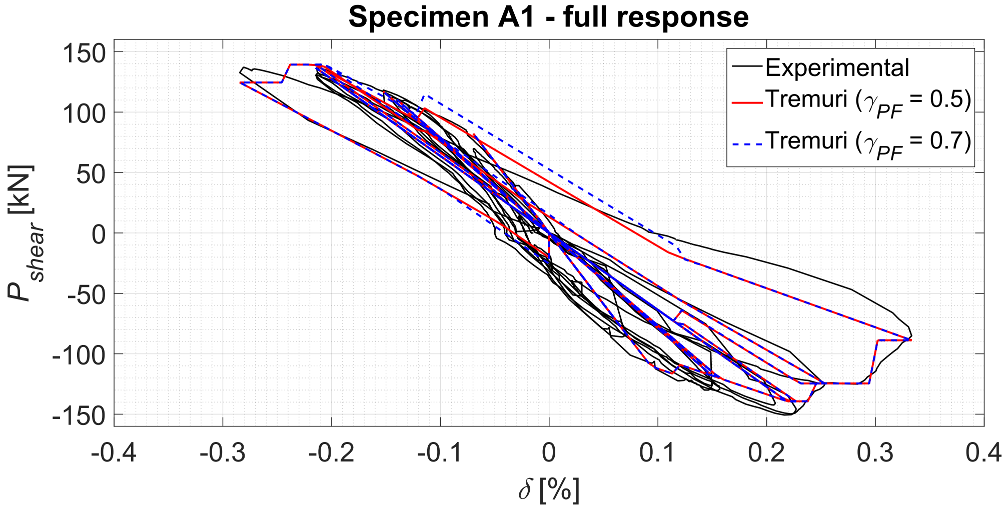

Figure IV.6: TREMURI - Influence on the numerical response of the parameter γ_{PF}

Additional investigations on the influence of the parameters of the material law derived from the experiments have been carried out. To this purpose, a numerical analysis is performed by considering the values given in Table IV.1 and by changing one parameter at a time (± 20 %). First, the elastic and shear moduli mainly affect the elasto-plastic phase with the slope of the curve. The higher the moduli, the higher is the slope (Figure IV.7). A reduction of 20 % of both moduli also leads to a slight decrease of the maximum horizontal shear (from - 1.4 % to 2.6 %). Then, the model response is highly sensitive to the parameters governing the shear and bending resistances (f_m, f_{v0} , f_{vm} and μ). Indeed, a variation of ± 20 % involves significant changes in the numerical results: for instance, a larger compressive strength makes the drift capacity of the model more dependent on the shear response, involving lower drift limits and reducing the strength in this case (see Figures IV.8). Finally, the drift limits only influence the length of the plateau and the damage level.

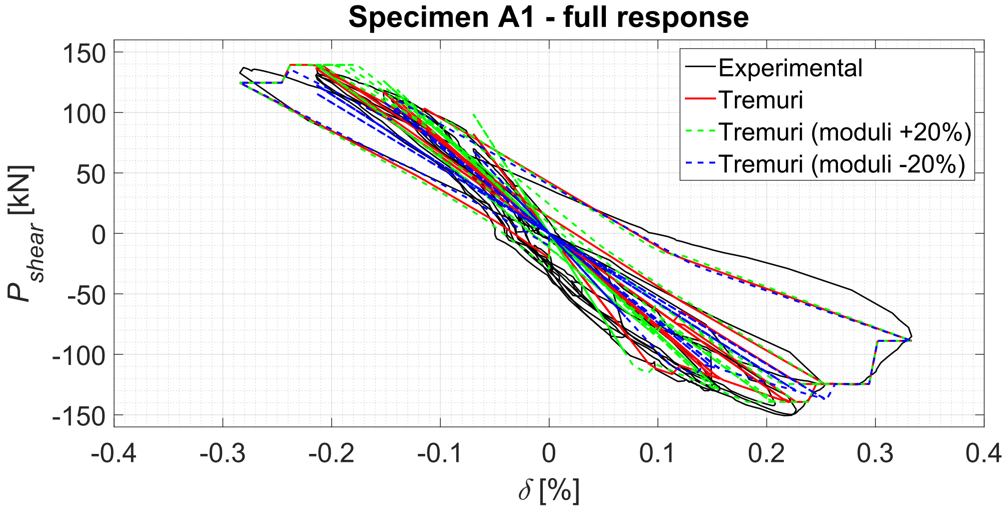

Figure IV.7: TREMURI - Influence on the numerical response of the E and G moduli

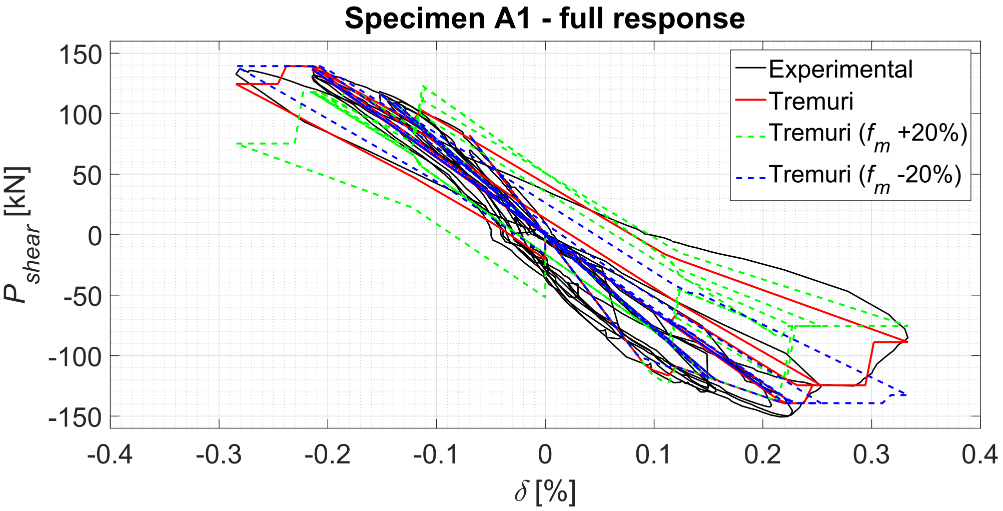

Figure IV.8: TREMURI - Influence on the numerical response of the parameters f_m

IV.3.1.2 Walls with acoustic layers

The walls including soundproofing rubber devices (walls A2/B2, see Figure IV.9 (a)) can be modelled according to two different philosophies. The first one is to represent explicitly the different components of the specimen, namely the rubber layers and the masonry wall. In this case, there are three beams elements (3-element model, Figure IV.9 (b)). The middle element is the masonry wall and its behaviour is characterised by the material law defined in Table IV.1, since it is the same panel as specimen A1. The beams at the bottom and top of this element correspond to the rubber layers. Their elastic and shear moduli are obtained from the experimental results and the drift limits are defined such as these elements remain in the elastic phase. The second possibility is to consider the different components as a whole modelled by a single beam element with equivalent properties (equivalent element model, Figure IV.9 (c)). In this case, the parameters are given in Table IV.2 and result from a calibration by trial and error. The main differences concern the moduli and the drift limits. It is also worth noticing that the compressive strength is halved in both approaches because of the interactions between the masonry and the rubber.

The numerical results are compared to the experimental measurements in Figure IV.10 to Figure IV.13, for the specimens A2 and B2 respectively.

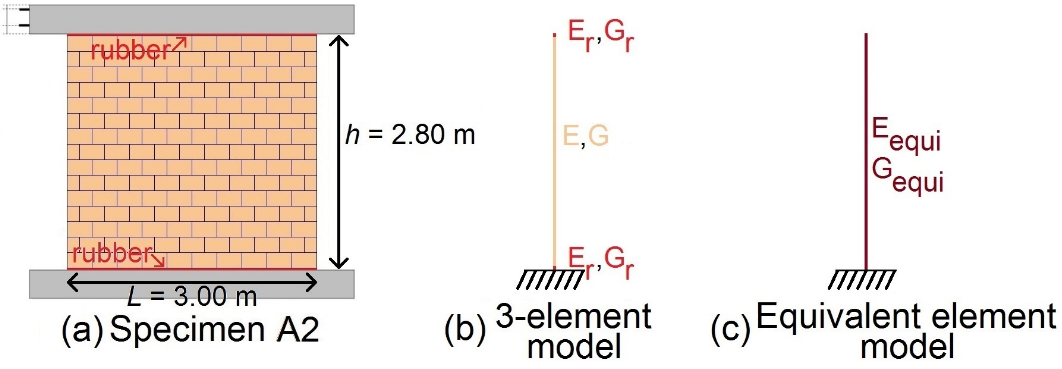

Figure IV.9: TREMURI - Models for the specimens with rubber

Table IV.2: TREMURI - Material law for walls A2 and B2 (equivalent element)

Param.	Value	Param.	Value	Param.	Value	Param.	Value
E	$3.32 \cdot 10^8$	$\delta_{3,PF}$	0.007500	α_{PF}	0.800	$\beta_{E,T3}$	0.825
G	$1.11 \cdot 10^8$	μ	0.4	β_{PF}	0.800	$\beta_{E,T4}$	0.500
ρ	850	k_{sec}/k_{el}	1.850	γ_{PF}	0.500	$\beta_{E,PF}$	0.850
f_m	$1.95 \cdot 10^6$	k_0	0.480	δ_{PF}	0.600	Mix SN	0.950
f_{v0}	$3.00 \cdot 10^5$	elem. type	0	$\delta_{4,T}$	0.002500	Mix DX	1.250
f_{vm}	$5.85 \cdot 10^5$	α_T	0.800	$\delta_{4,PF}$	0.007750		
verif. crit.	2	β_T	0.800	$\delta_{5,T}$	0.004000		
$\delta_{3,T}$	0.002000	γ_T	0.00	$\delta_{5,PF}$	0.008000		

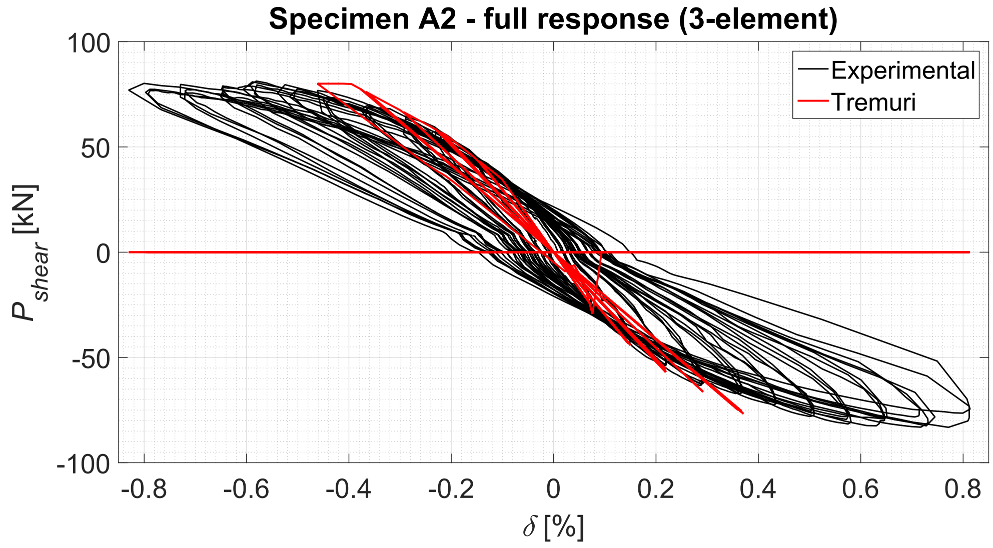

Figure IV.10: TREMURI - Comparison between the numerical and experimental results

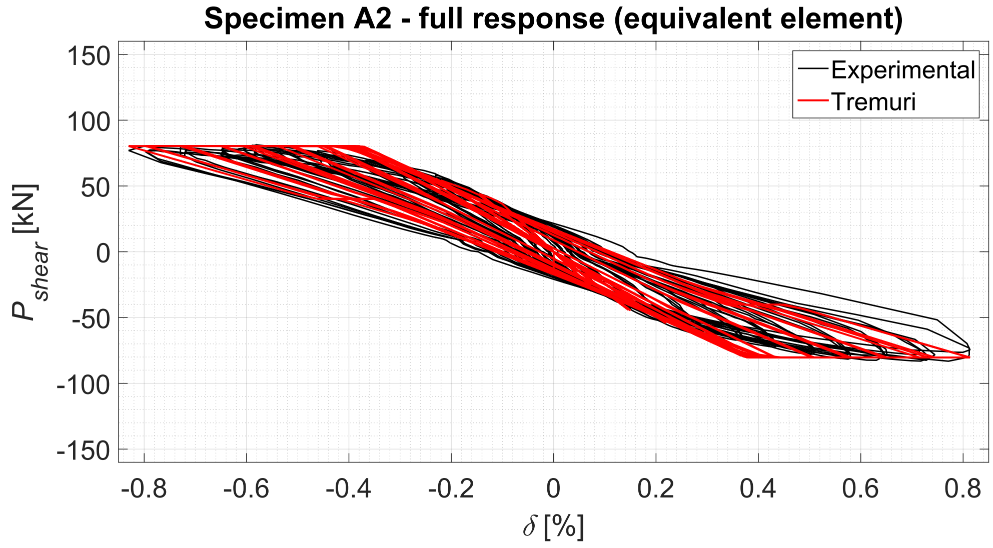

Figure IV.11: TREMURI - Comparison between the numerical and experimental results

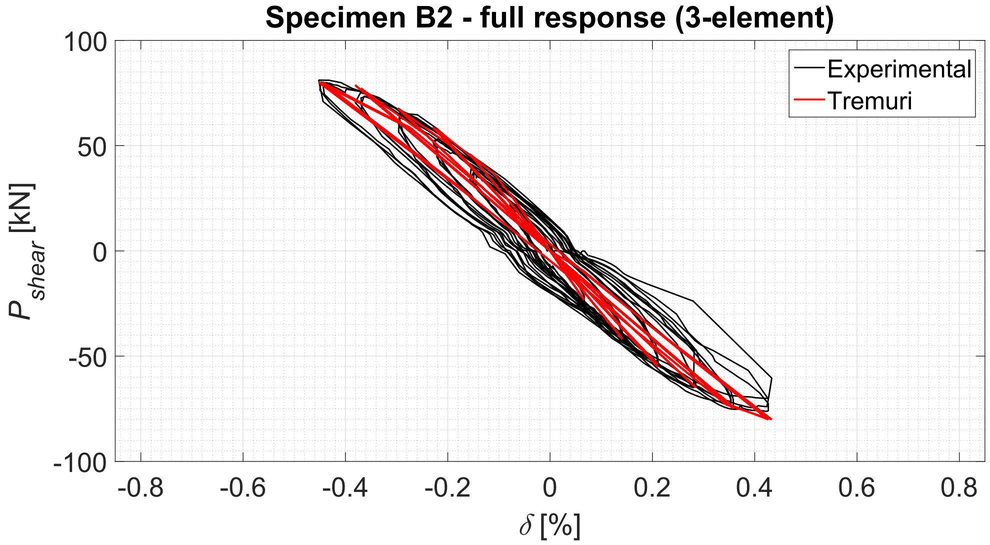

Figure IV.12: TREMURI - Comparison between the numerical and experimental results

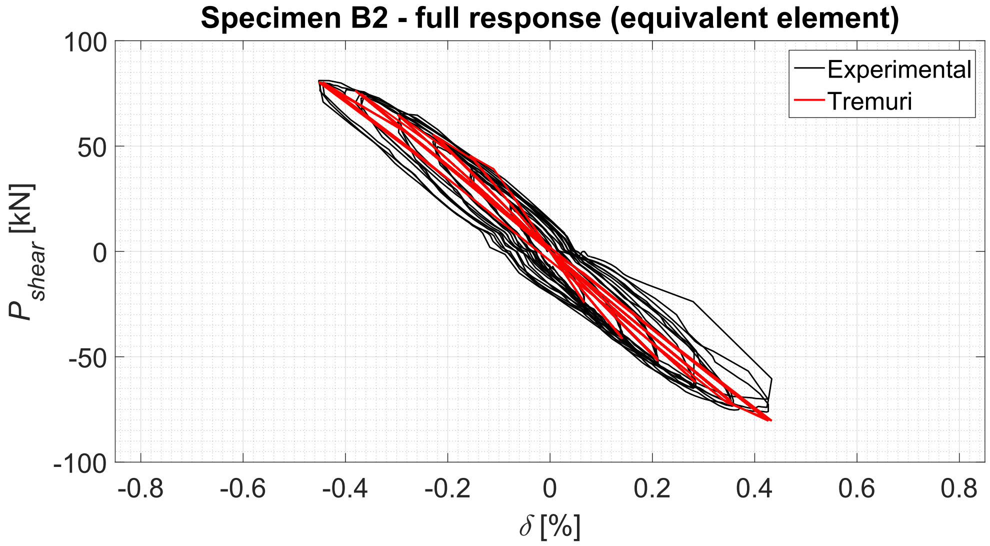

Figure IV.13: TREMURI - Comparison between the numerical and experimental results

Both models correctly predict the initial response of the specimens. In terms of maximum horizontal shear, the relative difference is limited to 5.5 %. Nevertheless, the stiffness of the model seems to decrease slower than that observed experimentally in the case of wall A2. The explanation lies in the vertical crack initiated during the compression phase of the experimental test (see Section II.2.3). Such a damaging cannot be taken into account with the macro-modelling approach, but has anyway to be avoided in practice. The wall B2 does not present this problem and the deterioration of the stiffness is well captured. Another issue is observed for the wall A2 when the drift is larger than 0.45 %, in the case of the 3-element model. There is a sudden jump from DL2 to DL5, meaning the collapse of the wall. Further investigations have revealed implementation flaws in the cyclic analysis for this specific case.

This is confirmed by performing a monotonic analysis with the 3-element model. The results of the monotonic analysis are in accordance with the experimental measurements and the predictions of the equivalent element model (see Figure IV.14). Thus, the observed problem is not due to the model, but is linked to the type of analysis.

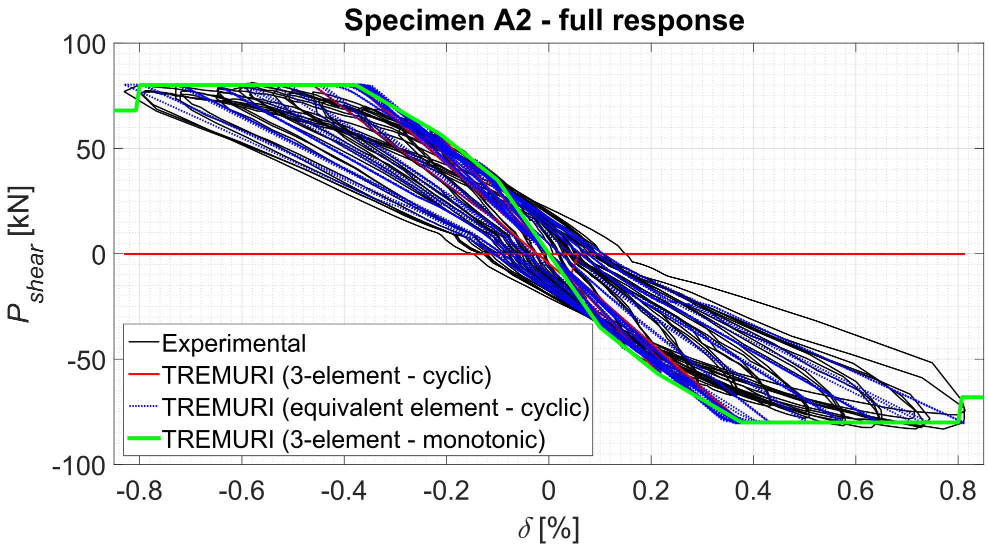

Figure IV.14: TREMURI - Numerical predictions for wall A2

IV.3.1.3 Walls with an opening

Two walls (A3 and B3) with an opening have been tested, but only the specimen B3 is modelled in TREMURI. The other has been rejected because of the local crushing of a masonry block directly supporting the RC lintel (see Section II.2.3). This type of failure is effectively impossible to consider with a modelling at the macro-scale. Discussions focus on the material law for the spandrel element and on the geometry of the piers.

On the one hand, the material law determined with the reference specimen A1 is affected to both piers. Only the parameters E ($1.98 \cdot 10^9$) and G ($5.49 \cdot 10^8$) are modified to be in accordance with the experimental results. Regarding the spandrel, additional modifications are required as this part of the masonry panels usually exhibits larger drift limits. Recommended values are given in [2]. No difference between the shear and bending behaviours is considered in terms of drifts. The modified values are tabulated in IV.3. Figure IV.15 compares the numerical results obtained by considering, for the spandrel element, the same material law as the law associated to the piers (in green) and those by using the values given in [2] (in red). The geometry of the specimen is automatically generated by TREMURI (see under). In the case of identical laws for piers and spandrels, a loss of resistance is observed, highlighted with a zoom-in. Furthermore, the model predicts heavy damage to the spandrel (DL4) which is inconsistent with the experimental observations. The modifications of the drift limits fix the problem related to the damage level and better target the maximum shear.

It is worth noticing that the experimental and numerical curves have clear differences, especially for negative drift. These differences are explained by experimental issues: a horizontal displacement has been measured during the compression phase. Then, the cyclic-test was performed with a displacement varying around this initial deflection. In the numerical modelling, the horizontal displacement resulting from the compression is not considered.

Table IV.3: TREMURI - Modified parameters of the material law related to the spandrel element (specimen B3)

Param.	Value	Param.	Value	Param.	Value	Param.	Value
$\delta_{3,T}$	0.012000	$\delta_{4,T}$	0.020000	$\delta_{5,T}$	0.026000	$\beta_{E,T3}$	1.00
$\delta_{3,PF}$	0.012000	$\delta_{4,PF}$	0.020000	$\delta_{5,PF}$	0.026000	$\beta_{E,T4}/\beta_{E,PF}$	0.800

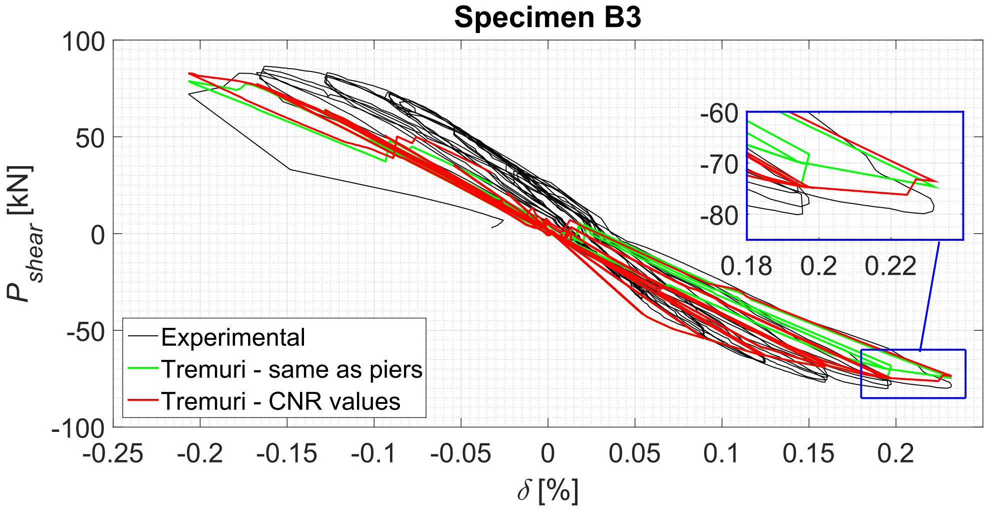

Figure IV.15: TREMURI - Influence of the drift limits and residual resistances for the spandrel (Wall B3)

On the other hand, different options for the height of the piers are worth being considered. Three variants are studied in the following, corresponding to the well known simplified models "Strong Spandrels - Weak Piers" (SSWP, see [122]) and "Weak Spandrel - Strong Piers" (WSSP) and to the geometry automatically defined by the TREMURI program. These variants are illustrated for a whole facade in Figure IV.16, taken from [57].

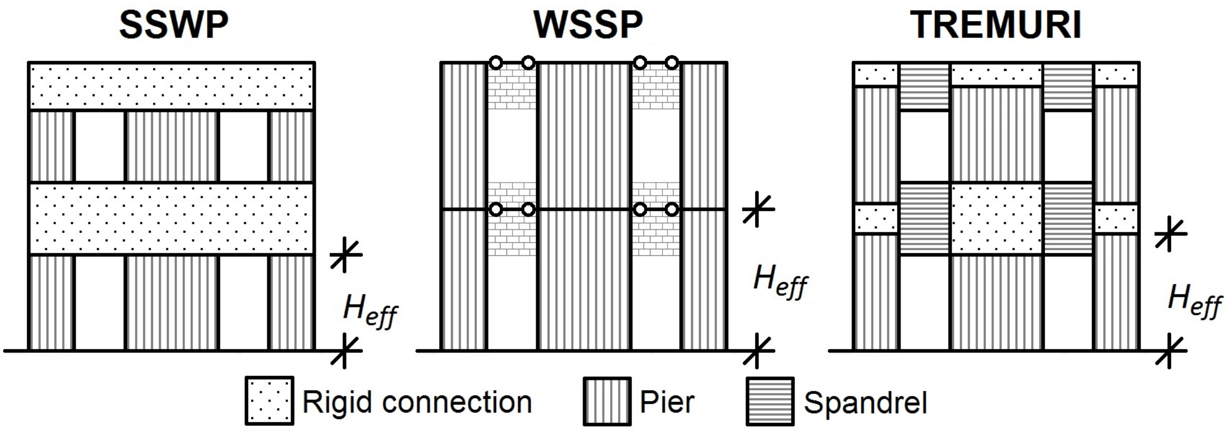

Figure IV.16: TREMURI - Studied variants for the geometry

A comparison of these 3 options is given in Figure IV.17. In terms of maximum shear, the limitation of the height of the pier to the height of the opening (SSWP model) provides the best results, as shown in Table IV.4. The presence of the RC lintel and its support length justify the assumption of a strong spandrel. Concerning the damage state, the piers remain in DL 3, while test observations suppose a higher damage level. Further investigations are required and a possible explanation is that the same mechanical properties are defined for both piers, whereas their length is different. Consequently, the shear modulus should be different, as concluded in Chapters II and III. Even though, the analysis of the overall response of a wall with an opening thanks to an equivalent frame model leads to relevant results.

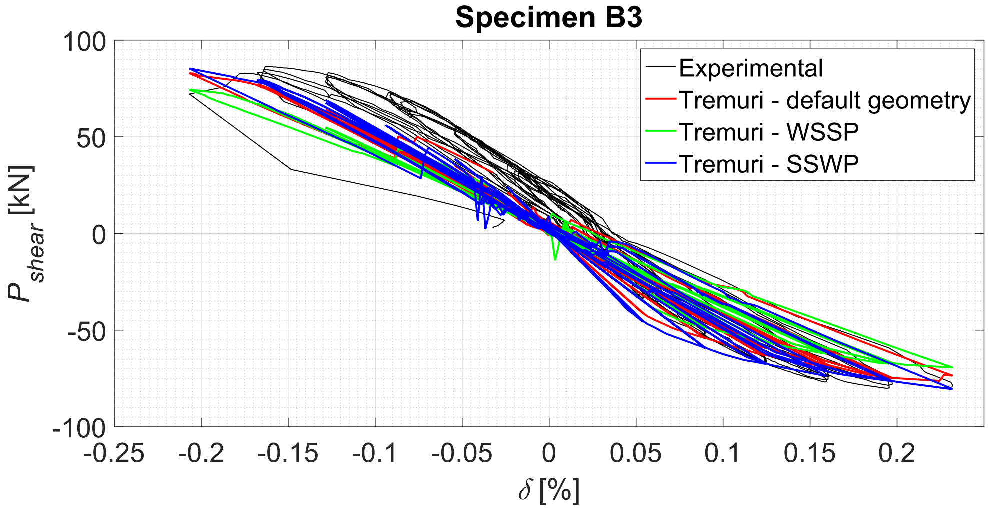

Figure IV.17: TREMURI - Influence of geometry of the piers (Wall B3)

Table IV.4: TREMURI - Relative difference [%] in terms of maximum shear (wall B3)

Geometry	Automatic.	WSSP	SSWP
Negative drift	-4.14 %	-13.93 %	-1.33 %
Positive drift	-4.84 %	-13.51 %	+0.56 %

IV.3.2 Shake table tests on simple walls

A dynamic analysis is performed in TREMURI, using the acceleration signals recorded at the level of the table during the shakes. The simple URM walls are represented by a single non-linear beam element and the additional mass is considered as punctual and acting on the node located at the top of the element. The model neglects therefore the distance between the top of the URM wall and the centroid of the additional mass as well as the rotary inertia of this latter. The parameters of the material law are defined in Table IV.1, except for the elastic and shear moduli for which values of the Timoshenko beam identification are used (see Chapter III).

Figures IV.18 and IV.19 compare the results of the analysis with the experimental force-displacement curve, for the long and short walls respectively. In both cases, the test corresponding to the highest in-plane acceleration is considered. The model predicts a plateau for the horizontal shear at 25.8 kN for the long wall and at 8.2 kN for the short wall, close to the experimental observations. Regarding the drift values, differences appear between the numerical analysis and the experiments. The maximum drift is underestimated for the short wall, while the increasing damage level of the long wall leads to a larger maximum drift and to its failure (DL5). These observations can be explained by the modelling of the mass and by differences in terms of global behaviour. Indeed, a pure rocking behaviour was observed during the experimental shakes, especially for the short wall, whereas the model assumes an interaction between rocking-bending and shear behaviours.

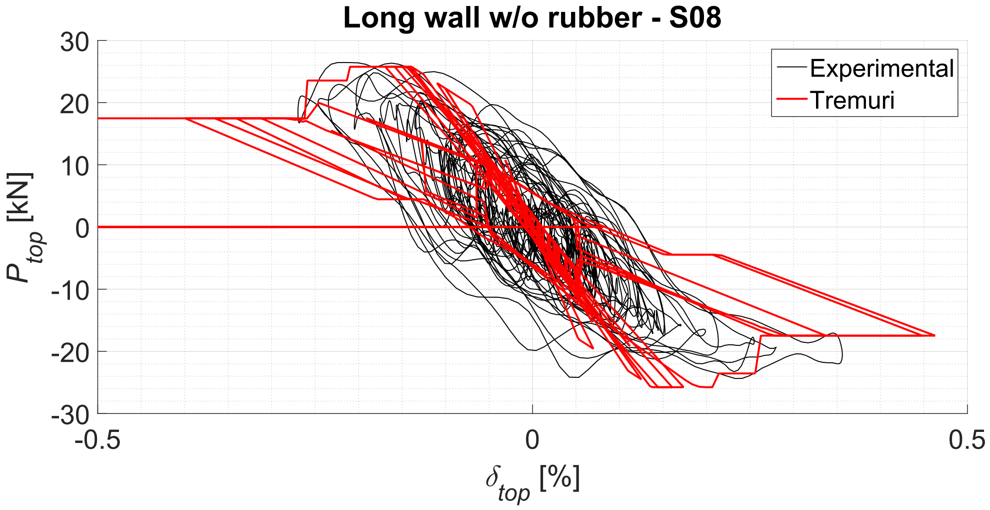

Figure IV.18: TREMURI - Comparison of numerical predictions and experimental measurement (Long wall without rubber)

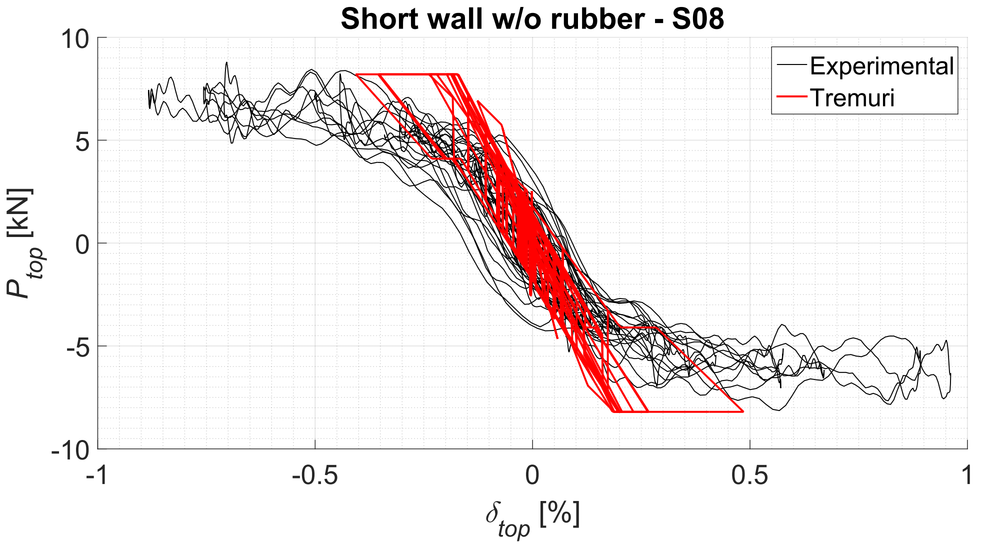

Figure IV.19: TREMURI - Comparison of numerical predictions and experimental measurement (Short wall without rubber)

IV.3.3 Static cyclic tests on T-shaped walls

The model for specimens with a non-rectangular cross-section is drawn in Figure IV.20. The section of the specimen subjected to in-plane loading is the shear wall and is modelled by a non-linear beam element. This element is defined between two 2D nodes and is identified as *pier 1*. The beam element for *pier 2* uses 3D nodes and corresponds to the perpendicular section, i.e. the flange. Both piers are connected together by an elastic beam between the nodes at their top. A large elastic modulus is chosen for the elastic beam in order to model the rigid connection between the shear wall and the flange. A displacement controlled analysis is performed.

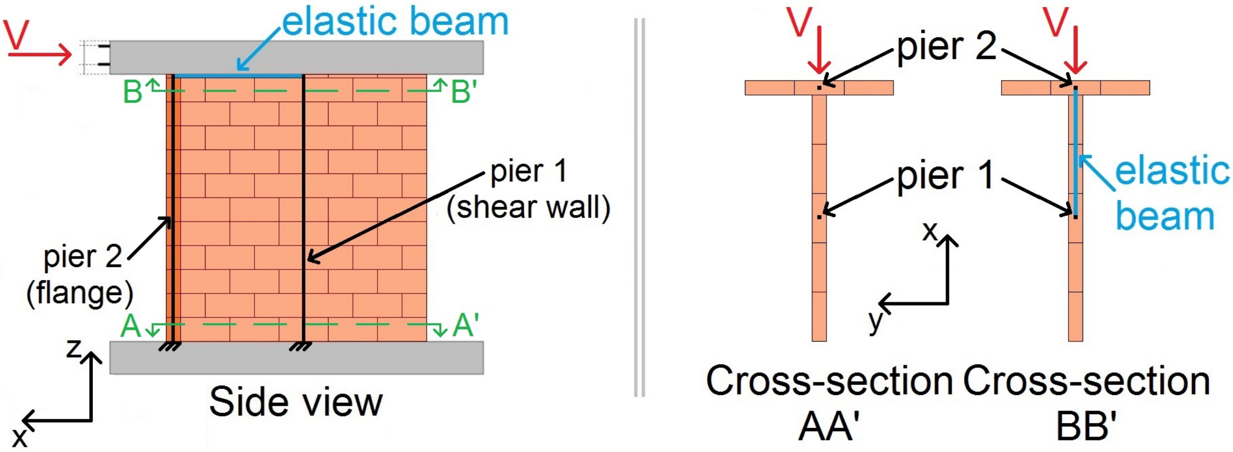

Figure IV.20: TREMURI - Models for the specimens with a non-rectangular cross-section

The same material law is defined for all the specimens (C1-3) and its parameters results from a calibration by trial and error based on the wall C1. The values of the parameters are given in Table IV.5. The elastic modulus is taken as the mean value of the three experimental results (see Table II.9). The shear modulus is also derived from the experiments and varies from one specimen to another due to its dependence on the compression level. It has also to be modified to target the right initial stiffness, as illustrated in Figure IV.21. This latter modification seems to be required because of the neglection of the flange. Indeed, TREMURI only considers the in-plane behaviour of the walls and the flange is perpendicular to the imposed displacement. The parameters related to the material and mechanical properties are given in Table II.6. Those defining the elasto-plastic phase, the hysteretic response, the residual resistance and the interaction area are set to the same values as the parameters of the material law for the wall A1. Both walls A1 and C1 effectively implement the same masonry bonding. The values for the drift limits $\delta_{3,T}$, $\delta_{3,PF}$, $\delta_{4,T}$ and $\delta_{4,PF}$ are calibrated, while $\delta_{5,T}$ and $\delta_{5,PF}$ are recommended in the Eurocode 8 [116].

The sensitivity of the model response to the parameters of the material law has been studied. Only those which have a significant influence are discussed. First, an increase/decrease of 20 % of the elastic and shear moduli (E, G) modifies the slope of the envelope, without any change for the maximum shear. Then, the maximum shear is influenced by the shear strength f_{vm}, but not by the compressive strength f_m. This translates a larger dependence of the model on the shear failure. The plateau indeed slightly increases with the shear strength (+4.59 % when f_{vm} is 20 % higher). Similar conclusions are observed for the drift limits: for instance, a variation of 20 % of $\delta_{3,T}$ affects the length of the plateau, while this latter is not shortened nor lengthened when $\delta_{3,PF}$ increases or decreases of the same percentage. Finally, the parameter for residual resistance β_{E3} has consequences on the magnitude of the jump observed for the largest positive drift (see below). The others parameters governing the residual resistance have no influence as the damage level predicted by the model is limited to DL3 in shear.

Table IV.5: TREMURI - Parameters of the material law related to specimen C1

Param.	Value	Param.	Value	Param.	Value	Param.	Value
E	$1.93 \cdot 10^9$	verif. crit.	2	β_T	0.800	$\delta_{5,T}$	0.004000
G (C1)	$6.45 \cdot 10^8$	$\delta_{3,T}$	0.002600	γ_T	0.000	$\delta_{5,PF}$	0.008000
G (C2)	$8.58 \cdot 10^8$	$\delta_{3,PF}$	0.003500	α_{PF}	0.800	β_{E3}	0.825
G (C3)	$1.38 \cdot 10^9$	μ	0.4	β_{PF}	0.800	β_{E4}	0.500
ρ	850	k_{sec}/k_{el}	1.850	γ_{PF}	0.500	β_{PF}	0.850
f_m	$4.40 \cdot 10^6$	k_0	0.700	δ_{PF}	0.600	Mix SN	0.950
f_{v0}	$3.00 \cdot 10^5$	elem. type	0	$\delta_{4,T}$	0.003000	Mix DX	1.250
f_{vm}	$6.75 \cdot 10^5$	α_T	0.800	$\delta_{4,PF}$	0.006500		

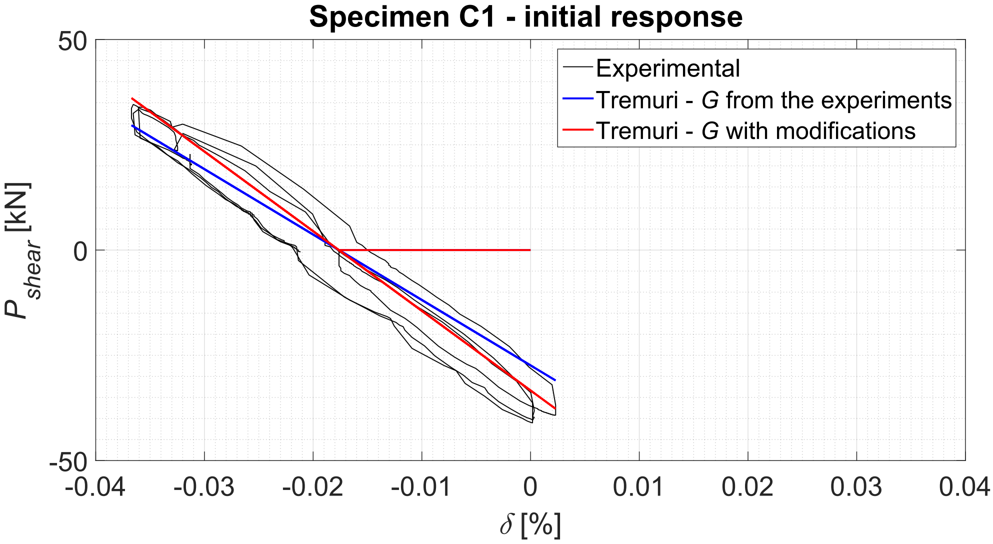

Figure IV.21: TREMURI - Comparison of the numerical predictions and experiment measurements (Initial stiffness - Wall C1)

Figures IV.22, IV.23 and IV.24 provide the results of the numerical analysis and compare them to the experimental force-displacement curves for the specimens C1, C2 and C3 respectively. The global response is well predicted by the numerical model at the macro-scale. Two main discrepancies are however pointed out.

First, the maximum shear is underestimated, as observed in Table IV.6. The underestimation depends on the compression level and the load direction. The contribution of the flange to the shear strength is neglected in TREMURI, explaining (i) why the numerical results are lower and (ii) why the relative difference increases with the compression level for negative drifts, while it remains approximately the same for positive drifts:

(i) The cross-section of a T-shaped wall is asymmetric due to the presence of the flange and, under the same shear load, the compressive length differs with the load direction. The compressive length is longer when the flange is decompressed (negative drifts) because the distance between the centroid and the most compressed side is longer than the half length. In comparison to a rectangular wall of the same geometry as considered in TREMURI, the shear capacity is thus increased. More details are given in Chapter V. When the flange is over-compressed, the centroid is closer to the most compressed side, but the flange takes part to the shear resistance. This contribution overcomes the effects of a reduction compressive length.

(ii) The relative difference between the numerical and experimental results increases with the compression load since the part of the flange influenced by the compression depends on the compression level (see Section II.3). This has consequences on the position of the centroid and, therefore, on the shear capacity.

Table IV.6: TREMURI - Relative difference [%] in terms of maximum shear (T-shaped walls)

Specimen	C1	C2	C3
Negative drifts	-16.49 %	-24.54 %	-22.89 %
Positive drifts	-15.64 %	-15.97 %	-13.08 %

Second, the damage level forecast by the model is DL3 for the wall C1 and to DL2 for the walls C2 and C3. However, a shear collapse was observed during the experimental campaign and corresponds to a damage level closer to DL4, in the light of the resistance loss in Figure IV.23 (circle) for instance. A possible explanation is the absence of cyclic deterioration of the walls in the material law. Indeed, the model behaves on the same force-displacement curve when several cycles are imposed with identical displacement level, whereas a progressive damaging was observed during the experiments. Another explanation is the dependence on the compression level of the drift capacity. The higher the compression, the smaller the drift capacity. The same drift limits are however used in the material law defined for all specimens.

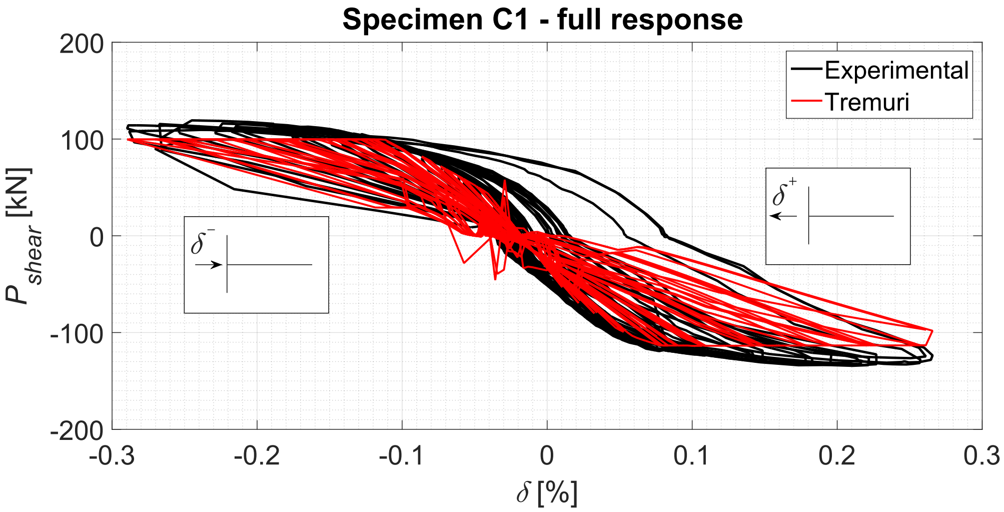

Figure IV.22: TREMURI - Comparison of numerical predictions and experimental measurement (Wall C1)

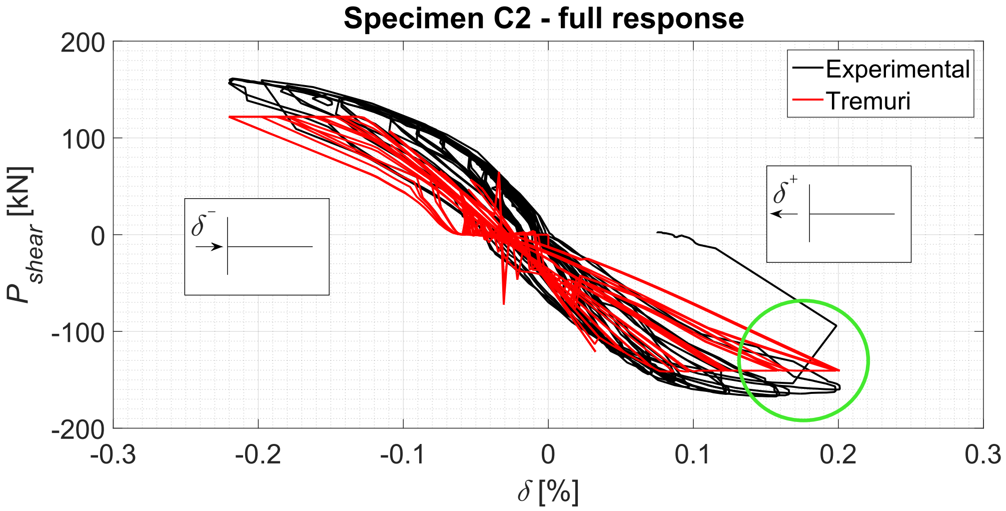

Figure IV.23: TREMURI - Comparison of numerical predictions and experimental measurement (Wall C2)

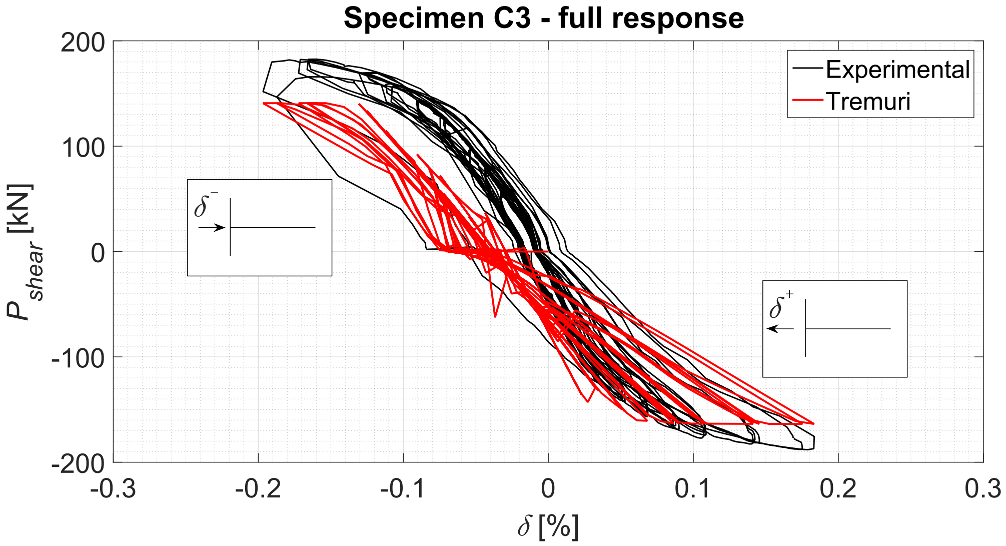

Figure IV.24: TREMURI - Comparison of numerical predictions and experimental measurement (Wall C3)

Note that the results of the analysis in TREMURI of walls including rubber devices and the frames with T- and L-shaped piers tested on the shake table are not presented because their interpretation requires more time.

IV.4 Conclusions

The numerical analysis of URM sub-structures by means of the equivalent frame approach implemented in TREMURI highlights that the use of a model with macro-elements provides relevant predictions of the overall response. A first advantage of this modelling strategy is the low computational demand. For instance, the numerical simulations in static conditions last between two and thirty seconds, the bounds corresponding to the cyclic analysis of the simple wall and of the specimen with an opening respectively. The dynamic analysis on the short wall without rubber has a duration of about ninety seconds. Another advantage is the easy definition of the input parameters. These latter are the material law and the geometry.

The definition of the parameters of the material law is the main challenging task when modelling a new type of masonry. First, several parameters should be provided by the producers or determined by the recommendations of the Eurocode 8, like the density ρ and the compressive and shear strengths, f_m, f_{v0} and f_{vm} and the coefficient of friction μ. Then, the parameters corresponding to the elasto-plastic phase (1), the hysteretic response (2), the residual resistance (3) and the interaction zone (4) can be set to the values recommended in Table IV.7, for the studied type of masonry bonding. This bonding consists in thin-layered glue-mortar joints and a tongue-and-groove system for the head joints, assembling clay masonry units. Finally, equivalent mechanical properties have to be used for the elastic and shear moduli and a calibration is necessary for the drift limits. For the considered masonry bonding, the equivalent elastic modulus E can be defined with respect to the compressive strength, namely $E = K_E f_m$ as expressed in the Eurocode, with $K_E = 600$ to 800. In particular, the equivalent shear modulus G can be taken as a percentage of E and depends on the compression level. Suggestions for the value of the percentage require more investigations. The calibration of the drift limits has been performed for two types of units and is only relevant for these units. Additional investigations should validate the obtained values.

Table IV.7: TREMURI - Recommended parameters for the studied type of masonry

(1)		(2)		(2)		(3)		(4)	
Param.	Value	Param	Value	Param.	Value	Param.	Value	Param.	Value
k_{sec}/k_{el}	1.850	α_T	0.800	α_{PF}	0.800	β_{E3}	0.825	Mix SN	0.950
k_0	0.700	β_T	0.800	β_{PF}	0.800	β_{E4}	0.500	Mix DX	1.250
		γ_T	0.000	γ_{PF}	0.500	β_{PF}	0.850		
				δ_{PF}	0.600				

Regarding the geometry of the specimens, the automatic meshing of TREMURI provides a suitable modelling. In the case of walls with an opening, the height of the piers could be reduced if the masonry spandrel is connected to RC elements (slab and lintel) with a efficient connection.

From the outcomes of the modelling of masonry structures presented in this chapter, the contribution of the walls perpendicular to the seismic action is found to be significant. The assessment of the maximum shear for single T-shaped walls in TREMURI could be improved with a due consideration for the perpendicular sections. This consideration should be accompanied by additional requirements, regarding the connections between perpendicular walls (vertical shear, etc.) especially. The importance of these sections could be mitigated in the context of a complete building.

Chapter V

Shear capacity of non-rectangular URM walls

V.1 Introduction
V.2 Compressive length for non-rectangular cross-section
V.3 Design procedure and comparison with experimental results
V.4 Conclusions

V.1 Introduction

The EN 1996-1-1 [26] provides recommendations for URM walls subjected to shear loading, for both the structural analysis and the verification at the ultimate limit state (ULS). On the one hand, specific rules are given for the masonry shear walls (§5.5.3) regarding the stiffness. This one has to be taken as the elastic stiffness of these walls, including any flanges. A flange defines an intersecting wall, or a portion of it, provided the connection between the shear wall and the flange is able to sustain the shear action and provided its buckling is prevented. Additional recommendations specify how to calculate the length of the flange, how to consider the presence of openings and how to distribute the compression and shear loading between the walls depending on the support conditions and the stiffness of the floors. On the other hand, the ULS verification is

$$V_{Ed} \quad \leq \quad V_{Rd} \tag{V.1}$$

where V_{Ed} [N] is the shear load applied to the masonry wall and V_{Rd} [N] is the design value of the shear resistance of this wall. The design value of the shear resistance is given by:

$$V_{Rd} \quad = \quad f_{vd}\, t\, l_c \tag{V.2}$$

where f_{vd} [N.mm^{-2}] is the design value of the shear strength of masonry, equal to $f_{vk0}/\gamma_M + 0.4\,\sigma_d$ with f_{vk0} [N.mm^{-2}], the characteristic initial shear strength under zero compression; σ_d [N.mm^{-2}], the design compressive stress perpendicular to the shear and γ_M [-], a partial factor of security. The parameter t [m] is the thickness of the shear wall and l_c [m] is the length of the compressed part of the wall. According to EN 1996-1-1, this compressive length should be calculated assuming a linear distribution of the compressive stresses and taking into account any openings, chases or recesses. There is no clear reference to the consideration of possible flanges in the calculation of the compressive length, even if a paragraph expresses that the connections between shear walls and flanges shall be verified for the vertical shear. The ULS verification also requires that the compressive length should remain positive (overturning) and that the vertical loading acting on the compressed part of the wall should be less than or equal to the compressive resistance (crushing).

The contribution to the shear resistance of any intersecting walls connected to the shear wall is not mentioned by the EN 1996-1-1. Therefore, the calculation of the compressive length is usually performed neglecting flanges. This conservative approach however leads to significant differences between standards predictions and experimental measurements (see Chapter II). Thus, this chapter is an attempt to improve the predictions given by the current European Standards for URM structures. To this purpose, the expression of the compressive length is developed with due consideration for any flanges. The rigorous formulation is based on simple mechanical principles and on the resistance of materials. Simplifications are then proposed and allow the determination of the compressive length by hand calculations. Finally, these developments are integrated to the design procedure in order to assess the shear resistance of the specimens described in Sections II.3 and II.5 and to compare it with the experimental measurements.

V.2 Compressive length for non-rectangular cross-section

V.2.1 Expression of the compressive length

A wall with a non-rectangular cross-section is considered in Figure V.1. The wall is subjected to an uniform vertical compression N_{Ed} [N] and a horizontal shear V_{Ed} is applied at its top. The shear wall corresponds to the section of the wall along the direction of the horizontal shear (y-direction) and has a length l_{shW} [m] and a thickness t_{shW} [m]. A part of the section perpendicular to the shear wall acts as a flange.

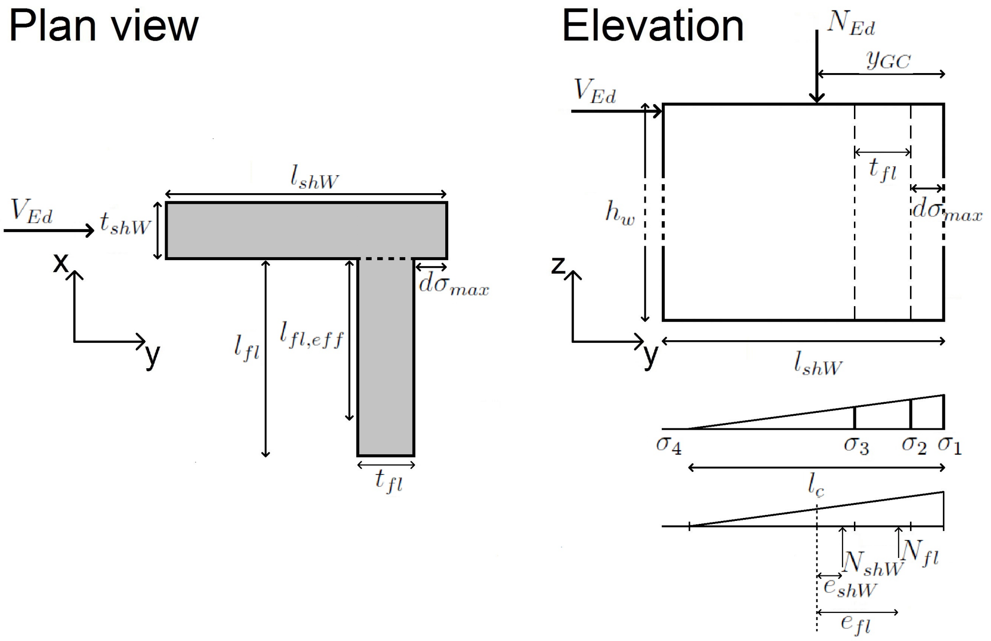

Figure V.1: Geometry of the wall with a non-rectangular cross-section

The effective length of the flange is determined according to the EN 1996-1-1. It is given by

$$l_{fl,eff} = \min \left\{ \begin{array}{c} h_w/5 \\ l_s/2 \\ h/2 \\ 6\,t_{fl} \end{array} \right. \tag{V.3}$$

where h_w [m] is the overall height of the wall, l_s [m] is the distance between shear walls connected to the perpendicular section (infinite in the considered case), h [m] is the clear height and t_{fl} [m] is the thickness of the perpendicular section. The effective length $l_{fl,eff}$ [m] is, at most, equal to the length of the perpendicular section l_{fl} [m]. The position of the flange is characterised by the parameter $d\sigma_{max}$ [m] which measures the distance from the point where the maximum vertical compressive stress is located (reference point) to the closest side of the flange. The position of the neutral axis of the wall in the y-direction with respect to the reference point is

$$y_{GC} = \frac{l_{shW}\, t_{shW}\, \frac{l_{shW}}{2} + l_{fl,eff}\, t_{tl}\left(d\sigma_{max} + \frac{t_{fl}}{2}\right)}{l_{shW}\, t_{shW} + l_{fl,eff}\, t_{tl}}. \tag{V.4}$$

The compressive length l_c is obtained by solving the equilibrium equations. Indeed, the horizontal shear V_{Ed} acting on the wall induces a bending moment M_{Ed} [Nm]. This latter is defined, in the case of a single wall, by

$$M_{Ed} = V_{Ed}\, h_w \tag{V.5}$$

and is usually expressed as a function of the vertical compression load N_{Ed}:

$$M_{Ed} = N_{Ed}\, e. \tag{V.6}$$

This is equivalent to an eccentric vertical compression N_{Ed} applied at a distance e [m] from the neutral axis of the wall. An uniform vertical compression of the wall is assumed here, but other distributions can be studied by increasing or decreasing the eccentricity e.

Masonry being considered as a material with no tensile strength, the Navier's equations are not valid and the eccentric vertical load N_{Ed} has to be balanced with a vertical force applied at a certain distance of the neutral axis of the wall. There are two contributions to this force: one coming from the shear wall, N_{shW} [N], and the other from the flange, N_{fl} [N]. They are located at a distance e_{shW} [m] and e_{fl} [m] from the neutral axis, respectively. These quantities are expressed by

$$N_{shW} = \frac{1}{2}(\sigma_1 + \sigma_4)\min(l_c\,;\, l_{shW})\, t_{shW} \tag{V.7}$$

$$e_{shW} = y_{GC} - \frac{2\sigma_4 + \sigma_1}{\sigma_4 + \sigma_1}\frac{1}{3}\min(l_c\,;\, l_{shW}) \tag{V.8}$$

$$N_{fl} = \frac{1}{2}(\sigma_2 + \sigma_3)\min\left(\max(l_c - d\sigma_{max}\,;\, 0)\,;\, t_{fl}\right) l_{fl,eff} \tag{V.9}$$

$$e_{fl} = (y_{GC} - d\sigma_{max}) - \frac{2\sigma_3 + \sigma_2}{\sigma_3 + \sigma_2}\frac{1}{3}\min\left(\max(l_c - d\sigma_{max}\,;\, 0)\,;\, t_{fl}\right) \tag{V.10}$$

where σ_i $(i = 1, \ldots, 4)$ is the compressive stress at four different locations, namely the extremities of the shear wall and at the intersections with the flange (see Figure V.1 (right)). It is positive in compression and cannot be lower than zero due to the lack of tensile strength. It is calculated as a function of the maximum compressive stress σ_{max} [N/m^2] by

$$\sigma_i = \begin{cases} \sigma_{max} & (i = 1) \\ \max\left(\frac{l_c - d\sigma_{max}}{l_c}\,;\, 0\right)\sigma_{max} & (i = 2) \\ \max\left(\frac{l_c - d\sigma_{max} - t_{fl}}{l_c}\,;\, 0\right)\sigma_{max} & (i = 3) \\ \max\left(\frac{l_c - l_{shW}}{l_c}\,;\, 0\right)\sigma_{max} & (i = 4) \end{cases}. \tag{V.11}$$

The assumption of a linear distribution of the vertical compressive stresses is made in accordance with the EN 1996-1-1 recommendation. The compressive length l_c and the maximum compressive stress σ_{max} are unknowns.

Introducing Eqs. V.7 to V.11 in the equilibrium equations, it follows

$$N_{Ed} = N_{shW} + N_{fl} = \frac{1}{2}\frac{\sigma_{max}}{l_c}\left[\bar{R} + \bar{T}\right] \tag{V.12}$$

and

$$M_{Ed} = N_{shW}\, e_{shW} + N_{fl}\, e_{fl} = \frac{1}{2}\frac{\sigma_{max}}{l_c}\left[y_{GC}\,\bar{R} - \bar{G} + (y_{GC} - d\sigma_{max})\,\bar{T} - \bar{H}\right] \tag{V.13}$$

with the groups

$$\begin{aligned}
\bar{R} &= \left[\max\left(2l_c - l_{shW}\,;\, l_c\right)\right]\left[\min\left(l_c\,;\, l_{shW}\right)\right] t_{shW} \\
\bar{G} &= \frac{1}{3}\left[\max\left(3l_c - 2l_{shW}\,;\, l_c\right)\right]\left[\min\left(l_c\,;\, l_{shW}\right)\right]^2 t_{shW} \\
\bar{T} &= \left[\max\left(2l_c - 2d\sigma_{max} - t_{fl}\,;\, l_c - d\sigma_{max}\,;\, 0\right)\right]\left[\min\left(\max\left(l_c - d\sigma_{max}\,;\, 0\right)\,;\, t_{fl}\right)\right] l_{fl,eff} \\
\bar{H} &= \frac{1}{3}\left[\max\left(3l_c - 3d\sigma_{max} - 2t_{fl}\,;\, l_c - d\sigma_{max}\,;\, 0\right)\right]\left[\min\left(\max\left(l_c - d\sigma_{max}\,;\, 0\right)\,;\, t_{fl}\right)\right]^2 l_{fl,eff}.
\end{aligned} \tag{V.14}$$

Eqs. V.12 and V.13 are two equations with two unknowns. The elimination of maximum compressive stress σ_{max} leads to

$$e = \frac{M_{Ed}}{N_{Ed}} = y_{GC} - \frac{\bar{G} + d\sigma_{max}\bar{T} + \bar{H}}{\bar{R} + \bar{T}}. \tag{V.15}$$

Eq. V.15 provides therefore the implicit expression of the compressive length l_c. It depends on the eccentricity e and on the geometry of the wall. It may be noted that the expression given by Eq. V.15 degenerates into the well known expression of the compressive length for a simple rectangular wall. Indeed, assuming no flange ($l_{fl,eff} = 0$ for instance), it comes

$$\begin{aligned}
e &= y_{GC} - \frac{\bar{G}}{\bar{R}} \\
&= y_{GC} - \frac{1}{3}\frac{\max\left(3l_c - 2l_{shW}\,;\, l_c\right)\min\left(l_c\,;\, l_{shW}\right)^2 t_{shW}}{\max\left(2l_c - l_{shW}\,;\, l_c\right)\min\left(l_c\,;\, l_{shW}\right) t_{shW}}.
\end{aligned} \tag{V.16}$$

The compressive length being limited to the length of the shear wall l_{shW}, the maximum and minimum functions are thus always equal to the compressive length. The position of the gravity centre of the rectangular wall with respect to the reference point is equal to $l_{shW}/2$. It follows

$$l_c = 3\left(\frac{l_{shW}}{2} - e\right) \tag{V.17}$$

where the factor 3 is a consequence of the assumption of a linear distribution of compressive stresses.

V.2.2 Linearisation of the expression

The relation between the compressive length l_c and the eccentricity e given by Eq. V.15 is non-linear due to the presence of the flange. Considering a wall with a rectangular cross-section, the relation effectively becomes Eq. V.17 in which these two quantities are simply proportional. Solving this non-linear equation (Eq. V.15) requires the use of numerical methods. In the following, a linearisation of this equation is proposed in the perspective of determining the compressive length by hand calculations with a good approximation.

In the case of a simple rectangular wall with a length l, there are two discontinuities in the line representing l_c in function of e. On the one hand, l_c remains equal to l as long as e is smaller than $l/6$ (full contact). On the other hand, it becomes zero as soon as e is larger than $l/2$ (overturning).

The proposed linearisation is based on these observations. It is indeed possible to determine the eccentricities for which a discontinuity occurs, i.e. the compressive length remains in full contact or the flange and a part of the shear wall are uplifted for instance. For the configuration drawn in Figure V.1, there are four discontinuities at most. Some of them can overlap, depending on the position of the flange. First, the absence of uplift means that $l_c = l_{shW}$. Introducing this in Eq. V.15 leads to

$$\begin{aligned}
\bar{R} &= l_{shW}^2\, t_{shW} \\
\bar{G} &= \frac{1}{3} l_{shW}^3\, t_{shW} \\
\bar{T} &= (2l_{shW} - 2d\sigma_{max} - t_{fl})\, t_{fl} l_{fl,eff} \\
\bar{H} &= \frac{1}{3}(3l_{shW} - 3d\sigma_{max} - 2t_{fl})\, t_{fl}^2 l_{fl,eff}.
\end{aligned} \tag{V.18}$$

The simplifications for $\bar{R}$ and $\bar{G}$ are obvious, while those for $\bar{T}$ and $\bar{H}$ rely on the condition that

$$d\sigma_{max} + t_{fl} \leq l_{shW} \tag{V.19}$$

for geometrical reasons. Therefore, the minimum eccentricity involving an uplift of the wall is

$$\begin{aligned}
e_m = {} & y_{GC} \\
& - \frac{l_{shW}^3 t_{shW} + \left[3d\sigma_{max}(2l_{shW} - 2d\sigma_{max} - t_{fl}) + (3l_{shW} - 3d\sigma_{max} - 2t_{fl})\, t_{fl}\right] t_{fl}\, l_{fl,eff}}{3\left[l_{shW}^2\, t_{shW} + (2l_{shW} - 2d\sigma_{max} - t_{fl})\, t_{fl}\, l_{fl,eff}\right]}.
\end{aligned} \tag{V.20}$$

Second, an uplift of the flange implies that $l_c \leq d\sigma_{max} + t_{fl}$. At the transition and with the condition given by Eq. V.19, it comes

$$\begin{aligned}
\bar{R} &= (d\sigma_{max} + t_{fl})^2\, t_{shW} \\
\bar{G} &= \frac{1}{3}(d\sigma_{max} + t_{fl})^3\, t_{shW} \\
\bar{T} &= t_{fl}^2 l_{fl,eff} \\
\bar{H} &= \frac{1}{3} t_{fl}^3 l_{fl,eff}
\end{aligned} \tag{V.21}$$

and the eccentricity is

$$e_{t,1} \quad = \quad y_{GC} - \frac{1}{3}\frac{\left(d\sigma_{max} + t_{fl}\right)^3 t_{shW} + 3d\sigma_{max}\, t_{fl}^2\, l_{fl,eff} + t_{fl}^3 l_{fl,eff}}{\left(d\sigma_{max} + t_{fl}\right)^2 t_{shW} + t_{fl}^2 l_{fl,eff}}. \tag{V.22}$$

Third, there is another transition when the flange is fully uplifted ($l_c \leq d\sigma_{max}$). In this case, the groups $\bar{T}$ and $\bar{H}$ disappear and the eccentricity is

$$e_{t,2} \quad = \quad y_{GC} - \frac{1}{3} d\sigma_{max}. \tag{V.23}$$

Finally, the eccentricity leading to a zero compressive length is given by Eq. V.24 as the groups $\bar{R}$, $\bar{G}$, $\bar{T}$ and $\bar{H}$ are null:

$$e_M \quad = \quad y_{GC} \tag{V.24}$$

Eqs. V.20, V.22, V.23 and V.24 provide the abscissae of points whose ordinates are l_{shW}, $d\sigma_{max} + t_{fl}$, $d\sigma_{max}$ and 0 respectively. Between these points, a linear interpolation is performed to calculate the compressive length corresponding to a given eccentricity. The exact equation and the linearised relation are illustrated in Figure V.2, assuming $d\sigma_{max} = \frac{l_{shW} - t_{fl}}{2}$ and $l_{fl,eff} = 6t_{fl}$.

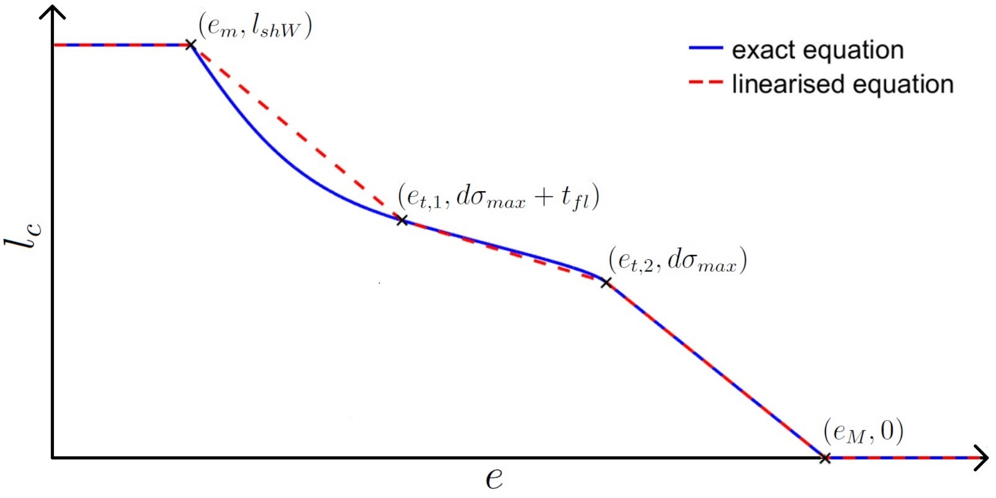

Figure V.2: Exact relation between l_c and e and linearised expression

V.2.3 Parametric study of the position and the length of the flange

Six parameters influence the compressive length l_c. The main one is the ratio e between the bending moment M_{Ed} and the vertical compression N_{Ed} acting on the wall. The others are geometrical parameters, with the dimensions of the shear wall and flange and the position of this latter.

Considering two different lengths for the shear wall and the same widespread thickness of load-bearing walls in countries like Belgium (14 cm) for both sections of the wall, this section studies the importance on the relation between l_c and e of the last two parameters, namely $d\sigma_{max}$ and $l_{fl,eff}$. The ratio between the effective length of the flange and the length of the shear wall is defined by the parameter r (Eq. V.25). Figure V.3 shows the cross-section of a non-rectangular wall assuming $d\sigma_{max} = 0$ and $r = 0$ (no flange), $r = 6\,t_{fl}$ or $r = 12\,t_{fl}$. The last two values for r correspond to the bounds given by Eq. V.3, considering a one-side and a two-side flange respectively and disregarding the influence of the height.

$$r = \frac{l_{fl,eff}}{l_{shW}} \tag{V.25}$$

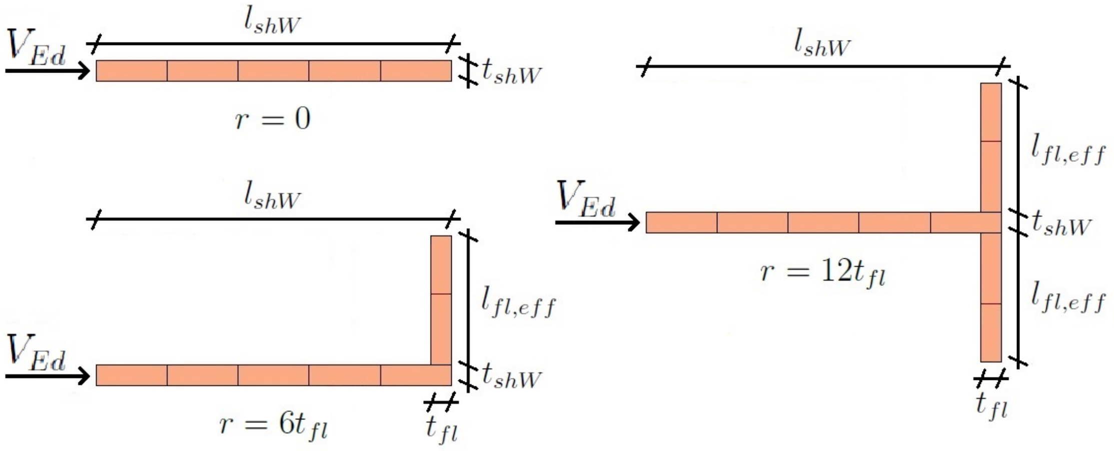

Figure V.3: Parametric study - Examples of geometry

For the parameter study, Eq. V.15 is nondimensionalized by dividing each term by the length of the shear wall l_{shW}. It reads

$$e^* = y^*_{GC} - \frac{\bar{G}^* + d\sigma^*_{max}\bar{T}^* + \bar{H}^*}{\bar{R}^* + \bar{T}^*} \tag{V.26}$$

with $e^* = e/l_{shW}$, $y^*_{GC} = y_{GC}/l_{shW}$, $d\sigma^*_{max} = d\sigma_{max}/l_{shW}$ and $\bar{R}^* = \bar{R}/l^3_{shW}$, $\bar{T}^* = \bar{T}/l^3_{shW}$, $\bar{G}^* = \bar{G}/l^4_{shW}$ and $\bar{H}^* = \bar{H}/l^4_{shW}$ in which $l^*_c = l_c/l_{shW}$.

Figures V.4 and V.5 show the relation $l^*_c - e^*$ for two chosen lengths of shear wall (700 mm and 2800 mm). Three different positions of the flange are investigated, namely a flange at the left extremity ($d\sigma^*_{max} = \frac{l_{shW}-t_{fl}}{l_{shW}}$), at mid-length ($d\sigma^*_{max} = \frac{l_{shW}-t_{fl}}{2\,l_{shW}}$) and at the right extremity ($d\sigma^*_{max} = 0$) of the shear wall. For each graph, the different curves are related to a given ratio r. The solid curves correspond to the exact equation and the dashed curves are related to the linearised relation.

Figures V.4 and V.5 show that the presence of a flange modifies the abscissa of the discontinuities (e^*_M, $e^*_{t,1}$, $e^*_{t,2}$ and e^*_m). The longer the flange, the larger the difference with a simple rectangular wall. The abscissae e^*_i ($i = m;\ t,1;\ t,2;\ M$) depend also on the position of the flange given by $d\sigma^*_{max}$. The influence of these two parameters (r and $d\sigma^*_{max}$) on e^*_i can be observed in Figure V.6. The eccentricities e^*_m and $e^*_{t,1}$ present a maximum for some positions of the flange, when the flange is at the right extremity of 2.8 m long shear wall for instance.

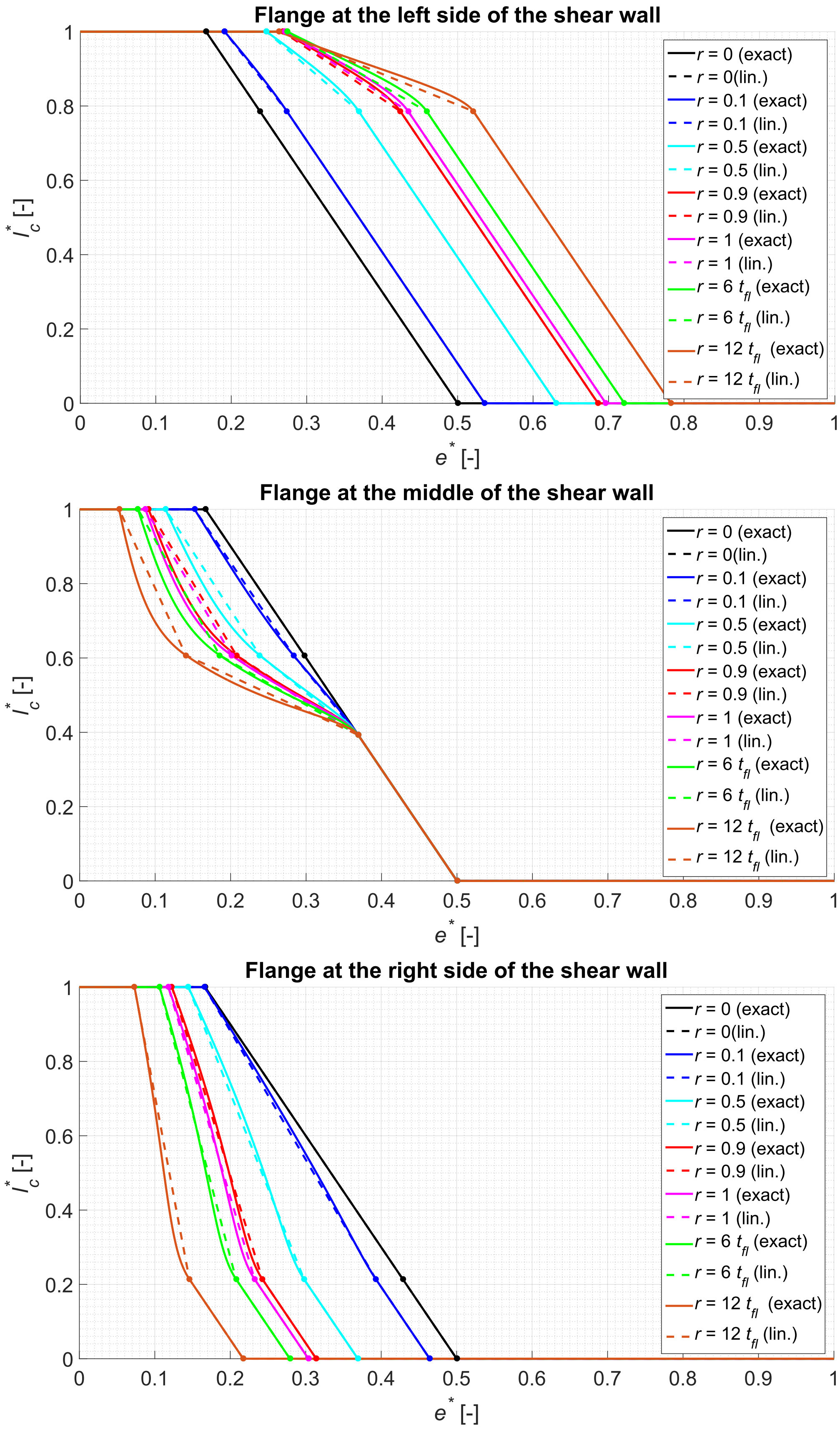

Figure V.4: Parametric study - evolution of the compressive length with respect to the eccentricity (0.7 m long shear wall)

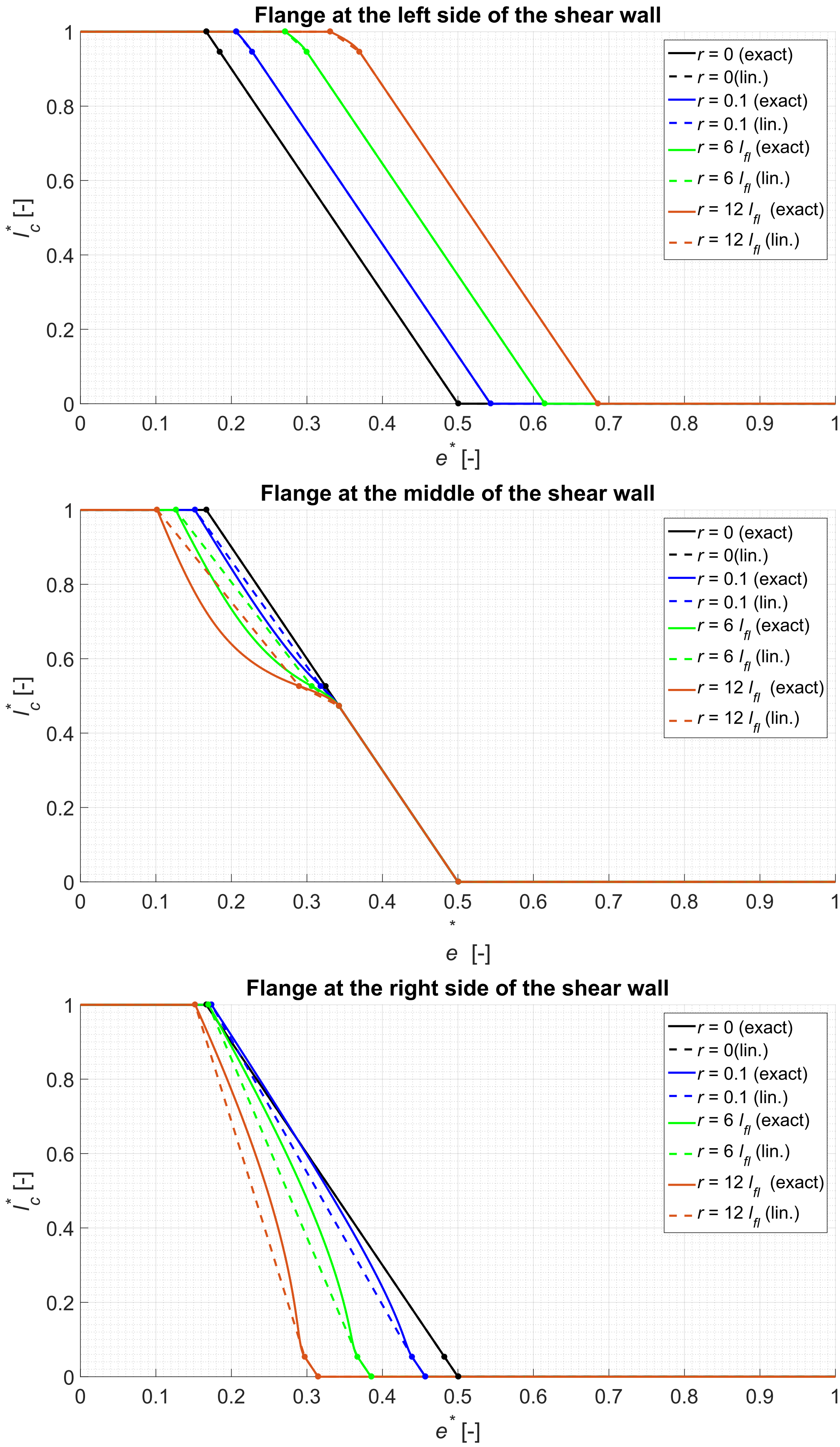

Figure V.5: Parametric study - evolution of the compressive length with respect to the eccentricity (2.8 m long shear wall)

Figure V.6 also proves that e^*_m and $e^*_{t,1}$ (e^*_M and $e^*_{t,2}$) are equal if $d\sigma^*_{max} = \frac{l_{shW}-t_{fl}}{l_{shW}}$ ($d\sigma^*_{max} = 0$). The variation of e^*_i with respect to the ratio r also depends on the length of the shear wall. Another effect of this latter is the reduction of the difference between the eccentricities $e^*_{t,1}$ and $e^*_{t,2}$ when it increases.

The comparison between the exact and the linearised equations (Figures V.4 and V.5) highlights that the curves merge once the eccentricity e^* is larger than $e^*_{t,2}$. When $e^* > e^*_{t,2}$, the slope of both exact and linearised curves are the same and corresponds to the slope of the wall without any flange since only a part of the shear wall remains compressed. In the case $e^* < e^*_{t,2}$, differences are observed between the equations, the exact expression being non-linear. The non-linearity is increased with the length of the flange. This observation is supported by Figure V.7 which highlights larger errors for longer flanges.

Finally, Figure V.7 leads to the conclusion that the simplified expression of the compressive length gives the same results (error $<$ 2%) as the exact expression in the case of $d\sigma^*_{max} = \frac{l_{shW}-t_{fl}}{l_{shW}}$ for both considered length of the shear wall. For $d\sigma^*_{max} = \frac{1}{2}\frac{l_{shW}-t_{fl}}{l_{shW}}$, a good approximation (error $\lesssim$ 10 %) is obtained in the case of $l_{shW} = 700$ mm and only if $r < 6\,t_{fl}$ in the case of $l_{shW} = 2800$ mm. For $d\sigma^*_{max} = 0$, the simplifications are acceptable (error $\lesssim$ 20 %) if $r < 6\,t_{fl}$ in the case of $l_{shW} = 700$ mm and if $r < 0.1$ in the case of $l_{shW} = 2800$ mm.

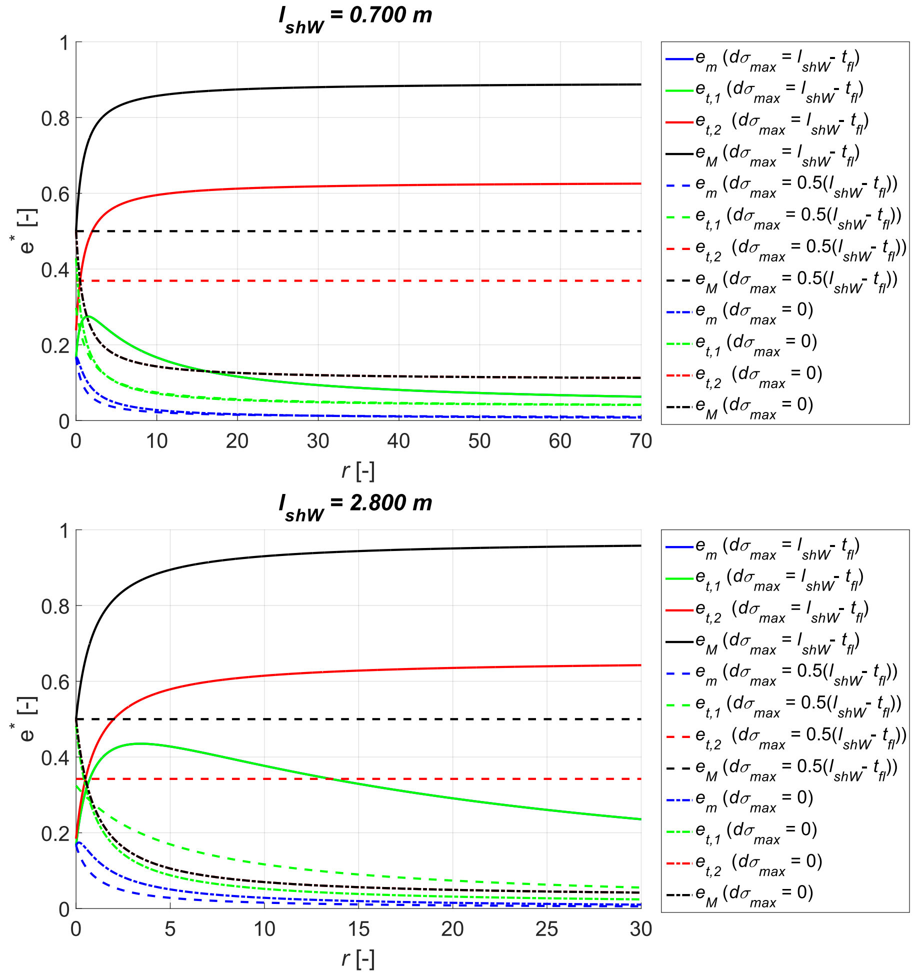

Figure V.6: Parametric study - eccentricities in function of the ratio r (top : 0.7 m long shear wall ; bottom : 2.8 m long shear wall)

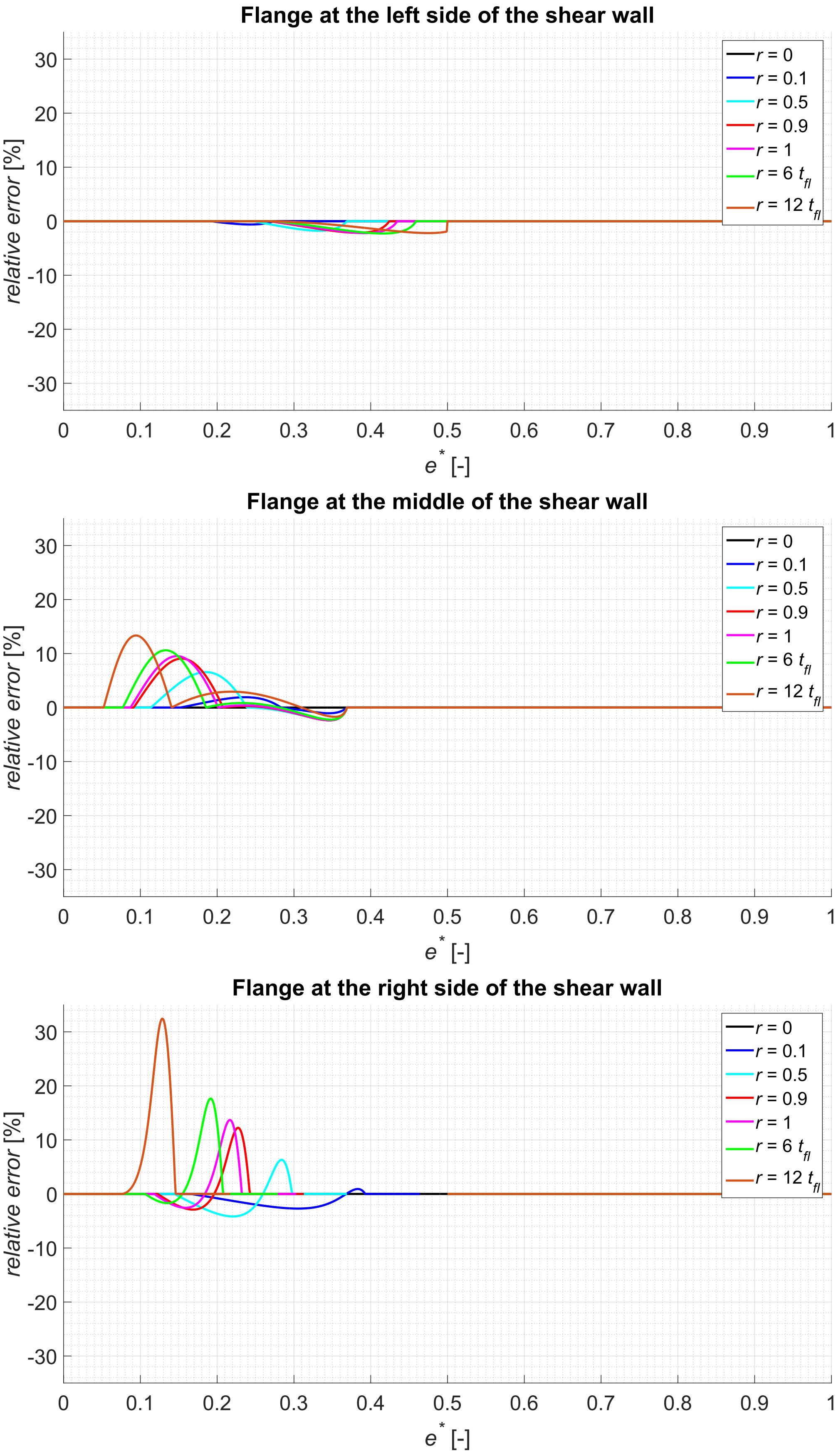

Figure V.7: Parametric study - relative error of the linearisation (0.7 m long shear wall)

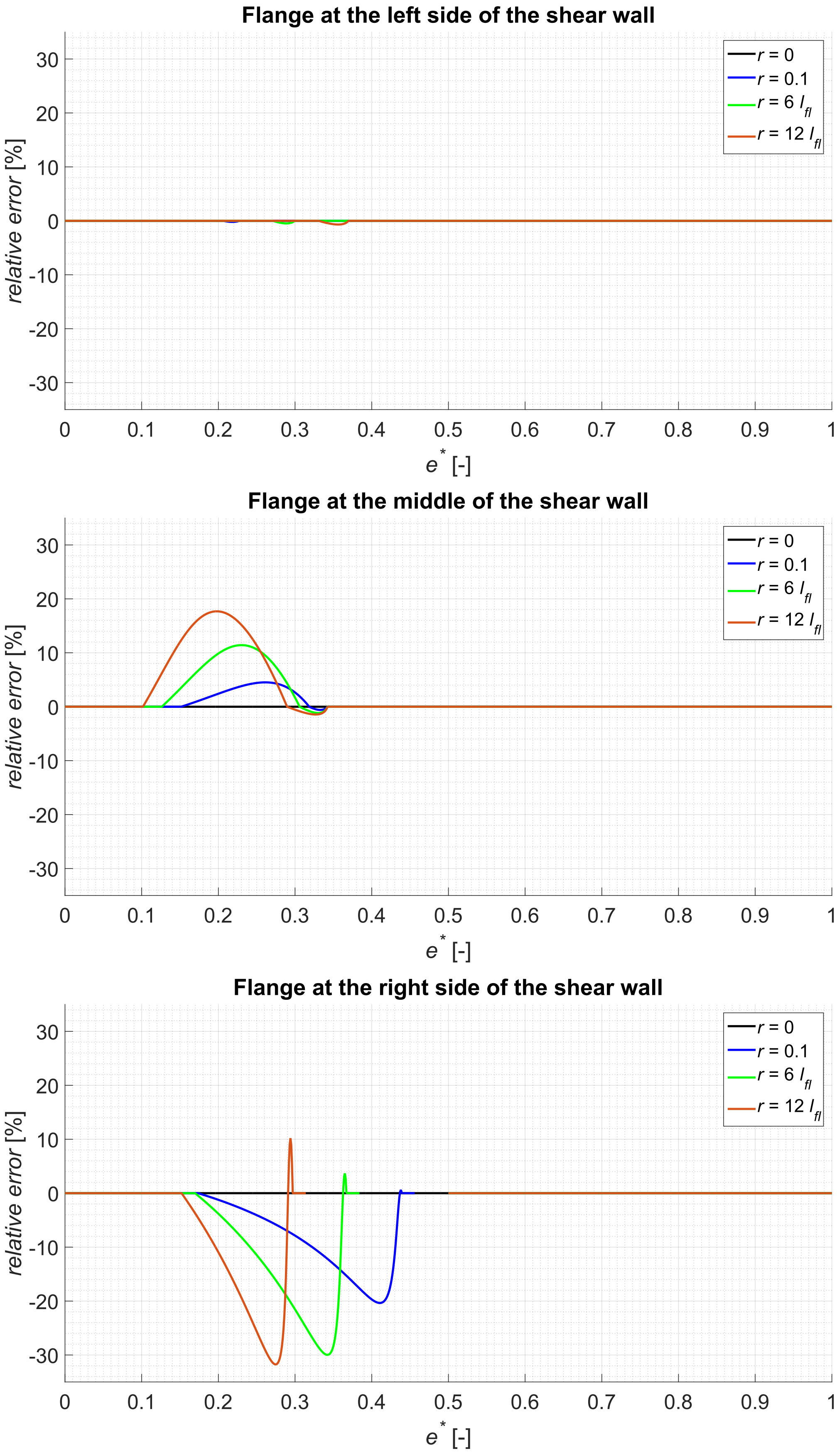

Figure V.8: Parametric study - relative error of the linearisation (2.8 m long shear wall)

V.3 Design procedure and comparison with experimental results

The design procedure follows the recommendations of the EN 1996-1-1 for URM walls subjected to a horizontal shear. First, the internal forces N_{Ed}, V_{Ed} and M_{Ed} acting on the studied wall have to be determined. These forces can be obtained by a numerical analysis of a model at the macro-scale, using an equivalent frame with beam elements for the piers and spandrels, as illustrated in Figure V.9. The beams representing the walls and the spandrel are located at their neutral axis and rigid arms connect the beam elements. The loads acting on the structure are defined according to the relevant sections of the Eurocodes.

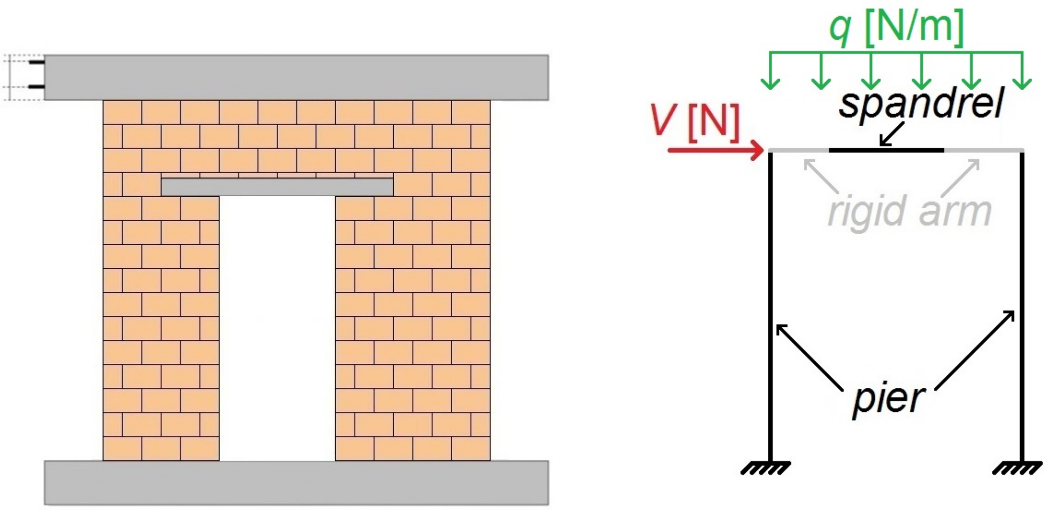

Figure V.9: Equivalent frame model

Then, the verification is carried out and first consists in the calculation of the compressive length corresponding to the ratio $e = M_{Ed}/N_{Ed}$ given by the analysis (Eq. V.15). The proposed methodology implements the expressions developed in the previous section (see Section V.2). Once the compressive length calculated, three limit states have to be verified :

- the shear resistance:

$$\begin{aligned} V_{Ed} &\leq V_{Rd} \\ &\leq f_{vd}\, A_c \end{aligned} \qquad \text{(V.27)}$$

- the compression resistance:

$$\begin{aligned} N_{Ed} &\leq N_{Rd} \\ &\leq f_d\, A_c \end{aligned} \qquad \text{(V.28)}$$

- the overturning:

$$l_c \geq 0 \qquad \text{(V.29)}$$

where A_c [m^2] is the area of the wall under compression and f_d [N.mm^{-2}] is the design compressive strength. Finally, the horizontal shear acting on the structure is increased until one of these three limit states is reached.

It is important to observe the difference between the criterion for the shear resistance given in Eq. V.1 and taken from the Eurocode 6 and the criterion of the proposed methodology (Eq. V.27). Indeed, the parameter A_c substitutes the product of t and l_c. This parameter is more general and clearly implies the consideration of the flanges, both in the calculation of the compressive length and the shear resistance.

The specimens described in Sections II.3 and II.5 are considered in the following. The experimental results highlighted large differences in terms of maximum horizontal shear when comparing the measurements with the results of a preliminary assessment performed according the rules of the Eurocodes and neglecting the presence of flanges. Table V.1 shows these differences for the T-shaped specimens tested in static-cyclic conditions. The positive direction corresponds to the over-compression of the perpendicular wall. As it can be observed, the prediction underestimates the shear resistance, from 12.5 % to 23.3 % depending on the load direction and the compression level. The absence of differences between the load directions is a main issue as the specimens are asymmetric.

Specimen	C1		C2		C3	
	Pred.	Exp.	Pred.	Exp.	Pred.	Exp.
Neg. direction [kN]	104.5	119.4	128.2	161.4	148.4	182.6
Pos. direction [kN]	104.5	134.2	128.2	167.2	148.4	188.1

Table V.1: Summary of the preliminary assessment and the experimental results for cyclic tests on non-rectangular walls

The results of the proposed procedure are presented in Figure V.10 and Table V.2 for the walls subjected to static-cyclic tests and in Figure V.11 for the specimens tested on the shake table. The Figures V.10 and V.11 plot the experimental force-displacement curves and compare them to the results of the assessments performed with (solid line) and without (dashed line) due consideration for the contribution of the flanges. In particular, the predictions obtained with TREMURI are also given (dotted line) for the static-cyclic tests. The detailed calculations for the specimen C1 are reported in Annex D.

Regarding the static-cyclic tests, the consideration of the flange results in a shear resistance close to the experimental results. A relative difference ranging from 2.4 to 6.5 % is observed with the exact formulation (see Table V.2). The use of the linearised expression leads to a relative difference from 2.2 % to 7.7 %. The largest difference between both formulations is equal to 2.9 % (wall C3, flange over-compressed). In terms of compressive length, this corresponds to a relative error of 7.6 %.

It is worth noticing that, during the experiments, the vertical compression was supposed to be applied on the shear wall only. Nevertheless, a part of the flange sustains this compression as the flange and the shear wall are glued together. The larger the compression load, the longer the part of the flange. The determination of the involved length of the flanges requires further studies. In the present case, this length is taken as the length minimizing the relative difference between the maximum shear given by the assessment and the experiments, in both directions. The involved length is found to be equal to 91 mm, 210 mm and 259 mm for the wall C1, C2 and C3 respectively (see Annex D).

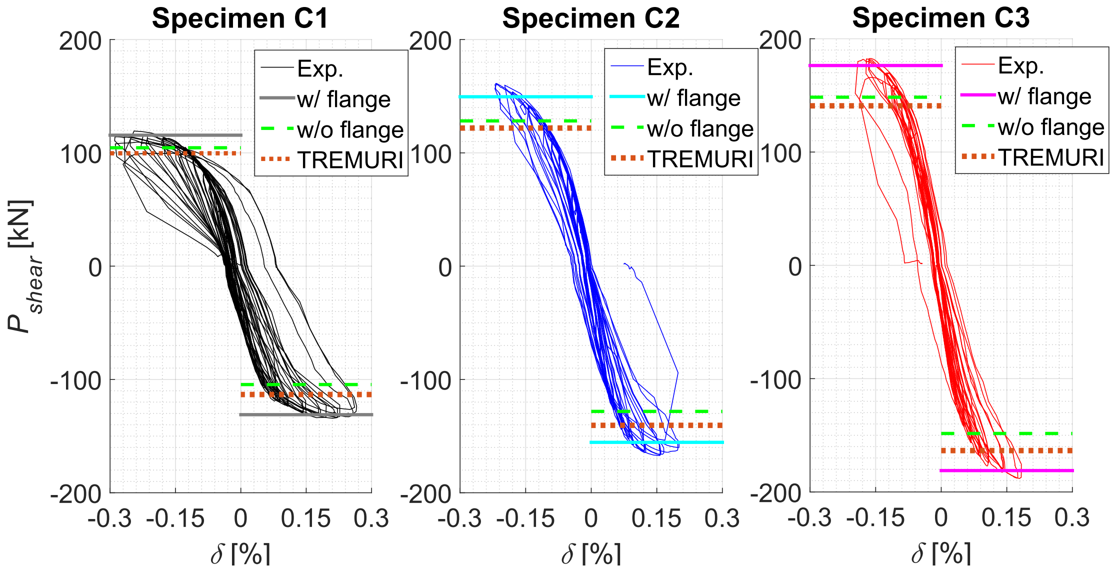

Figure V.10: Comparison of the proposed procedure with experimental results - static-cyclic tests

Specimen	C1	C2	C3
Neg. direction [kN]	116.6	151.0	177.8
Pos. direction [kN]	131.0	156.4	183.0

Table V.2: Summary of the preliminary assessment and the experimental results for cyclic tests on non-rectangular walls

Concerning the shake tables tests, the frame with T-shaped piers failed under an acceleration in the y-direction. In the perpendicular direction, the specimen presented in clear rocking behaviour. The collapse of the L-shaped frame occurred for a y-shake when the slab was supported by the flanges only. These three configurations are drawn in blue in Figure V.11 because they exhibit well-defined plateaus. The application of the proposed procedure seems to provide the shear force for which these plateaus develop. For the other configurations, the experimental curve is in red and the assessed maximum shear over-estimates the experimental values, except for the x-shake on the frame with L-shaped piers fully loaded. In this case, a plateau is initiated and is also well approximated by the assessment. As a conclusion, the shear capacity of URM structures including non-rectangular walls and subjected to the seismic action can be predict by an equivalent static approach implementing the calculation of the shear resistance with due consideration for any flanges.

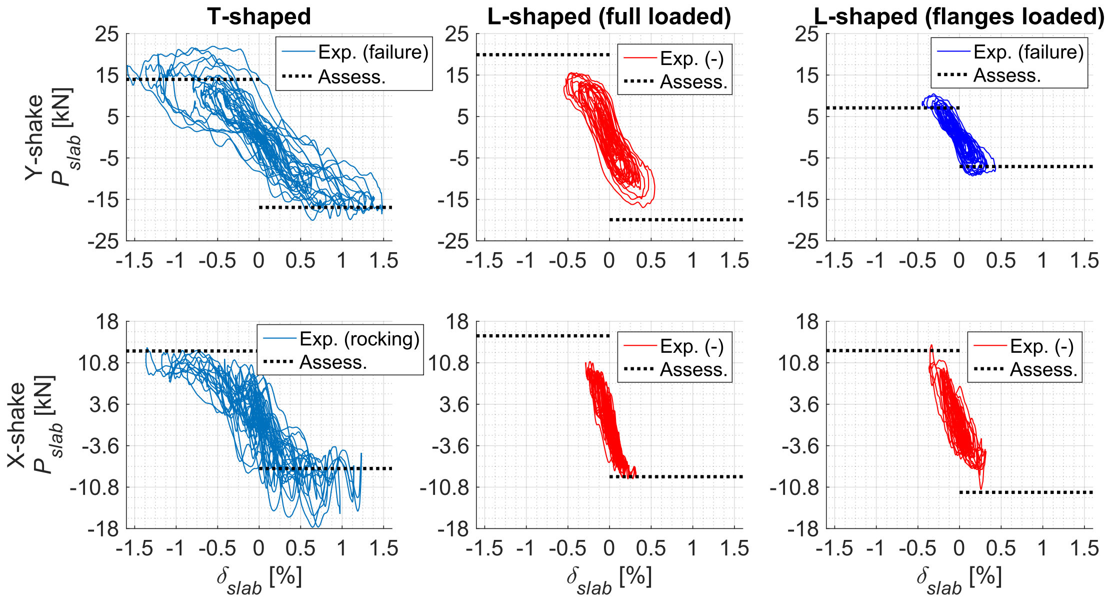

Figure V.11: Comparison of the proposed procedure with experimental results - shake table tests

V.4 Conclusions

This chapter is dedicated to the assessment of the shear resistance of URM walls with non-rectangular cross-section. The recommendations of the current European Standards on the contribution of flanges to the shear resistance are not explicit, leading to their neglection usually. Such an approach is conservative and underestimates the shear resistance of the walls.

In the perspective of improving the assessment of the shear resistance, the expression of the compressive length is developed and includes the contribution of the perpendicular sections. The eccentricity, i.e. ratio between the bending moment and the compressive force acting on the wall, is a main parameter of the equation, as well as the geometry of the wall. Simplifications of this expression are then suggested, based on the determination of the eccentricities corresponding to specific values of the compressive length and on the linear interpolation between these points. Finally, a design procedure including the developments is performed and the results are compared to the measurements from experimental tests on URM specimens. The comparisons show that the assessed shear resistance is in accordance with the experimental results corresponding to static-cyclic tests. For the specimens subjected to shake table tests, the assessment provides a good approximation of the plateau observed in the force-displacement curves.

The proposed methodology improves therefore the assessment of the shear resistance of URM walls with non-rectangular cross-section.

Chapter VI

Rocking behaviour of two stacked blocks including flexible layers

---

VI.1 Introduction
VI.2 Rocking behaviour of specimens without rubber
VI.3 Rocking behaviour of specimens including rubber layers
VI.4 Conclusions

VI.1 Introduction

The general rocking behaviour observed during the experimental campaigns on the shake table (see Chapter II, Section II.4), especially for the short walls, has triggered some interest in modelling this behaviour. Rocking has been originally studied by Housner in 1963 [45] with the aim of explaining the survival of tall slender structures during earthquakes. A single rectangular block resting on a horizontal base, both supposed rigid, has been considered and the equations describing the rocking motion (RM) have been developed under the assumptions of neither sliding between the block and its support nor bouncing. Numerous scientific contributions resulted from and extended this “inverted pendulum” model.

Some authors deeper investigated the simple model of Housner. Yim et al. [128] proposed a numerical procedure to solve the non-linear equations governing the RM, considering horizontal and vertical ground accelerations. They highlighted an important sensitivity to the geometry of the block and to the details of the ground motion. The rocking response under sinusoidal acceleration was characterised by Spanos and Koh [114], while Zhang and Makris [130] considered cycloidal pulses. More recently, Kounadis [54] determined the minimum acceleration leading to overturning instability. Alternatives to the model of Housner were also studied. Prieto and Lourenço [100] unified the piecewise equations for the RM with a new formulation and Prieto et al. [101] developed a tool based on the Discrete Element method for the numerical modelling of the rigid block.

Extensions of the simple model focused on the different assumptions made by Housner. First, a flexible support was introduced. Psycharis and Jennings [104] compared the Winckler model and a simplified unilateral two-spring model in order to consider an elastic foundation. It was concluded that both solutions were equivalent, allowing the use of the simple one. This type of foundation was also studied by Koh [52] and Palmeri and Markis or Ma and Butterworth [91, 66], using the Winckler model or the simplified model respectively. Vassilou and Makris [73] examined, numerically, the RM of rigid blocks on linear visco-elastic and single/double concave spherical sliding bearings, while an experimental campaign was carried out by ElGawady et al. [32] and showed the significant influence on the RM of the material (concrete, timber, steel or rubber) at the base of the rigid block. Second, the assumptions of neither sliding nor bouncing were discussed. Shenton III and Jones [113] identified five modes of response (rest, slide, rock, slide-rock and free flight) and provided criteria for their initiation with corresponding equations of motion. Third, the deformability of the block has been taken into account. Psycharis [103] carried out a parametric analysis on a SDOF oscillator with a harmonic excitation and outlined the importance of the ratio of the natural period of the structure to the period of excitation. Oliveto et al. [89] enhanced previous models with a novel set of coordinates and transition conditions and Acikgos and DeJong [3] were focused on the interaction between elasticity and rocking. Finally, an interest in asymmetric blocks and tilted foundations was given by Plaut et al. [97]. Borosheck and Romo [11] modified the overturning criteria to consider the asymmetry, whereas Contento and Di Egidio [21] investigated the base isolation of these bodies.

Besides these extensions, the theory developed by Housner was compared to an equivalent SDOF oscillator with damping in the perspective of translating the research work into design procedures (see Priestley et al. [99]). Nevertheless, Makris and Konstantinidis [73] showed that this analogy is oversimplified and the related design approach should be abandoned. A new tentative of design procedure was presented by Kelly [49] in order to substitute for the special study required by the last version of the code in New-Zealand.

This literature review outlines a great interest in the rocking behaviour, but this was mainly limited to single block. Few research focused on the dynamic behaviour of stacked blocks. The analytical expression of the equations translating the RM of 2-stacked blocks was established by Psycharis [102], considering no sliding. Spanos et al. [115] improved this formulation by adding different contributions to the transition criteria between the different geometrical configurations and proposed an alternative method for the linearisation of the piecewise equations. Kounadis et al. [55] continued the work of assessing the minimum amplitude of the ground excitation leading to the overturning instability. Only one experimental campaign on rocking multi-block structures lying on a rigid support has been found. It was performed at the National Laboratory of Civil Engineering (LNEC) [94]. Regarding the design procedures, DeJong and Dimitrakopoulos proposed a methodology to derive approximate equivalence between rocking blocks and SDOF structures [28].

This chapter aims at reproducing the rocking behaviour of the 0.72-m long walls, observed during the third experimental campaign described in Chapter II and, in particular, in Section II.4. On the one hand, the specimen without soundproofing devices is first assumed to be represented by the simple model of Housner. The original theory however requires several adjustments, in order to take into account the additional steel mass for instance. A comparison is then made with a bi-block model used to consider properly the upper mass, a priori likely to rock with respect to the underlying wall. On the other hand, a new rocking model is derived for the specimen with rubber devices. It aims at modelling 2-stacked-block structures with viscous and flexible interfaces between the blocks as well as between the bottom block and the foundation. The properties of these interfaces are deduced from experimental data and highly influence the model response. Solving the equations related to the different models adopts a numerical scheme resorting to an event-driven strategy whose principles are detailed in [29].

VI.2 Rocking behaviour of specimens without rubber

VI.2.1 Modified Housner's theory

The theory developed by Housner considers a single block whose geometry is given in Figure VI.1 (a). A review of this theory is given in the following. The single block is assumed rigid and resting on a rigid base. It is subjected to a horizontal ground acceleration $\ddot{u}_g(t)$ [m.s^{-2}] and cannot slide nor bounce. Three different configurations are thus possible and are characterised by the time-dependent angle $\theta(t)$ [rad], representing the rotation of the block: the block can be quiescent ($\theta = 0$), rotate clockwise around its corner O ($\theta > 0$) or exhibit a counterclockwise rotation around its corner O' ($\theta < 0$). The equations of motion related to RM of these patterns are obtained by the Lagrange's method, using D'Alembert principle, namely

$$I_O\ddot{\theta} + mGr\sin(\theta_{cr} - \theta) = -m\ddot{u}_g r\cos(\theta_{cr} - \theta) \qquad \text{(VI.1)}$$

$$I_{O'}\ddot{\theta} - mGr\sin(\theta_{cr} + \theta) = -m\ddot{u}_g r\cos(\theta_{cr} + \theta) \qquad \text{(VI.2)}$$

if $\theta > 0$ and if $\theta < 0$ respectively. In Eqs. VI.1 and VI.2, I_O ($I_{O'}$) [kg.m^2] is the moment of inertia with respect to the point O (O'), G [m.s^{-2}] is the gravitational acceleration and

$m = \rho(2b)(2h)t$ [kg] is the specific mass of the system, where ρ [kg.m^{-3}] is the density of the block, t [m] is its thickness and b [m] and h [m] are its half-length and half-height respectively. Considering $\theta > 0$, the parameter $r = \sqrt{b^2 + h^2}$ [m] gives the distance between the centroid of the block and the rotating point O. The angle $\theta_{cr} = \arctan(b/h)$ [-] is the angle between the line r and the vertical. The dot symbol indicates derivatives with respect to time.

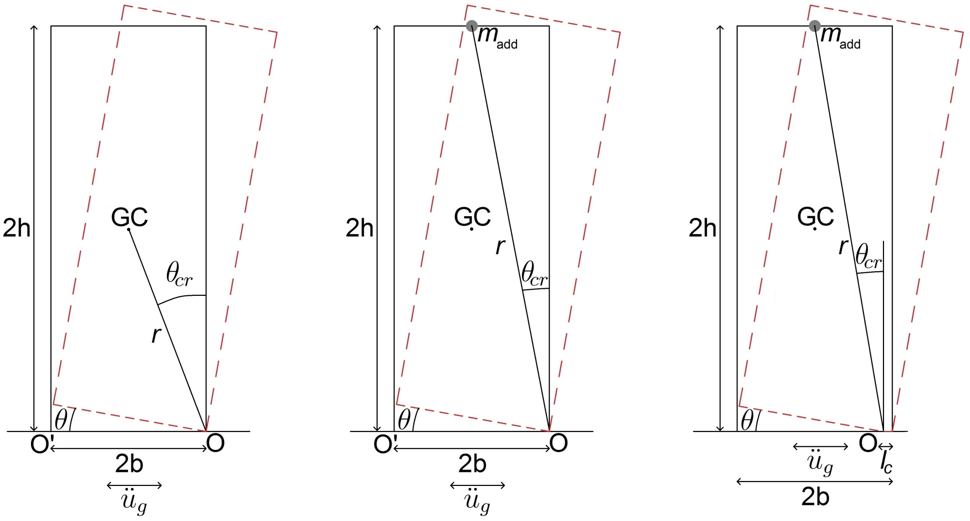

(a) (b) (c)

Figure VI.1: Rocking behaviour - single rigid block

The transition between the different configurations is governed by criteria. The initiation of motion of the block requires that the overturning moment induced by the horizontal ground acceleration $\ddot{u}_g$ exceeds the restoring moment due to the gravity G, leading to the conditions

$$\mp\frac{\cos(\theta_{cr})}{\sin(\theta_{cr})}\frac{\ddot{u}_g(t)}{G} \quad -1 > \quad 0 \tag{VI.3}$$

depending on whether the block starts to rock around O or O'. The transition between the RM around one corner to another is translated by a change in sign of the angle θ. This happens when the block passes through the vertical position and, thus, hits its support. The impact of the block against the support is accompanied with a dissipation of energy. At the moment of impact, the block has kinetic energy only. The energy dissipation is therefore translated by a reduction of the angular velocity $\dot{\theta}$ [rad.s^{-1}]. Under the assumption of an inelastic impact (no bouncing), the angular momentum with respect to O' is conserved. Thanks to this conservation, the angular velocity immediately after the impact, $\dot{\theta}_a$, can be expressed as a function of the angular velocity immediately before it, $\dot{\theta}_b$:

$$I_{o'}\dot{\theta}_a \quad = \quad I_o\dot{\theta}_b - 2mr^2\sin^2(\theta_{cr})\,\dot{\theta}_b \tag{VI.4}$$

It follows

$$e \quad = \frac{\dot{\theta}_a}{\dot{\theta}_b} \quad = 1 - \frac{2mr^2}{I_{o'}}\sin^2(\theta_{cr}) < 1 \tag{VI.5}$$

with e, the coefficient of restitution. The block comes back to rest when, at the moment of an impact, the sign of the angular velocity $\dot{\theta}_a$ is opposite to the sign of the angle θ_a (the angle immediately after the impact).

The comparison between the model of Housner and the specimen without rubber tested experimentally on a shake table (see Section II.4) highlights differences, due to the additional steel mass at the top of the URM wall in particular. In a first approximation, the wall can be assumed as rigid and the additional mass is considered as punctual, as illustrated in Figure VI.1 (b). The presence of this latter involves the translation of the position of the centroid of the system (block + additional mass), influencing the parameters m, r, θ_{cr} and I_O ($I_{O'}$) in Eqs. VI.1 to VI.5. Indeed,

$$m = \rho(2b)(2h)t + m_{add} \simeq m_{add} \tag{VI.6}$$

as the specific mass of the walls (159 kg) can be neglected in comparison to the additional mass (5000 kg), leading to

$$r = \sqrt{b^2 + (2h)^2}\,; \quad \theta_{cr} = \arctan\left(\tfrac{b}{2h}\right) \quad ; \; I_O = mr^2. \tag{VI.7}$$

Provided Eqs. VI.6 and VI.7 are used for the calculation of the parameters m, r, θ_{cr} and I_O ($I_{O'}$), the equations of motion Eqs. VI.1 and VI.2 remain valid for the RM of the modified system, as well as the criteria for the transition between configurations (Eq. VI.3). The coefficient of restitution becomes

$$e = 1 - 2\sin^2(\theta_{cr})\,. \tag{VI.8}$$

The adopted numerical scheme consists in the time-integration of the linearised equations of motion describing the current configuration of the system. Assuming that the angle θ is small, the linearised equations are given by:

$$I_O\ddot{\theta} - mGr\cos(\theta_{cr})\,\theta = -m\ddot{u}_g r\cos(\theta_{cr}) - mGr\sin(\theta_{cr}) \quad if \quad \theta > 0 \tag{VI.9}$$

$$I_O\ddot{\theta} - mGr\cos(\theta_{cr})\,\theta = -m\ddot{u}_g r\cos(\theta_{cr}) + mGr\sin(\theta_{cr}) \quad if \quad \theta < 0. \tag{VI.10}$$

As soon as the configuration of the system changes, the integration is stopped and an event-driven strategy [29] is activated for the handling of the transition. An event localization function is first applied in the perspective of detecting accurately the moment of the transition. The update of the system variables is then operated. The equations of motion corresponding to the new configuration are chosen and the integration restarts. The transition is detected thanks to gap functions. These functions are defined by the criteria for the transition between configurations. Therefore, there are as many gap functions as there are criteria, namely three for the studied model. There is a change when one gap function presents a root.

VI.2.2 Application of the modified Housner's theory

The inputs of the model described in the previous section are the geometry of the masonry wall (b and h), the magnitude of the additional mass m and the horizontal ground acceleration $\ddot{u}_g(t)$. The short wall without rubber is considered in the following and is initially at rest. Figure VI.2 shows the results given by the model in comparison to the experimental measurements related to the seismic test S08. According to the model, the system remains quiescent under the applied ground acceleration. This is confirmed by Figure VI.3 which represents the time evolution of gap functions. The curves representing Eq. VI.3 never cross the x-axis, translating no initiation of motion.

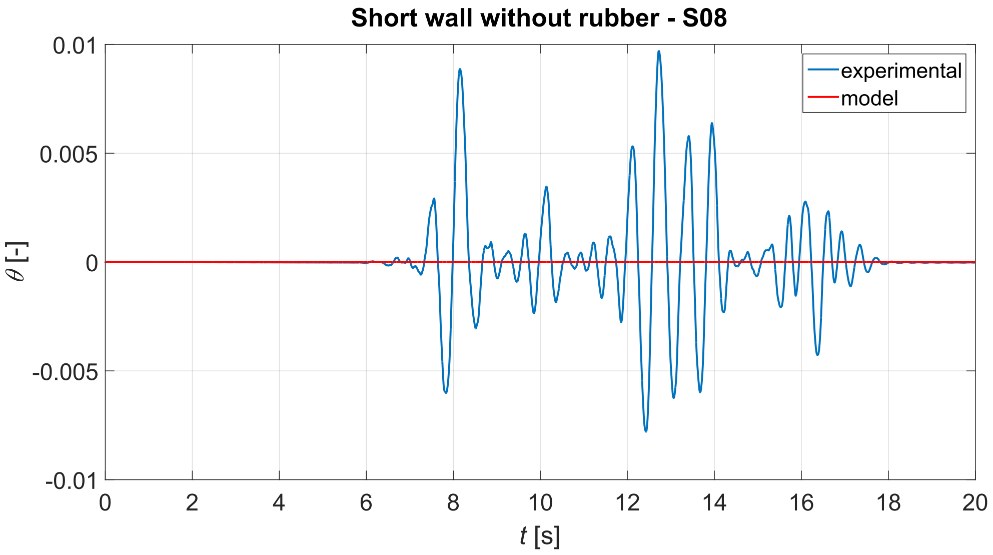

Figure VI.2: Rocking behaviour - Comparisons of the model predictions (rigid) with experimental measurements - S08

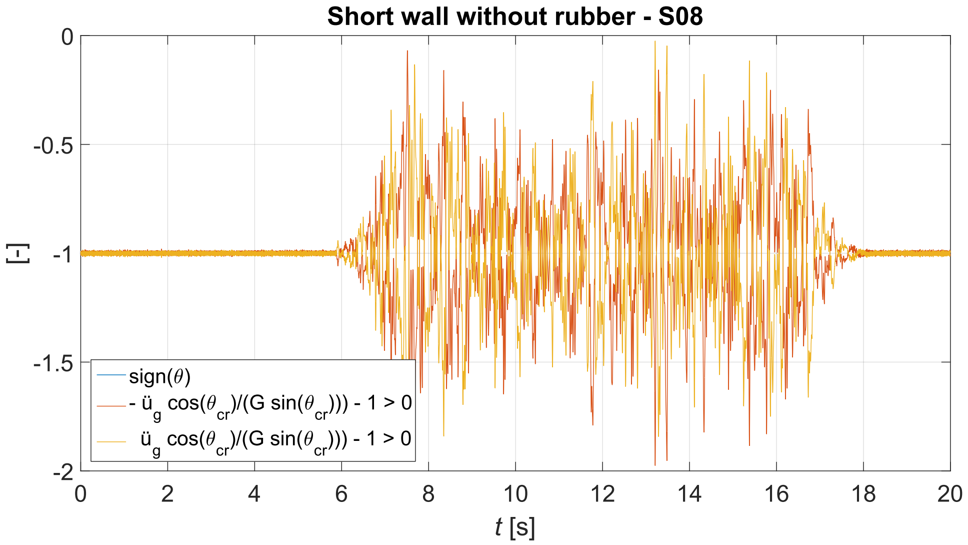

Figure VI.3: Rocking behaviour - Gap functions of seismic test S08

The absence of motion makes questionable the modelling of the URM wall with an additional mass by a single rigid block. A possible reason is the assumption on the position of the points O and O'. These points are the corners of the block since it is supposed rigid. Considering studied URM walls, block is not perfectly rigid due to the open vertical joints and, therefore, the contact with the support is not punctual. The contact length can be assessed by the compressive length l_c [m] (see Chapter V) and the rotating point in contact is the point of zero strain. The criteria for the initiation of motion and the modified parameters θ_{cr} and r are thus expressed by

$$\mp \frac{r\cos(\theta_{cr})}{r\sin(\theta_{cr})-l_c}\frac{\ddot{u}_g(t)}{G} - 1 > 0$$

$$\theta_{cr} = \arctan\left(\frac{|b-l_c|}{2h}\right) \quad ; \quad r = \sqrt{(|b-l_c|)^2 + (2h)^2} \qquad \text{(VI.11)}$$

A similar approach has been proposed by Costa et al. [22]. These modifications are drawn in Figure VI.1 (c) and lead to the results presented in Figure VI.4. The model predicts the initiation of the RM after 7 seconds, slightly postponed in comparison to the experimental measurements (around 6.5 seconds). Three rocking phases can be observed experimentally, approximately between $t = 7\,s$ and $t = 9\,s$, between $t = 12\,s$ and $t = 14\,s$ and between $t = 15\,s$ and $t = 18\,s$ respectively. The model provides similar predictions, but is not able to capture the magnitude nor the frequency of the RM. Moreover, the experimental behaviour is more damped when looking at the last rocking phase.

Consequently, the modelling of the specimens without rubber by a single rigid block is not suitable. There are two main issues. On the one hand, the consideration of the additional mass should be improved. Indeed, this latter has been taken into account by its magnitude and by translating the centroid of the system. Its geometry and moment of inertia have however been neglected, as well as the possibility for it to rock on the URM wall. On the other hand, the position of the rotating point is questionable. This should also affect the expression of the coefficient of restitution e given that the contact between the block and its support is not punctual.

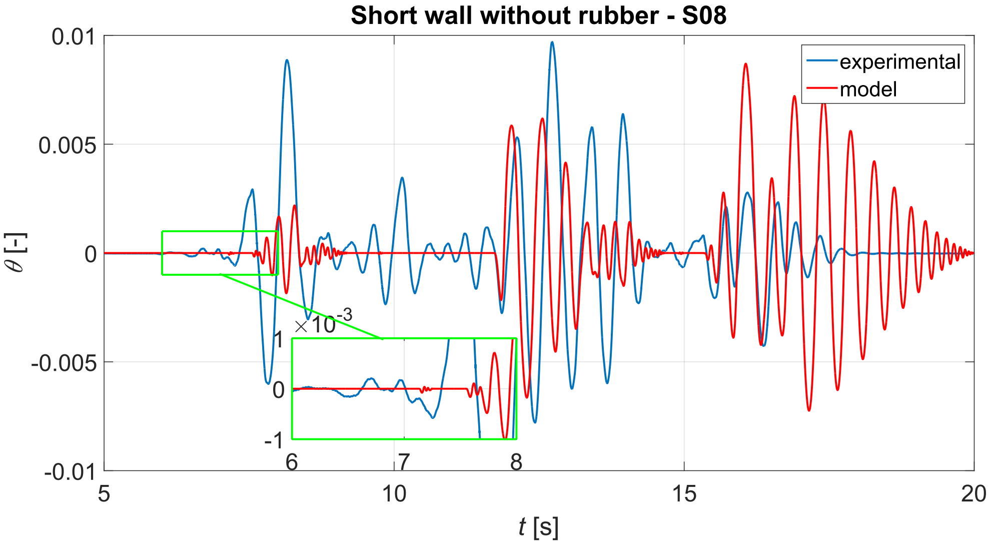

Figure VI.4: Rocking behaviour - Comparisons of the model predictions (modified) with experimental measurements - S08

VI.2.3 2-stacked-block model

In the perspective of improving the modelling of the wall without rubber tested experimentally, the 2-stacked-block model developed by Spanos et al. [115] is implemented. The lower block represents the URM wall and the upper block models the additional mass. Both blocks are assumed rigid and are characterised by their geometry (half-length b_i [m] and half-height h_i [m], with $i = 1, 2$ for the lower and upper blocks respectively), mass m_i [kg] and moment of inertia with respect to the rotating point I_{O_i} [kg.m^2] (or $I_{O'_i}$). The system has 9 different configurations. It can be at rest or exhibit one of the configurations illustrated in Figure VI.5. There are two coordinates, namely the angles θ_1 and θ_2, which measure the rotation of the lower and upper blocks respectively. They are positive clockwise.

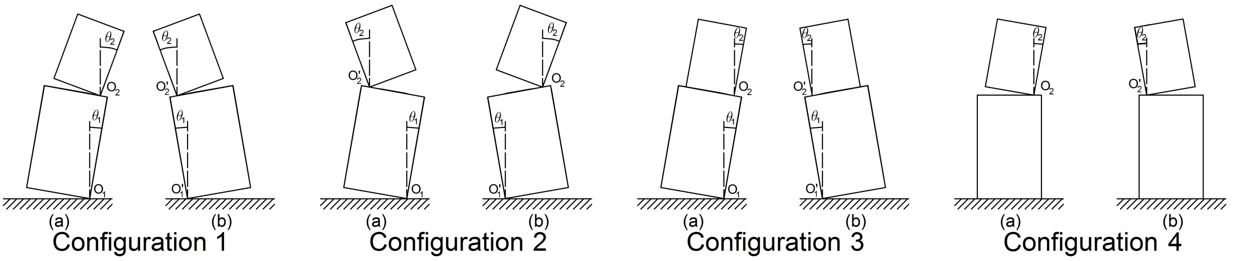

Figure VI.5: Rocking behaviour - Configurations of the 2-stacked blocks model

The equations governing the RM, obtained by the Lagrange's method, are detailed in [115] for all configurations. Those related to the configuration 2 (a) are given in Eqs. VI.12 and VI.13, under horizontal and vertical ground accelerations $\ddot{u}_g(t)$ [m.s^{-2}] and $\ddot{w}_g(t)$ [m.s^{-2}]. They are

$$\begin{aligned}(I_{O_1} + m_2 l'^2)\,\ddot{\theta} + m_2 l' r_2 \cos(\gamma_2)\,\ddot{\theta}_2 + m_2 l' r_2 \cos(\gamma_2)\,\dot{\theta}_2^2 \\ - m_1 G r_1 \sin(\theta_1 - \theta_{cr,1}) - m_2 G l' \sin(\theta_1 - \beta') \\ = -\left[m_1 r_1 \cos(\theta_1 - \theta_{cr,1}) + m_2 l' \cos(\theta_1 - \beta')\right]\ddot{u}_g \\ + \left[m_1 r_1 \sin(\theta_1 - \theta_{cr,1}) + m_2 l' \sin(\theta_1 - \beta')\right]\ddot{w}_g\end{aligned} \tag{VI.12}$$

$$\begin{aligned}m_2 l' r_2 \cos(\gamma_2)\,\ddot{\theta}_1 + I_{O_2}\ddot{\theta}_2 - m_2 l' r_2 \cos(\gamma_2)\,\dot{\theta}_1^2 - m_2 G r_2 \sin(\theta_2 - \theta_{cr,2}) \\ = m_2 r_2 \left[\cos(\theta_2 - \theta_{cr,2})\,\ddot{u}_g + \sin(\theta_2 - \theta_{cr,2})\,\ddot{w}_g\right]\end{aligned} \tag{VI.13}$$

with $\gamma_2 = \theta_1 - \theta_2 + \theta_{cr,2} + \beta'$. The parameters of these equations are shown in Figure VI.6. In addition to the mass m_i and the moment of inertia, I_{O_i} or $I_{O'_i}$, with respect to the rotating point of each block, r_i [m] is the distance between the centroid and the point around which the block rotates (see Eq. VI.14), $\theta_{cr,i}$ [-] is the angle between the line r_i and the vertical, l' [m] is the distance between the rotating points of each block (i.e. O$_1$ and O'$_2$ in this case) and β' [-] is the angle between the line l' and the vertical.

$$r_1 = \sqrt{b_1^2 + h_1^2} \quad ; \quad r_2 = \sqrt{\min(b_1, b_2)^2 + h_2^2} \tag{VI.14}$$

The transitions between the different configurations of the system are illustrated in Figure VI.7. They are handled by the gap functions given in Eq. VI.15. The event-driven strategy deals with one transition at a time, i.e. a system at rest cannot directly reach the configuration 1 (a), but requires to pass by the configuration 3 or 4 (a) first for instance. Just after an impact, the angular velocity of both blocks has to be calculated. These two unknowns are determined thanks to two equations, obtained by the application of the principle of conservation of the angular momentum around the rotating point of each block. The coefficients of restitution e_i for each block are derived from these equations.

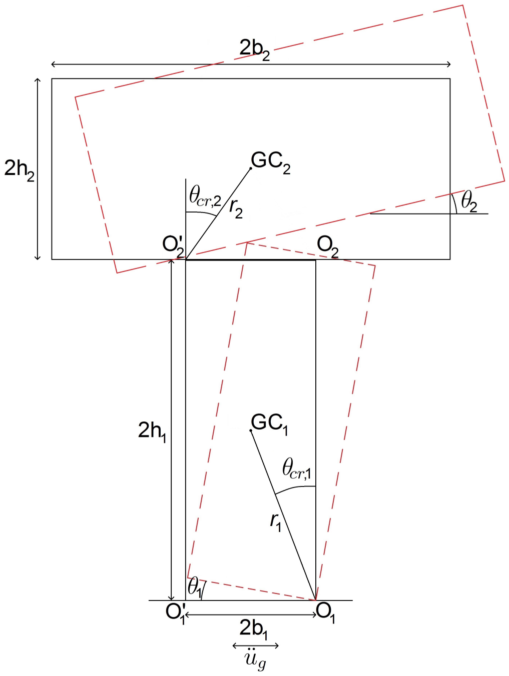
$2b_2$
$2h_2$
GC_2
$\theta_{cr,2}$
r_2
θ_2
O'_2
O_2
$2h_1$
GC_1
$\theta_{cr,1}$
r_1
θ_1
O'_1
O_1
$2b_1$
$\ddot{u}_g$

Figure VI.6: Rocking behaviour - Parameters of the 2-stacked blocks model (Config. 2 (a))

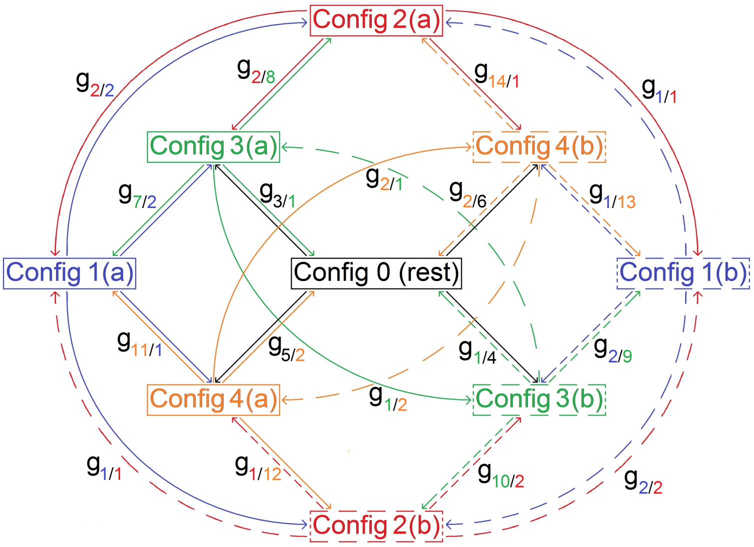
Config 2(a)
$g_{2/2}$
$g_{2/8}$
$g_{14/1}$
$g_{1/1}$
Config 3(a)
Config 4(b)
$g_{2/1}$
$g_{7/2}$
$g_{3/1}$
$g_{2/6}$
$g_{1/13}$
Config 1(a)
Config 0 (rest)
Config 1(b)
$g_{11/1}$
$g_{5/2}$
$g_{1/4}$
$g_{2/9}$
Config 4(a)
$g_{1/2}$
Config 3(b)
$g_{1/1}$
$g_{1/12}$
$g_{10/2}$
$g_{2/2}$
Config 2(b)

Figure VI.7: Rocking behaviour - Transitions between the configurations of the system

$$
\begin{aligned}
g(1) &= \theta_1 \\
g(2) &= \theta_2 - \theta_1 \\
g(3) &= -h_g \ddot{u}_g - b_1 \left(g + \ddot{w}_g\right) \\
g(4) &= +h_g \ddot{u}_g - b_1 \left(g + \ddot{w}_g\right) \\
g(5) &= -h_2 \ddot{u}_g - b \left(g + \ddot{w}_g\right) \\
g(6) &= +h_2 \ddot{u}_g - b \left(g + \ddot{w}_g\right) \\
g(7) &= -\cos\left(\theta_{cr,2} - \theta_1\right) \ddot{u}_g - \sin\left(\theta_{cr,2} - \theta_1\right) \left(G + \ddot{w}_g\right) \\
&\quad -d \cos\left(\theta_{cr,2} + \omega\right) \dot{\theta}_1^2 - \left[d \sin\left(\theta_{cr,2} + \omega\right) + \frac{I_{g2}}{m_2 r_2}\right] \ddot{\theta}_1 \\
g(8) &= +\cos\left(\theta_{cr,2} + \theta_1\right) \ddot{u}_g - \sin\left(\theta_{cr,2} + \theta_1\right) \left(G + \ddot{w}_g\right) \\
&\quad +d \cos\left(-\theta_{cr,2} + \omega\right) \dot{\theta}_1^2 + \left[d \sin\left(-\theta_{cr,2} + \omega\right) + \frac{I_{g2}}{m_2 r_2}\right] \ddot{\theta}_1 \\
g(9) &= +\cos\left(\theta_{cr,2} + \theta_1\right) \ddot{u}_g - \sin\left(\theta_{cr,2} + \theta_1\right) \left(G + \ddot{w}_g\right) \\
&\quad -d \cos\left(\theta_{cr,2} + \omega\right) \dot{\theta}_1^2 + \left[d \sin\left(\theta_{cr,2} + \omega\right) + \frac{I_{g2}}{m_2 r_2}\right] \ddot{\theta}_1 \\
g(10) &= -\cos\left(\theta_{cr,2} - \theta_1\right) \ddot{u}_g - \sin\left(\theta_{cr,2} - \theta_1\right) \left(G + \ddot{w}_g\right) \\
&\quad +d \cos\left(-\theta_{cr,2} + \omega\right) \dot{\theta}_1^2 - \left[d \sin\left(-\theta_{cr,2} + \omega\right) + \frac{I_{g2}}{m_2 r_2}\right] \ddot{\theta}_1 \\
g(11) &= -\left(m_1 + 2m_2\right) h_1 \ddot{u}_g - \left(m_1 b_1 + m_2 \xi\right) \left(G + \ddot{w}_g\right) \\
&\quad -m_2 r_2 \left[2h_1 \sin\left(\theta_{cr,2} - \theta_2\right) - \xi \cos\left(\theta_{cr,2} - \theta_2\right)\right] \dot{\theta}_2^2 \\
&\quad -m_2 r_2 \left[\xi \sin\left(\theta_{cr,2} - \theta_2\right) + 2h_1 \cos\left(\theta_{cr,2} - \theta_2\right)\right] \ddot{\theta}_2 \\
g(12) &= +\left(m_1 + 2m_2\right) h_1 \ddot{u}_g - \left(m_1 b_1 + m_2 \xi'\right) \left(G + \ddot{w}_g\right) \\
&\quad +m_2 r_2 \left[2h_1 \sin\left(\theta_{cr,2} - \theta_2\right) + \xi' \cos\left(\theta_{cr,2} - \theta_2\right)\right] \dot{\theta}_2^2 \\
&\quad -m_2 r_2 \left[\xi' \sin\left(\theta_{cr,2} - \theta_2\right) - 2h_1 \cos\left(\theta_{cr,2} - \theta_2\right)\right] \ddot{\theta}_2 \\
g(13) &= +\left(m_1 + 2m_2\right) h_1 \ddot{u}_g - \left(m_1 b_1 + m_2 \xi\right) \left(G + \ddot{w}_g\right) \\
&\quad -m_2 r_2 \left[2h_1 \sin\left(\theta_{cr,2} + \theta_2\right) - \xi \cos\left(\theta_{cr,2} + \theta_2\right)\right] \dot{\theta}_2^2 \\
&\quad +m_2 r_2 \left[\xi \sin\left(\theta_{cr,2} + \theta_2\right) + 2h_1 \cos\left(\theta_{cr,2} + \theta_2\right)\right] \ddot{\theta}_2 \\
g(14) &= -\left(m_1 + 2m_2\right) h_1 \ddot{u}_g - \left(m_1 b_1 + m_2 \xi'\right) \left(G + \ddot{w}_g\right) \\
&\quad +m_2 r_2 \left[2h_1 \sin\left(\theta_{cr,2} + \theta_2\right) + \xi' \cos\left(\theta_{cr,2} + \theta_2\right)\right] \dot{\theta}_2^2 \\
&\quad +m_2 r_2 \left[\xi' \sin\left(\theta_{cr,2} + \theta_2\right) - 2h_1 \cos\left(\theta_{cr,2} + \theta_2\right)\right] \ddot{\theta}_2
\end{aligned}
\tag{VI.15}
$$

with $b = \min\left(b_1, b_2\right)$ and where

$$
\begin{gathered}
h_g = \tfrac{m_1 h_1 + m_2 \left(2h_1 + h_2\right)}{m_1 + m_2} \\
d = \sqrt{\left(2h_1 + h_2\right)^2 + b_1^2} \qquad \omega = \arctan\left(\frac{2h_1 + h_2}{b_1}\right) \\
\xi = b_1 - b \qquad \xi' = 2b_1 - \xi
\end{gathered}
\tag{VI.16}
$$

The predictions of the bi-block model are shown in Figure VI.8 (left) under the assumption of rigid blocks, involving the rotation of the blocks around the corners at their base (points O_1, O_1', O_2 or O_2' in Figure VI.6). The system is set in motion (configuration 3 (a)) around $t = 7.5\,\mathrm{s}$, but the rotations are insignificant ($\theta_1 = \theta_2 < 10^{-4}$). Figure VI.8 (right) presents the results for the model including modifications for the position of the rotating points. The modifications are similar to those implemented for the modified Housner's theory. The initiation of the rocking motion is relatively well approximated by the model. Nevertheless, the time evolution of the angle characterising the motion of the blocks is not in accordance with the experimental measurements.

As a conclusion, the modelling of the specimens without rubber thanks to a 2-stacked-block model is not appropriate. Contrary to the conclusions of the previous section, the problem is not due to the lack of a proper modelling of the additional steel mass placed on the URM walls. The main issue concerns the use of a rigid block to model the URM wall. Indeed, the contact between the wall and its support cannot be considered as punctual. Moreover, this modification makes irrelevant the use of the principle of conservation of the angular momentum for the calculation of the coefficient of restitution.

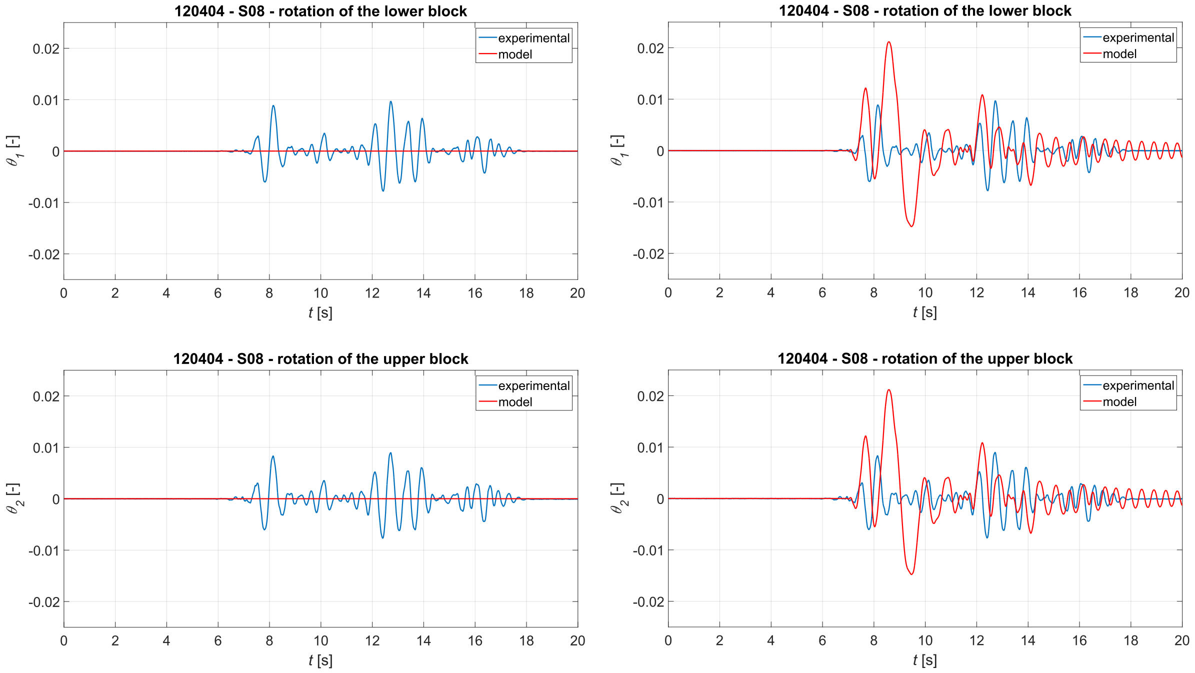

Figure VI.8: Rocking behaviour - Comparisons of the predictions of the 2-stack blocks model (left : rigid ; right : modified) with experimental measurements - short wall without rubber -S08)

VI.3 Rocking behaviour of specimens including rubber layers

VI.3.1 2-stacked blocks with flexible and viscous interfaces model

The URM wall including rubber soundproofing devices is modelled by 2-stacked blocks including flexible and viscous interfaces, illustrated in Figure VI.9 (left). The blocks are supposed rigid and characterised by a length $2b_i$ [m], a height $2h_i$ [m], a thickness t_i [m], a mass m_i [kg] and a moment of inertia I_{GC_i} [kg.m^2], GC_i being the centroid of the block and with $i = 1, 2$ for the lower and the upper block respectively. The interface between the support and lower block (between the lower and upper block) has a height e_b [m] (e_t [m]) and the same thickness t_i as the block they support. It is supposed to behave linearly and elastically. An interface is made of springs with a stiffness per unit length k_b [kg.m^{-1}.s^{-2}] (k_t [kg.m^{-1}.s^{-2}]) and dampers with a viscosity per unit length c_b [kg.m^{-1}.s^{-1}] (c_t [kg.m^{-1}.s^{-1}]). The parameters k_b, k_t, c_b and c_t are defined by

$$\begin{aligned} k_b &= E_r \frac{t_1}{e_b} \quad ; \quad c_b = 2\sqrt{k_b 2b_1 \left(m_1 + m_2\right)} \frac{\xi_r}{2b_1} \\ k_t &= E_r \frac{t_2}{e_t} \quad ; \quad c_t = 2\sqrt{k_t 2b m_2} \frac{\xi_r}{2b} \end{aligned} \tag{VI.17}$$

where $b = \min\left(b_1, b_2\right)$ and E_r [N.m^{-2}] and ξ_r [-] are the elastic modulus and the damping ratio of the interfaces, to be calibrated. Unilateral springs are considered, involving an uplift when the upward vertical displacement at any point is larger than the deflection due to gravity load.

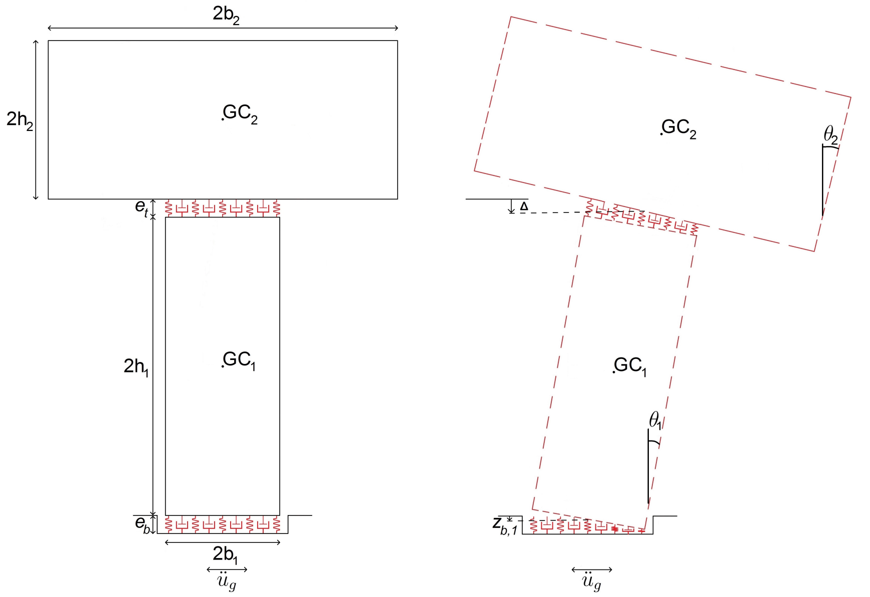

Figure VI.9: Rocking behaviour - 2-stacked blocks with flexible and viscous interfaces

Equations of motion

The model describes the RM with four variables: the rotation θ_i [-] of the blocks with respect to the vertical and the vertical displacement z_{b_i}[m] of the interfaces ($i = 1, 2$). They are denoted in Figure VI.9 (right) in which $\Delta = z_{b_1} - (2h_1 + e_t)(1 - \cos\theta_1) + z_{b_2}\cos\theta_1$. The model assumes that there is no bouncing, nor sliding. Four different configurations can be observed, namely (i) no uplift, (ii) uplift of the lower block, (iii) uplift of the upper block or (iv) uplift of both blocks.

The equations of motion for the different configurations are obtained by the Lagrange's method. The exact expression of these equations is developed for the configuration without uplift (i). The kinetic energy of the system is

$$\begin{aligned} T &= T_1 + T_2 \\ &= \frac{1}{2} I_{GC_1} \dot{\theta}_1^2 + \frac{1}{2} m_1 \left(\dot{x}_{GC_1}^2 + \dot{z}_{GG_1}^2 \right) \\ &\quad + \frac{1}{2} I_{GC_2} \dot{\theta}_2^2 + \frac{1}{2} m_2 \left(\dot{x}_{GC_2}^2 + \dot{z}_{GC_2}^2 \right) \end{aligned} \qquad \text{(VI.18)}$$

where $\dot{x}_{GC_i}$ and $\dot{z}_{GC_i}$ are the horizontal and vertical velocities of the centroid of the blocks:

$$\begin{aligned} \dot{x}_{GC_1} &= h_1 \cos(\theta_1) \dot{\theta}_1 \\ \dot{z}_{GC_1} &= \dot{z}_{b_1} - h_1 \sin(\theta_1) \dot{\theta}_1 \\ \dot{x}_{GC_2} &= (2h_1 + e_t + z_{b_2}) \cos(\theta_1) \dot{\theta}_1 + \dot{z}_{b_2} \sin(\theta_1) + h_2 \cos(\theta_2) \dot{\theta}_2 \\ \dot{z}_{GC_2} &= \dot{z}_{b_1} - (2h_1 + e_t + z_{b_2}) \sin(\theta_1) \dot{\theta}_1 + \dot{z}_{b_2} \cos(\theta_1) - h_2 \sin(\theta_2) \dot{\theta}_2. \end{aligned} \qquad \text{(VI.19)}$$

The dot symbol indicates derivatives with respect to time.

The potential energy is

$$V = V_1 + V_2 = m_1 G h_{GC_1} + m_2 G h_{GC_2} \qquad \text{(VI.20)}$$

with

$$\begin{aligned} h_{GC_1} &= z_{b_1} + h_1 \cos(\theta_1) \\ h_{GC_2} &= z_{b_1} + (2h_1 + e_t + z_{b_2}) \cos(\theta_1) + h_2 \cos(\theta_2) \end{aligned} \qquad \text{(VI.21)}$$

The generalized forces $Q_{\mathbf{u}(j)}$ ($j = 1, 2, 3, 4$) result from the horizontal and vertical ground accelerations $\ddot{u}_g(t)$ [m.s^{-2}] and $\ddot{w}_g(t)$ [m.s^{-2}] applied to the system. Other contributions come from the energy $E_{s,b}$ or $E_{s,t}$ stored in the springs and the energy $E_{d,b}$ or $E_{d,t}$ dissipated in the dampers of both interfaces, so that

$$\begin{aligned} Q_{\mathbf{u}(j)} &= \sum_i \left(\frac{\partial x_{CG_i}}{\partial \mathbf{u}(j)} F_{x,GC_i} + \frac{\partial z_{CG_i}}{\partial \mathbf{u}(j)} F_{z,GC_i} \right) \\ &\quad + \frac{\partial E_{s,b}}{\partial \mathbf{u}(j)} + \frac{\partial E_{s,t}}{\partial \mathbf{u}(j)} + \frac{\partial E_{d,t}}{\partial \dot{\mathbf{u}}(j)} + \frac{\partial E_{d,b}}{\partial \dot{\mathbf{u}}(j)} \end{aligned} \qquad \text{(VI.22)}$$

where $\mathbf{u}$ is the vector gathering the variables of the system. The parameters(x_{GC_i}; z_{GC_i}) give the coordinates of the point where act the forces $F_{x,GC_i} = -m_i \ddot{u}_g$ and $F_{z,GC_i} = -m_i \ddot{w}_g$ due to the ground accelerations. The energy stored in the springs and dissipated in the dampers of the interfaces are expressed by

$$\begin{aligned}
E_{s,b} &= \frac{1}{2} k_b \int\limits_{-b_1}^{b1} \left[z_{b_1} - x \sin\left(\theta_2 - \theta_1\right)\right]^2 dx = \frac{1}{3} k_b b_1^3 \sin^2 \theta_1 + k_b b_1 z_{b_1}^2 \\
E_{s,t} &= \frac{1}{2} k_t \int\limits_{-b}^{b} \left[z_{b_2} - x \sin \theta_1\right]^2 dx = \frac{1}{3} k_t b^3 \sin^2\left(\theta_2 - \theta_1\right) + k_t b z_{b_1}^2 \\
E_{d,b} &= \frac{1}{2} c_b \int\limits_{-b_1}^{b1} \left[\dot{z}_{b_1} - x \cos\left(\theta_1\right) \dot{\theta}_1\right]^2 dx = \frac{1}{3} c_b b_1^3 \cos^2\left(\theta_1\right) \dot{\theta}_1^2 + c_b b_1 \dot{z}_{b_1}^2 \\
E_{d,t} &= \frac{1}{2} c_t \int\limits_{-b_1}^{b1} \left[\dot{z}_{b_1} - x \cos\left(\theta_2 - \theta_1\right) \left(\dot{\theta}_2 - \dot{\theta}_1\right)\right]^2 dx \\
&= \frac{1}{3} c_t b^3 \cos^2\left(\theta_2 - \theta_1\right) \left(\dot{\theta}_2 - \dot{\theta}_1\right)^2 + c_t b \dot{z}_{b_2}^2
\end{aligned} \tag{VI.23}$$

The equations of motion are therefore (Eqs. VI.24 to VI.27):

$$\begin{aligned}
&\left[I_{GC_1} + m_1 h_1^2 + m_2\left(2h_1 + e_t + z_{b_2}\right)\right] \ddot{\theta}_1 + m_2 h_2 \left(2h_1 + e_t + z_{b_2}\right) \cos\left(\theta_2 - \theta_1\right) \ddot{\theta}_2 \\
&\qquad + m_2\left(2h_1 + e_t + 2z_{b_2}\right) \dot{z}_{b_2} \dot{\theta}_1 + m_2 h_2 \left(2h_1 + e_t + z_{b_2}\right) \sin\left(\theta_2 - \theta_1\right) \dot{\theta}_2^2 \\
&\quad - \left[m_1 h_1 + m_2\left(2h_1 + e_t + z_{b_2}\right)\right] \sin\left(\theta_1\right) \ddot{z}_{b_1} - G\left[m_1 h_1 + m_2\left(2h_1 + e_t + z_{b_2}\right)\right] \sin\left(\theta_1\right) \\
&\qquad = -\frac{2}{3} k_b b_1^3 \sin\theta_1 \cos\theta_1 + \frac{2}{3} k_t b^3 \sin\left(\theta_2 - \theta_1\right) \cos\left(\theta_2 - \theta_1\right) \\
&\qquad - \frac{2}{3} c_b b_1^3 \cos^2\left(\theta_1\right) \dot{\theta}_1 + \frac{2}{3} c_t b^3 \cos^2\left(\theta_2 - \theta_1\right) \left(\dot{\theta}_2 - \dot{\theta}_1\right) \\
&\qquad - \ddot{u}_g \left[m_1 h_1 \cos\theta_1 + m_2\left(2h_1 + e_t + z_{b_2}\right) \cos\theta_1\right] \\
&\qquad + \ddot{w}_g \left[m_1 h_1 \sin\theta_1 + m_2\left(2h_1 + e_t + z_{b_2}\right) \sin\theta_1\right]
\end{aligned} \tag{VI.24}$$

$$\begin{aligned}
&m_2 h_2 \left(2h_1 + e_t + z_{b_2}\right) \cos\left(\theta_2 - \theta_1\right) \ddot{\theta}_1 + \left[I_{GC_2} + m_2 h_2^2\right] \ddot{\theta}_2 \\
&\qquad + 2 m_2 h_2 \cos\left(\theta_2 - \theta_1\right) \dot{z}_{b_2} \dot{\theta}_1 + m_2 h_2 \left(2h_1 + e_t + z_{b_2}\right) \sin\left(\theta_2 - \theta_1\right) \dot{\theta}_1^2 \\
&\qquad - m_2 h_2 \sin\left(\theta_2\right) \ddot{z}_{b_1} + m_2 h_2 \sin\left(\theta_2 - \theta_1\right) \ddot{z}_{b_2} - m_2 G h_2 \sin\left(\theta_2\right) \\
&\qquad = -\frac{2}{3} k_t b^3 \sin\left(\theta_2 - \theta_1\right) \cos\left(\theta_2 - \theta_1\right) \\
&\qquad - \frac{2}{3} c_t b^3 \cos^2\left(\theta_2 - \theta_1\right) \left(\dot{\theta}_2 - \dot{\theta}_1\right) \\
&\qquad - \ddot{u}_g \left[m_2 h_2 \cos\theta_2\right] + \ddot{w}_g \left[m_2 h_2 \sin\theta_2\right]
\end{aligned} \tag{VI.25}$$

$$\begin{aligned}
&-\left[m_1 h_1 \sin\theta_1 + m_2\left(2h_1 + e_t + z_{b_2}\right)\sin\theta_1\right]\ddot{\theta}_1 - m_2 h_2 \sin\left(\theta_2\right)\ddot{\theta}_2 + \left(m_1 + m_2\right)\ddot{z}_{b_1} + m_2\cos\left(\theta_2\right)\ddot{z}_{b_2} \\
&-2m_2\sin\left(\theta_1\right)\dot{z}_{b_2}\dot{\theta}_1 - \cos\left(\theta_1\right)\left[m_1 h_1 + m_2\left(2h_1 + e_t + z_{b_2}\right)\right]\dot{\theta}_1^2 - m_2 h_2\cos\left(\theta_2\right)\dot{\theta}_2^2 + G\left(m_1 + m_2\right) \\
&\qquad = -2k_b b_1 z_{b_1} - 2c_b b_1 \dot{z}_{b_1} - \ddot{w}_g\left(m_1 + m_2\right) \qquad \text{(VI.26)}
\end{aligned}$$

$$\begin{aligned}
&-m_2 h_2 \sin\left(\theta_2 - \theta_1\right)\ddot{\theta}_2 + m_1\cos\left(\theta_1\right)\ddot{z}_{b_1} + m_2\ddot{z}_{b_2} \\
&\quad - m_2\left(2h_1 + e_t + z_{b_2}\right)\dot{\theta}_1^2 - m_2 h_2\cos\left(\theta_2 - \theta_1\right)\dot{\theta}_2^2 + Gm_2\cos\left(\theta_1\right) \\
&\qquad = -2k_t b z_{b_2} - 2c_t b\dot{z}_{b_2} - \ddot{u}_g m_2\sin\left(\theta_1\right) - \ddot{w}_g m_2\cos\left(\theta_1\right) \qquad \text{(VI.27)}
\end{aligned}$$

Transition between configurations

The configuration in which the system behaves is defined by two parameters g_b and g_t. Their values depend on the gap functions, given in Eq. VI.28:

$$\begin{aligned}
g(1) &= b_1\left[sign\left(\theta_1\right)\right]\theta_1 + z_{b_1} \\
g(2) &= b\left[sign\left(\theta_2 - \theta_1\right)\right]\left(\theta_2 - \theta_1\right) + z_{b_2} \qquad \text{(VI.28)}
\end{aligned}$$

respectively. For instance, g_b is equal to 0 if $g(1)$ is positive, translating the uplift of the lower block, and to 1 if $g(1)$ is negative.

Implementation in the numerical scheme with event-driven strategy

The equations of motion have to be linearised for the use in the adopted numerical scheme with the event-driven strategy. They are presented in a matrix form in Eq. VI.29:

$$\mathbf{M}\ddot{\mathbf{u}} + \mathbf{C}\dot{\mathbf{u}} + \mathbf{K}\mathbf{u} = \mathbf{f} \qquad \text{(VI.29)}$$

with

$$\mathbf{M} = \begin{bmatrix} I_{GC_1} + m_1 h_1^2 + m_2\left(2h_1 + e_t\right)^2 & m_2 h_2\left(2h_1 + e_t\right) & 0 & 0 \\ m_2 h_2\left(2h_1 + e_t\right) & I_{GC_2} + m_2 h_2^2 & 0 & 0 \\ 0 & 0 & m_1 + m_2 & m_2 \\ 0 & 0 & m_2 & m_2 \end{bmatrix} \qquad \text{(VI.30)}$$

$$\mathbf{C} = \begin{bmatrix} \varphi_1 c_b b_1^3 + \varphi_1^{'} c_t b^3 & -\varphi_1^{'} c_t b^3 & -\varphi_2 c_b b_1^2 & \varphi_2^{'} c_t b^2 \\ -\varphi_1^{'} c_t b^3 & \varphi_1^{'} c_t b^3 & 0 & -\varphi_2^{'} c_t b^2 \\ -\varphi_2 c_b b_1^2 & 0 & 3\varphi_1 c_b b_1 & 0 \\ \varphi_2^{'} c_t b^2 & -\varphi_2^{'} c_t b^2 & 0 & 3\varphi_1^{'} c_t b \end{bmatrix} \qquad \text{(VI.31)}$$

$$\mathbf{K} = \begin{bmatrix} \mathbf{K}_{1,1} & -\varphi_1^{'} k_t b^3 & -\varphi_2^{'} k_b b_1^2 & \varphi_2^{'} k_t b^2 \\ -\varphi_1^{'} k_t b^3 & \mathbf{K}_{2,2} & 0 & -\varphi_2^{'} k_t b^2 \\ -\varphi_2^{'} k_b b_1^2 & 0 & 3\varphi_1 k_b b_1 & 0 \\ \varphi_2^{'} k_t b^2 & -\varphi_2^{'} k_t b^2 & 0 & 3\varphi_1^{'} k_t b \end{bmatrix} \qquad \text{(VI.32)}$$

$$\mathbf{f} = \begin{bmatrix} -\left[m_1 h_1 + m_2\left(2h_1 + e_t\right)\right]\ddot{u}_g \\ -m_2 h_2 \ddot{u}_g \\ -\left(m_1 + m_2\right)\left(\ddot{w}_g + G\right) \\ -m_2\left(\ddot{w}_g + G\right) \end{bmatrix}. \tag{VI.33}$$

with $\varphi_1 = \frac{1+g_b}{3}$, $\varphi_2 = \frac{1-g_b}{2}$, $\varphi_1^{'} = \frac{1+g_t}{3}$, $\varphi_2^{'} = \frac{1-g_t}{2}$, and

$$\begin{aligned} \mathbf{K}_{1,1} &= -m_1 G h_1 - m_2 G\left(2h_1 + e_t\right) + \varphi_1 k_b b_1^3 + \varphi_1^{'} k_t b^3 \\ \mathbf{K}_{2,2} &= -m_2 G h_2 + \varphi_1^{'} k_t b^3. \end{aligned} \tag{VI.34}$$

The energy dissipation in this model is a continuous process. The viscous and flexible interfaces indeed dissipate energy through damping in the dash-pots.

VI.3.2 Application of the 2-stacked blocks with flexible and viscous interfaces model

The model developed in the previous section is used to reproduce the experimental measurements of the seismic test S06 on the short wall with rubber (see Section II.4). In addition to the geometry of the specimen, it is necessary to define an elastic modulus and a damping ratio as input for the interfaces. A first guess for the elastic modulus of the rubber interfaces is given in Chapter III, but has to be reduced because of the effects of repeated shakes.

Figure VI.10 shows the time evolution of the rotations of both blocks obtained with the current model and compares them with the experimental measurements. The inputs for the interfaces are 4.45 MPa for the elastic modulus and 72 % for the damping ratio. The former value is included in the range given by the producer (see Annex A). The predictions of the model are in good agreement with the experimental data. Both the initiation of the rocking motion and the maximum rocking angle are well captured. In comparison to the models used for the specimen without rubber, the assumption of a rigid block for the modelling of the URM wall seems to be relevant. This can be explained by the presence of the rubber layers. Indeed, the stiffness of these interfaces is much lower than the stiffness of the URM wall and the assumption on this latter is found to be more realistic. Some slight discrepancies are however observed, especially for the amplitude of the rotation just before the initiation of the motion and for the damping at the end of the simulation, when the specimen is in free rocking.

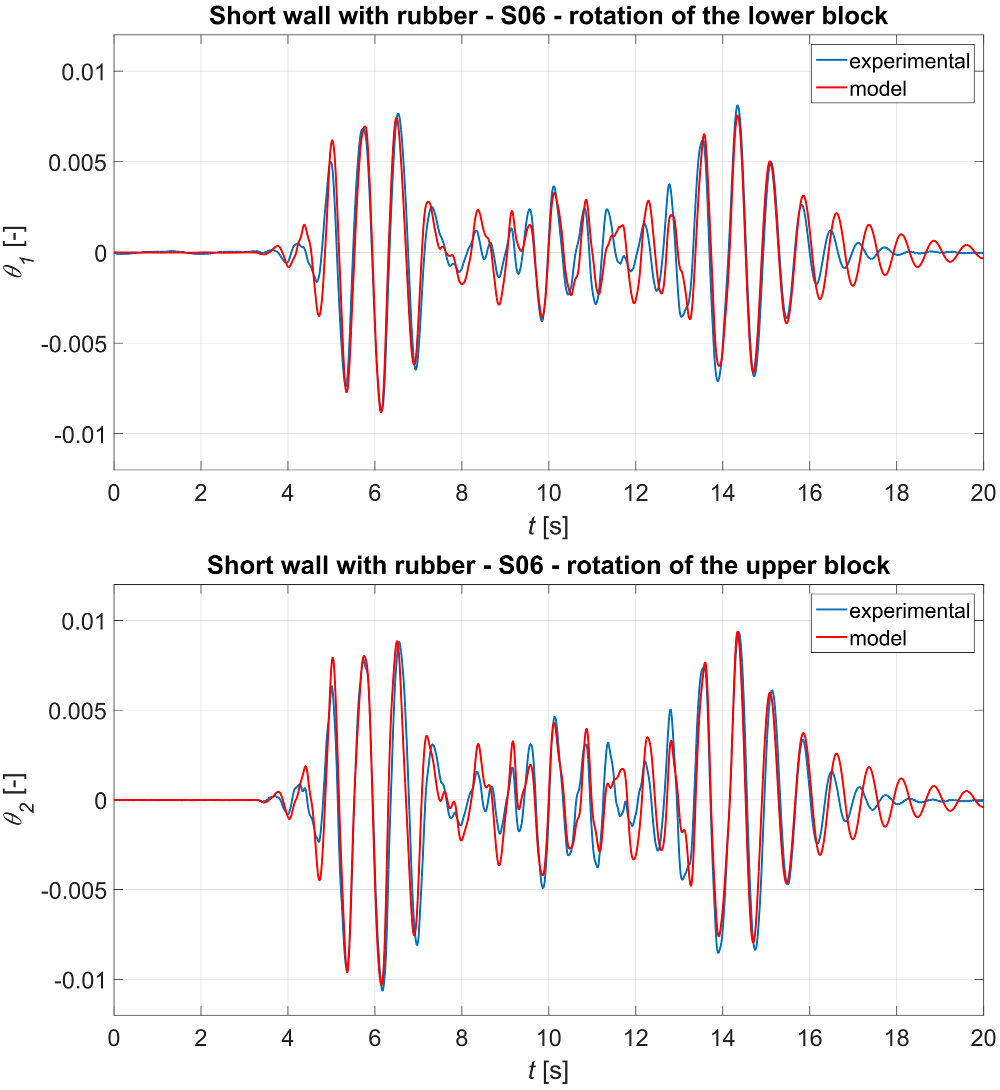

Short wall with rubber - S06 - rotation of the lower block

Short wall with rubber - S06 - rotation of the upper block

Figure VI.10: Rocking behaviour - Comparisons of the predictions of the 2-stacked blocks with flexible and viscous interfaces model with experimental measurements (short wall with rubber - S06)

VI.4 Conclusions

This chapter focuses on the rocking behaviour of 0.72 m long URM walls including soundproofing rubber devices. These walls are built in clay masonry with glued horizontal joints and empty head joints (tongue-and-groove system). This interest is motivated by observations of the shake table tests on these specimens (see Section II.4) during which a significant RM was experienced for the shakes at the highest acceleration levels.

Considering the specimen without any acoustic layer, the experimental measurements are first compared to the predictions of a model, based on the simple theory of Housner and modified to consider the additional mass placed at the top of the wall. It is found that a proper modelling of the additional mass is required and that the assumption of a rigid block for the URM wall is questionable. A second model is therefore implemented with the developments of Spanos et al. [115]. Despite an appropriate consideration of the additional mass, the predictions of the model did not provide relevant results. Thus, the studied URM wall cannot be assumed as rigid and the modelling of its rocking behaviour requires additional investigations. Existing models seem inadequate for the studied type of masonry because they supposed that the base of the block is rigid. The energy dissipation at the impacts is a main issue since the blocks do not rotate around their corners and, thus, the use of the principle of conservation of the angular momentum is not valid.

Regarding the specimen with soundproofing devices, a new 2-stacked-block model is developed. This model includes flexible and viscous interfaces between the lower block and the foundation, as well as between the lower and upper blocks which represents the main innovation. The numerical results are in good agreement with the experimental data. In this case, the presence of the rubber interfaces makes relevant the use of rigid blocks for the modelling of URM wall. The amplitude just after the initiation of the rocking motion and the behaviour in free rocking could be improved by, for instance, defining another type of material law for the interfaces.

Chapter VII

Conclusions and perspectives

VII.1Conclusions
VII.2Perspectives for future works

VII.1 Conclusions

This thesis focuses on URM sub-structures implementing a particular masonry bonding for constructional efficiency purposes. Hollow clay blocks of relatively limited thickness (max. 15 cm) and high compressive strength, up to 15 MPa, are assembled by glue-mortar with thin-bed layered joints and a tongue-and-groove system for the head joints. Specific details can be included, namely 1-cm thick rubber layers at their bottom and top, for soundproofing reasons. The structures can also display an opening or a non-rectangular horizontal cross-section. The main objective of this thesis is to contribute to the improvement of the design of these URM structures in low-to-moderate seismic areas, like Belgium, thanks to a better understanding of their actual behaviour. In these regions, URM is traditionally used as load-bearing solution for private dwellings (low- and mid-rise buildings), but it recently found applications in multi-storey structures, like apartment buildings up to 5-6 levels.

In this perspective, experimental campaigns have been performed and aimed at developing a better understanding of the seismic in-plane behaviour of URM sub-structures and at investigating the influence of soundproofing devices, openings and perpendicular walls. These campaigns included static-cyclic tests with displacement controlled and shake table tests with increasing acceleration level. A total of 14 specimens have been tested. The main conclusions are the following:

- the soundproofing rubber devices affect the response of the URM walls under both vertical compression and horizontal shear loads. They indeed increase the deformability of the walls. Due to the interaction between the rubber and the masonry, the compression resistance is reduced in comparison to classical configurations without rubber (1 MPa). In a presented campaign (see Section II.2), the level was halved for specimen with acoustic layers. Moreover, the stiffness is reduced due to the presence of rubber, inducing larger vertical and, most importantly, horizontal displacements. The lateral stiffness is roughly divided by 3 when rubber layers are added. A positive effect of the rubber is the observation of a better dissipation of the seismic energy thanks to these acoustic devices.

- in the presence of an opening, the masonry spandrel has to be associated with RC elements, namely a lintel and a slab. A particular attention should be given to the support length of the lintel in order to allow assuming an effective coupling between the piers.

- a wall perpendicular to the seismic action could improve the shear resistance of the wall composed of two perpendicular sections, provided that the connection between the perpendicular sections does not fail in shear.

Based on experimental research, the non-linear response of URM walls subjected to in-plane shear loading can be characterised. Figure VII.1 shows the general shape of the force-displacement curve related to these walls. In design procedure, this curve is simplified and a bilinear curve is considered. Three parameters define this latter and their calibration is a main outcome of the different chapters of this thesis. Chapters II and III provide information on the stiffness k_{ini} of the curve through the characterisation of equivalent elastic and shear moduli, assuming that the URM specimens can be modelled by homogeneous and isotropic beams. Such an approach involves a dependence of the shear modulus on the compression level. Chapter IV deals with the definition of a material law valid for the studied type of masonry, independently of the geometry of the walls. It compares the force-displacement curve obtained by the experimental measurements with the results of a numerical model. The main conclusion is that the maximum horizontal shear V_{max} can be predicted by an equivalent frame model with a good approximation. In chapter V, the determination of the maximum horizontal shear V_{max} of walls with a non-rectangular cross-section is improved with due consideration for the contribution of sections of walls perpendicular to the seismic action. Simplifications are proposed to allow the calculation by hand. These improvements could be easily implemented in current existing numerical tools. Finally, the maximum drift δ_{max} is assessed in Chapter II for some configurations and calibrated for the material law in Chapter IV. This maximum drift corresponds to a shear failure, the wall being still able to withstand the gravity loads. Additional investigations are however required to clarify the influence of several parameters (compression level, failure mode, etc.) on the drift values. For instance, the possibility for walls to rock does not modify the internal forces to which the walls are submitted, but increases the maximum acceleration they can sustain. Indeed, the horizontal shear is limited and presents a plateau, but the drift capacity of the walls is significantly increased.

In general, it is found that the studied type of masonry exhibits a larger strength, but its behaviour is more brittle than historical masonry.

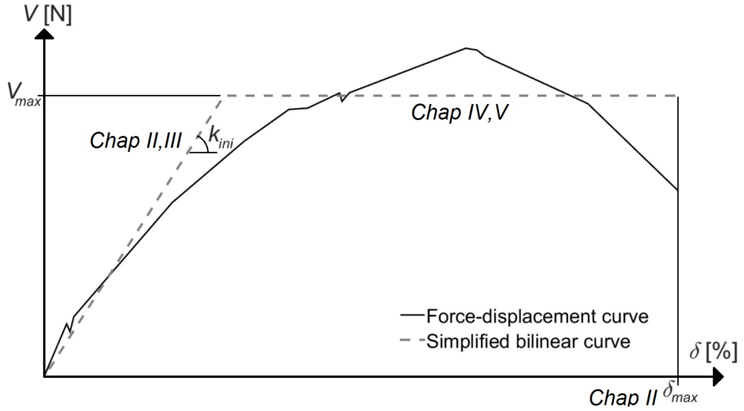

Figure VII.1: Force-displacement curve for URM wall under in-plane shear loading

The experimental campaign also raises interest in the rocking behaviour of blocks. Chapter VI is dedicated to the comparison of different existing rocking models and introduces a new rocking model. It is concluded that the studied type of masonry can be assumed as rigid in presence of rubber layers only. In their absence, such an assumption is not suitable and a main issue is the handling of the transition between configurations of motion with an impact.

VII.2 Perspectives for future works

The design of load-bearing URM structures in low-to-moderate seismic regions is an essential challenge in the field of civil engineering in view of the large number of buildings implementing this structural solution. A better understanding of the seismic response is therefore required to represent properly this specific action and to ensure a sufficient safety level.

Further research are still necessary, especially for new types of masonry bonding. Moreover, technical solutions have been developed by the industry to face the more and more demanding standards in terms of individual comfort. These solutions modify the seismic response and also need to be investigated. According to the author, future works could be focused on:

- the characterisation of an equivalent shear modulus: the assessment of equivalent mechanical properties highlighted a dependence on the compression level and on the length of the wall for the shear modulus. It is well known that the strength capacity of URM walls is influenced by the compression level and their stiffness seems to be affected as well. Regarding the length of the wall, this can be explained by the use of empty vertical joints. Indeed, the number of head joints varies with the length of the wall and it can be expected that a larger number of joints involves a larger lateral deformability. Theses effects have to be studied by testing, in cyclic conditions for example, identical walls subjected to different compression levels and/or walls with various lengths under the same compression level. An alternative is to characterise the fundamental frequency of these specimens and to derive equivalent mechanical properties thanks to a frequency equation established with appropriate boundary conditions.

- the contribution to the shear resistance of perpendicular walls: taking into account the walls perpendicular to the seismic action should improve the seismic design of URM structures, especially for buildings whose floors are one-way spanning. Different points have to be investigated. First, the length of the perpendicular walls which contributes to the resistance has to be defined. Then, criteria for the efficiency of the connection have to be established. Finally, attention should be paid to the influence of the compression level and to the effects of a possible torsion. Additional tests could also help to the validation of the proposed modifications for the estimation of the compressive length by hand calculations.

- the integration of a material law including progressive damaging: the modelling at the macro-scale of the tested specimens with equivalent frames shows that the beam response does not change when the magnitude of the controlled displacement is kept at a same level. On the contrary, experiments evidence a progressive damaging and the failure can occur after few cycles at the same amplitude. In order to model this configuration, an update of the material law will be useful.

- the extension to entire building: the modelling of the tested specimens and the calibration of a material law for the studied type of masonry are the necessary first step. This material law can be used for the analysis of entire buildings and the assessment of their seismic performance.

Besides the aspects related to URM structures, the modelling of the rocking motion should receive interest for the formulation of the energy dissipation at the impacts. Different models have been developed for blocks on a rigid support and all assume that, at least, the base of the block is rigid. The main consequence is that the blocks can only rotate around the corners of their base. The transition from one rotation point to the other is then accompanied by a sudden decrease of the angular velocity (impact). The importance of the jump is determined thanks to the principle of conservation of the angular momentum, but experimental tests showed that this procedure is irrelevant and alternatives should be found.

Bibliography

[1] Experimental Investigation of Unreinforced Brick Masonry Walls in Flexure. *Journal of Structural Engineering*, 130(3):423–432, 2004.

[2] Cnr dt 212 2013. istruzioni per la valutazione affidabilistica della sicurezza sismica di edifici esistenti. *Consiglio nazionale delle ricerche (in Italian)*, 2014.

[3] Sinan Acikgoz and Matthew J DeJong. The interaction of elasticity and rocking in flexible structures allowed to uplift. *Earthquake Engineering & Structural Dynamics*, 41(15):2177–2194, 2012.

[4] Masoud Ansari, Nader Jalili, and Ebrahim Esmailzadeh. Exact frequency analysis of a rotating cantilever beam with tip mass subjected to torsional-bending vibrations. *Journal of Vibration and Acoustics*, 133(4), 2011.

[5] A Anthoine, G Magonette, and Guido Magenes. Shear-compression testing and analysis of brick masonry walls. In *Proceedings of the 10th European conference on earthquake engineering*, 1995.

[6] Amjad J Aref and Kiarash M Dolatshahi. A three-dimensional cyclic meso-scale numerical procedure for simulation of unreinforced masonry structures. *Computers & Structures*, 120:9–23, 2013.

[7] G. Bergamo, M. Eusebio, G. Manfredi, and A. Prota. Shake table tests on a tuff masonry building. In *8th US National Conference on Earthquake Engineering 2006*, volume 7, pages 4172–4181, 2006.

[8] Katrin Beyer. Peak and residual strengths of brick masonry spandrels. *Engineering Structures*, 41:533–547, aug 2012.

[9] M Lj Bojić and DL Loveday. The influence on building thermal behavior of the insulation/masonry distribution in a three-layered construction. *Energy and buildings*, 26(2):153–157, 1997.

[10] Danielle EM Bond, William W Clark, and Mark Kimber. Configuring wall layers for improved insulation performance. *Applied energy*, 112:235–245, 2013.

[11] RL Boroscheck and David Romo. Overturning criteria for non-anchored non-symmetric rigid bodies. In *Proceeding of the 13th world conference on earthquake engineering*, pages 1–6, 2004.

[12] Jitendra K Bothara, Rajesh P Dhakal, and John B Mander. Seismic performance of an unreinforced masonry building: An experimental investigation. *Earthquake Engineering & Structural Dynamics*, 39(June 2009):45–68, 2009.

[13] F Braga and D Liberatore. A finite element for the analysis of the response of masonry buildings. In *Proceedings of 5th North American masonry conference*, 1990.

[14] J C Bruch Jr and T P Mitchell. Vibrations of a mass-loaded clamped-free Timoshenko beam. *Journal of Sound and Vibration*, 114(2):341–345, 1987.

[15] I. Calio and A. Greco. Free vibrations of Timoshenko beam-columns on Pasternak foundations. *Journal of Vibration and Control*, 19(5):686–696, February 2012.

[16] Ivo Caliò, Massimo Marletta, and Bartolomeo Pantò. A new discrete element model for the evaluation of the seismic behaviour of unreinforced masonry buildings. *Engineering Structures*, 40:327–338, 2012.

[17] T Camelbeeck and M de Becker. Le séisme de liège du 8 novembre 1983. *Ciel et terre (in French)*, 100(1):13–19, 1984.

[18] Roberto Capozucca. Experimental analysis of historic masonry walls reinforced by CFRP under in-plane cyclic loading. *Composite Structures*, 94(1):277–289, 2011.

[19] S Cattari and S Lagomarsino. Masonry structures. *Developments in the field of displacement based seismic assessment, IUSS Press (PAVIA) and EUCENTRE*, page 524, 2013.

[20] C Chiarabba, A Amato, M Anselmi, P Baccheschi, I Bianchi, M Cattaneo, G Cecere, L Chiaraluce, MG Ciaccio, P De Gori, et al. The 2009 l'aquila (central italy) mw6. 3 earthquake: Main shock and aftershocks. *Geophysical Research Letters*, 36(18), 2009.

[21] A Contento and A Di Egidio. Investigations into the benefits of base isolation for non-symmetric rigid blocks. *Earthquake Engineering & Structural Dynamics*, 38(7):849–866, 2009.

[22] Alexandre A. Costa, António Arêde, Alfredo Campos Costa, Andrea Penna, and Aníbal Costa. Out-of-plane behaviour of a full scale stone masonry façade. Part 2: shaking table tests. *Earthquake Engineering & Structural Dynamics*, 42(14):n/a–n/a, jun 2013.

[23] Alexandre a. Costa, Andrea Penna, and Guido Magenes. *Seismic Performance of Autoclaved Aerated Concrete (AAC) Masonry: From Experimental Testing of the In-Plane Capacity of Walls to Building Response Simulation*, volume 15. jan 2011.

[24] Francesca da Porto, Manuel Grendene, and Claudio Modena. Estimation of load reduction factors for clay masonry walls. *Earthquake Engineering & Structural Dynamics*, 38(10):1155–1174, August 2009.

[25] Francesca da Porto, Giovanni Guidi, Enrico Garbin, D Ph, and Claudio Modena. In-Plane Behavior of Clay Masonry Walls : Experimental Testing and Finite-Element Modeling. 136(November):1379–1392, 2010.

[26] Comité Européen de Normalisation. Eurocode 6: Design of masonry structures - part 1-1: General rules for reinforced and unreinforced masonry structures. *Comit Europen de Normalisation: Brussels, Belgium*, 2005.

[27] Hervé Degée, Vincent Denoël, PAULO Candeias, A Campos Costa, and E Coelho. Experimental investigation on the seismic behaviour of north european masonry houses. In *Proceedings of SISMICA 07, Sismic Congress*, page 12, 2007.

[28] Matthew J DeJong and Elias G Dimitrakopoulos. Dynamically equivalent rocking structures. *Earthquake engineering & structural dynamics*, 43(10):1543–1563, 2014.

[29] Alexandre Depouhon, Emmanuel Detournay, and Vincent Denoël. Event-driven integration of linear structural dynamics models under unilateral elastic constraints. *Computer Methods in Applied Mechanics and Engineering*, 276:312–340, 2014.

[30] Comune di Genova. Catedrale di s. lorenzo.

[31] Kiarash M Dolatshahi and Amjad J Aref. Two-dimensional computational framework of meso-scale rigid and line interface elements for masonry structures. *Engineering Structures*, 33(12):3657–3667, 2011.

[32] Mohamed A ElGawady, Quincy Ma, John W Butterworth, and Jason Ingham. Effects of interface material on the performance of free rocking blocks. *Earthquake Engineering & Structural Dynamics*, 40(4):375–392, 2011.

[33] E. Esmailzadeh and a.R. Ohadi. Vibration and Stability Analysis of Non-Uniform Timoshenko Beams Under Axial and Distributed Tangential Loads. *Journal of Sound and Vibration*, 236(3):443–456, September 2000.

[34] CEN Eurocode. Eurocode 6: Design of masonry structures - part 1 - common rules for reinforced and unreinforced masonry structures. Technical report, EN-1996-1-1, 2005.

[35] SH Farchaly and MG Shebl. Exact frequency and mode shape formulae for studying vibration and stability of Timoshenko beam system. *Journal of sound and vibration*, 180:205–227, 1995.

[36] Guy Focant. l'hÃŽtel de ville de liÃšge.

[37] Department for Communities and The Rt Hon Grant Shapps Local Government. English housing survey 2008: housing stock report. pages 1–174, 2010.

[38] Y Gregoire. Compressive strength of masonry according to eurocode 6: A contribution to the study of the influence of shape factors. *Masonry International*, 20(2):69, 2007.

[39] M C Griffith, J Vaculik, N T K Lam, J Wilson, and E Lumantarna. Cyclic testing of unreinforced masonry walls in two-way bending. *Earthquake Engineering & Structural Dynamics*, 36(6):801–821, may 2007.

[40] MC Griffith and AW Page. On the seismic capacity of typical DPC and slip joints in unreinforced masonry buildings. *Australian Journal of Structural Engineering*, 2(1):133–140, 1998.

[41] SM Han, H Benaroya, and T Wei. Dynamics of transversely vibrating beams using four engineering theories. *Journal of Sound and Vibration*, 225:935–988, 1999.

[42] Emeritus AW Hendry. Masonry walls: materials and construction. *Construction and Building Materials*, 15(8):323–330, 2001.

[43] J.a. Hernández-Urrea and J. Dario Aristizábal-Ochoa. Static and dynamic stability of an elastically restrained Beck column with an attached end mass. *Journal of Sound and Vibration*, 312(4-5):789–800, May 2008.

[44] Pedro A Hidalgo, RL Mayes, HD McNiven, and RW Clough. Cyclic loading tests of masonry single piers, volume 1–height to width ratio of 2. *University of California, Berkeley, Earthquake Engineering Research Center Report No. UCB/EERC-78/27*, 1978.

[45] George W Housner. The behavior of inverted pendulum structures during earthquakes. *Bulletin of the seismological society of America*, 53(2):403–417, 1963.

[46] Andreas J Kappos, Gregory G Penelis, and Christos G Drakopoulos. Evaluation of simplified models for lateral load analysis of unreinforced masonry buildings. *Journal of structural Engineering*, 128(7):890–897, 2002.

[47] FV Karantoni and FN Lirantzaki. Seismic behaviour of "simple masonry buildings" according to en 1998. *Earthquake Resistant Engineering Structures VII*, 104:83, 2009.

[48] MT Kazemi, MH Asl, A Bakhshi, and FR Rofooei. Shaking Table Study of a Full-Scale Single Storey Confined Brick Masonry Building. *sid.ir*, 17(3):184–193, 2010.

[49] Trevor E Kelly. Tentative seismic design guilelines for rocking structures. *Bulletin of the New Zealand Society for Earthquake Engineering*, 42(4):239, 2009.

[50] N. Khaji, M. Shafiei, and M. Jalalpour. Closed-form solutions for crack detection problem of Timoshenko beams with various boundary conditions. *International Journal of Mechanical Sciences*, 51(9-10):667–681, September 2009.

[51] I K Khan and H Abbas. Static and dynamic response of cost effective unreinforced brick masonry buildings. *Archives of Civil and Mechanical Engineering*, 11(4):921–941, 2011.

[52] Aik-Siong Koh, Pol D Spanos, and Jose M Roesset. Harmonic rocking of rigid block on flexible foundation. *Journal of engineering mechanics*, 112(11):1165–1180, 1986.

[53] Elisabeth Kossecka and Jan Kosny. Influence of insulation configuration on heating and cooling loads in a continuously used building. *Energy and Buildings*, 34(4):321–331, 2002.

[54] Anthony N Kounadis. On the overturning instability of a rectangular rigid block under ground excitation. *Open Mechanics Journal*, 4:43–57, 2010.

[55] Anthony N Kounadis, George J Papadopoulos, and Demetrios M Cotsovos. Overturning instability of a two-rigid block system under ground excitation. *ZAMM-Journal of Applied Mathematics and Mechanics/Zeitschrift für Angewandte Mathematik und Mechanik*, 92(7):536–557, 2012.

[56] Yan Hoe Kwok and Alfredo Hua-Sing Ang. *Seismic damage analysis and design of unreinforced masonry buildings*. PhD thesis, University of Illinois at Urbana-Champaign, 1987.

[57] Sergio Lagomarsino, Andrea Penna, Alessandro Galasco, and Serena Cattari. Tremuri program: an equivalent frame model for the nonlinear seismic analysis of masonry buildings. *Engineering Structures*, 56:1787–1799, 2013.

[58] Willy Leclercq. Le tremblement de terre Ã liÃšge, le 9 novembre 1983, avait fait de gros dÃ©gÃ¢ts.

[59] Taeyong Lee and RS Lakes. Anisotropic polyurethane foam with poisson'sratio greater than 1. *Journal of Materials Science*, 32(9):2397–2401, 1997.

[60] X.-F. Li, Y.-a. Kang, and J.-X. Wu. Exact frequency equations of free vibration of exponentially functionally graded beams. *Applied Acoustics*, 74(3):413–420, March 2013.

[61] XF Li. Free Vibration of Axially Loaded Shear Beams Carrying Elastically Restrained Lumped-Tip Masses via Asymptotic Timoshenko Beam Theory. *Journal of Engineering Mechanics*, 139(4):418–428, 2013.

[62] PAULO B Lourenco. *Computational strategies for masonry structures*. TU Delft, Delft University of Technology, 1996.

[63] Paulo B Lourenço and Graça Vasconcelos. Modern masonry structures and earthquakes: reinforced or unreinforced? In *15th International Symposium of MASE (Macedonian Structural Engineering Association)*, pages 1–19, 2013.

[64] K H Low. A modified Dunkerley formula for eigenfrequencies of beams carrying concentrated masses. *International Journal of Mechanical Sciences*, 42:1287–1305, 2000.

[65] K.H. Low. Comparisons of experimental and numerical frequencies for classical beams carrying a mass in-span. *International Journal of Mechanical Sciences*, 41(12):1515–1531, December 1999.

[66] Quincy T Ma and John W Butterworth. Simplified expressions for modelling rigid rocking structures on two-spring foundations. *Bulletin of the New Zealand Society for Earthquake Engineering*, 45(1):31–39, 2012.

[67] L Macorini and BA Izzuddin. Nonlinear analysis of masonry structures using mesoscale partitioned modelling. *Advances in Engineering Software*, 60:58–69, 2013.

[68] G Magenes and AD Fontana. Simplified non-linear seismic analysis of masonry buildings. In *Proc. Br. Masonry Soc. No. 8*, pages 190–195, 1998.

[69] G Magenes, A Galasco, A Penna, and M Da Paré. In-plane cyclic shear tests of undressed double leaf stone masonry panels. *... of the 14th European Conference of ...*, 2010.

[70] Guido Magenes. Masonry building design in seismic areas: recent experiences and prospects from a european standpoint. In *First European conference on earthquake engineering and seismology*, 2006.

[71] Guido Magenes, Gregory R Kingsley, and Gian Michele Calvi. *Seismic testing of a full-scale, two-story masonry building: test procedure and measured experimental response.* Consiglio nazionale delle ricerche, Gruppo nazionale per la Difesa dai terremoti, 1995.

[72] L Majkut. Free and forced vibrations of timoshenko beams described by single difference equation. *Journal of Theoretical and Applied Mechanics*, 47(1):193–210, 2009.

[73] Nicos Makris and Dimitrios Konstantinidis. The rocking spectrum and the limitations of practical design methodologies. *Earthquake engineering & structural dynamics*, 32(2):265–289, 2003.

[74] Rui Marques and Paulo B Lourenço. Possibilities and comparison of structural component models for the seismic assessment of modern unreinforced masonry buildings. *Computers & Structures*, 89(21):2079–2091, 2011.

[75] Dirk R W Martens. Thermal Break with Cellular Glass Units in Load-Bearing Masonry Walls. *9th International Masonry Conference*, pages 1–10, 2014.

[76] TJ Massart, RHJ Peerlings, and MGD Geers. An enhanced multi-scale approach for masonry wall computations with localization of damage. *International journal for numerical methods in engineering*, 69(5):1022–1059, 2007.

[77] Ronald L Mayes, Yutaro Omote, and Ray W Clough. *Cyclic Shear Tests of Masonry Piers.* Earthquake Engineering Research Center, University of California, 1976.

[78] R Meli. Behavior of masonry walls under lateral loads. In *Fifth World Conference on Earthquake Engineering*, 1973.

[79] Yalcin Mengi and Hugh D McNiven. A mathematical model for the in-plane nonlinear earthquake behaviour of unreinforced masonry walls. part 1: Experiments and proposed model. *Earthquake engineering & structural dynamics*, 18(2):233–247, 1989.

[80] BCN Mercatoris and TJ Massart. A coupled two-scale computational scheme for the failure of periodic quasi-brittle thin planar shells and its application to masonry. *International journal for numerical methods in engineering*, 85(9):1177–1206, 2011.

[81] C Michel, B Zapico, P Lestuzzi, F J Molina, and F Weber. Quantification of fundamental frequency drop for unreinforced masonry buildings from dynamic tests. *Earthquake Engineering & Structural Dynamics*, 40(11):1283–1296, sep 2011.

[82] Jelena Milosevic, Mário Lopes, António Sousa Gago, and Rita Bento. In-plane seismic response of rubble stone masonry specimens by means of static cyclic tests. *Construction and Building Materials*, 82:9–19, 2015.

[83] Nebojsa Mojsilovic, Goran Simundic, and Adrian Page. Masonry wallettes with damp-proof course membrane subjected to cyclic shear: An experimental study. *Construction and Building Materials*, 24(11):2135–2144, 2010.

[84] S. Naguleswaran. Vibration and stability of an Euler-Bernoulli beam with up to three-step changes in cross-section and in axial force. *International Journal of Mechanical Sciences*, 45(9):1563–1579, September 2003.

[85] T. Nakagawa, T. Narafu, H. Imai, T. Hanazato, Q. Ali, and C. Minowa. Collapse behavior of a brick masonry house using a shaking table and numerical simulation based on the extended distinct element method. *Bulletin of Earthquake Engineering*, 10(1):269–283, jun 2011.

[86] Photo News. Le sÃ©isme de 1983 n'avait pas fait qu'une victime Ã liÃšge: deux jeunes sont morts quelques jours plus tard.

[87] The University of Liège's Library. Orbi, institutional open repository and bibliography of the university of liège.

[88] D.C.D. Oguamanam. Free vibration of beams with finite mass rigid tip load and flexural-torsional coupling. *International Journal of Mechanical Sciences*, 45(6-7):963–979, June 2003.

[89] Giuseppe Oliveto, Ivo Calio, and Annalisa Greco. Large displacement behaviour of a structural model with foundation uplift under impulsive and earthquake excitations. *Earthquake engineering & structural dynamics*, 32(3):369–393, 2003.

[90] Adrian W Page. Finite element model for masonry. *Journal of the Structural Division*, 104(8):1267–1285, 1978.

[91] Alessandro Palmeri and Nicos Makris. Response analysis of rigid structures rocking on viscoelastic foundation. *Earthquake Engineering & Structural Dynamics*, 37(7):1039–1063, 2008.

[92] B. Pantò, E. Raka, F. Cannizzaro, G. Camata, S. Caddemi, E. Spacone, and I. Caliò. Numerical macro-modeling of unreinforced masonry structures: A critical appraisal. *Civil-Comp Proceedings*, 108, 2015.

[93] Jocelyn Paquette and Michel Bruneau. Pseudo-dynamic testing of unreinforced masonry building with flexible diaphragm. *Journal of Structural Engineering*, (June):708–716, 2003.

[94] Fernando Peña, Paulo B Lourenço, and Alfredo Campos-Costa. Experimental dynamic behavior of free-standing multi-block structures under seismic loadings. *Journal of Earthquake Engineering*, 12(6):953–979, 2008.

[95] Luis Pérez-Lombard, José Ortiz, and Christine Pout. A review on buildings energy consumption information. *Energy and buildings*, 40(3):394–398, 2008.

[96] J Pina-Henriques and Paulo B Lourenço. Masonry compression: a numerical investigation at the meso-level. *Engineering computations*, 23(4):382–407, 2006.

[97] RH Plaut, WT Fielder, and LN Virgin. Fractal behavior of an asymmetric rigid block overturning due to harmonic motion of a tilted foundation. *Chaos, Solitons & Fractals*, 7(2):177–196, 1996.

[98] MJN Priestley and DO Bridgeman. *Seismic resistance of brick masonry walls.* NZ Pottery and Ceramics Research Institute, 1974.

[99] MJN Priestley, RJ Evison, and AJ Carr. Seismic response of structures free to rock on their foundations. *Bulletin of the New Zealand National Society for Earthquake Engineering*, 11(3):141–150, 1978.

[100] Francisco Prieto and Paulo B Lourenço. On the rocking behavior of rigid objects. *Meccanica*, 40(2):121–133, 2005.

[101] Francisco Prieto, Fernando Peña, Paulo B Lourenço, and José V Lemos. Numerical simulation of rigid blocks subjected to rocking motion. 2006.

[102] Ioannis N Psycharis. Dynamic behaviour of rocking two-block assemblies. *Earthquake Engineering & Structural Dynamics*, 19(4):555–575, 1990.

[103] Ioannis N Psycharis. Effect of base uplift on dynamic response of sdof structures. *Journal of Structural Engineering*, 117(3):733–754, 1991.

[104] Ioannis N Psycharis and Paul C Jennings. Rocking of slender rigid bodies allowed to uplift. *Earthquake Engineering & Structural Dynamics*, 11(1):57–76, 1983.

[105] Etablissement public de coopÃ©ration culturelle du Pont du Gard. Le pont du gard.

[106] Pere Roca, Miguel Cervera, Giuseppe Gariup, et al. Structural analysis of masonry historical constructions. classical and advanced approaches. *Archives of Computational Methods in Engineering*, 17(3):299–325, 2010.

[107] Wienerberger sa. Le quartier durable.

[108] Enhanced Safety and Masonry Structures. ESECMaSE - Enhanced Safety and Efficient Construction of Masonry Structures in Europe Periodic Activity Report / Publishable Executive Summary. 9:4–7, 2008.

[109] Hassan Salarieh and Mehrdaad Ghorashi. Free vibration of Timoshenko beam with finite mass rigid tip load and flexural-torsional coupling. *International Journal of Mechanical Sciences*, 48(7):763–779, July 2006.

[110] Amir Hosein Salmanpour, Nebojsa Mojsilovic, and Joseph Schwartz. Deformation capacity of unreinforced masonry walls subjected to in-plane loading: a state-of-the-art review. *International Journal of Advanced Structural Engineering (IJASE)*, 5(1):1–12, 2013.

[111] D. Schermer. Pseudodynamic tests on full scale masonry walls. In *Advances in Earthquake Engineering*, volume 9, pages 303–313, 2001.

[112] D. Schermer. Seismic behaviour of Autoclaved Aerated Concrete masonry constructions. In *Autoclaved Aerated Concrete Innovation and Development - Proceedings of the 4th International Conference on Autoclaved Aerated Concrete*, pages 387–394, 2005.

[113] Harry W Shenton III and Nicholas P Jones. Base excitation of rigid bodies. i: Formulation. *Journal of Engineering Mechanics*, 117(10):2286–2306, 1991.

[114] Pol D Spanos and Aik-Siong Koh. Rocking of rigid blocks due to harmonic shaking. *Journal of Engineering Mechanics*, 110(11):1627–1642, 1984.

[115] Pol D Spanos, Panayiotis C Roussis, and Nikolaos PA Politis. Dynamic analysis of stacked rigid blocks. *Soil Dynamics and Earthquake Engineering*, 21(7):559–578, 2001.

[116] British Standard. Eurocode 8: Design of structures for earthquake resistance. 2005.

[117] Virgine Stassen. Les belges et leur maison, January 2014. Online; posted 20-January-2014.

[118] John William Strutt. *The theory of sound*. 1877.

[119] S P Timoshenko. Philosophical Magazine, Series 6, 41, 744-746. *On the correction for shear of the differential equation for transverse vibrations of bars of uniform cross-section*, 1921.

[120] S P Timoshenko and J N Goodier. *Theory of Elasticity*. McGraw-Hill Book Company, New-York, third edition, 1987.

[121] Stephan P Timoshenko. X. On the transverse vibrations of bars of uniform cross-section. *The London, Edinburgh, and Dublin Philosophical Magazine and Journal of Science*, 43(253):125–131, 1922.

[122] Miha Tomaževič. Dynamic modelling of masonry buildings: storey mechanism model as a simple alternative. *Earthquake engineering & structural dynamics*, 15(6):731–749, 1987.

[123] Miha Tomazevic. *Earthquake-resistant design of masonry buildings*, volume 1. World Scientific, 1999.

[124] Miha Tomaževič and Polona Weiss. Displacement capacity of masonry buildings as a basis for the assessment of behavior factor: an experimental study. *Bulletin of Earthquake Engineering*, 8(6):1267–1294, apr 2010.

[125] K Beyer M Tondelli and S Petry S Peloso. Dynamic testing of a four-storey building with reinforced concrete and unreinforced masonry walls : Prediction and test results. pages 1–24.

[126] Christian Vögeli, Nebojša Mojsilović, and Božidar Stojadinović. Masonry wallettes with a soft layer bed joint: Behaviour under static-cyclic loading. *Engineering Structures*, 86:16–32, 2015.

[127] D Williams and JC Scrivener. Response of reinforced masonry shear walls to static and dynamic cyclic loading. In *Proceedings of the 5th World Conference on Earthquake Engineering, Inst. As. for Earthquake Engineering*, pages 1491–1494, 1973.

[128] Chik-Sing Yim, Anil K Chopra, and Joseph Penzien. Rocking response of rigid blocks to earthquakes. *Earthquake Engineering & Structural Dynamics*, 8(6):565–587, 1980.

[129] H. Zhang, Y.a. Kang, and X.F. Li. Stability and vibration analysis of axially-loaded shear beam-columns carrying elastically restrained mass. *Applied Mathematical Modelling*, 37(16-17):8237–8250, September 2013.

[130] Jian Zhang and Nicos Makris. Rocking response of free-standing blocks under cycloidal pulses. *Journal of Engineering Mechanics*, 127(5):473–483, 2001.

[131] Mills J. Zhuge Y. The behaviour of masonry walls containing a damp proof course under cyclic loads. In *Proceedings of the 2nd Australasian structural engineering conference*, pages 655–661, 1998.

[132] K. Zilch and D. C. Schermer. Experimental investigations on the behaviour of unreinforced masonry-constructions under seismic loadings. In *8th US National Conference on Earthquake Engineering 2006*, volume 7, pages 4243–4252, 2006.

Appendix A

Characteristics of the soundproofing rubber layer

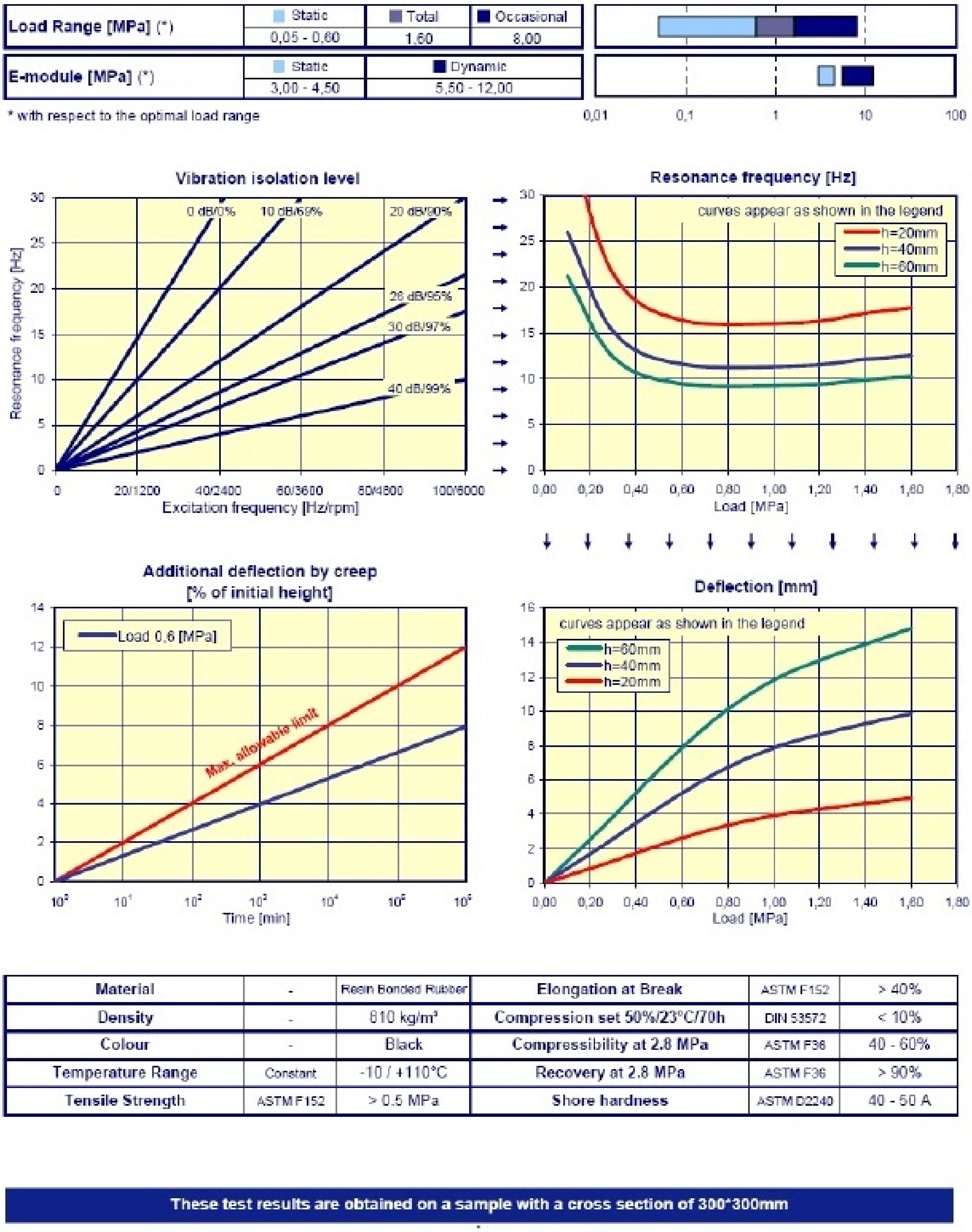

Load Range [MPa] (*)	■ Static	■ Total	■ Occasional
	0,05 - 0,60	1,60	8,00
E-module [MPa] (*)	■ Static	■ Dynamic	
	3,00 - 4,50	5,50 - 12,00	

* with respect to the optimal load range

Material	-	Resin Bonded Rubber	**Elongation at Break**	ASTM F152	> 40%
Density	-	810 kg/m³	**Compression set 50%/23°C/70h**	DIN 53572	< 10%
Colour	-	Black	**Compressibility at 2.8 MPa**	ASTM F36	40 - 60%
Temperature Range	Constant	-10 / +110°C	**Recovery at 2.8 MPa**	ASTM F36	> 90%
Tensile Strength	ASTM F152	> 0.5 MPa	**Shore hardness**	ASTM D2240	40 - 50 A

These test results are obtained on a sample with a cross section of 300*300mm

Figure A.1: Characteristics of the soundproofing rubber layers

Appendix B

Frequency equations

B.1 Frequency equation - first model

The frequency equation of the first model is given by

$$\begin{aligned}\left(1+\frac{\bar{P}}{k'G^*A^*}\right)(M_1+M_2+M_3)&\\ +\left({\omega^*}^2 m^*-\bar{P}\bar{Q}\right)M_4&\\ -\frac{1}{k'G^*A^*}\frac{(1+\lambda^2)}{\lambda^2}\frac{a^*b^*}{({a^*}^2-{b^*}^2)}\bar{Q}M_5 &= 0\end{aligned}$$

where

$$\begin{aligned}\bar{Q} &= {\omega^*}^2\left(m^*{h_b^*}^2+I_{cin}^*\right)\\ \bar{P} &= \omega^* m^* h_b^{*2}\end{aligned}$$

and

$$\begin{aligned}M_1 &= \left[-2a^*b^*+\left({a^*}^2-{b^*}^2\right)\sin a^*\sinh b^*-\frac{{a^*}^2{\varphi_a^*}^2+{b^*}^2{\varphi_b^*}^2}{\varphi_a^*\varphi_b^*}\cos a^*\cosh b^*\right]\\ M_2 &= \bar{P}\left[\frac{a^*\varphi_a^*-b^*\varphi_b^*}{\varphi_a^*\varphi_b^*}(1-\cos a^*\cosh b^*)+\frac{a^*\varphi_b^*+b^*\varphi_a^*}{\varphi_a^*\varphi_b^*}\sin a^*\sinh b^*\right]\\ M_3 &= \left({a^*}^2+{b^*}^2\right)\bar{Q}\left[\frac{1}{\varphi_a^*}\cos a^*\sinh b^*+\frac{1}{\varphi_b^*}\sin a^*\cosh b^*\right]\\ M_4 &= \frac{1}{k'G^*A^*}\frac{(1+\lambda^2)}{\lambda^2}\frac{\left({a^*}^2+{b^*}^2\right)}{({a^*}^2-{b^*}^2)}\left[\frac{a^*b^*}{\varphi_a^*}\sin a^*\cosh b^*-\frac{a^*b^*}{\varphi_b^*}\cos a^*\sinh b^*\right]\\ M_5 &= \left[2{\omega^*}^2m^*+(a^*\varphi_a^*-b^*\varphi_b^*)\bar{Q}\right](1-\cos a^*\cosh b^*)\\ &\quad+\left[\frac{{\varphi_b^*}^2-{\varphi_a^*}^2}{\varphi_a^*\varphi_b^*}{\omega^*}^2m^*+(b^*\varphi_a^*+a^*\varphi_b^*)\bar{Q}\right]\sin a^*\sinh b^*\end{aligned}$$

B.2 Frequency equation - second model

The frequency equation of the second model is given by

$$\bar{L}N_1+\frac{(1+\lambda^2)}{\lambda^2}\frac{\bar{J}}{({a^*}^2-{b^*}^2)}N_2+\frac{1}{\lambda^2}\frac{\bar{F}}{({a^*}^2-{b^*}^2)}N_3+\frac{(1+\lambda^2)}{\lambda^2}\frac{\bar{S}}{({a^*}^2-{b^*}^2)}N_4=0$$

with

$$\begin{aligned}
\bar{L} &= 1+\frac{\omega^{*} m^{*} h_b^{*}}{k' G^{*} A^{*}}-\frac{\omega^{*2} m^{*}}{K_{t,t}^{*}} \\
\bar{J} &= \frac{\omega^{*^{2}} m^{*}}{k' G^{*} A^{*}}+\frac{\omega^{*2} m^{*} h_b^{*}}{K_{t,t}^{*}} a^{*}\left(a^{*}-\varphi_a^{*}\right) \\
\bar{F} &= \frac{\omega^{*^{2}}}{k' G^{*} A^{*}}\left(\left(m^{*} h_b^{*2}+I_{cin}^{*}\right)-\frac{m^{*} h_b^{*}}{K_{r,t}^{*}}\right) \\
\bar{S} &= \frac{1}{K_{r,t}^{*}} \frac{\omega^{*^{2}}}{k' G^{*} A^{*}}\left(m^{*} h_b^{*2}+I_{cin}^{*}\right)
\end{aligned} \tag{B.1}$$

and where

$$\begin{aligned}
N_1 = & \left(1-\frac{\bar{Q}}{K_{r,t}^{*}}\right)\left[2 a^{*} b^{*}-\left(a^{*2}-b^{*2}\right) \sin a^{*} \sinh b^{*}+-\frac{a^{*2} \varphi_a^{*2}+b^{*2} \varphi_b^{*2}}{\varphi_a^{*} \varphi_b^{*}} \cos a^{*} \cosh b^{*}\right] \\
& -\bar{P}\left[\frac{a^{*} \varphi_a^{*}-b^{*} \varphi_b^{*}}{\varphi_a^{*} \varphi_b^{*}}\left(1-\cos a^{*} \cosh b^{*}\right)+\frac{a^{*} \varphi_b^{*}+b^{*} \varphi_a^{*}}{\varphi_a^{*} \varphi_b^{*}} \sin a^{*} \sinh b^{*}\right] \\
& -\left(a^{*2}+b^{*2}\right) \bar{Q}\left[\frac{1}{\varphi_a^{*}} \cos a^{*} \sinh b^{*}+\frac{1}{\varphi_b^{*}} \sin a^{*} \cosh b^{*}\right] \\
& -\frac{a^{*2}+b^{*2}}{K_{r,b}^{*}}\left(1-\frac{\bar{Q}}{K_{r,t}^{*}}\right)\left[\frac{a^{*2}}{\varphi_b^{*}} \sin a^{*} \cosh b^{*}-\frac{b^{*2}}{\varphi_a^{*}} \cos a^{*} \sinh b^{*}\right] \\
& -\frac{1}{K_{r,b}^{*}} \frac{\left(a^{*2}+b^{*2}\right)}{\varphi_a^{*} \varphi_b^{*}}\left[\bar{P}\left(a^{*} \sin a^{*} \cosh b^{*}+b^{*} \cos a^{*} \sinh b^{*}\right)+\bar{Q}\left(a^{*2}+b^{*2}\right) \cos a^{*} \cosh b^{*}\right] \\
& -\frac{k' G^{*} A^{*}}{K_{t,b}^{*}} \frac{\lambda^2}{\left(1+\lambda^2\right)}\left(a^{*4}-b^{*4}\right)\left(1-\frac{\bar{Q}}{K_{r,t}^{*}}\right)\left[\frac{b^{*}}{a^{*} \varphi_a^{*}} \sin a^{*} \cosh b^{*}+\frac{a^{*}}{b^{*} \varphi_b^{*}} \cos a^{*} \sinh b^{*}\right] \\
& +\frac{k' G^{*} A^{*}}{K_{t,b}^{*}} \frac{\lambda^2}{\left(1+\lambda^2\right)} \frac{\left(a^{*4}-b^{*4}\right)}{a^{*} \varphi_a^{*} b^{*} \varphi_b^{*}} \\
& \qquad \left[\bar{P}\left(b^{*} \sin a^{*} \cosh b^{*}-a^{*} \cos a^{*} \sinh b^{*}\right)+\bar{Q}\left(a^{*2}+b^{*2}\right) \sin a^{*} \sinh b^{*}\right] \\
& +\frac{k' G^{*} A^{*}}{K_{t,b}^{*} K_{r,b}^{*}} \frac{\lambda^2}{\left(1+\lambda^2\right)}\left(a^{*2}-b^{*2}\right)\left(1-\frac{\bar{Q}}{K_{r,t}^{*}}\right) \\
& \qquad \left[2 a^{*} b^{*}\left(1-\cos a^{*} \cosh b^{*}\right)+\frac{a^{*4} \varphi_a^{*2}-b^{*4} \varphi_b^{*2}}{a^{*} \varphi_a^{*} b^{*} \varphi_b^{*}} \sin a^{*} \sinh b^{*}\right] \\
& -\frac{k' G^{*} A^{*}}{K_{t,b}^{*} K_{r,b}^{*}} \frac{\lambda^2}{\left(1+\lambda^2\right)} \frac{\left(a^{*2}-b^{*2}\right) \bar{P}}{\varphi_a^{*} \varphi_b^{*}} \\
& \qquad \left[\left(a^{*} \varphi_a^{*}-b^{*} \varphi_b^{*}\right)\left(1-\cos a^{*} \cosh b^{*}\right)-\frac{a^{*2} \varphi_a^{*}+b^{*2} \varphi_b^{*}}{a^{*} b^{*}\left(1+\lambda^2\right)} \sin a^{*} \sinh b^{*}\right] \\
& +\frac{k' G^{*} A^{*}}{K_{t,b}^{*} K_{r,b}^{*}} \frac{\lambda^2}{\left(1+\lambda^2\right)}\left(a^{*4}-b^{*4}\right) \bar{Q}\left(\frac{b^{*}}{a^{*} \varphi_a^{*}} \sin a^{*} \cosh b^{*}+\frac{a^{*}}{b^{*} \varphi_b^{*}} \cos a^{*} \sinh b^{*}\right)
\end{aligned}$$

$$
\begin{aligned}
N_2 \;=\; & -\left(a^{*^2}+b^{*^2}\right) a^* b^* \left(1-\frac{\bar{Q}}{K^*_{r,t}}\right)\left[\frac{1}{\varphi^*_a}\sin a^*\cosh b^* - \frac{1}{\varphi^*_b}\cos a^*\sinh b^*\right] \\
& -\frac{k' G^* A^*}{K^*_{t,t}}\frac{\lambda^2}{(1+\lambda^2)}\frac{\left(a^{*^2}-b^{*^2}\right)}{\varphi^*_a\varphi^*_b}\bar{P} \\
& \qquad \left[\left(a^*\varphi^*_a - b^*\varphi^*_b\right)\left(1-\cos a^*\cosh b^*\right) + \left(a^*\varphi^*_b + b^*\varphi^*_a\right)\sin a^*\sinh b^*\right] \\
& +\bar{Q}\left[2a^*b^*\left(1-\cos a^*\cosh b^*\right) + a^*b^*\frac{\varphi^{*^2}_b-\varphi^{*^2}_a}{\varphi^*_a\varphi^*_b}\sin a^*\sinh b^*\right] \\
& -\left(1-\frac{\bar{Q}}{K^*_{r,t}}\right)\frac{a^*b^*}{K^*_{r,b}}\frac{\left(a^{*^2}+b^{*^2}\right)^2}{\varphi^*_a\varphi^*_b}\sin a^*\sinh b^* \\
& +\frac{\left(a^{*^2}+b^{*^2}\right)}{K^*_{r,b}}\bar{Q}\left[\frac{a^*b^*}{\varphi^*_a}\sin a^*\cosh b^* - \frac{a^*b^*}{\varphi^*_b}\cos a^*\sinh b^*\right] \\
& -\frac{\left(a^{*^2}+b^{*^2}\right)}{K^*_{r,b}}\frac{k' G^* A^*}{K^*_{t,t}}\frac{\lambda^2}{(1+\lambda^2)}\frac{\left(a^{*^2}-b^{*^2}\right)}{\varphi^*_a\varphi^*_b}\bar{P}\left[a^*\sin a^*\cosh b^* + b^*\cos a^*\sinh b^*\right] \\
& -\frac{k' G^* A^*}{K^*_{t,b}}\frac{\lambda^2}{(1+\lambda^2)}\left(a^{*^2}-b^{*^2}\right)\frac{\left(a^{*^2}+b^{*^2}\right)^2}{\varphi^*_a\varphi^*_b}\left(1-\frac{\bar{Q}}{K^*_{r,t}}\right)\cos a^*\cosh b^* \\
& +\frac{k' G^* A^*}{K^*_{t,b}}\frac{\lambda^2}{(1+\lambda^2)}\left(a^{*^2}-b^{*^2}\right)\left(a^{*^2}+b^{*^2}\right)\bar{Q}\left[\frac{1}{\varphi^*_b}\sin a^*\cosh b^* + \frac{1}{\varphi^*_a}\cos a^*\sinh b^*\right] \\
& +\frac{k' G^* A^*}{K^*_{t,b}}\frac{k' G^* A^*}{K^*_{t,t}}\left(\frac{\lambda^2}{(1+\lambda^2)}\right)^2\left(a^{*^2}-b^{*^2}\right)^2 \\
& \qquad \frac{\left(a^{*^2}+b^{*^2}\right)}{\varphi^*_a\varphi^*_b}\bar{P}\left[\frac{1}{a^*}\sin a^*\cosh b^* - \frac{1}{b^*}\cos a^*\sinh b^*\right] \\
& +\frac{k' G^* A^*}{K^*_{t,b}K^*_{r,b}}\frac{\lambda^2}{(1+\lambda^2)}\left(a^{*^4}-b^{*^4}\right)\left(1-\frac{\bar{Q}}{K^*_{r,t}}\right)\left[\frac{a^{*^2}}{\varphi^*_b}\sin a^*\cosh b^* - \frac{b^{*^2}}{\varphi^*_a}\cos a^*\sinh b^*\right] \\
& +\frac{k' G^* A^*}{K^*_{t,b}K^*_{r,b}}\frac{\lambda^2}{(1+\lambda^2)}\left(a^{*^2}-b^{*^2}\right)\bar{Q} \\
& \qquad \left[2a^*b^* - \left(a^{*^2}-b^{*^2}\right)\sin a^*\sinh b^* + \frac{a^{*^2}\varphi^{*^2}_a + b^{*^2}\varphi^{*^2}_b}{\varphi^*_a\varphi^*_b}\cos a^*\cosh b^*\right] \\
& +\frac{k' G^* A^*}{K^*_{t,b}K^*_{r,b}}\frac{k' G^* A^*}{K^*_{t,t}}\left(\frac{\lambda^2}{(1+\lambda^2)}\right)^2\left(a^{*^2}-b^{*^2}\right)^2\bar{P} \\
& \qquad \left[-\frac{a^*\varphi^*_a - b^*\varphi^*_b}{\varphi^*_a\varphi^*_b}\left(1-\cos a^*\cosh b^*\right) + \left(\frac{a^{*^2}}{b^*\varphi^*_b} + \frac{b^{*^2}}{a^*\varphi^*_a}\right)\sin a^*\sinh b^*\right]
\end{aligned}
$$

$$
\begin{aligned}
N_3 \;=\;& a^*b^*\left(a^{*^2}+b^{*^2}\right)\left(1+\lambda^2\right)\bar{P}\left[\frac{1}{\varphi_a^*}\sin a^*\cosh b^*-\frac{1}{\varphi_b^*}\cos a^*\sinh b^*\right]\\
&+a^*b^*\left(1+\lambda^2\right)\bar{Q}\left[\left(a^*\varphi_a^*-b^*\varphi_b^*\right)\left(1-\cos a^*\cosh b^*\right)+\left(a^*\varphi_b^*+b^*\varphi_a^*\right)\sin a^*\sinh b^*\right]\\
&+\frac{k'G^*A^*}{K_{t,t}^*}\lambda^2\left(a^{*^2}-b^{*^2}\right)\bar{\bar{P}}\left[2a^*b^*-\left(a^{*^2}-b^{*^2}\right)\sin a^*\sinh b^*+\frac{a^{*^2}\varphi_a^{*^2}+b^{*^2}\varphi_b^{*^2}}{\varphi_a^*\varphi_b^*}\cos a^*\cosh b^*\right]\\
&+\frac{\left(1+\lambda^2\right)}{K_{r,b}^*}\bar{P}a^*b^*\frac{\left(a^{*^2}+b^{*^2}\right)^2}{\varphi_a^*\varphi_b^*}\sin a^*\sinh b^*\\
&-\frac{\lambda^2}{K_{r,b}^*}\frac{k'G^*A^*}{K_{t,t}^*}\left(a^{*^4}-b^{*^4}\right)\bar{P}\left(\frac{a^{*^2}}{\varphi_b^*}\sin a^*\cosh b^*-\frac{b^{*^2}}{\varphi_a^*}\cos a^*\sinh b^*\right)\\
&+\frac{\left(1+\lambda^2\right)}{K_{r,b}^*}a^*b^*\left(a^{*^2}+b^{*^2}\right)\bar{Q}\left[a^*\sin a^*\cosh b^*+b^*\cos a^*\sinh b^*\right]\\
&+\frac{k'G^*A^*}{K_{t,b}^*}\lambda^2\left(a^{*^4}-b^{*^4}\right)\bar{P}\frac{a^{*^2}+b^{*^2}}{\varphi_a^*\varphi_b^*}\cos a^*\cosh b^*\\
&+\frac{k'G^*A^*}{K_{t,b}^*}\frac{k'G^*A^*}{K_{t,t}^*}\frac{\lambda^4}{\left(1+\lambda^2\right)}\left(a^{*^2}+b^{*^2}\right)\left(a^{*^2}-b^{*^2}\right)^2\bar{P}\left[\frac{b^*}{a^*\varphi_a^*}\sin a^*\cosh b^*+\frac{a^*}{b^*\varphi_b^*}\cos a^*\sinh b^*\right]\\
&-\frac{k'G^*A^*}{K_{t,b}^*}\lambda^2\left(a^{*^4}-b^{*^4}\right)\bar{Q}\left[b^*\sin a^*\cosh b^*-a^*\cos a^*\sinh b^*\right]\\
&-\frac{k'G^*A^*}{K_{t,b}^*}\lambda^2\left(a^{*^4}-b^{*^4}\right)\bar{P}\left[\frac{a^{*^2}}{\varphi_b^*}\sin a^*\cosh b^*-\frac{b^{*^2}}{\varphi_a^*}\cos a^*\sinh b^*\right]\\
&+\frac{k'G^*A^*}{K_{t,b}^*}\frac{k'G^*A^*}{K_{t,t}^*}\frac{\lambda^4}{\left(1+\lambda^2\right)}\left(a^{*^2}-b^{*^2}\right)^2\bar{P}\\
&\qquad\qquad\left[2a^*b^*\left(1-\cos a^*\cosh b^*\right)+\frac{\frac{a^{*^3}}{b^*}\varphi_a^2-\frac{b^{*^3}}{a^*}\varphi_b^{*^2}}{\varphi_a^*\varphi_b^*}\sin a^*\sinh b^*\right]\\
&+\frac{k'G^*A^*}{K_{t,b}^*}\lambda^2\left(a^{*^2}-b^{*^2}\right)\bar{Q}\\
&\qquad\qquad\left[a^*b^*\left(a^*\varphi_a^*-b^*\varphi_b^*\right)\left(1-\cos a^*\cosh b^*\right)-\left(a^{*^3}\varphi_a^*+b^{*^3}\varphi_b^*\right)\sin a^*\sinh b^*\right]
\end{aligned}
$$

$$
\begin{aligned}
N_4 \;=\; & -\left(1+\lambda^2\right)a^*b^*\left(1-\frac{\bar{Q}}{K^*_{r,t}}\right) \\
& \qquad \left[\left({a^*}^3\varphi^*_a+{b^*}^3\varphi^*_b\right)\left(1+\cos a^*\cosh b^*\right)+a^*b^*\left(a^*\varphi^*_a-b^*\varphi^*_b\right)\sin a^*\sinh b^*\right] \\
& -\left(1+\lambda^2\right)a^*b^*\bar{P}\left[\left({a^*}^2-{b^*}^2\right)\left(1-\cos a^*\cosh b^*\right)-\frac{{a^*}^2{\varphi^*_a}^2+{b^*}^2{\varphi^*_b}^2}{\varphi^*_a\varphi^*_b}\sin a^*\sinh b^*\right] \\
& +\left(1+\lambda^2\right)a^*b^*\left({a^*}^2+{b^*}^2\right)\bar{Q}\left[\varphi^*_a\sin a^*\cosh b^*+\overset{*}{\varphi_b}\cos a^*\sinh b^*\right] \\
& -\frac{k'G^*A^*}{K^*_{t,t}}\lambda^2\left({a^*}^2-{b^*}^2\right)\bar{P}\left[\left({a^*}^3\frac{\varphi^*_a}{\varphi^*_b}-{b^*}^3\right)\sin a^*\cosh b^*-\left({b^*}^3\frac{\varphi^*_b}{\varphi^*_a}-{a^*}^3\right)\cos a^*\sinh b^*\right] \\
& -\frac{\left(1+\lambda^2\right)}{K^*_{r,b}}{a^*}^2{b^*}^2\left({a^*}^2+{b^*}^2\right)\left(1-\frac{\bar{Q}}{K^*_{r,t}}\right)\left[a^*\cos a^*\sinh b^*-b^*\sin a^*\cosh b^*\right] \\
& +\frac{\left(1+\lambda^2\right)}{K^*_{r,b}}{a^*}^2{b^*}^2\left({a^*}^2+{b^*}^2\right)\bar{P}\left[\frac{a^*}{b^*\varphi^*_b}\cos a^*\sinh b^*+\frac{b^*}{a^*\varphi^*_a}\sin a^*\cosh b^*\right] \\
& +\frac{\left(1+\lambda^2\right)}{K^*_{r,b}}{a^*}^2{b^*}^2\left({a^*}^2+{b^*}^2\right)\bar{Q}\left(\frac{a^*}{b^*}+\frac{b^*}{a^*}\right)\cos a^*\cosh b^* \\
& -\frac{\lambda^2}{K^*_{r,b}}\frac{k'G^*A^*}{K^*_{t,t}}\left({a^*}^4-{b^*}^4\right)\bar{P}\left(\frac{{a^*}^3}{\varphi^*_b}-\frac{{b^*}^3}{\varphi^*_a}\right)\cos a^*\cosh b^* \\
& +\frac{k'G^*A^*}{K^*_{t,b}}\lambda^2a^*b^*\left({a^*}^4-{b^*}^4\right)\left(1-\frac{\bar{Q}}{K^*_{r,t}}\right)\left[a^*\sin a^*\cosh b^*+b^*\cos a^*\sinh b^*\right] \\
& -\frac{k'G^*A^*}{K^*_{t,b}}\lambda^2\left({a^*}^4-{b^*}^4\right)\bar{P}\left[\frac{{a^*}^2}{\varphi^*_b}\sin a^*\cosh b^*-\frac{{b^*}^2}{\varphi^*_a}\cos a^*\sinh b^*\right] \\
& -\frac{k'G^*A^*}{K^*_{t,b}}\lambda^2\left({a^*}^2+{b^*}^2\right)^2\left({a^*}^2-{b^*}^2\right)\bar{Q}\sin a^*\sinh b^* \\
& +\frac{k'G^*A^*}{K^*_{t,b}}\frac{k'G^*A^*}{K^*_{t,t}}\frac{\lambda^4}{\left(1+\lambda^2\right)}\left({a^*}^2-{b^*}^2\right)^2\left({a^*}^2+{b^*}^2\right)\bar{P}\left(\frac{{a^*}^2}{b^*\varphi^*_b}-\frac{{b^*}^2}{a^*\varphi^*_a}\right)\sin a^*\sinh b^* \\
& -\frac{k'G^*A^*}{K^*_{t,b}K^*_{r,b}}\lambda^2a^*b^*\left({a^*}^2-{b^*}^2\right)\left(1-\frac{\bar{Q}}{K^*_{r,t}}\right) \\
& \qquad \left[\left({a^*}^3\varphi_a+{b^*}^3\varphi_b\right)\left(1-\cos a^*\cosh b^*\right)+a^*b^*\left(a^*\varphi^*_a-b^*\varphi^*_b\right)\sin a^*\sinh b^*\right] \\
& -\frac{k'G^*A^*}{K^*_{t,b}K^*_{r,b}}\lambda^2a^*b^*\left({a^*}^2-{b^*}^2\right)\bar{P} \\
& \qquad \left[\left({a^*}^2-{b^*}^2\right)+2a^*b^*\sin a^*\sinh b^*+\frac{\frac{{a^*}^3}{b^*}{\varphi^*_a}^2-\frac{{b^*}^3}{a^*}{\varphi^*_b}^2}{\varphi^*_a\varphi^*_b}\cos a^*\cosh b^*\right] \\
& -\frac{k'G^*A^*}{K^*_{t,b}K^*_{r,b}}\lambda^2\left({a^*}^2-{b^*}^2\right)\bar{Q} \\
& \qquad \left[\varphi^*_b\left({b^*}^4+{a^*}^2{b^*}^2\right)\sin a^*\cosh b^*+\varphi^*_a\left({a^*}^4+{a^*}^2{b^*}^2\right)\cos a^*\sinh b^*\right] \\
& -\frac{k'G^*A^*}{K^*_{t,b}K^*_{r,b}}\frac{k'G^*A^*}{K^*_{t,t}}\frac{\lambda^4}{\left(1+\lambda^2\right)}\left({a^*}^2-{b^*}^2\right)^2\bar{P} \\
& \qquad \left[\left({b^*}^4\varphi^*_b-{a^*}^3b^*\varphi^*_a\right)\sin a^*\cosh b^*-\left({a^*}^4\varphi^*_a-a^*{b^*}^3\varphi^*_b\right)\cos a^*\sinh b^*\right]
\end{aligned}
$$

Appendix C

TREMURI - Parameters of the material law

Table C.1: TREMURI program - parameters of the material law

Parameter	Value	
E	-	Elastic modulus (secant value)
G	-	Shear modulus (secant value)
ρ	-	Density
f_m	-	Compressive strength of the masonry
f_{v0}	-	Initial shear strength of the masonry
f_{vm}	-	Shear strength of the masonry
verification criterion	-	user choice between Turnsek and Cacovic Mohr-Coulomb Mann and Müller
$\delta_{3,T}$	-	limit drift for DL 3 (shear failure)
$\delta_{3,PF}$	-	limit drift for DL 3 (bending failure)
μ	-	Friction coefficient
k_{sec}/k_{el}	2.000	Ratio of between secant and elastic stiffnesses
k_0	0.700	Limit of the initial elastic phase
element type	-	0 if pier 1 if spandrel
α_T	0.800	
β_T	0.800	Hysteretic response - stiffness degradation (shear failure)
γ_T	0.000	Hysteretic response - slope of recharge (shear failure)
α_{PF}	0.800	Hysteretic response - slope of discharge (bending failure)
β_{PF}	0.800	Hysteretic response - stiffness degradation (bending failure)
γ_{PF}	0.700	Hysteretic response - slope of recharge (bending failure)
δ_{PF}	0.600	Hysteretic response - dissipation (bending failure)
$\delta_{4,T}$	-	limit drift for DL 4 (shear failure)
$\delta_{4,PF}$	-	limit drift for DL 4 (bending failure)
$\delta_{5,T}$	-	limit drift for DL 5 (shear failure)
$\delta_{5,PF}$	-	limit drift for DL 5 (bending failure)
$\beta_{E,3}$	0.700	Residual resistance - DL 3 (shear failure)
$\beta_{E,4}$	0.400	Residual resistance - DL 4 (shear failure)
$\beta_{E,PF}$	0.500	Residual resistance (bending failure)
Mix SN	0.950	Boundaries of the domain where a mix failure is considered
Mix DX	1.250	

Appendix D

Compressive length - example of calculation

An example of the design procedure for a URM wall with non-rectangular cross-section subjected to a shear loading is given in this annex. The expressions of the compressive length developed in Chapter V are implemented in this procedure.

A wall with a T-shaped horizontal cross-section is considered. Its geometry is given in Figure D.1 . There are two flanges, one on each side of the shear wall. The effective length of both flanges is $l_{fl,eff} = \min\left(h_{shW}/5\,;\,h_{shW}/2\,;\,6t_{fl}\right) = 0.560$ m, h_w being equal to 2.800 m. The gravity centre of the wall is therefore located at a distance y_G [m] with respect to the side where the maximum vertical compression stress is located (reference point):

$$y_{GC} \quad = \quad \frac{\frac{l_{shW}^2}{2} t_{shW} + 2 l_{fl,eff}\left(d\sigma_{max} + \frac{t_{fl}}{2}\right)}{l_{shW} t_{shW} + 2 l_{fl,eff} t_{fl}}$$

with $d\sigma_{max}$ equals to l_{shW} when the horizontal shear $V_{Ed} > 0$ and 0 when $V_{Ed} < 0$, leading to $y_{GC} = 1.741\,\mathrm{m}$ and $y_{GC} = 0.954\,\mathrm{m}$ respectively.

The wall is characterised by a compressive strength $f_k = 4.36\,\mathrm{MPa}$, a shear strength under no compression $f_{vk,0} = 0.3\,\mathrm{MPa}$

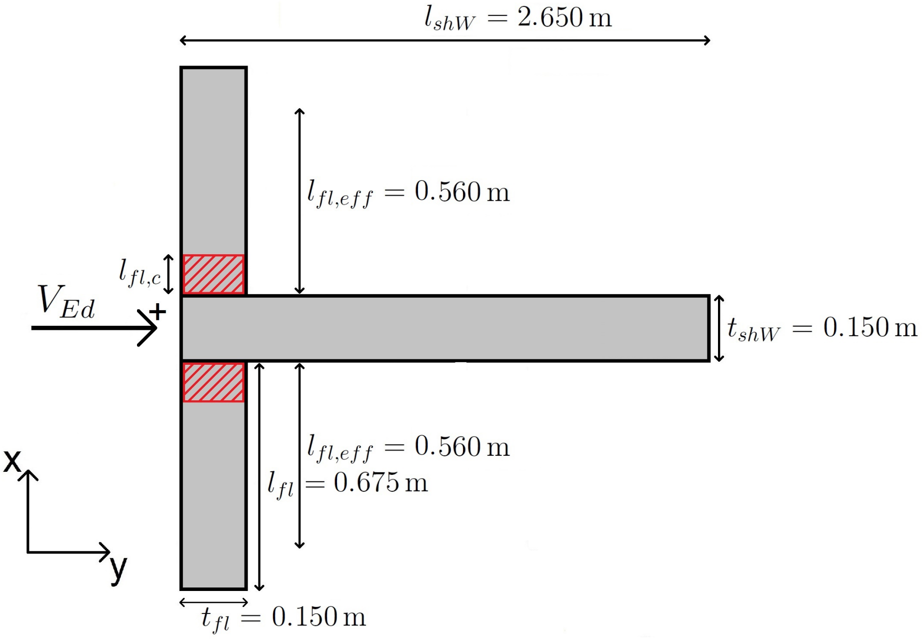
$l_{shW} = 2.650\,\mathrm{m}$
$l_{fl,eff} = 0.560\,\mathrm{m}$
$l_{fl,c}$
V_{Ed}
+
$t_{shW} = 0.150\,\mathrm{m}$
$l_{fl,eff} = 0.560\,\mathrm{m}$
$l_{fl} = 0.675\,\mathrm{m}$
x
y
$t_{fl} = 0.150\,\mathrm{m}$

Figure D.1: Geometry of the example

The design methodology first consists in the determination of the internal forces acting on the wall. The wall is subjected to its own weight N_{pp} and to a vertical compression N_{Ed}, simulating the structural load. Regarding the experimental tests, this latter mainly acts on the shear wall, but also on a part of both flanges as the flanges are connected to the shear wall. The length $l_{fl,c}$[m] of this part has to be estimated and depends on the compression level. The vertical compression N_{Ed} is thus applied at a distance

$$y_{N_{Ed}} = \frac{\frac{l_{shW}^2}{2} t_{shW} + 2 l_{fl,c}\left(d\sigma_{max} + \frac{t_{fl}}{2}\right)}{l_{shW} t_{shW} + 2 l_{fl,c} t_{fl}} \tag{D.1}$$

from the reference point. The expression of the bending moment M_{Ed} induced by the horizontal shear V_{Ed} and the compression load N_{Ed} is given by

$$M_{Ed} = V_{Ed} h_w + N_{Ed} \left(y_{GC} - y_{N_{Ed}} \right)$$

and the eccentricity is

$$e = \frac{M_{Ed}}{N_{Ed} + N_{pp}}$$

with N_{pp}, the compression due to the weight of the wall. This latter acts at the centroid of the wall and, hence, does not involve a bending moment.

Then, the compressive length l_c [m] can be calculated with the exact (Eq. V.15) and simplified expressions given in Chapter V. The use of the exact expression requires the use of a numerical tool to calculate the value of the compressive length with respect to the eccentricity.

Once the compressive length determined, three limit states have to be verified (Eqs. V.27, V.28 and V.29):

- the shear resistance

$$\begin{aligned} V_{Ed} &\leq V_{Rd} \\ &\leq f_{vd} \, A_c \end{aligned} \tag{D.2}$$

with $f_{vd} = f_{vk0}/\gamma_M + 0.4\,\sigma_d$.

- the compression resistance

$$\begin{aligned} N_{Ed} &\leq N_{Rd} \\ &\leq f_d \, A_c \end{aligned} \tag{D.3}$$

with $f_d = f_k/\gamma_M$.

- the overturning

$$l_c \geq 0 \tag{D.4}$$

The parameter A_c [m^2] is the area of the wall under compression and $\sigma_d = \left(N_{pp} + N_{Ed} \right) / A_c$ and γ_M is taken as equal to unity in this example.

A first guess of the horizontal shear V_{Ed} is made and the methodology is applied. The value of V_{Ed} is then increased until one of the three limit states is not verified. If the initial value of V_{Ed} does not verify all the limit states, it has to be reduced. This iterative procedure leads to the shear resistance of the studied wall. Table D.1 tabulates the values of the main parameters when the exact expression of the compressive length is used.

Table D.1: Results of the methodology for the detailed example

	$V_{Ed} > 0$		$V_{Ed} < 0$	
Parameter	Value	Units	Value	Units
$l_{fl,c}$	0.091	m	0.091	m
$y_{N_{Ed}}$	1.414	m	1.246	m
N_{Ed}	298 125	N	298 125	N
N_{pp}	14009	N	14009	N
V_{Ed}	116 581	N	131019	N
M_{Ed}	$4.236 \cdot 10^5$	Nm	$2.801 \cdot 10^5$	Nm
e	1.357	m	0.897	mm
l_c	1.151	m	0.174	m
A_c	0.173	m^2	0194	m^2
f_{vk}	0.675	MPa	0.675	MPa
N_{Rd}	753 651	N	846 988	N
V_{Rd}	116 582	N	131020	N

The results show that the wall fails in shear under a load of 116 581 N when the flange is decompressed ($V_{Ed} > 0$) and of 131 019 N when this latter is over-compressed ($V_{Ed} < 0$). The use of the simplified expression for the calculation of the compressive length gives similar results, namely 116 681 N and 131 185 N. The compressive length is slightly overestimated by the simplified relation when the flange is over-compressed (+ 0.9 %). When the contribution of flanges is neglected, the application of the procedure results in the same value for both directions of loading, namely 104 460 N. The relative difference is therefore about 10 % and 20 %, for $V_{Ed} > 0$ and $V_{Ed} < 0$ respectively.

In this example, it is found that $l_{fl,c} = 0.091\,\text{m}$ provides the lowest difference with the experimental results, in both directions of shear loading.

Curriculum Vitae

Christophe Mordant
Department of Architecture, Geology, Environment and Constructions
Université de Liège
4000 Liège - Belgium

Education

2012-2016 Université de Liège
Doctor of Philosophy in Civil Engineering

2010-2012 Université de Liège
Master of Science in Civil Engineering
Master dissertation : Contribution to experimental tests on the seismic behaviour of masonry structural elements

2007-2010 Université de Liège
Bachelor of Art in Civil Engineering

Professional experience

2013 Research Engineer, Université de Liège

Publications

Journal Articles

1. Mordant, C., Degée, H., Denoël, V. (2016). *Identification of equivalent mechanical properties for unreinforced masonry walls.* International Journal of Masonry Research and Innovation (under review).

2. Jäger, A., Mendes, L., Degée, H., Mordant, C., Lu, S. (2014). *Rütteltisch-Versuche an Gebäuden aus wärmedämmendem Ziegelmauerwerk.* Mauerwerk, 18(2), 67–77.

Chapters of a book

1. Mordant, C., Dietz, M., Taylor, C., & Degée, H. (2015). *Seismic Behaviour of Thin-Bed Layered Unreinforced Clay Masonry Frames with T- or L-Shaped Piers.* In Experimental Research in Earthquake Engineering (pp. 269–293). Springer International Publishing.

2. Jäger, A., Lu, S., Degée, H., Mordant, C., Chioccariello, A. Rakicevic Z., SIn A., Ilki & M., Fardis (Eds.), Seismic Evaluation and Rehabilitation of Structures, Geotechnical, Geological and Earthquake Engineering 26 (pp. 77–93). Springer.endova, V., Mendes, L., Candeias, P., Campos Costa, A., Correia, A.A., Coelho, E. (2015). *Full-scale Testing of Modern Unreinforced Thermal Insulation Clay Block Masonry Houses.* In Experimental Research in Earthquake Engineering (pp. 229–246). Springer International Publishing.

3. Mordant, C., Dietz, M., Taylor, C., Plumier, A., & Degée, H. (2014). *Seismic behavior of Thin-Bed Layered Unreinforced Clay Masonry Shear Walls Including Soundproofing Elements.* In Seismic Evaluation and Rehabilitation of Structures (pp. 77–93). Springer International Publishing.

International conference papers

1. Mordant, C., Denoël, V., & Degée, H. (2016). *Seismic behaviour of Land T-shaped unreinforced masonry shear walls.* Proceedings of the 16th International Brick and Block Masonry Conference (pp. 1767–1775).
2. Mordant, & Degée, H., Vandoren, B. (2016). *Comparison of equivalent beam models and refined approaches for the modelling of masonry portal frames.* Proceedings of the 16th International Brick and Block Masonry Conference (p. 263–268).
3. Mordant, C., Denoël, V., & Degée, H. (2015). *Comparison of experimental results and numerical modelling of unreinforced load-bearing masonry structures subjected to earthquake loading.* Proceedings of the SECED 2015 Conference: Earthquake Risk and Engineering towards a Resilient World.
4. Mordant, C., Denoël, V., & Degée, H. (2015). *Rocking behaviour of simple unreinforced load-bearing masonry walls including soundproofing rubber layers.* Proceedings of 5th ECCOMAS Thematic Conference on Computational Methods in Structural Dynamics and Earthquake Engineering.
5. Cattari, S., Chioccariello, A., Degée, H., Doneux, Lagomarsino, S., & Mordant, C. (2014). *Seismic assessment of masonry buildings from shaking table tests and nonlinear dynamic simulations by proper orthogonal decomposition (POD).* Proceedings of the Second European Conference on Earthquake Engineering and Seismology.
6. Degée, H., Mordant, C., Candeias, P., Mendes, L., Campos Costa, A., Coelho, E., Lu, S., & Jaëger, A. (2014). *Seismic performances of modern unreinforced thermal insulation clay blocks masonry houses.* Proceedings of the 9th International Conference on Structural Dynamics, EURODYN 2014 (pp. 323 -328).
7. Mendes, L., Candeias, P., Correia, A., Campos Costa, A., Coelho, E., Jäger, A., Lu, S., Degée, H., & Mordant, C. (2014). *Full-scale seismic testing of modern unreinforced thermal insulation clay block masonry houses.* Proceedings of the 9th International Masonry Conference 2014.
8. Mordant, C., & Degée, H. (2014). *Shake table tests on unreinforced load-bearing masonry sub-structures.* Proceedings of the Second European Conference on Earthquake Engineering and Seismology.
9. Mordant, C., Dietz, M., Taylor, C., & Degée, H. (2014). *Shaking table tests on unreinforced load-bearing masonry frames.* Proceedings of the 9th International Conference on Structural Dynamics, EURODYN 2014 (pp. 229-236).
10. Mordant, C., Taylor, C., Dietz, M., Vasseur, L., & Degée, H. (2014). *Shaking table tests on unreinforced load-bearing masonry structures.* Shaking table tests on unreinforced load-bearing masonry structures

11. Vasseur, L., Mordant, C., & Degée, H. (2014). *Experimental testing on modern clay masonry structures.* Proceedings of the Second European Conference on Earthquake Engineering and Seismology.

12. Mordant, C., Dietz, M., & Degée, H. (2013). *Experimental tests on the seismic behaviour of unreinforced load-bearing masonry structures.* Proceedings of Vienna Congress on recent advances in earthquake engineering and structural dynamics (VEESD 2013).

13. Mordant, C., Vasseur, L., & Degée, H. (2013). *Seismic performances of modern unreinforced multi-storey clay masonry buildings based on pushover analysis.* Proceedings of Vienna Congress on recent advances in earthquake engineering and structural dynamics (VEESD 2013) (pp. 241).

14. Mordant, C., Dietz, M., & Degée, H. (2013). *Shaking table tests on unreinforced load-bearing masonry walls - Comparison with simple rocking models.* Proceedings of the 4th International Conference on Computational Methods in Structural Dynamics and Earthquake Engineering, Proceedings - An IACM Special Interest Conference (pp. 2849-2865).

15. Degée, H., Mordant, C., Lascar, L., & Vasseur, L. (2013). *Assessment of the seismic performances of modern unreinforced multi-storey clay masonry buildings.* Proceedings of the 4th International Conference on Computational Methods in Structural Dynamics and Earthquake Engineering, Proceedings - An IACM Special Interest Conference.